PERMEABILITY - PAST AND PRESENT- IN CONTINENTAL CRUSTAL BASEMENT

Stephen John Hay
B. Sc. (Hons.) Dundee.

Thesis submitted in fulfilment of the degree of Doctor of Philosophy (by research) in the Faculty of Science, Department of Geology, University of Glasgow.

October 1988.

To Fiona, for all her support.

ACKNOWLEDGEMENTS

Jeremy Hall, as the principal supervisor, was the inspiration behind this project. He kindly allowed me access to ten years of unpublished permeability data and note books, as well as lending me his collection of cores. Our discussions throughout the period, provided me with invaluable information and his comments were always worthwhile. Thanks must also go to his family, for their hospitality during my stay with them in St. John's. Any advancements I have been able to make upon his original works are largely due to his guidance over the three years.

Gene Simmons contribution to this work extends far beyond the time I spent in his laboratory at Massachusetts Institute of Technology. He provided me with literally hundreds of hours of S.E.M. time, thousands of Polaroid prints, accommodation and car. Gene, along with Dorothy Richter, made me feel very much at home and I shall always be in their debt.

At the Scottish Universities Research and Reactor Centre, East Kilbride, the efforts of Tony Fallick and Joe Hamilton were appreciated. I benefitted greatly from their comments, our discussions and from using equipment under their supervision.

Colin Farrow took over as principal supervisor when Jeremy Hall left for Canada, and provided help when required in the last year. His tireless assistance with computing was, at all times, appreciated. He also read over, and commented on, the drafts of this thesis.

Mike Russell provided facilities for fluid inclusion analysis at Strathclyde University, as well as his time for discussions, for which I am grateful.

Discussions, comments, and help (in one form or another) from Gawen Jenkin, John Brint, Mark Wood, Gill Whelan and Simon George are all appreciated.

Technical assistance by Bob Cumberland, George Gordon, Kenny Roberts, George Bruce, Robert MacDonald and Roddy Morrison at Glasgow made things much easier. The photographic assistance of Douglas MacLean throughout my time at Glasgow, and also in producing the plates and figures for this thesis, was invaluable.

At S. U. R. R. C., Terry Donnely, Peter Ainsworth, Allison MacDonald, Julie Gerc, Ward Scott, Andrew Tait and Fred Cornwalis provided technical assistance. Julie Gerc and Allison MacDonald ran some oxygen samples, Adrian Boyce analysed the Barite, and Mitch Macintyre ran the K/Ar sample, they are all kindly thanked; as are the technicians at Strathclyde University who prepared the fluid inclusion wafers. Tom Wissler and Carolyn Emerson provided help with the S.E.M. work at MIT and MUN respectively.

My parents are thanked for their financial assistance in my first year, I promise to

pay it back some day!

Final thanks go to Fiona, for putting up with me and the many other efforts she made to help me.

This work was funded by a NERC studentship. S.E.M. analysis carried out at MIT was funded by NERC and Gene Simmons (through a United States Department of Energy grant). S.E.M. analysis carried out at MUN was financed by NERC and Jeremy Hall (through his NSERC operating grant). All incidental costs, incurred during this research, were paid for by the author.

LIST OF CONTENTS

LIST OF FIGURES

Chapter 5

Chapter 6

Appendix

LIST OF TABLES

Chapter 2

Chapter 4

Chapter 5

Chapter 6

LIST OF PLATES

Chapter 4

Notation of variables in equations

Crack closure, porosity and permeability equations

All permeability units are equivalent to darcy where, L = centimetres, M = grammes and T = seconds.

Variable			Dimensions
a	=	Crack aspect ratio	- - - - -
A	=	Surface area for flow	(L^2)
b	=	Crack half width	(L)
b_o	=	Original crack half width	(L)
B	=	Constant related to free gas movement	- - - - -
β_s	=	Rock compressibility	$(ML^{-1}T^{-2})$
B_{vol}	=	Bulk volume of rock	(L^3)
C	=	Constant related to flow type	- - - - -
D	=	Rock core diameter	(L)
ΔP	=	Pressure head gradient	$(ML^{-1}T^{-2})$
ΔL	=	Flow path length gradient	(L)
ΔV_p	=	Change in pore volume	(L^3)
E	=	Crack-wall asperities absolute height	(L)
ε	=	Young's modulus	$(ML^{-1}T^{-2})$
F	=	Fracture surface characteristic factor	- - - - -
g	=	Acceleration due to gravity	(LT^{-2})
γ	=	Kin ematic fluid viscosity	$(ML^{-1}T^{-1})$
h	=	Crack-wall asperitie distribution factor	- - - - -
K	=	Permeability	(L^2)
K_a	=	Apparent permeability	(L^2)
K_f	=	Fracture permeability	(L^2)
K_o	=	Original permeability	(L^2)
K_s	=	System permeability	(L^2)
K_t	=	True permeability	(L^2)
l	=	Crack length	(L)
λ	=	Average free movement of gas	(L)
P	=	Pressure	$(ML^{-1}T^{-2})$

P_a	=	Upstream pressure	$(ML^{-1}T^{-2})$
P_c	=	Confining pressure	$(ML^{-1}T^{-2})$
P_e	=	Effective pressure	$(ML^{-1}T^{-2})$
P_m	=	Average pressure	$(ML^{-1}T^{-2})$
P_o	=	Original pressure	$(ML^{-1}T^{-2})$
P_p	=	Pore pressure	$(ML^{-1}T^{-2})$
Px	=	Downstream pressure (atmospheric)	$(ML^{-1}T^{-2})$
μ	=	dynamic fluid viscosity	$(ML^{-1}T^{-1})$
NC	=	Number of cracks	- - - - -
n_b	=	Background linear crack density	- - - - -
n_i	=	Intergranular linear crack density	- - - - -
η	=	Porosity	%
Q	=	Flow rate	(L^3T^{-1})
Q_m	=	Mass flow rate	(L^3T^{-1})
Q_p	=	Flow rate at pressure p	(L^3T^{-1})
r	=	Channel width	(L)
re	=	Core outer radius	(L)
rw	=	Core central bore radius	(L)
ρ	=	Fluid density	(ML^{-3})
S	=	Fracture roughness constant	- - - - -
Ss	=	Fracture spacing	(L)
T	=	Tortuosity factor	(L)
V	=	Poisson's ratio	- - - - -
V_{vol}	=	Void volume	(L^3)
W_{dry}	=	Core dry weight	(M)
W_{sat}	=	Core saturated weight	(M)
l_o	=	Crack length orthogonal to flow direction	(L)
l_p	=	Crack length orthogonal to flow direction	(L)

Isotope equations

A	=	Avagadro's constant (6.022045×10^{-23} mol^{-1})
$Abx_{(n)}$	=	Abundance of normal element
$Abx_{(s)}$	=	Abundance of spike
α	=	Fractionation factor
β	=	Mol. % cation substitution
β^-	=	Beta particle
δ	=	Isotopic ratio of a substance, relative to a standard
Δ	=	The difference in isotopic ratios between two substances
γ	=	Anti neutrino
K	=	Equilibrium constant
K.E.	=	Kinetic energy
K_T	=	Total potassium content
λ	=	Decay constant (10^{-11} Y^{-1})
$\lambda\beta$	=	$^{40}K \rightarrow {}^{40}Ca$ decay constant (4.962×10^{-11} Y^{-1})
λe	=	$^{40}K \rightarrow {}^{40}Ar$ decay constant (0.581×10^{-11} Y^{-1})
m	=	Mass
N	=	Number of atoms of normal element
Q	=	Decay energy
R_{SAMP}	=	Isotopic ratio of the sample
R_{STD}	=	Isotopic ratio of the standard
Rxy	=	Ratio of isotopes x and y in a mixture
S	=	Number of atoms in the spike
T	=	Absolute temperature Kelvin ($K = °C + 273.15$)
t	=	Time of formation (ma)
v	=	Velocity
W	=	Atomic weight

SUMMARY

The examination of microcracks from the Lewisian of the northwest highlands of Scotland, has revealed the sequential development of microcrack networks, sealed by minerals deposited from fluids passing along them. Comparisons, between open and sealed microcracks, indicate that both thermal and mechanical stresses were active in the formation of the cracks. Several mechanisms which may allow a crack to remain open under compressive stress have been seen, and it is found that microcracks may act as recurring fluid pathways. Observations on the crack-sealing minerals have allowed inferences on the nature of fluid flow within the Lewisian crystalline basement to be made.

The sealed cracks were formed as a result of both localized, and regional, periods of fluid flow through the basement. This fluid flow took place over a period spanning some two billion years (from the Archaean Badcallian metamorphic event, to the late-Proterozoic Torridonian rifting). Several magnetite crack sealing events, specific to lithologies and structures, occurred during pre-Torridonian times. These were associated with the Scourian and Laxfordian metamorphic cycles. However, most sealed cracks are post-tectonic.

Four main post-Laxfordian regional sealing events have been identified, and are characterized by the sealing mineral sequence of; K-feldspar + calcite; prehnite + albite + calcite; pumpellyite + quartz + calcite; and stilpnomelane. Crack-crack intersections indicate that this sequence of crack sealing is consistent throughout the Lewisian's central region. Investigation of these sealed cracks, using mineral PTX considerations, stable isotopes, fluid inclusions and radiometric isotopes, suggest that this sequence relates to a period of hydrothermal activity within the Lewisian complex, associated with Torridonian basin subsidence and rifting.

The study suggests that the fluid passing along the cracks was originally a surface derived meteoric water. This permeated into the basement gneisses along subvertical, NE-SW, microcracks and joints, which were dilating during the Torridonian extension. Pressure estimates suggest that the currently exposed Lewisian surface was in the region of 3 km deep when the fractures were sealing. The precipitated mineral sequence was the result of a cooling and evolving hydrothermal system, progressing from about 350 °C to 250 °C with time. Changes in fluid character, over the time of fracture sealing, can be accounted for by a combination of fluid / wall-rock interaction and deepening of the Torridonian rift valley.

The present day porosities and permeabilities of Lewisian gneisses are low, averaging less than 1% for porosity, and in the region of 100 nd to 10 μd (10^{-19}-10^{-17} m^2) for permeability. Both of these properties are inhomogeneous between lithologies and within samples. Estimates of porosity, using S.E.M. photographs, have shown that porosity can be considered at two separate levels within crystalline rocks. Firstly, porosity due to background cracks (grain boundary and intragranular cracks), and secondly, porosity due to intergranular cracks. Using S.E.M. pictures, the porosity can be quite closely estimated.

A model has been developed whereby the present permeability of a crystalline rock can be accurately estimated by calculations involving the width and length of the fractures, and the linear crack density. Application of this model, to sealed cracks found in the Lewisian, suggest that most crack arrays would have accounted for permeabilities of between 1 and 10 μd. This is within the present day limits for most of the Lewisian rocks. The sealed cracks present within the Lewisian (and used in palaeopermeability calculations) largely formed when the presently exposed gneiss was close (<5 km) to the surface. For this reason little information has been gained on the possible nature of fluid flow within the lower crust.

CHAPTER 1

MICROCRACKS IN ROCKS: A SUMMARY

1.1 Introduction to the project

Highly reflective lower continental crust is a feature found on many of the deep seismic reflection profiles of the last decade, that have been used to image the major crustal structure of the earth. Some of the best examples of such reflective lower crust come from the BIRPS group (British Institutions Reflection Profiling Syndicate), whose deep lines off the West coast of the United Kingdom have consistently imaged deep reflectors. WINCH (Western Isles North Channel Line) and SWAT (South Western Approaches Traverse) are two of the better examples, shot across the northwest European extensional margin, to the West of Scotland and in the southwest approaches to the English Channel respectively.

The repetition of the profile found in SWAT and WINCH, on other profiles around the U.K. coast, led to the term a "typical BIRP" (Matthews & Cheadle 1986). A typical BIRP consists of a seismically transparent upper crust, a highly reflective lower crust and a pronounced Moho at about 10 seconds two way time. The crust and mantle are often dissected by a series of dipping reflectors representing the image of major faults, such as the Outer Isles Fault Zone or the Flannan Thrust.

Reflective lower crust has also been imaged by COCORP (Consortium for Continental Reflection Profiling) in many lines, including the CALCRUST line over the North American Cordillera (Henyey *et al.* 1987) and in the Mojave Desert (Louie & Clayton 1987). In Canada, the LITHOPROBE group (Canadian programme for the study of the continental lithosphere) have imaged lower crustal reflectors across Vancouver Island (Green *et al.* 1987). Similar reflective lower crust has also been imaged by the French group ECORS (Etude de la croute Continentale et Oceanique par reflexion et refraction seismiques) across the Bay of Biscay and the Paris Basin (Pinet *et al.* 1987). Although these packages of short subhorizontal reflections have become well recognised as representing lower continental crust, the features producing the reflectors is a strong topic for debate.

Various hypotheses have been put forward to explain the reflectors presence and the physical contrasts within the lower continental crust that are required for their production. These include igneous layering (Smithson *et al.* 1987), shear zones (Louie & Clayton 1987, Smithson *et al.* 1987) and free pore fluid (Jones 1987, Louie & Clayton 1987). Others, such as Hall (1987), prefer a combination of layering and shearing, with reflectivity enhanced by layer-variable water content.

The idea that a free, or trapped, pore fluid may be responsible, either partly or

wholly, for the reflections, stems from coincident electromagnetic (EM) studies and seismic reflection profiles. These have been carried out in various parts of the world, i.e. the Scottish Southern Uplands (Beamish & Smythe 1986), Vancouver Island (Green *et al.* 1987), Rhenish Massif (Meissner *et al.* 1983, Jodicke *et al.* 1983), northern France (Bois *et al.* 1986) and the Adirondacks (Connerney *et al.* 1980, Klemperer *et al.* 1985). These studies indicate that the reflective lower crust is coincident with a zone of low resistivity, or high conductivity, perhaps consistent with a free fluid phase.

Jones (1987) proposed a model to explain the high conductivity and reflectivities of the crust based on the model for fluid circulatory systems of Etheridge *et al.* (1983). He postulated a dry upper crust with no fluid and resistivities of about 10^4 Ωm. The top of the lower crust, or the Conrad discontinuity, marked the top of the reflective zone where temperatures were in the range of 400 °C - 500 °C. Here fluid generated by dehydration reactions at a deeper level was free, but trapped against the impermeable upper crust. In this area resistivities dropped closer to 10 Ωm, and fluid in this zone my be undergoing active circulation. The third layer is the lower-lower crust. This also contains a free fluid phase, but not in interconnected pores. Hence resistivities are higher (of the order of 10^2 -10^3 Ωm). If the top of the impermeable zone is at about 400 °C, as Jones suggests, it approximately corresponds to the temperature derived for the top of the reflective zone which, from comparisons of heat flow and seismic reflection, occurs between 300 °C and 400 °C (Klemperer 1987).

Studies on crystalline rock at low temperatures (300 °C - 600 °C) and pressures (0.5 - 2 kb) (Brantley *et al.* 1986, Vaughan *et al.* 1986), have shown that fluids permeate through them primarily along intersecting open fractures with a low aspect ratio (Brace 1977, Hadley 1976). These fractures become sealed by mineral phases precipitated from the passing fluid (Brantley *et al.* 1986, Vaughan *et al.* 1986). It follows that sealed fractures record evidence of fluid flow events which occurred within a rock, and may provide an insight into the nature of fluid processes acting within the crust.

The discovery of a suite of sealed microcracks within the Lewisian gneiss of N.W. Scotland (Hall 1986) forwarded the possibility that evidence for free fluid phases within the deep crust may be preserved as sealed cracks. The nature of the Lewisian , an old and dry region of crust, enhanced this possibility, as it might be expected to retain evidence of a long history of fluid flow since its formation.

The aim of the project was to investigate the sealed microcracks found within the Lewisian gneiss, and to assess the porosity and permeability these cracks may have afforded the gneiss at depth. It was hoped this would provide an indicator as to the level of

fluid phase which may be present within insitu lower to mid-crustal rocks today.

1.2 Microcracks: classification by origin, location and size

Microcracks may be classified by two main methods (see Simmons & Richter 1976). The first, relies on the method of formation of the crack, which can be derived by the fractures morphological character. The second, a more general method, is based on the relation of the microcrack to the crystals of the rock.

1.2.1 Classification by mode of crack formation

The origins of microcracks in rock may be due to many processes. Essentially, they are produced when " local stress exceeds local strength " (Simmons & Richter 1976). These local stresses are either mechanically or thermally induced. The types of microfracture found and their modes of formation, as described by Simmons & Richter, are as follows:

δPδT cracks.

Stress induced cracks (SIC).

Radial cracks about totally enclosed grains (RDC).

Concentric cracks about totally enclosed grains (CNC).

Tube cracks (TBC).

Thermal cycling cracks (TCC).

Thermal gradient cracks (TGC).

Shock induced cracks (SHIC).

Cleavage cracks (CLC).

Thin section cracks (TSC).

Cracks of unknown origin (UC).

A summarized account of the characteristics and formation of these cracks is given below.

δ PδT cracks

Termed δPδT due to their formation as result of pressure and temperature interaction. These cracks are essentially a function of the tensor properties and relative orientation of adjacent mineral pairs. δPδT cracks are confined to grain boundary locations and are believed to form where "the average linear strain in the vicinity of the grain boundary exceeds the average linear strength". They are believed to be produced primarily during uplift and unroofing.

Stress induced cracks

These are formed as a result of, and in relation to, non-hydrostatic stress within the rock and are independent of crystallographic orientations. They tend to be the largest microcrack type, often existing as orientated arrays. Their development may be along grain boundary systems, or may be partly affected by them. They are usually transgranular and extend through several crystals.

Radial and concentric cracks

The principal reason for the formation of these cracks is the mismatch of volumetric properties between host and enclosed crystal, which leads to stress buildup. The resulting fractures may be one of three types:

(a) coincident grain boundary fracture;

(b) non-coincident grain boundary fracture; and

(c) radial fracture extending from the grain boundary.

As before, pressure and temperature control their formation.

Tube cracks

Tube cracks (or microtubes) are common in many rocks and may, or may not, be crystallographically controlled. It is common for them to emanate from grain boundaries, and several different methods of formation have been suggested, including:

(a) tube cracks as solution features due to primary or secondary groundwater; and

(b) tube cracks as features produced by partly healed flat cracks.

Such microtubes have been studied by Richter & Simmons (1977) and Shirey *et al.* (1980).

Thermal cycling cracks

Thermal cycling produces predominantly coincident grainboundary cracks. These have a significant effect on the physical properties of rocks and can be recognised from other grain boundary cracks in this way. They often totally surround crystals and are relatively wide. Non-coincident varieties are rare (see Simmons & Cooper 1978).

Thermal gradient cracks

Thermal gradient cracks are formed as a result of stress produced by high thermal gradients in a rock. These have not been investigated but are likely to be grain boundary systems.

Shock induced cracks

These have principally been described from rocks involved in nuclear tests, impact craters and lunar samples. Shock induced cracks have a large effect on the physical properties of their host rock. They are characteristically intergranular (or "multi-grain") cracks, many of which lie in parallel subsets. They have been studied by Siegfried *et al.* (1977) and Padovani *et al.* (1978).

Cleavage cracks

The orientation of cleavage cracks is entirely due to the crystallographic orientation of their host mineral. They very often have perpendicular microtubes growing from the cleavage crack into the host mineral. Cleavage cracks are especially common in pyroxene and feldspar.

Thin section cracks and cracks of unknown origin

Thin section cracks are formed as a result of the process of thin section making and can be common. However, careful cutting and polishing sequences largely eliminate them (Simmons & Richter 1976) .

Finally, any other crack which cannot be accommodated an aforementioned set, is termed of unknown origin. They are usually complex systems and rarely found.

1.2.2 Classification by crack morphology

The ten formational criteria can be combined to form four basic morphological types of crack, as outlined by Simmons & Richter (1976) and Kranz (1983). These are:

(a) grain boundary cracks;
(b) intracrystalline or intragranular cracks;
(c) cleavage cracks; and
(d) intercrystalline or intergranular cracks.

Grain boundary cracks

This group covers any fracture which runs in a concordant manner along a crystal-crystal edge, or one which runs for a short distance into the crystal from the crystal edge. Mineralogy is believed to be a primary control (Padovani *et al.* 1982), along with the tectonothermal history of the host rock.

Intracrystalline or intragranular cracks

Under the classification of Simmons & Richter (1976), these are wholly confined to a single crystal and should not terminate at a crystal boundary. Many intragranular cracks appear to be extensional and they have sharp walls and tips, where they are mechanically formed, or rough walls and blunt tips, where solution may be a method of formation.

Cleavage cracks

These are essentially intragranular cracks in which the direction of propagation is controlled by the orientation of the host crystal's lattice. They are confined to a single crystal and have a strong mineralogical control.

Intercrystalline or intergranular cracks

Intergranular cracks are the widest and the longest of the cracks. They are usually transgranular (cutting more than one crystal), and are formed as a result of a tectonic stress of a non-hydrostatic nature. In mechanically stressed rock, the crack tip to crack tip orientation is usually sub-parallel to the macroscopic maximum stress direction, and their extension is parallel to the minimum deviatoric stress direction. Most of these cracks are extensional, although those exhibiting only shear, or a combination of both shear and extension, are found.

This classification results in some confusion. The example illustrated in Plate 4.2c is clearly a cleavage crack and relates only to the cleavage of the pyroxene. However, if the classification were to be strictly adhered to, it would be classified as a non-coincident grain boundary crack because it terminates at the grain boundary. As a result of this ambiguity, throughout this thesis there will be three main crack sets used:

(a) grain boundary cracks, to describe coincident grain boundary cracks;
(b) intragranular cracks, to describe true intragranular cracks, cleavage cracks and the non-coincident grain boundary cracks of Simmons & Richter (1976); and
(c) intergranular cracks, to describe the large transgranular cracks which cross cut more than one mineral.

This classification is felt to be sufficient to describe the fracture morphology and occurrence in relation to the crystals. While this does not describe the formation of the fractures as succinctly as that of Simmons & Richter (1976), it closely follows their broader classification and that of Kranz (1983)(with the exception of cleavage cracks,

here grouped with the intragranular cracks).

1.2.3 Microcrack size and shape

The sizes of microcracks have been studied by many workers, using a variety of methods (see Kranz 1983 for a summary). A microcrack as defined by Simmons & Richter (1976) is:

> "An opening that occurs in rocks, where one dimension is much less than the other two. The width to length ratio (2b/l), or crack aspect ratio (a), must be less than 10^{-2} and is usually 10^{-3} to 10^{-5}. Length may be as great as meters, but typically is in the order of micrometers".

This therefore excludes faults and vugs, but may include some joints. Kranz (1983) summarized the overall conclusions on fracture size, aspect ratio and crack densities (the number of cracks per unit area) from some twenty-one previous workers. His conclusions can be summarized as follows:

> In relation to applied stress, longer cracks are more commonly observed in stressed as opposed to unstressed rock. The average crack length increases and the average aspect ratio decreases as the applied stress increases. The crack densities increase, and change from spatially random to non-random higher density regions, as stress is increased. Crack densities decrease rapidly away from a fault, and the increase in stress favours the formation of intergranular cracks (as seen by the lowering of the grain boundary to intergranular crack ratio).
>
> Mineralogy also plays a role in the density of cracks within a rock. Generally the stiffest materials contain the greatest number of cracks, but susceptibility to cleavage cracking along the existing weakness of a crystal may be equally important. Similarly at high pressures, generation of fractures is greatest in stiff materials, whereas minerals like calcite prefer twinning to fracturing. Aspect ratios; either measured directly using the optical microscope and S.E.M.; or indirectly using seismic velocity, resistivity and differential strain analysis (DSA), are in the order of 10^{-3} to 10^{-5}.

In many respects, the size and aspect ratio of a fracture describes its shape. However, this is limited to two dimensions and to single simple cracks whose orientations do not deviate greatly from planar. There have been many descriptions and reports of

crack morphologies which differ from the simple, flat, "penny shaped" crack used almost exclusively in theoretical models. The use of a simple shape is easily understood, as the models would become unreasonably complex if every irregularity were considered. Studies on fracture permeability have shown that irregularities can affect fluid flow and therefore errors in simple models are present. However in some studies, simple crack theory and practice are remarkably similar. DSA is one such area (see Simmons *et al.* 1978).

1.3 Response of cracks to mechanically induced stress

1.3.1 Conditions for crack opening

Mechanisms of fracture opening can be thought of as being due to one of two factors: a response to thermally induced stresses; or, as a response to mechanically induced stresses.

The work of Batzle *et al.* (1980) on Westerly granite and Frederick diabase showed how pre-existing fractures could be opened as a response to their direction with regard to the maximum stress direction. Here, simultaneous shear, extension and compression were seen acting on crack arrays in ways dependent on their orientation relative to that of the principal compressive stress. Observations showed loose crystals or irregular walls may maintain open porosity and prevent the crack from closing under compressive stress.

On a larger scale, during the geothermal experiment at Camborne (Pine & Batchelor 1984), water pressure effectively increased the horizontal stress ratio from about 1: 2.5 to 1: 5 at a depth of 2 km. Consequent shearing along uneven joint walls induced increases in porosity and permeability, causing the run away of water to depth.

To seal a crack with minerals requires the presence of cracks that remain open at depth prior to sealing. There are several ways this may occur. The first, relies on an increase in fluid pressure to a level greater than the confining stress perpendicular to the crack. This situation may arise in two ways.

Firstly, fluids may be expelled via dehydration during a metamorphic event, or crystallization of an igneous melt. The increase in fluid pressure splits the rock in a direction dependent on the differential stress directions, and if fluid pressure is maintained, the crack may remain open. Secondly, a reduction of ambient stress, and a resulting relative change in fluid pressure may cause the latter to exceed the former. Here two situations may arise. A reduction in confining pressure during an uplift phase, and the expansion of trapped fluid by "degasing", might allow the formation of horizontal cracks. These may allow trapped fluid to permeate through the rock. These cracks would tend to

close when fluid pressure subsides as in the first case. Alternatively the onset of a strong extensional stress, modulated by an orthogonal compressive component, would lead to fracturing on imposition of hydraulic pressure, as was demonstrated by the geothermal experiment at Camborne (Pine & Batchelor 1984). This type of fluid/fracture/stress interaction is envisaged to explain the stratiform exhalative ore deposits of Navan and Silvermines, Ireland (Russell 1978, Mills *et al.* 1987). There extension allows the downward percolation of sea water to generate hydrothermal convection cells which deepen and expand with time. The fluid permeation would initially be along pre-existing joint sets.

1.3.2 Crack growth, growth paths and interactions

The growth of a fracture is quantified by the velocity of crack tip propagation. The velocity range important for crack growth is termed the "subcritical range". Subcritical crack growth consists of velocities in the range of 1 cm/sec to 10^{-7} cm/sec. Subcritical crack growth is a function of stress at the crack tip, and also of the corrosive ability of the fluid brought up to the crack tip. However, the relative importance of these factors is not quantitatively qualified, and growth is thought also to depend on pressure, temperature, stress, mineralogy and rock porosity.

The velocity of fracture opening is a function of applied stress, water pressure and temperature (Anderson & Grew 1977). In an elastic medium, subjected to a deviatoric stress, the magnitude of the stress concentration around the crack is inversely proportional to the square root of the distance from the crack tip. If the applied stresses are tensional, the crack extensional force increases with crack length, accelerating the crack forward. Under compressive stresses, the crack extension force diminishes as the crack propagates so that the crack reaches a stable position and stops unless additional stress is applied (Kranz 1983). Dunning *et al.* (1980) believe the limiting factor in subcritical crack growth is the amount of fluid that can be transported to the crack tip.

Growth path is generally controlled by the overall maximum stress direction, but the presence of anisotropy in rocks (due to cleavage planes, pores, other cracks, inclusions and crystal edges) all contribute to the local propagation path by modifying the stress field in their vicinity. This results in fractures which may be intergranular, but partly run along cleavage planes or grain boundaries.

The interaction of microcracks in arrays causes major fractures in stressed rock. The linkage, dilation and geometery of vein arrays has been studied by Beach (1975, 1980 a) and Nicholson & Pollard (1985). These workers have developed quantitative models, whereby the size, spacings and angles of echelon arrays allow the description of extension

and dilation. Thereby providing an understanding of how arrays might develop.

1.3.3 Conditions for crack closure

As pressure increases, crack porosity decreases with most or all dry cracks effectively closed by pressures exceeding 100 - 200 Mpa (see DSA results of Feves & Simmons 1976, Seigfried & Simmons 1978, Wang & Simmons 1978). Wang & Simmons (1978) suggest that crystalline rocks may be crack free in-situ, with cracks forming due to stress relief when the rocks are brought to the surface. However, observations on sealed, or partly sealed, microcracks suggest they remain open and may be at least partly connected at depth.

Crack closure is affected by wall roughness, with the closure rate dependent on the height and distribution of asperities on the wall. Confining pressure crushes asperities leaving irreparable damage. On subsequent pressure cycles, the asperities characteristics having changed, a different response is found (Sprunt & Brace 1974).

Batzle *et al.* (1980) also watched fracture closure in response to stress in a uniaxially loaded S.E.M mount. Under the S.E.M., they saw cracks of different character acted differently. Thermally produced cracks with smooth walls closed smoothly. However, rough cracks with mismatched walls could only partly close, or would close only after asperities or debris lodged in the crack were crushed.

1.4 Cracks and thermally induced stress

Thermally induced stress, upon heating or cooling of a rock, may produce microfractures. This fracturing is accomplished through differential thermal expansion, or contraction, between crystals with different thermo-elastic moduli, or between crystals with similar mineralogy but misaligned crystallographic axes. The primary product is grain boundary cracks, but intragranular cracks may develop at internal crystal discontinuities (Bruner 1979). Experiments have shown that the absolute value of temperature, the heating/cooling rate, mineralogy and confining pressure all affect the density and character of thermally induced microcracks. New fracturing may begin at 70 - 80 °C, but this only begins after the previous maximum temperature has been surpassed (Yong & Wang 1980). Heating above this temperature produces more cracks, due to grain boundary separation and intergranular cracking (Simmons & Richter 1976, Sprunt & Brace 1974). Pre-existing cracks, formed at lower temperatures, get larger on heating.

Due to its large thermal expansion anisotropy, the presence of quartz has the most dramatic effect in the production of thermally induced cracks. The relative absence of crack porosity in dolerite, compared to granite, has been attributed to this (Simmons &

Cooper 1978). By measuring acoustic emissions, Yong & Wang (1980) showed that microcracking rate could be dependent on heating rate. Similarly, Johnson & Gangi (1980) showed that the growth of a fracture, from a grain boundary or an intragranular crack, could be dependent on the thermal gradient within the rock.

1.5 The effect of microcracks on the physical properties of rocks

The effect of microcracks on the physical properties of rocks has been studied by many workers over the last 20 years. The influence of microcracks and joints on seismic velocity has been documented by Birch (1960), Simmons (1964), Nur & Simmons (1969), Takeuchi & Simmons (1973), O'Connell & Budiansky (1974), Hadley (1976), Feves *et al.*(1977), Padovani *et al.* (1978) and Park & Simmons (1982). With regard to the Lewisian of northwest Scotland, the seismic investigations by Hall & Simmons (1978), Ali (1983) and Hall & Ali (1985) have all involved, to a variable degree, the effects of open microcracks.

Of these studies Nur & Simmons (1969), Takeuchi & Simmons (1973) and Hadley (1976) have paid special attention to the influence of water saturation (in microcracks) on seismic velocity in crystalline rocks. The other works principally deal with the response of seismic velocity to confining pressure and microcrack closure. The physical effects of microcracks on rocks have been summarized by Feves *et al.* (1977). The overall effects are as follows :

> As microcrack dilatancy and density decrease under a confining pressure, the seismic velocity of the fractured rock is found to increase. The closure of the microcracks results in the increase of both Vp and Vs toward the values found in the rock's uncracked state. Vs shows a faster recovery than Vp, with most cracks closed under a confining pressure of between 1 and 2 kb. A maximum rate of recovery, to the uncracked levels, is found at confining pressures of less than 500 bars. This represents the initial closure of the larger fractures. It also indicates that open fractures will be significantly reduced in size within the top 2 km of the crust, with nearly all becoming closed by 4 -6 km in depth.

The density and dilatancy of microcracks will clearly have a large influence on the compressibility of crystalline rocks. Theoretical models developed by Walsh (1965), to account for the compressibility due to flat penny-shaped cracks, have been successfully applied to compressional studies by Simmons *et al.* (1974), with the development of

differential strain analysis (DSA). Here the aspect ratio of a fracture can be related to the pressure required to close it by the equation

$$P = \frac{\pi \varepsilon a}{4\left(1 - V^2\right)} .$$

This equation predicts that cracks with a low aspect ratio will close at a lesser confining pressure than cracks of a high aspect ratio. Further work using DSA showed that fractures which formed under different conditions had different responses to compressibility (Simmons *et al.* 1978). Most fractures in igneous rock closed under pressures of less than 500 bars, but pressures of up to 2kb were required to close fractures in shocked terrestrial, and lunar, rocks.

The effect of a fluid phase within the fractures affects the compressional P-wave velocity more than the shear wave velocity. While the addition of water has no affect on Vs, it significantly increases Vp at low confining pressures (Nur & Simmons 1969, Hadley 1976), with no affect once confining pressures of about 1 kb are reached. The more saturated the sample, the larger the value of Vp at low confining pressures.

Thermal expansion of fractured rock has been studied by Cooper & Simmons (1977). They concluded that the presence of fractures in the rock, prior to heating, resulted in a reduction in thermal expansion perpendicular to the plane of greatest fracture concentration. The cause for this is the thermal expansion of some minerals into the already existing crack space.

1.6 Porosity and permeability of crystalline rocks

The porosity and permeability values for crystalline rocks have recently been summarized by Brace (1984) and Wolff (1981). Values are highly variable, both within a single lithology and across the field of crystalline rocks, but certain conclusions and ranges exist.

Mean porosities of igneous and metamorphic rocks, as summarized by Wolff are shown in Fig. 1.1 Although the range is large, a bias exists to the range 0.1-1%. These low values can be accounted for by small fractures in fresh rock. Larger values of 10% up to 85% are due to vesicular basalts and pumice. Porosity in crystalline rocks exists as either pores in the form of vugs, vesicles or dissolution cavities; or as fractures due to faults, joints or microcracks.

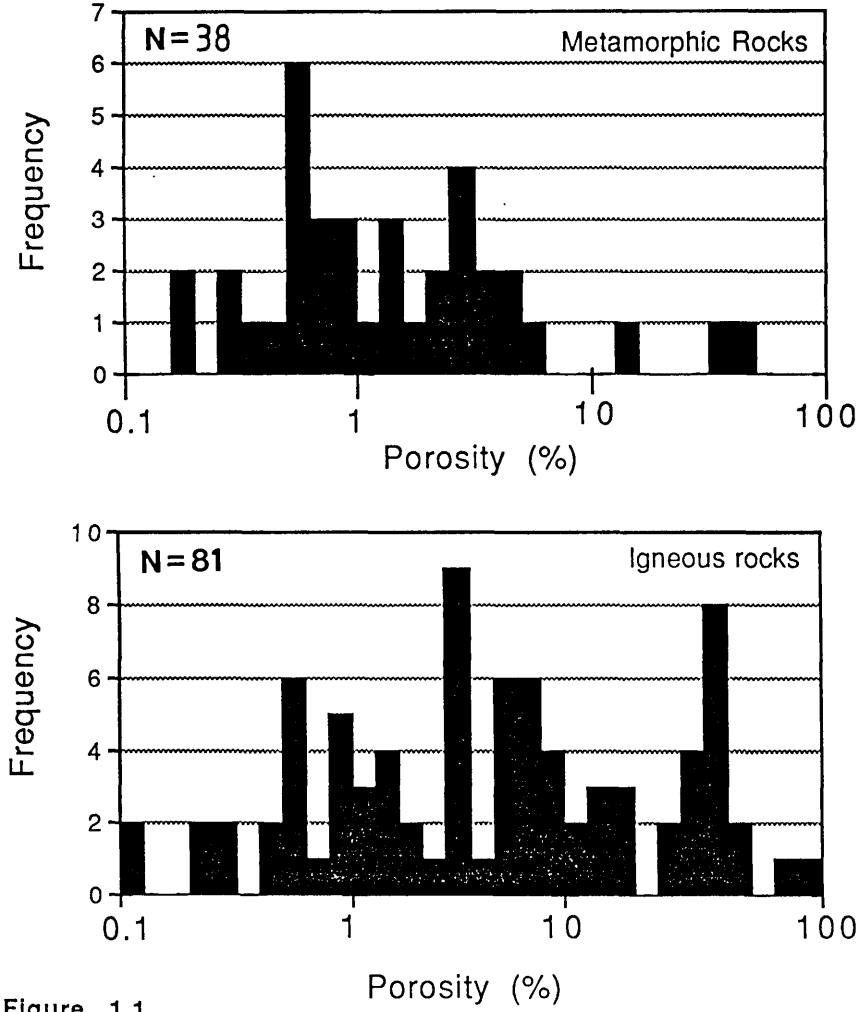

Figure 1.1

Mean porosities of metamorphic and igneous rocks. Data taken from Wolff (1981).

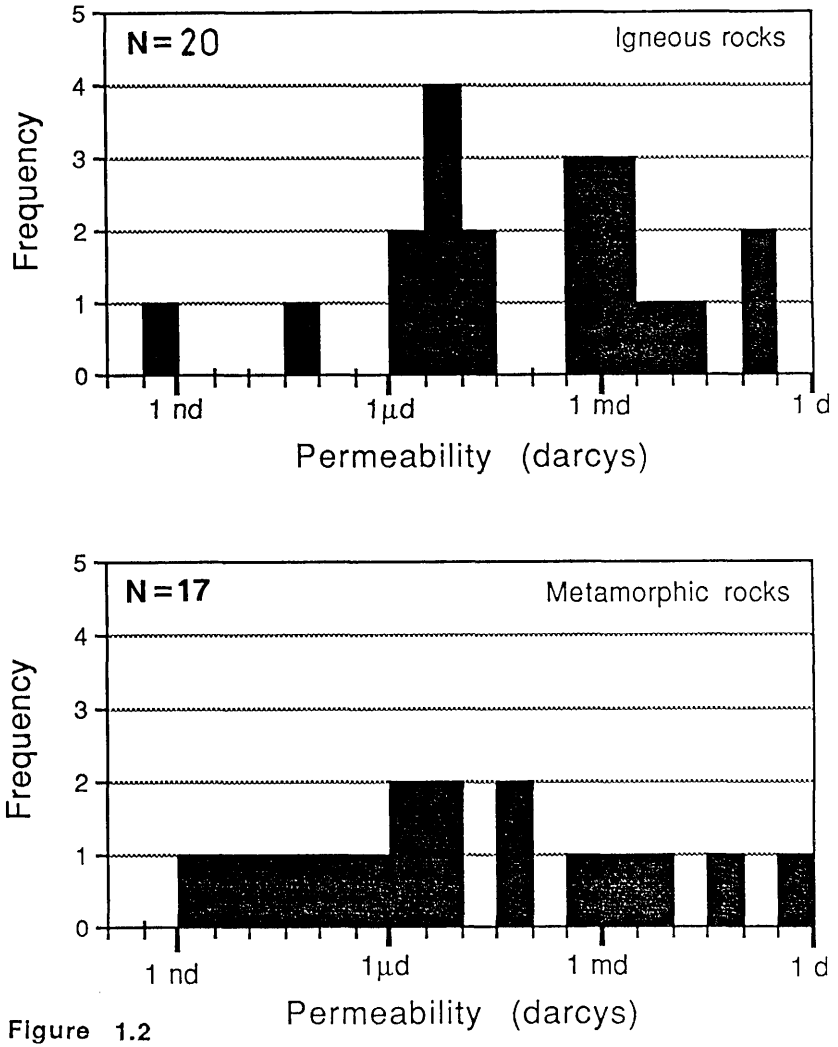

Figure 1.2

Mean permeabilities of metamorphic and igneous rocks. Data taken from Wolff (1981).

Permeability is a measurement of the hydraulic conductivity of a material. The units used to express permeability are the darcy. A darcy is defined as the permeability of a medium allowing the passage of 1 cm^3/sec of a fluid, whose viscosity is 1 cp with a pressure gradient of 1 atmosphere per centimetre through a surface area if 1 cm^2. Thus,

$$K = \frac{\mu Q}{A} \times \frac{\Delta L}{\Delta P}$$

and by definition,

$$1\ \text{Darcy} = \frac{1\ \text{cP}.\ 1\ \text{cm}^3/\text{s}}{1\ \text{cm}^2} \times \frac{1}{1\ \text{atm}/\text{cm}} .$$

Permeability is highly variable within crystalline rocks, and has been shown to depend on several factors.

(a) Size of permeability test.

Brace (1984) demonstrated that well tests of crystalline rock showed significantly greater permeability than lab scale tests on cores, and occasional permeabilities of 10-100 darcys (10^{-12} -10^{-10} m^2) may exist. Average well test values lie around the region of 1md (10^{-15} m^2). For lab scale tests, the permeability of a rock may be reduced by as much as 3 or 4 orders of magnitude in comparison with a well test on the same lithology, and permeabilities of 10^{-19} -10^{-21} m^2 (or 100 - 1 nd) are common. Ranges of up to 9 orders of magnitude have been found to exist within a single lithology.

(b) Fracture size, spacing and intersections.

Theoretically a rock may have a large density of fractures, but, so long as none intersect, permeability should be zero. Permeability of igneous and metamorphic rocks, as summarized by Wolff, are shown in Fig. 1.2. The large range of values is evident.

The Navier-Stokes equation can be used to relate permeability to the width and length of the flow path. The permeability of a fracture was derived in this way by Iwai (1976). By analogy to Darcy's law, permeability due to a single fracture (K_f) is defined as

$$K_f = \frac{\gamma\ 2\ b^3}{12\ \mu} .$$

If fracture spacing is F_s, then system permeability (K_s) becomes

$$K_s = \frac{\gamma 2b^3}{12\mu} \times \frac{1}{F_s} .$$

This assumes that the flow of the system is the sum of the flow of the individual fractures. Thus the permeability of the system is therefore dependent on the width and spacing of the fractures present as permeable pathways. This is known as the cubic law of fracture fluid flow, and has been shown to hold under varying conditions of stress/strain and wall roughness, with slight corrections where necessary. The law is always obeyed for fracture permeability (Witherspoon *et al.* 1980).

1.6.1 Modifications to the cubic law

A simpler version of the cubic law is provided in Witherspoon *et al.* (1980), where

$$\frac{Q}{\Delta h} = C(2b)^3 ,$$

and C is a constant which varies depending on flow type. Either of two types of flow may exist through a core, depending on the setup of the permeability test. These are radial or straight flow. For radial flow:

$$C = \left(\frac{2\pi}{\ln\left(\frac{re}{rw}\right)}\right)\left(\frac{\rho g}{12\mu}\right) ,$$

whereas, in the case of straight flow

$$C = \left(\frac{l_o}{l_p}\right)\left(\frac{\rho g}{12\mu}\right) .$$

These equations are valid for open fractures with parallel smooth sides. However, friction and wall roughness have an effect on the flow through a fracture. Joint roughness, or the absolute height of the asperities on the fracture wall (E), can be related to a frictional component (F), by the equation

$$F = \left[1 + 6.0\left(\frac{E}{2b}\right)^{1.5}\right] .$$

When $F \geq 1$, or the walls are rough, the cubic law becomes

$$\frac{Q}{\Delta h} = \frac{C}{F}(2\,b)^3$$

1.7 Reduction of permeability

The reduction of permeability can occur in two ways, either by physical narrowing of the fractures as a result of an applied strain, or by the blocking of the fractures due to mineral deposition or crack sealing.

1.7.1 Permeability reduction due to compression

In recent studies, many workers have touched on the subject of the response of permeability to stress Gangi (1978), Morrow *et al.* (1986), Bernabe (1986), Engelder & Scholz (1981), Walsh (1981), Raven & Gale (1985), Walsh & Brace (1984), and Zoback & Byerlee (1975 a, 1975 b). The overall conclusions of all these workers is, that as pressure is increased, permeability drops. This is as one would expect, because as pressure increases, microcrack porosity drops.

The relationship between effective pressure (P_e) and permeability can be represented by the equation

$$\ln P_e \propto K^{\frac{1}{3}}$$

(Walsh 1981). The effective pressure is the confining pressure (P_c) minus a function of pore pressure (P_p), where

$$P_e = P_c - S \times P_p .$$

S depends on the fracture roughness and is usually between 0.5 and 1.0. More accurately

$$S = 1 - \frac{V_{vol} \times \beta_s}{\left(\frac{\Delta V_p}{\Delta P}\right)} ,$$

where the function $\left(\frac{\Delta V_p}{\Delta P}\right)$ is the rate of change in pore volume with applied hydrostatic pressure. Morrow *et al.* (1986), and Bernabe (1986), have used this equation to derive the value of S for Westerly and Barre granites. For Westerly granite, S was always close to 1, ± 0.1, whereas for Barre granite, S was always between 0.6 and 0.7.

Walsh (1981) showed that the equation $\ln P_e \propto K^{\frac{1}{3}}$ required a correction for fracture shape during pressure change, which resulted in the equation becoming

$$\left(\frac{K}{K_o}\right)^{\frac{1}{3}} = 1 - \left(\frac{\sqrt{2h}}{b_o}\right) \ln\left(\frac{P}{P_o}\right)_e .$$

This can then be rewritten as the general equation

$$K^{\frac{1}{3}} = A + B \times \ln P_e .$$

This equation indicates there is an inverse power relationship between permeability and confining pressure. In pressure cycling experiments, such as those carried out by Morrow *et al.* (1986) and Bernabe (1986), a non-elastic change occurs. Whereby, as pressure increases, permeability drops; and as pressure is released, the permeability increases, but not to its original level. This is due to the closure of the cracks which do not reopen to their original levels.

1.7.2 Permeability reduction by fracture sealing and healing

Fracture sealing is the term reserved for the closing of (or reduction in) open space within a fracture, by the growth of a mineral into the open space. The sealing mineral should be different than the fracture's host mineral. Crack healing is the closing of a fracture by growth of a mineral the same as the wall rock mineral. Sealed cracks are easily seen, but healed ones may only be seen by inclusion trails, or occasionally, by cathode luminescence techniques.

The role of the crack healing/sealing, in the permeability reduction of granite, was illustrated by Vaughan *et al.* (1986). Passing hot (300 °C) fluid through a core of Westerly granite, it was discovered that the permeability decreased by a factor of 25 over a two week period. Most cracks were sealed by quartz, and nearly all quartz grain boundaries were sealed. Calculation of porosity reduction due to uniform dissolution and reprecipitation of quartz, indicated that porosity reduction should be in the order of 10%, corresponding to permeability reduction of nearly 30%. However, and actual permeability reduction of 96% was found. This indicated: the non-uniform precipitation of material in critical narrow places; the precipitation of other minerals besides quartz; or crack

healing. Brantley *et al.* (1986), showed that crack healing may be a quick process, estimating times of some 2000 hours to seal a 100 μm crack. This healing is very fast with regard to the geological time scale.

1.8 Summary

1. Microcracks can be classified either by their mode of formation, or by their relationship to the host rock minerals. As it stands presently, the classification can result in the confusion of terms. Three principal types of crack occur in relation to the rock fabric: the grain boundary crack; the intragranular crack; and the intergranular crack.

2. The response of microcracks to mechanical and thermal stress are well known. The mechanical response to compressive stress can be modelled using flat "penny shaped" analogies, providing data suggesting most microcracks close at pressures of 100 to 200 Mpa (equivalent to depths exceeding 3 km). However, S.E.M. observations on cracks suggest that irregularities in shape may allow microcracks to remain open at greater pressures.

3. The effects of microcracks upon the physical properties of crystalline rocks have been extensively investigated, and are very well constrained. Most physical parameters are influenced by the presence of microcracks.

4. The permeability of crystalline rock is highly variable and is dependent on several factors, including the size of the permeability test, and the size and spacing of fractures within the rock. In more detail, the permeability of a fracture is proportional to the cube of the fractures width, with the permeability of a rock being inversely proportional to the spacing of the fractures. Under compressive stresses, permeability is inversely proportional to the natural log of the confining pressure.

5. Fracture permeability in crystalline rocks may be a transitory feature due to crack sealing and healing. Minerals deposited from fluid may seal up critical intersections, causing large permeability reductions for relatively small porosity reductions. Some evidence suggests that fractures may become healed very soon after opening.

CHAPTER 2

THE GEOLOGY OF THE NORTHWEST HIGHLANDS

2.1 Basic divisions of the Lewisian complex

The Lewisian complex of northwest Scotland constitutes the oldest recognised suite of rocks within the British Isles. It consists of Archaean and Proterozoic ortho- and paragneiss, schists and granites; bordering, and forming the foreland to, the Caledonian orogenic belt. The Lewisian has been investigated for a period approximating 100 years. It is one of the most intensely studied (and best understood) segments of Precambrian crust in the World.

The initial studies on the region, and still primary references for research, were carried out in the late 19th and early 20th Century by a team of survey geologists lead by Peach, and two Edinburgh geologists Jehu & Craig.

The work of the survey resulted in the publication of the Geological Survey of Great Britain memoir entitled "The geological structure of the northwest Highlands of Scotland" (Peach *et al.* 1907) and in the, one and as yet only, published set of geological maps. Jehu & Craig were responsible for the initial surveying of the Outer Hebridean section of Lewisian crust. They published a regional study over a series of five volumes (Jehu & Craig 1923, 1925, 1926, 1927, 1934). Both sets of work are of similar quality and the documented geological descriptions are as useful today as they were then.

This project is concerned with samples taken only from the mainland belt of the Lewisian complex, and for that reason only the geology of this region is discussed in detail. Some mention to the Outer Hebrides is made by necessity.

In the initial studies (Peach *et al.* 1907), three regional divisions were noticed within the mainland Lewisian. Each possessed a separate geological character to its adjacent division, both in lithology and structure. The main characters of the three regions are outlined below. It is a division still used today.

2.1.1 The northern region.

The northern region consists of the Lewisian outcrop in the area between Durness and Rispond, along the North coast of Sutherland, continuing South to the line marked by Loch Laxford. The lithologies present consist primarily of hornblende and biotite quartzo-feldspathic gneisses, mostly retaining amphibolite mineralogy. Having undergone polyphase deformation and metamorphism, the major tectonic structures are large SE trending antiforms with attenuated pinch synforms. Injection complexes, consisting of granite / pegmatite sheets and migmatites, are found in the pinched synforms at Rispond

and Loch Laxford.

2.1.2 The central region

The Lewisian outcrop, between Loch Laxford to the North and Gruinard Bay to the South, constitutes the central region. This comprises of subhorizontal to gently folded intermediate pyroxene granulites with many minor basic, ultrabasic and occasional anorthositic bodies and lenses. Polyphase metamorphism and deformation has resulted in large scale open folds trending NW. These are dissected by later NW-SE and W-E shear zone systems. The central region is bounded by migmatitic injection complexes at both Loch Laxford (the junction with the northern region) and Gruinard Bay (the junction with the southern region).

2.1.3 The southern region

In many respects, the geology of the southern region is similar to that of the northern region. Hornblende and biotite quartzo-feldspathic gneisses, preserving amphibolite grade assemblages are again dominant. Polyphase deformation results in large SE trending antiforms with pinch synforms. However, preserved in these synforms are a sequence of metasediments which may possess a cover to basement relationship with the gneiss.

In both southern and northern regions, the Lewisian complex is in places overlain by younger unmetamorphosed sedimentary cover. Two lithological units lie directly over the gneisses. The oldest is the Torridonian, a thick (up to 7km) unconformable unit of fluvial and aeolian clastic redbeds. It is composed of arkosic sandstones, conglomerates and marls of Proterozoic age. The younger unit is the Cambro-Ordovician shelf sequence of orthoquartzites, mudstones and limestones. These lie with an angular unconformity upon the Torridonian sequence and overstep to lie directly upon the Lewisian (see Fig. 2.1).

2.1.4 Basic tectonic divisions

The differentiation of the complex progressed when studies, in the Torridon and the Scourie to Loch Laxford areas, revealed that a suite of basic dykes, termed the Scourie dykes, could be used as time markers between two phases of deformation (Sutton & Watson 1951). In the Scourie area, the dykes cross cut the granulite fabric, and are essentially undeformed. However, toward Loch Laxford, the same dyke swarm becomes both deformed and metamorphosed by a later tectono-metamorphic event which occurred under amphibolite facies conditions. The granulite facies event, subsequently dated as Archaean (~2800 ma), was termed the Badcallian metamorphism and assigned to a Scourian cycle of

tectono-metamorphic events. The later amphibolite facies event was termed the Laxfordian metamorphism. This was subsequently dated as being of early-Proterozoic age (~ 1900 ma)

Following the geological study of Evans & Tarney (1964), Evans (1965) published a geochonological study of the central region gneisses near Lochinver, some 30 miles south of Scourie. A major tectono-metamorphic event was found to intervene between the Badcallian and the Laxfordian. This was dated at ~2200 ma (a date subsequently redefined). Thus, the Lewisian complex was found to be composed of three geological regions formed over a period encompassing three separate tectono-metamorphic events. This period spanned some 1000 ma from the Archaean to the mid-Proterozoic.

2.2 The Lewisian complex during the Archaean

The oldest recognised lithological assemblages lie within the central region of pyroxene granulites. These are basic, ultrabasic, anorthositic and tonalitic masses which follow a calk-alkaline trend and are preserved primarily as tectonic pods. Preserved in many of these pods are primary igneous cumulate features, such as density stratification and cross-bedding. They are thought to represent igneous bodies disrupted during the gneiss forming episode. Single bodies were tectonically fragmented and can be traced as pods and lenses.

Along with small metasedimentary units and postulated metavolcanics, these comprise the protolithic assemblage for the Lewisian complex, known as the Gaelic Supergroup (Bowes 1976). Using Sm/Nd isotope study, Hamilton *et al.* (1979) concluded that the respective parts of the protolithic assemblage (the Gaelic Supergroup) were differentiated from the mantle at a similar time, approximately 2950 ± 50 ma. Similar ages are common place. Pb/Pb isochron ages of 2890 ± 180 ma have been derived from the Gruinard Bay gneisses (Moorbath *et al.* 1969, Moorbath & Park 1972), and 2900 ± 100 ma (Moorbath *et al.* 1969) from various gneisses and granulites by the same method. In attempting to unravel the ages of the events that occurred within this assemblage, Chapman & Moorbath (1977) concluded that the Gaelic Supergroup represented part of a single crustal accretion event, which was subsequently raised to granulite facies.

Early phases of folding, the Scourian F_1, occurred immediately prior to the Badcallian granulite facies metamorphism. These can be seen throughout the central region. The F_1 folds are tight, subisoclinal, intrafolial, and possess strong elongation of quartz parallel to their axial planes. The elongated ribbon quartz and the banding of the granulites were overprinted by the thermal high. This followed the isoclinal folding, and

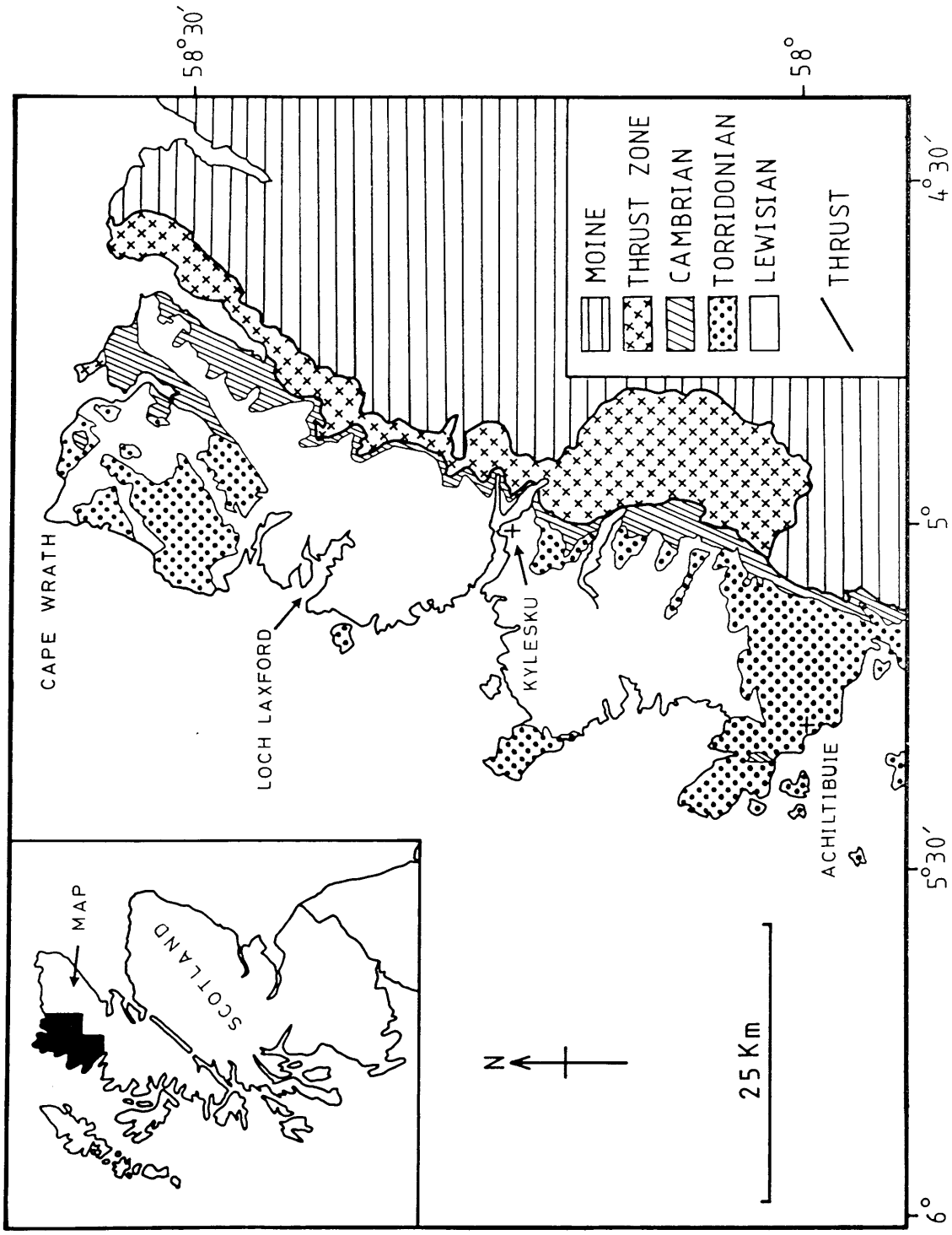

Figure 2.1 Geological map of the northwest Highlands, from Achiltibuie to Durness. Redrawn from 1: 253,440 Geological Survey sheet #5.

led to the formation of the granular two-pyroxene polygonal mosaic so prevalent in these rocks.

The recumbent nature of the F_1 folds suggests that crustal thickening was associated with a horizontal style tectonism. Evidence of repeated sequences of metasedimentary belts, attributed to thrust layering, can be found (Davies 1976). This event also disrupted the protolithic units and caused the gneissification of the region. This granulite assemblage is termed the Kylesku Group (Khoury 1968).

Using Rb/Sr, Pb/Pb and U/Pb isotope studies, the Badcallian metamorphism has been dated at about 2700 ma (Pidgeon & Bowes 1972, Chapman & Moorbath 1977, Humphries & Cliff 1982). Based on the Sm/Nd dates of Hamilton *et al.* (1979), the Badcallian metamorphism occurred some 200-250 ma after the period of crustal accretion.

During the Badcallian metamorphism, the central region granulites became geochemically depleted of LIL and LRE elements. As a result they now possess very low concentrations of U, Th, Cs, Rb and K. The causes and conditions of this high grade metamorphism have been summarized by Barnicoat (1987) and Sills & Rollinson (1987). Geothermobarometry, on garnet/pyroxene assemblages, suggest the peak granulite facies metamorphism occurred at temperatures of some 1000 °C, and pressures of 12-15 kb (Savage & Sills 1980). To account for such conditions, Barnicoat (1987) favours a model of increased temperatures and pressures by tectonic thickening via overthrusting. This would allow elevated temperatures due to a blanketing of the heat source. Structural evidence suggests this may be possible. Lower temperatures and pressures (in the region of 750-800 °C and 7-8 kb) have been obtained from the compositions of pyroxene/garnet simplectic rims (Sills & Rollinson 1987). These lower temperatures are thought to represent re-equlibriation reactions toward lower grade assemblages nearing the end of the Badcallian. Other experimentally derived data, from varying mineral assemblages (Barnicoat & O'Hara 1979, Barnicoat 1983, Rollinson 1981), broadly agree with these estimates (see Sills & Rollinson 1987).

Such pressures and temperatures would correspond to crustal depths of about 35 km, in a crust 60 km thick, modelled with heatflow values of 50 mWm^{-2} (Barnicoat 1987). This is higher than todays average of 30 mWm^{-2} .

The early structural fabrics seen in the northern region compare well with those related to the early-Scourian F_1 (associated with the Badcallian metamorphism). The first folding was intrafolial, subisoclinal and tight, almost identical in morphology to the Scourian F_1 of the central region. In places such as Rispond, both the structural and metamorphic evidence suggest the rocks of the northern region were in existence during

the Archaean, and were deformed and metamorphosed during the Badcallian episode. Two amphibolite generations can be found at Rispond. One generation relates to the large upright Laxfordian folds (F_2). An earlier one, visible in the F_2 fold hinges, is thought to relate to an earlier amphibolite facies metamorphism, and is contemporaneous with the early subisoclinal folding in the central region granulites (Findlay 1970). It is envisaged that the northern region underwent metamorphism, at lower temperatures and pressures (in comparison to the central region), during the same Badcallian event in the Archaean. The northern region, termed the Rhiconich Group (Dash 1969), is thought to be a supercrustal higher level contemporary to the Kylesku Group. Sutton & Watson (1962) believed it to be a metasomatically altered equivalent. However, the geochemical differences are thought to be too severe for this to be plausible (Bowes 1972).

The amphibolite facies metamorphism of the northern region can account for the geochemically undepleted nature of this area. Failure to attain granulite facies would ensure that the large scale mobility and homogenization of LIL and LRE elements, which must have occurred in the central region, could not occur.

The high pressures and temperatures which occurred in the central region caused very little melting. Only in occasional places, such as Achmelvich, do Badcallian migmatites occur. Here, the water pressure was high enough to allow partial melting during dehydration. One of the current favourite suggestions to account for dehydration without melting is to involve a CO_2 flush from the mantle. It is suggested this would reduce the partial pressure of water and encourage dehydration reactions to occur without any partial melting (Park & Tarney 1987).

Following the Badcallian metamorphism, the central region underwent two phases of folding which deform the granulite banding (Bowes & Hopgood 1973). The first, the Scourian F_2, resulted in small monoclinal folds with occasional pegmatite intrusions along their hinge zones. These pegmatites have been dated at 2490 ± 20 ma by the Rb/Sr method (Evans & Lambert 1974). The second, the Scourian F_3, are large scale open folds which control the regional trend of the banding as seen today. The Kylesku Fold (Khoury 1968) is the most prominent and has strong NW-SE axial planar joints. No retrogression of the granulites is associated with these late-Scourian folds.

2.3 The Lewisian complex during the Proterozoic

2.3.1 Pre-Laxfordian

The investigation into the Scourie dykes of the Assynt region (Evans & Tarney 1964), and the subsequent chronological study of the gneisses around Lochinver (Evans 1965), confirmed the presence of an early-Proterozoic period of regional metamorphism. Dated at about 2200 ma by the K/Ar method, this episode was termed the Inverian (Evans 1965) (This 2200 ma age is now known to be too young for the Inverian).

Three main categories of Inverian structure are believed to exist (Park & Tarney 1987). These are:

(a) broad shear zones, unaffected by later Laxfordian reworking, such as the Claisfearn Zone of Sutton & Watson (1951) between Scourie and Loch Laxford (Fig 2.2);

(b) narrow shear zones, cutting and retrogressing the Scourian rocks of the central region, such as the NW-SE trending monoclinal fold belts mapped by Khoury (1968,1969); and

(c) Regions where high Inverian strain is speculated to have occurred, but the zone is reworked by later Laxfordian movements.

Reworking within the shear zones occurred under amphibolite facies (Khoury 1968, Beach 1976). This was due to the influx of hydrous fluids along these zones. Initial retrogression postdates the pre-Inverian pegmatites dated at 2490 ± 20 ma (Evans & Lambert 1974) and precedes the emplacement of the Scourie dykes, dated at 2390 ± 20 ma (Chapman 1979). Geothermobarometry suggests retrogression occurred at temperatures in the region of 550-650 °C (Sills 1983, Sills & Rollinson 1987). Pressures of 4.78 kb have been determined using garnet / sillimanite / quartz assemblages (Sills & Rollinson 1987). The Inverian is only known to be preserved in mainland central region exposures. Hebridean Lewisian retains no evidence for this phase, and this is perhaps due to later intense Laxfordian reworking of the crust (Fettes & Mendum 1981).

The structural relationships between the Inverian monoclinal fold belts and the Scourie dykes were demonstrated by Khoury (1968). Most dykes in the Scourie to Lochinver region are intruded along the steep limbs of the monoclinal folds (see Fig. 2.3) and crosscut the Inverian fabric. The orientation of the Scourie dyke suite is heavily dependent on pre-existing crustal weak zones exploited during emplacement. The Inverian monoclinal folds may also be controlled in their orientations by the strong axial planar NW jointing, associated with the Scourian F_3 Kylesku Fold. (D. Bowes pers. comm).

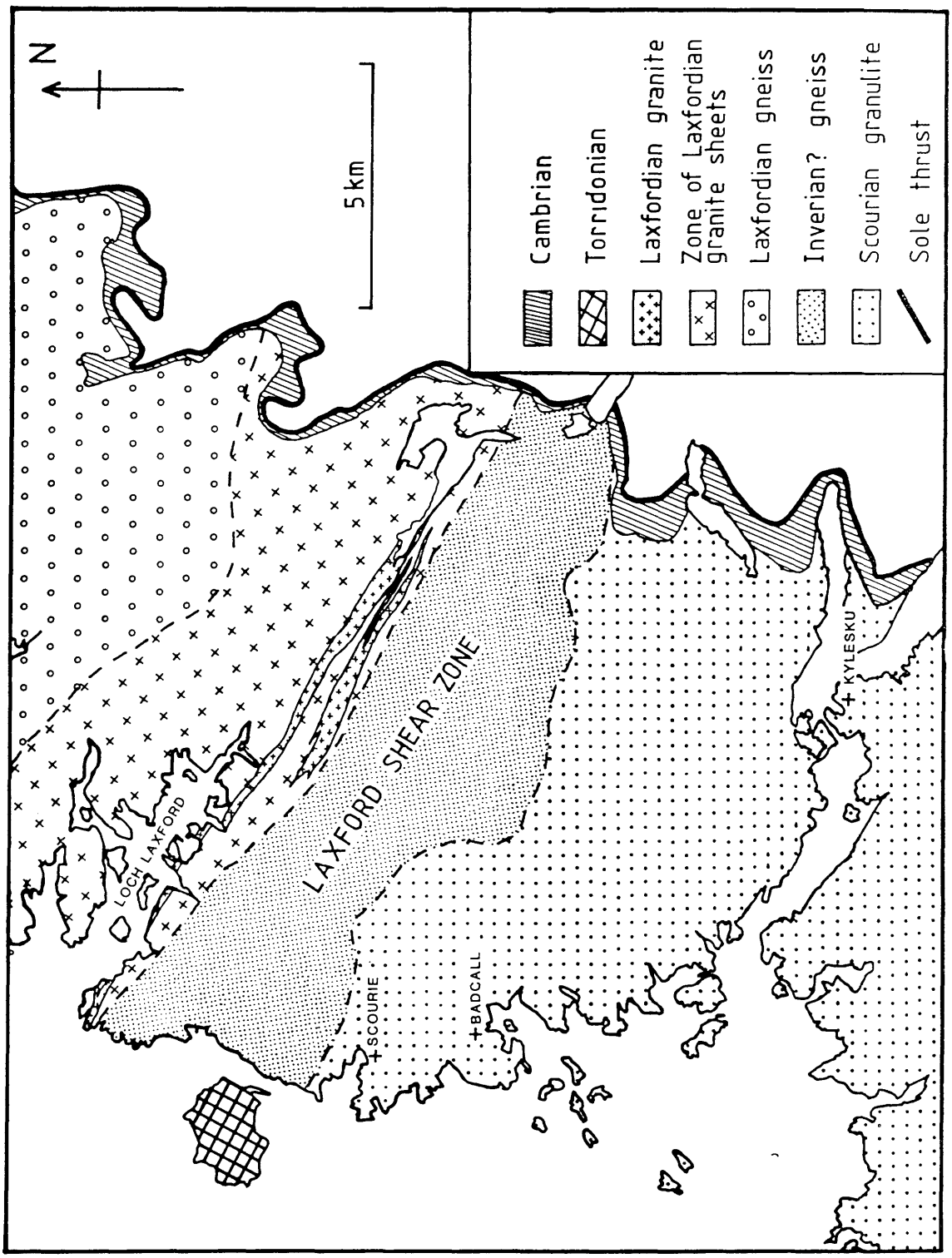

Figure 2.2 Geological map of the region between Loch Laxford and Kylesku. Redrawn from 1: 63,360 Geological Survey sheet #'s 107, 113.

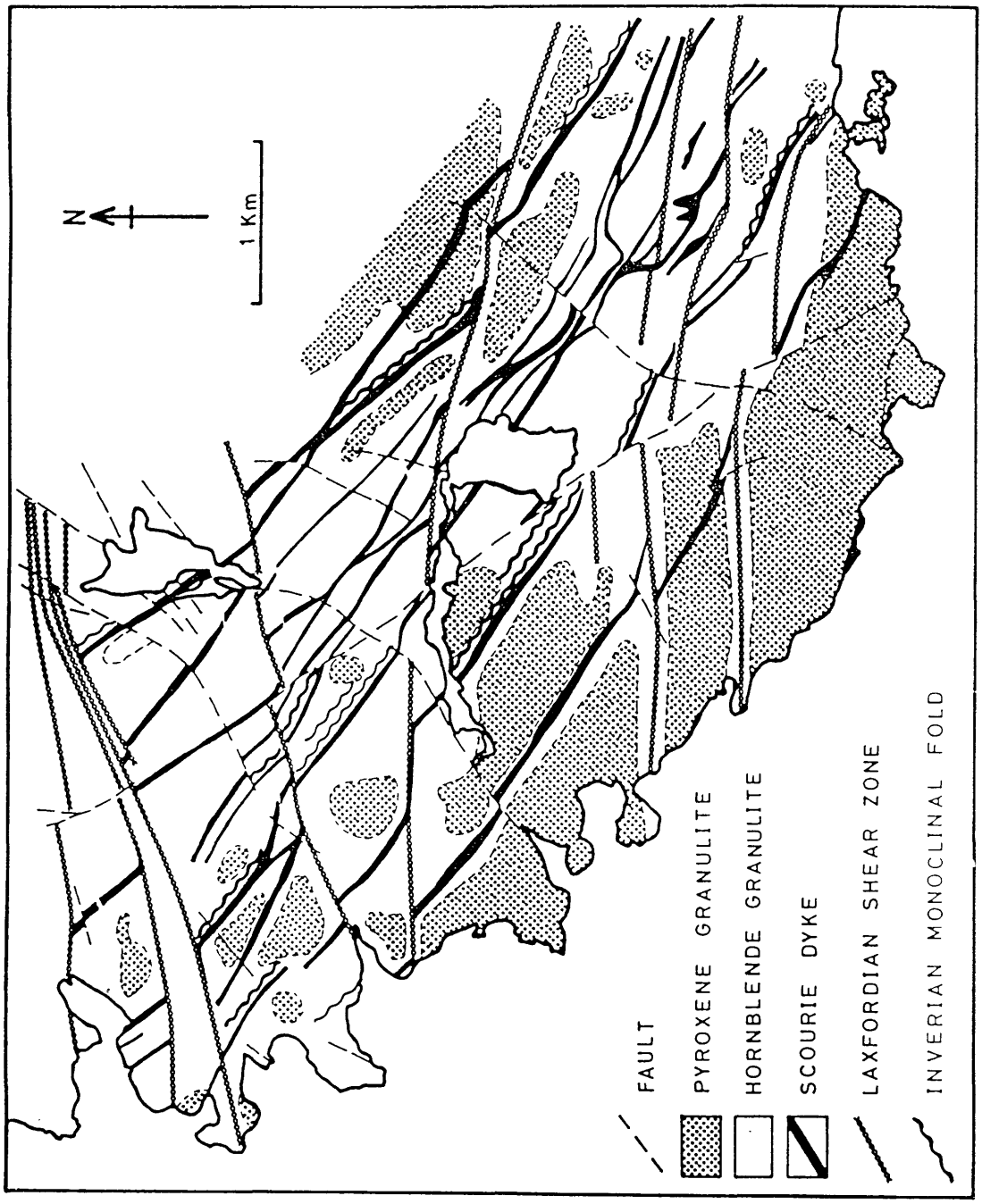

Figure 2.3 Detailed geological map of the granulite terrain between Geisgeil and Kylesku. Redrawn from original map of Khoury (1968).

The Scourie dykes are believed to have been emplaced at depth (O'Hara 1961, Park & Cresswell 1972, Tarney 1973). They yield geothermometry temperatures of 600 °C from garnet/clinopyroxene and garnet/hornblende assemblages . There are four main geochemical types of Scourie dyke (Tarney & Weaver 1987): bronzite picrites; norites; olivine gabbros; and quartz dolerites (which are most common). These all show a "continental" trace element signature, enriched in LIL and LRE elements. The magmas must have their signatures inherited from sub-Lewisian continental lithosphere, as the Lewisian granulites of the central region are heavily depleted in such elements.

The emplacement of the Scourie dykes represents considerable crustal extension. They are believed to be derived from at least two distinct mantle sources. The one supplying the picritic/noritic magma being more refractory with respect to major elements, but showing a greater relative enrichment in LIL and LRE elements (Tarney & Weaver 1987).

The recent dating of the Scourie dykes at 2395 ± 20 ma (Chapman 1979), shows that the initial date of 2200 ma by Evans (1965) is too young for the Inverian, and a date around 2450 ma would be more appropriate. The status of the Inverian is still arguable. Apparently no new crust was formed, and it cannot be classed as a separate tectonic cycle. Bowes (1978), and Watson (1983), class the Inverian as a late-Scourian event, perhaps an epiorogenic phase. It has also been suggested that the Inverian represent a preorogenic rifting phase prior to the Laxfordian, with the initiation of a new tectonic cycle by tensional splitting of the shield formed during the Scourian (Wright 1985 unpub.). A time span of some 400 ma, between the Scourie dykes and the Laxfordian, suggests that the Inverian is more likely to be associated with the Scourian. However, its limited outcrop may ensure that it remains enigmatic for some time to come.

2.3.2 Laxfordian

The beginning of the Laxfordian cycle can be recognised with the deposition of what are now metasediments and the extrusion of lavas associated with crustal extension. The extension is believed to be of a transtensional nature, thus producing strike-slip faults (Coward & Park 1987). The metasedimentary lithologies preserved in the Gairloch to Loch Maree region are known as the Loch Maree Group (Watson 1975).

This assemblage of schistose metasediments include banded ironstones, graphitic schists, quartz magnetite schists, marbles, pelites, manganese schists and amphibolites. The amphibolites, derived either from lavas or sills, are referred to as the Letterewe Basaltic Suite. A basement to cover relationship has not been reported and this has

previously led to confusion with regard to their age (see Watson 1983). Many of the initial units within the group, as described by Park (1966), have now been identified as tectonic slices producing an interleaved sequence (Bickerman *et al.* 1975).

Using Sm-Nd age dating techniques, O'Nions *et al.* (1983) were able to model the age of sedimentation and the age of crustal residence for the metasediments. They defined a Proterozoic age of 2000 ma as the time of deposition, and concluded that the sediments were composed of material derived from both pre-existing gneiss and new crustal material.

The volumes of igneous material extruded, and the deep water nature of the sediments, indicate quite extensive crustal thinning in the Loch Maree to Gairloch region during the early-Proterozoic. There has been discussion as to whether this is the same extension as was responsible for the Scourie dyke emplacement, and whether or not the lavas were derived from the same magma, with the dykes acting as feeders to the surface (see Park & Tarney 1987). The main Scourie dyke suite is dated at 2395 ± 20 ma (Chapman 1979), and these must therefore be considerably older than the Loch Maree Group. Some minor dykes in the Assynt area have been dated at about 2000 ma (Evans & Tarney 1964). The South Harris Igneous Complex has also been dated as early-Proterozoic, yielding Sm/Nd ages of 2180 ± 60 ma, with the latest emplacement of the tonalite at 1860 ± 50 ma (Cliff *et al.* 1983). The South Harris Igneous Complex is not considered similar enough in chemistry to be related to the Loch Maree Group (Park & Tarney 1987) but it, and the later dykes in Assynt, must have been emplaced under the same tectonic regime as the Loch Maree Group (even if they are not comagmatic).

The Laxfordian metamorphic and deformational phases are termed the Durness Episode. Three phases of deformation are believed to have occurred (Bowes 1968). However, the Gualin phase, or D_1 of Bowes (1968), was defined when it was thought that the northern and southern regions were not involved in the Scourian deformation phases, but represented post-Scourian cover. It is now thought these terrains were present during the Scourian, and that the Gualin phase is the Scourian deformation prior to the Badcallian metamorphism.

Laxfordian D_1 resulted in the formation of essentially horizontal shear zones and recumbent folds under amphibolite facies (Coward & Park 1987). The tectonic regime is envisaged to be one of transtension, resulting in strike slip shear zones, which are of localized development. A minor phase of vein emplacement separates this phase from the Laxfordian D_2, or Dionard phase, of deformation. This was the major phase and resulted in the development of the large SE plunging folds. This produced the antiforms at Strath Dionard and Loch Tolle, and the pinch synforms, such as the Letterewe Synform (which

preserves the Loch Maree Group at its core). The major crustal shear zones found at Loch Laxford, Canisp, Gairloch, South Harris and Ness also developed during this phase (although the Loch Laxford structure is believed to be a reactivated Inverian structure). The Lewisian was at mid-crustal level, in a dextral transpressional regime (Coward & Park 1987). The major retrogressional effects within the shear zones have been discussed in several papers (Beach 1973, 1980 b, Sills 1983, Sills & Rollinson 1987, Cartwright 1988). The pyroxene granulites were hydrated (Fig. 2.3), and K-rich fluids influxed up the shear zones. This is believed to have been from an anatectic source below the presently eroded level. The gneisses of the northern and southern regions developed new fabrics in response to the deformation, and greenschist facies assemblages developed in the shear zones.

In the Outer Hebrides, granulite facies was attained in part of the South Harris Igneous Complex. This is known as the Rodil Metamorphic phase (Wright 1985 unpub.). This occurred after emplacement of the tonalite, but before shearing took place within the Langavat Belt. The shearing retrogressed the pyroxenes and garnets of the anorthosite-gabbro-tonalite complex, and is part of the Dionard phase (or Laxfordian D_2). Therefore, the granulite facies metamorphism was earlier than the peak Laxfordian amphibolite metamorphism.

The final deformational phase, D_3, or the Leacach phase, resulted in open brittle folds and minor brittle shear zones which deform earlier structures.

Geochronological studies have tended to produce widespread ages for the Laxfordian cycle. Rb/Sr ages of 1942 ± 98 ma and 1710 ± 160 ma have been obtained from the Loch Maree Group (Bickerman *et al.* 1975). In the Outer Hebrides, the Rodil Metamorphic phase has been dated at 1870 ma (Cliff *et al.* 1983). In the northern belt, Rb/Sr dates of 1905 ± 185 ma, and 1714 ± 130 ma have been derived from quartzo-feldspathic gneiss (Lambert & Holland 1972, Lyon & Bowes 1977). Therefore, it would appear that peak metamorphism took place over the period between 1900 and 1750 ma, being slightly earlier in the Outer Hebrides than on the mainland.

The epiorogenic phases of the Laxfordian are marked by the late development of injection complexes and migmatites at various places, including Loch Laxford, South Harris, Rispond and Gruinard Bay. This episode is termed the Harris episode (Wright 1985 unpub.). The complexes are post-tectonic and have provided similar U-Pb and Rb/Sr dates. 1717 ± 75 ma from Loch Laxford (Lyon & Bowes 1977), and 1713 ± 34 ma and 1688 ± 47 ma from South Harris (van Breemen *et al.* 1971). This indicates that the epiorogenic phase occurred about 50 ma after the end of major Laxfordian

metamorphism, at about 1750 ma . Later K/Ar dates of 1405 ma and 1295 ma from biotites within granite at Rispond may represent uplift effects in mid-Proterozoic post-Laxfordian times (Lyon & Bowes 1977).

The tectono-metamorphic history of the Lewisian complex is summarized in Table 2.1.

Table 2.1 A summarized tectono-metamorphic history of the Lewisian.

Ma	EVENT
2950-2900	Crustal accretion, formation of protolithic assemblage consisting of supracrustals, ultrabasic, basic and tonalitic intrusives.
2800-2650	Badcallian metamorphism and deformation, granulite facies in deeper central region, amphibolite facies in shallower northern region. Associated with early horizontal tectonism and tight isoclinal folding.
2650-2400	Epiorogenic open folding, minor basic intrusions and K-pegmatite emplacement. Initiation of NW-SE trending inverian monoclinal fold "shear zones" associated with segmentation of Archaean blocks.
2400-2200	Continuing development of Inverian monoclinal fold belts, the emplacement of Na-pegmatites and the Scourie dyke suite of dolerites and norites.
2200-	Crustal extension, formation of the Loch Maree Group of supracrustals, emplacement of the South Harris Igneous Complex.
1900-	Laxfordian cycle of metamorphism and deformation.
1700	Widespread amphibolite facies metamorphism, granulite facies reached on South Harris. Major period of crustal shortening, with major SE plunging folding. Pinched synforms acted as major shear zones (South Harris, Loch Laxford). Juxtaposition of different crustal levels at Loch Laxford and Gruinard Bay. Numerous brittle-ductile shear zones within the central region act as fluid conduits. Greenschist metamorphism in shear zones.
1750-1650	Development of granitic migmatitic injection complexes at Loch Laxford, South Harris and Rispond.
1650?	Emplacement of late basic dykes, which crosscut Laxfordian shear zones and Laxfordian granite sheets.

2.4 The overlying sedimentary sequences

Unconformably overlying the Lewisian complex are the Proterozoic Torridonian red-beds and the Lower Palaeozoic Cambro-Ordovician sequence (Fig. 2.1). It is not intended to describe these sequences fully. More than adequate summaries of the Torridonian have been given by Stewart (1969, 1988a, 1988b) and Johnson (1983), and the Cambro-ordovician sequence has been described by Swett (1969) and Walton (1983). However, It is important to understand the development and tectonic setting of these sequences because of their probable influence on post-Laxfordian fluid flow within the basement.

2.4.1 The geology of the Torridonian

The Torridonian can be divided into two groups: the lower-most Stoer Group; and the succeeding unconformable Torridon Group.

The Stoer Group is approximately 2km thick where best exposed on the Stoer peninsula. It consists of a fluvial sequence of breccias, conglomerates, mudstones and arkosic sandstones. The sequence fines upwards, both overall and within single units, representing alluvial fans of varying size. The lower-most breccias are locally derived, and contain angular clasts of Lewisian gneiss, as well as blocks which have moved only a matter of meters from their original position. The overlying conglomerates and arkoses are more distal, with sources in the region of 10-15 km from their present location (Stewart 1988a). These initial deposits infill the basement topography, often being preserved against the Lewisian gneiss as off lap sequences. This is particularly well developed at Clachtoll and Rubh' a' Choin, surrounding Enard Bay. Between the members of the Stoer Group, palaeocurrents may reverse up to 180 °, suggesting deposition in fault controlled rifts (Stewart 1982). The possibility of rift faults is enhanced by the occurrence of the Stac Fada Member, a volcanic mudflow containing clasts of undersaturated volcanic glass.

An angular unconformity of 25-30 ° exists between the Stoer Group and the Torridon Group, with lithification of the Stoer Group having occurred prior to Torridon Group deposition. This implies a considerable break in time, as is suggested by the Rb/Sr whole rock dates of Moorbath *et al.* (1969). They yielded dates of 968 ± 24 ma for the Stoer Group diagenesis, and 777 ± 24 ma for the diagenesis of the Torridon Group. A break of some 200 ma between groups.

The Torridon Group is some 5km thick and is divided into four formations: the Diabeg; Applecross; Aultbea; and Cailleach Head formations.

The Diabeg Formation is confined to the South of Gairloch. Fining upwards from

breccias to sandstones and shale it represents a continuing fill of the Lewisian topography. It consists of locally derived alluvial fans, containing reworked Stoer Group sediment, building out into valleys, with shale deposition in ephemeral lakes.

The Applecross Formation is the thickest, and most widespread of the formations, outcropping from Rhum to Cape Wrath. In the Assynt to Cape Wrath region the unconformity is often planar, and the underlying gneisses heavily weathered to palaeosols (Williams 1968). The Applecross Formation itself is of fluvial origin, having been deposited in shallow sinuous channels up to 30m wide. These formed part of a braided sequence (Selley 1969). The lower-most Applecross Formation consists of fineing upwards fan deposits, whose origins lie near the Outer Hebrides (Williams 1969). Indicating a sediment source to the West of the present Torridonian outcrop. The Applecross Formation finally buried the Lewisian topography, with basin subsidence and sedimentary accumulation appearing to have been fast. This is indicated by the large scale bed contortion, due to fluid overpressure and upward moving pore water.

Succeeding the Applecross Formation is the Aultbea Formation, a continuation of the Applecross Formation, but finer grained sandstones as opposed to the coarser Applecross Formation arkoses. Contorted bedding is again common, and the source for the sediment perhaps more distal. The Cailleach Head Formation consists of several upward coarsening sequences of shale to tabular sandstone. It represents cyclic deltaic deposits into freshwater lakes and is confined to the Gairloch to Achiltibuie region.

2.4.1.1 The tectonic setting of the Torridonian

Williams (1969) presented an interpretation where the Torridonian developed from the detritus produced during the weathering and retreat of an upstanding mountain chain. This lay in the region of the Outer Hebrides. Large alluvial fans built outward to the SE, forming clastic wedges off a SE dipping Lewisian topography. The interpretation is based on Applecross Formation palaeoflow directions. However, the sharp reversals of the palaeoflow directions within the Stoer Group, and the basic volcanism, suggest sedimentation in a fault controlled rift environment (Stewart 1982). It may be argued that the palaeoflow reversals in the Stoer Group could equally well be due to sediment deposition from opposite sides of a palaeovalley, or that the grid sampling method of Williams (1968) is not rigorous enough (especially as many local variations in bed dip occur in the Applecross Formation (P. Nicholson pers. com.)). Laying these questions aside, it is currently believed that the main source for the Torridon Group was to the West of the present exposure, and that source lithologies are not presently found in the Lewisian outcrop (Williams 1969). The western most extent of the Torridonian is believed to be

marked by the Minch Fault, and Torridonian rocks are thought to underlie the Permo-Triassic in the Minches (Smythe *et al.* 1972). The favored model at present is the Torridonian lying within a NE-SW Proterozoic rift-valley, with the western bounding fault to the rift perhaps being marked by the Minch Fault. Stewart (1982) argues that the lack of palaeoflow directions from the East suggests the proposed eastern bounding faults were smaller, resulting in an asymmetric rift. This rift would have lain on the eastern margin of Laurentia, and may have been connected with a phase of crustal extension preceding the opening of the Iapetus Ocean (Stewart 1988a).

2.4.2 The Cambro-Ordovician sequence of the northwest highlands

The Cambro-Ordovician succession of the northwest highlands represents a transgressive sequence. The planar unconformity oversteps the Torridonian, allowing deposition directly upon the Lewisian basement. The sequence fines upwards, from basal conglomerate, through quartzarenites, into siltstones with grits, and finally thick limestones.

The basal unit consists of thin basal conglomerates, overlain by well sorted quartzarenites, subordinate arkoses and subarkoses (Swett 1969). These are believed to represent subtidal and intertidal sands deposited as the erosional front of the transgression. This unit is succeeded by the 'Pipe Rock', a similar lithology, but rich in bioturbation burrows. Again an intertidal environment is suggested. Together these units are termed the Eriboll Sandstone, and commonly miscalled the Cambrian Quartzite.

Below this unit, the Lewisian surface is often altered, with both quartz and feldspar becoming altered to clays and muscovite. This alteration, termed agalmatolite (Peach *et al.* 1907), is not only exposed on the surface, but extends for some meters down joint planes into the gneiss (Russell & Allison 1985). This is believed to be due to alkaline weathering by the Cambrian sea water, and may play an important role in the formation of the overlying Fucoid Beds (Russell & Allison 1985).

The Fucoid Beds are essentially dolomitic siltstones (Swett 1969) with very high levels of potassium, as authigenic K-feldspar (Bowie *et al.* 1966). The discovery of anhydrite and celestite with $\delta^{34}S$ values typical of early-Cambrian seawater (Allison & Russell 1985) led to the interpretation of the Fucoid Beds as a lagoonal deposited feldspathic mud. For periods there was regression from lagoons to sabkhas, allowing the formation of the evaporites. The high (8-12%) potassium content is explained with regard to the formation of agalmatolite allowing the release of potassium during deep alkali weathering of the Precambrian basement. This potassium was then redeposited in the Fucoid Beds and Dalradian Basin (Russell & Allison 1985).

Previously the Fucoid beds were interpreted as being a continuation of the marine transgression, with the Salterella Grit (formerly Serpulite Grit), a regressive sequence (Walton 1983). However, in the light of the proposed lagoonal nature of the Fucoid Beds, the Salterella Grit can be considered as a continuation of the transgression.

The sequence is capped by the thick deposits of the Durness Limestone, which spans the Cambro-Ordovician boundary. The boundary is marked by a gap in the sequence, now preserved as a karst surface, with the mid to upper-Cambrian missing (Palmer *et al.* 1980). The Durness Limestone itself is divided up into various units, composed of limestone, dolomitic limestone and dolstone (see Walton 1983). Chert bands or layers of chert nodules sporadically occur and the diagenetic history is discussed by Swett (1969). Stromatolites are common in the sequence near Durness, and a shallow shelf environment, with sedimentation rate paralleling subsidence, is envisaged (Swett 1969)

In summation, the Cambro-Ordovician is generally accepted to be a marine transgressive sequence, laid down in a near shore to marginal shelf environment, on the eastern margin of Laurentia. Southeast of this the Dalradian Basin and the Iapetus Ocean were involved in active extension.

CHAPTER 3

THE GEOLOGY OF THE FEATURES STUDIED

3.1 The chosen area of study and the sampling strategy

Samples for this study were taken from the central and northern Lewisian regions. This was because these regions are well exposed, well documented and possess a wide range of structures and lithologies.

The work of Hall (1986, 1987), established that the sealed fractures present within the Lewisian gneiss are all post-tectonic with reference to their host lithology. This can be seen where they cross cut the metamorphic fabric of the rock. However, the reasons for, and timing of, fracture sealing were unknown. The sampling was therefore designed to maximize the prospect of:

(a) discovering the time of fracture sealing;

(b) discovering the processes in operation during and involved with fracture sealing; and

(c) identifying the conduits for fluid movement.

Samples used for the investigation of sealed fractures were taken from specific zones chosen for their likelihood to have allowed fluid circulation. As the Kylesku Group granulites are essentially "dry", sampling was possible over Inverian and Laxfordian structures where fluid movement was known to have occurred (as is indicated by the hydration of the granulites). These sites are characterized by high fracture densities which are likely to enhance their prospects of post-tectonic fluid flow.

Other basement sites included the igneous rocks of the Scourie dyke suite and Laxfordian granites, as well as the country rock granulites and gneisses. By sampling over a wide lithological and geological suite, as well as a large geographical area, it was hoped it would be possible to identify any fluid flow operating within individual lithologies or structures, as well as any fluid flow operating on a regional scale.

The Torridonian and Cambrian unconformities also represent periods when the Lewisian basement is likely to have been saturated in water. Sampling was carried out at the three major unconformities within the region, that is, at the base of the Stoer Group, the Torridon Group and the Cambrian. It was hoped that this would allow any influence of these post-Laxfordian events on the basement fluid flow to be recognised.

Core samples used in the study of open cracks, porosity and permeability were collected by Professor Jeremy Hall.

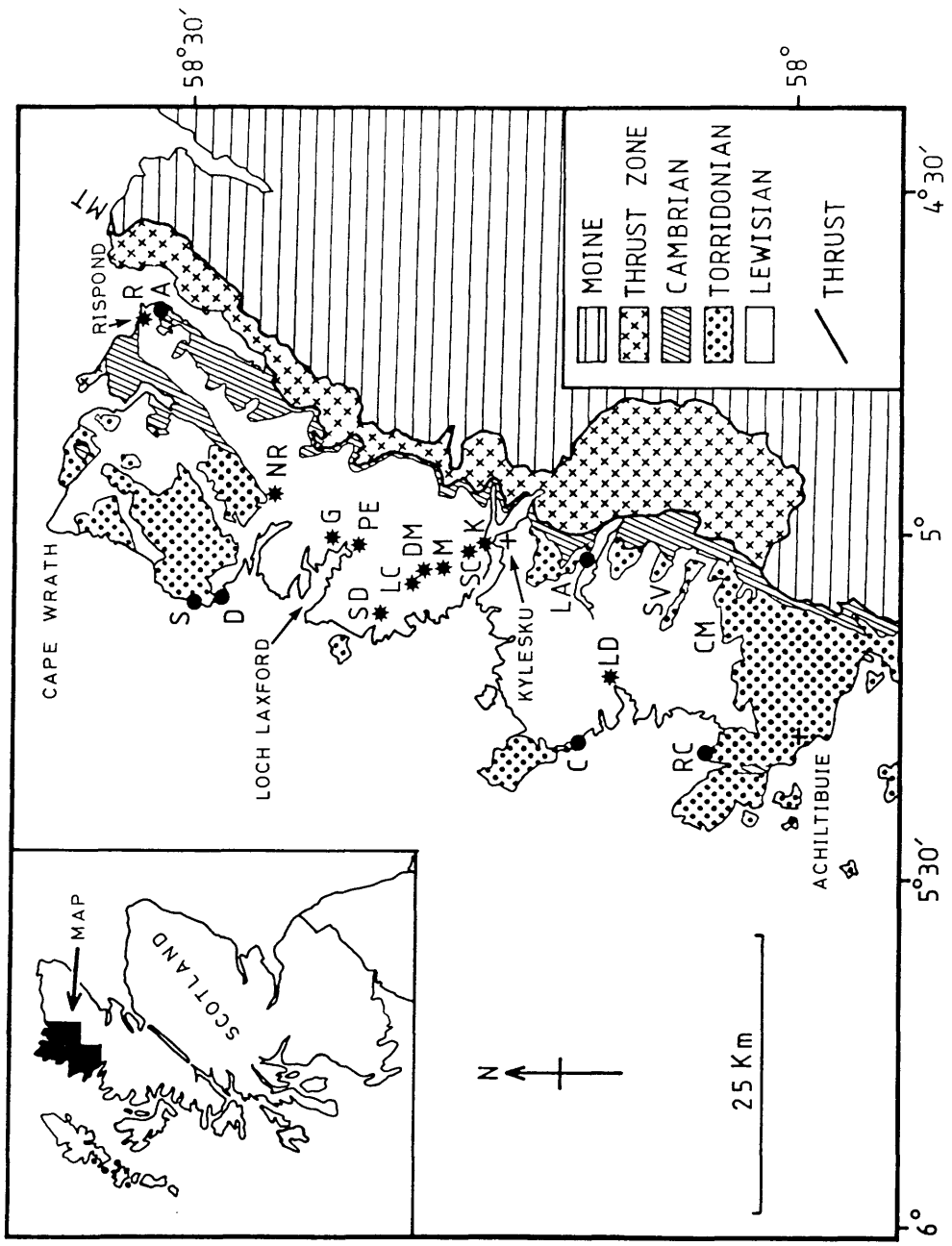

Figure 3.1 Location map for sample sites described in Chapter 3. ✶ = Lewisian gneiss sample sites, ● = Torridonian and Cambrian unconformity sample sites. **A** = agalmatolite at Cambrian unconformity (Rispond). **C** = Torridonian unconformity (Clachtoll). **CM** = Cul Mor. D= Torridonian unconformity (Dorman). **DM** = Scourie dyke intruded along an Inverian monoclinal fold (Loch a' Mhinidh). **G** = granite vein (Laxford Bay). **K** = Kylesku granulites (Kylesku). LA = Torridonian unconformity (Loch Assynt). **LC** = Laxfordian fold - crush shear zone (Geisgeil). **LD** = Scourie dyke (Lochinver) .**M** = Inverian monoclinal fold (Duartmore). **MT** = Moine Thrust. **NR** = Laxfordian gneiss (Rhiconich). **PE** = pegmatite vein (Laxford Bridge). **R** = Laxfordian gneiss (Rispond). **RC** = Torridonian unconformity (Rubh' a' Choin). **S** = Torridonian unconformity (Sheigra). **SC** = sheared Scourie dyke Margin (Kylestrome). **SD** = Scourie dyke (Scourie). **SV** = Suilven . Geology taken from 1:253,440 Geological Survey sheet # 5.

3.2 Method of sampling

The chosen features and localities were sampled by one, or both, of two methods. Traverse sampling and specific sampling.

Traverse sampling was necessary as small microcracks could not be seen in the field. This method consisted of sampling at regularly spaced intervals across a basement structure, or unconformity, thus obtaining a sealed microcrack profile.

Specific sampling was carried out with a portable field drill, and provided 1 inch cores. This was aimed at sealed cracks visible at outcrop scale. The larger sealed cracks were intended to provide material for isotope analysis. The primary use for the traverse samples was to investigate the sealed microcrack systems under the microscope.

3.3 Basement sample sites

Basement sampling took place across a selection of the lithological and tectonic units, between Kylesku and Loch Laxford in the central region, and at Rhiconich and Rispond in the northern region (Fig 3.1). By sampling across shear zones (see Fig 2.3), where jointing and fracturing have a high density, the likelihood of finding sealed fractures should be increased.

3.3.1 Basement sample sites (traverse sampling)

3.3.1.1 Kylesku Group granulites (NC 227 338) (Fig. 3.9a)

The pyroxene granulites of the Kylesku Group were sampled at the northern landfall of the Kylesku Bridge. This location lies on the western limb of the major Scourian F_3 Kylesku Fold. The granulites have a constant NW subhorizontal dip across the road cutting. Banding is 1-3 cm wide and consists of mafic and felsic layers. Occasional small pinched out hornblendite pods deflect the banding, which is folded in tight, recumbent, intrafolial folds. These Scourian F_1 folds are overprinted by the granoblastic Badcallian fabric. Quartz, which is often blue or opalescent, forms a polygonal mosaic with andesine and both ortho- and clinopyroxene. Ilmenite and magnetite occupy the interpolygonal crystal boundaries. In many cases pyroxene exhibits slight retrogression, in the form of coronas of hornblende, actinolite, or biotite.

3.3.1.2 Inverian monoclinal fold belt (NC 200 367) (Fig3.2 and 3.9b)

The Inverian monoclinal fold belts trend NW, forming Z-folds looking down their gently SE-plunging fold axis. This belt is cut by the Kylesku-Scourie road at Duartmore Forest, and exposed as a vertical cutting to the East of the road.

The steep limb is complex due to refolded earlier folds unrelated to the monoclinal folding (Khoury 1969). The flat limbs consist of banded pyroxene and hornblende granulites, becoming hornblende rich toward the fold. An axial planar foliation is developed across the steep limb, but the main fissile layer remains the gneissose banding. Pinch and swell structures are common, with flattening and shear occurring across the steep limb (which is about 80 m wide). The complex folds are tight isoclines and monoclines, often distorted or sheared during the development of the large monoclinal fold. On the SW edge of the fold, discrete shear zones break up the SW flat limb.

Within the flat limbs, deformation and retrogression are found to increase toward the steep limb. Pyroxene becomes mantled by fibrous hornblende rims, with plagioclase showing slight sericitization along crystal boundaries and twin planes. The crystal size is not refined, and the coarse granoblastic texture is preserved. Where retrogression has been more pervasive the pyroxenes are totally retrogressed, becoming replaced by radiating clusters of fibrous amphibole. These form pseudomorphs of the polygonal pyroxenes. The amphibole composition often varies from the edge to the centre, with an outer rim of blue green hornblende, and an inner knot of actinolite. The retrogression is essentially a passive one, with little evidence of directed pressure during amphibole growth. In localized zones of high strain, the rock becomes granulated and recrystallized, into a fine grained aggregate of hornblende and quartz. Plagioclase is larger but subidioblastic. This suggests the plagioclase was a component in the recrystallization reaction which can be explained by

$$Opx + Cpx + Plag + H_20 = Hb + Qtz.$$

Excess calcium produced in this reaction is used in the alteration of ilmenite to sphene, where

$$Ilm + Ca = Sph.$$

Once into the steep limb the subhorizontal granulites become subvertical, and banding is attenuated. Quartz becomes streaked and ribboned and, along with hornblende, forms lenses. Plagioclase most often exists as augen, many of which show evidence of rotation and banding deflection. Clinozoisite and epidote, a product of sausseritization, become common near plagioclase which is often heavily sericitized. Marginal granulation occurs within the larger crystals, and biotites have grown along foliation planes (an effect which may be of

Laxfordian age). Occasionally granular aggregates of hornblende have recrystallized to form a single large hornblende poikiloblast with granular quartz inclusions. This reflects the growth of hornblende, attempting to reach equilibrium, in a post-tectonic thermal high.

3.3.1.3 Scourie dyke at Scourie (NC 168 442) (Fig 3.4 and 3.9c)

The location of this Scourie dyke is on the Scourie -Laxford Bridge road, 1 km East of Scourie. It outcrops, as a vertical N-facing road cutting, next to Loch a' Bhadaidh Daraich. The medium to coarse dolerite dyke is 60 m wide and discordant to the coarse banded hornblende granulites. Trending NW, the dyke may have been emplaced along a small Inverian monoclinal fold exposed to the SW contact. The margins of the dyke are insitu except for a 1-2 cm sheared zone of amphibolite along the NE edge. Here slight banding deflection can be found in the granulites.

The country rock granulites are coarse hornblende granulites which exhibit only slight post granulite strain features. However, plagioclase shows heavy uniform alteration to sericite. Toward the dyke contacts the granulite becomes slightly deformed, with a refined crystal size and a cross foliation of biotite. This either relates to the monoclinal fold, or to edge parallel shear. The dyke is strongly sheared at its NE margin, having taken up most of the deformation in a 1-2 cm wide zone. This results in a well foliated amphibolite composed of equant fine grained granoblasts, elongated in the direction of the foliation. Foliation persists for several cm's into the dyke. The schistosity is spaced and lenses of plagioclase exist, producing a gneissose fabric. 50 cm into the dyke, it is unsheared and exists as a diapthorized dolerite, with subidioblastic pyroxene cores surrounded by hornblende and actinolite. Original igneous texture is preserved by plagioclase and the pyroxenes, which are now partially pseudomorphed.

3.3.1.4 Scourie dyke emplaced along an Inverian monoclinal fold belt (NC189 379) (Fig. 3.6)

A Scourie dyke with a superimposed Laxfordian fabric runs NW along the subvertical steep limb of an Inverian monoclinal fold belt at Loch a' Mhinidh, East of the Kylesku-Scourie road. The NE side of the structure was mapped using a plane table.

The flat limb consists of subhorizontal, gently undulating granulites, giving way southwestward to subvertical gneisses and hornblende schists. The dyke margin is strongly foliated and crystal size is small. However, this increases away from the edge of the dyke . Near the steep limb, the granulites have a secondary cleavage. This relates to the

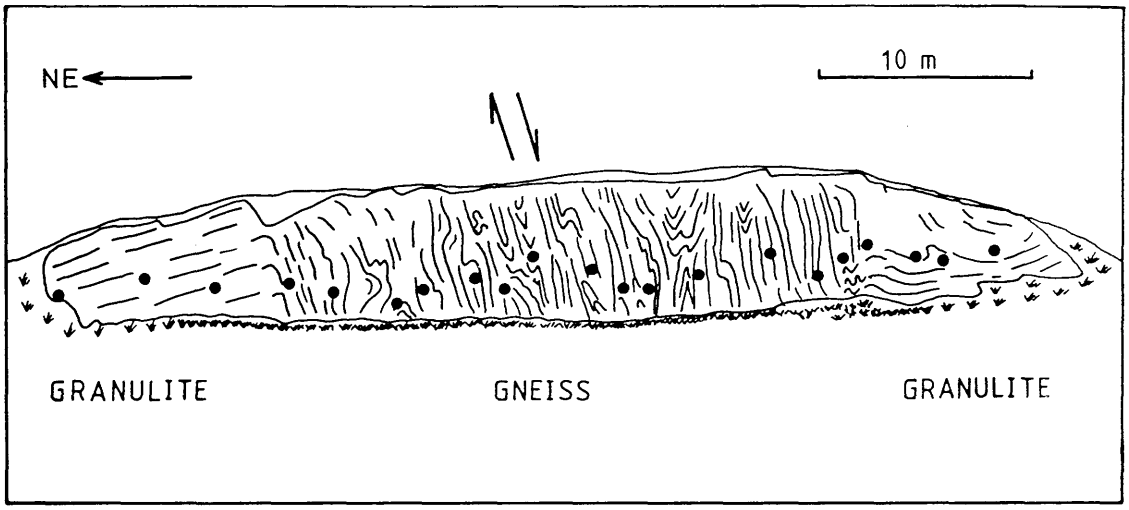

Figure 3.2 Field sketch of the Inverian monoclinal fold belt at Duartmore (prefix-M). Grid reference NC 200 367. ● = Sample point.

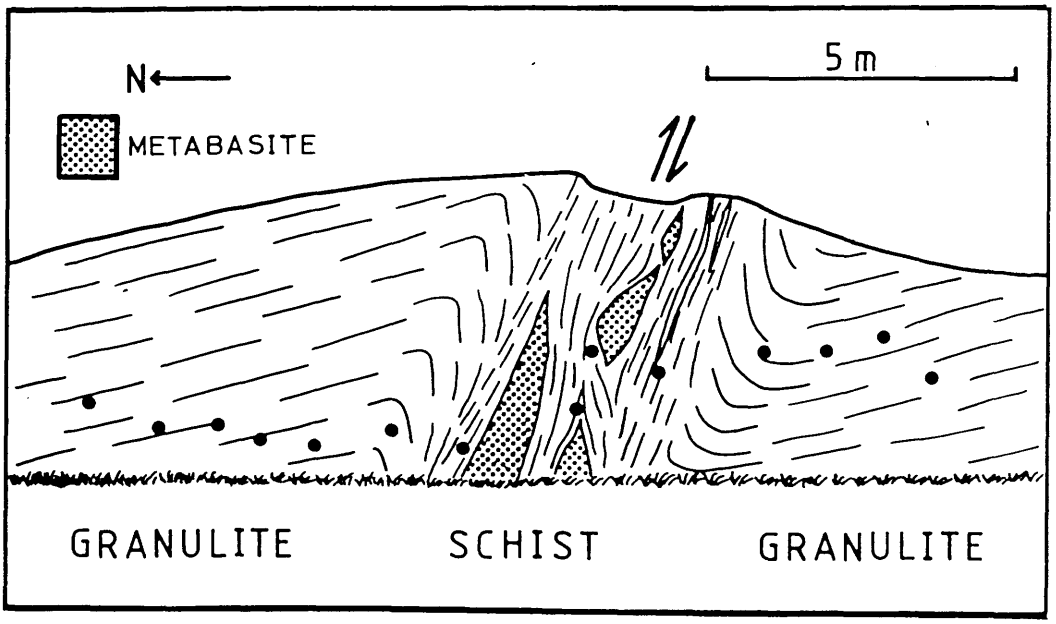

Figure 3.3 Field sketch of the Laxfordian shear zone near Geisgeil (prefix-LC). Grid reference NC 174 397. ● = sample point

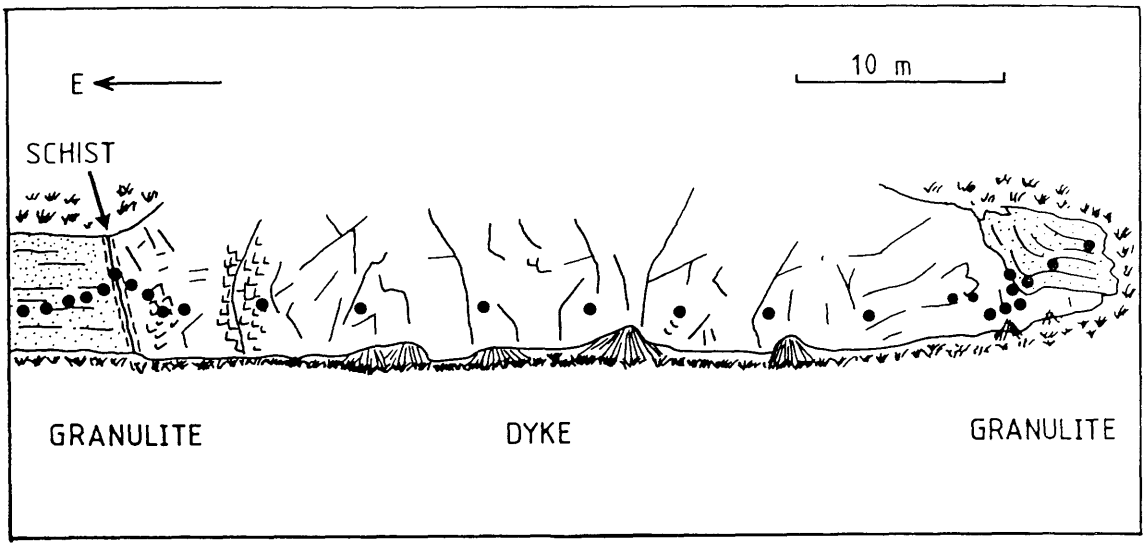

Figure 3.4 Field sketch of the Scourie dyke near Scourie (prefix-SD). Grid reference NC 168 442. ● = sample point.

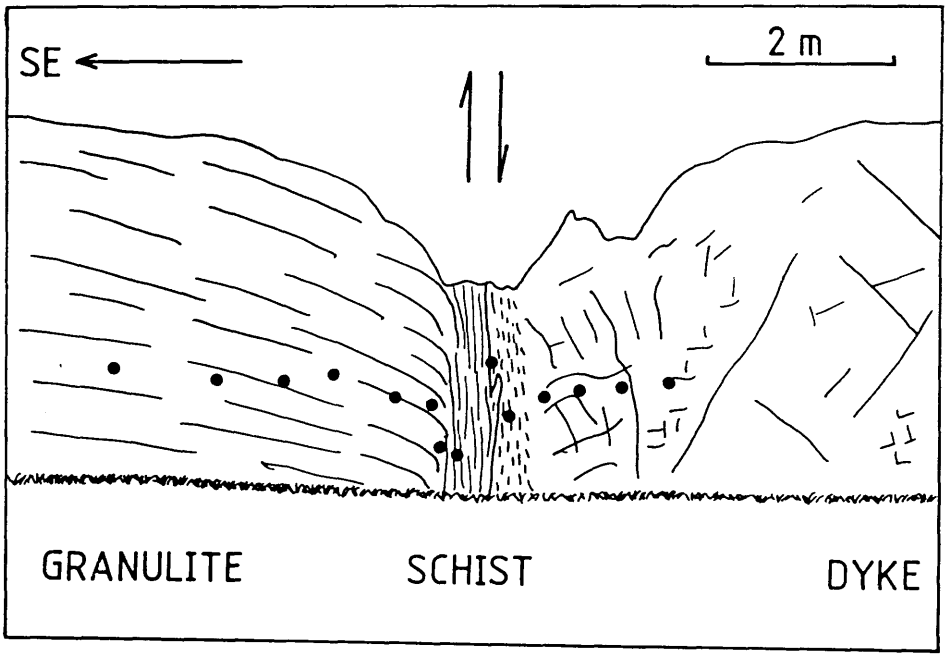

Figure 3.5 Field sketch of the sheared Scourie dyke, Kylestrome (prefix-SC). Grid reference NC 217 347. ● = sample point

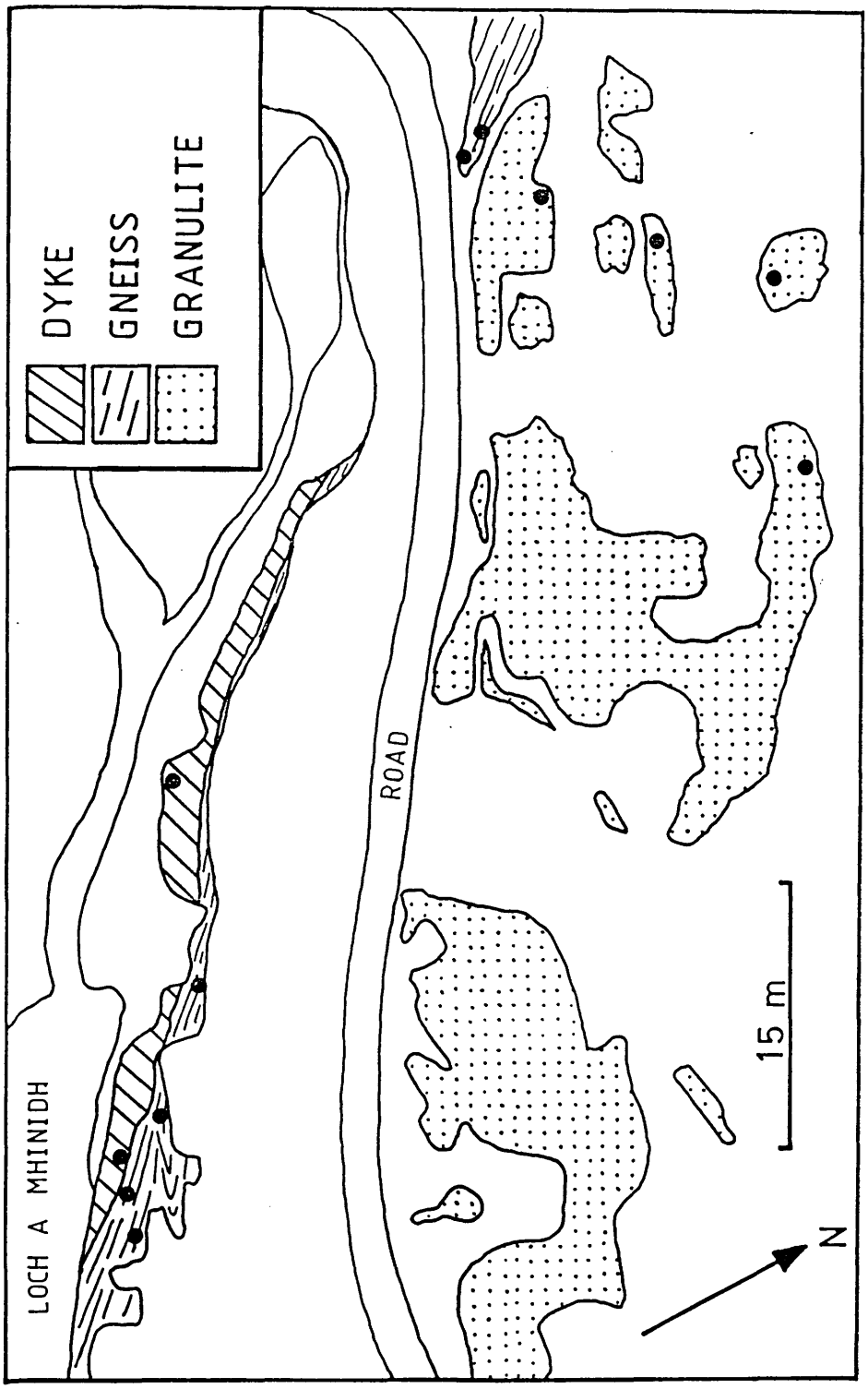

Figure 3.6 Location map for Scourie dyke emplaced along an Inverian monoclinal fold belt at Loch a' Mhinidh. (prefix-DM). Grid reference NC 109 379. ● = sample point.

monocline, with the granulites and schists showing evidence of minor fold interference. Ductile shear zones are common within the dyke, breaking it up into augen blocks surrounded by foliated amphibolite schist. The location of these shears perhaps being controlled by the original joints in the dyke.

Consisting of hornblende, plagioclase, biotite and quartz, the Scourie dyke has a strong Laxfordian foliation subparallel to the dyke margin. This produces a SE plunging lineation. The existence of subidiomorphic hornblende and quartz, in a poikilotopic relationship, points to the break down of pyroxene and plagioclase. Biotite is a result of the introduction of K^+ in fluids. Away from the margins the dyke is coarse grained. Toward the margin the dyke becomes progressively more tectonized. This produces a granular mosaic of hornblende, plagioclase, K-feldspar, quartz and biotite. The foliation being picked out by the mafics.

The country rock next to the dyke is also tectonized, with a coarse schistosity picked out by hornblende and opaque ores. Quartz has deformed in a ductile manner, with large granomorphs transformed to ribbon quartz. Plagioclase is heavily sericitized and large idiomorphic epidotes occur. The ilmenites become altered to sphene and the following reactions are suggested:

$$Opx + Cpx + Plag + K^+ + H_20 = Hb + Qtz + Bio;$$

$$Ca\ Plag = Alb + Epi + Ca^{2+};$$

$$Ca + Ilm = Sph.$$

The country rock becomes coarser in crystal size, with large granoblasts of quartz and plagioclase surrounded by polygonal finer grained crystals. Hornblende becomes poikilotopic with quartz, however, marginal granulation of poikiloblasts can be found. This indicates polyphase metamorphism and deformation relating to the Inverian and Laxfordian. Pyroxene has been broken down into quartz, hornblende, and biotite with pyroxene pseudomorphed by hornblende and quartz aggregates. Once into the flat limb the country rocks become coarser granulites (as opposed to the flaggy gneisses of the steep limb). The plagioclase and quartz are deformed, via kink-bands and grain boundary granulation, into large subidioblastic and smaller idioblastic crystals. Biotite growth appears to be static, in the form of fibrous knots.

3.3.1.5 Sheared Scourie dyke margin (NC 217 347) (Fig. 3.5 and 3.9e)

On the Kylesku-Scourie road, at the Kylestrome turn off, an E-facing road cutting exposes coarsely banded hornblende granulites. The granulites are truncated by a NW trending dolerite Scourie dyke. Only one margin of the dyke is visible. It is subvertical and has been

affected by Laxfordian shearing, resulting in a penetrative margin parallel foliation within the granulites and the dyke. Deflection of the banding and lineations indicate a sinistral strike-slip movement, with the country rock downthrown to the SW.

The granulites comprise of a mosaic of quartz, plagioclase and amphibole pseudomorphs (after pyroxene). They become progressively tectonized toward the shear zone, with intragranular and grainboundary granulation planes producing an island mosaic texture. Hornblende and quartz granomorphs exist after pyroxene, with biotite present next to opaque ores. Plagioclase, an albite has abundant epidote-clinozoisite inclusions. Occasional poikilotopic hornblende crystals, with quartz inclusions, are also present.

Toward the shear zone the crystal size becomes refined and the banding thins. Mortar textured crystal boundaries are common, and low pressure quartz granulomorph beards have grown in the pressure shadow of plagioclase augen. Shearing and granulation are concentrated along layers producing polygonal islands surrounded by mortar textured granulomorphs. In the shear zone quartz becomes streaked and ribboned. These ribbons are deflected around plagioclase augen, which are sericitized.

The Scourie dyke caught up in the shearing has also undergone grain scale refinement. Pyroxenes have broken down to produce hornblende, biotite and quartz, in what was originally a quartz free diorite. Poikilotopic hornblende is common, and plagioclase, both sericitized and sausseritized, is preserved as augen. Outside the shear zone the dyke retains many of its igneous features. Plagioclase laths are most common, and original pyroxene occurs, only slightly diapthorized to amphibole rims. Opaques are distributed around the original pyroxenes (which show a subophitic texture). Some brittle shearing and, marginal sericitization, of plagioclase is common. Biotite grows adjacent to opaques and there is little evidence for strain.

3.3.1.6 Laxfordian fold crush belt (NC 174 394) (Fig. 3.3 and 3.10a)
The Laxfordian fold crush belt sampled is an E-W shear zone which outcrops in a road cutting on the Kylesku-Scourie road, at the northern turn off to Loch Duartbeg, near Geisgeil. The belt is about 4 m wide and plunges steeply to the North. Roll-over folds and lineations suggest dextral transpression, resulting in thrusting of the northern side over the southern. A post-Laxfordian basic dyke cuts the northern limb of the roll-over fold. The shear zone consists of a central zone of hornblende schist, containing a boudinaged and foliated basic sheet. Outside the central schist zone there is a zone of subvertically banded amphibolite gneiss with concordant pegmatite veins. This then passes out of the shear into hornblende granulites which follow the regional dip to the NW.

The granulites surrounding the shear zone are subhorizontal and retrogressed to

hornblende granulite. Pyroxene is not present and evidence for the original nature of the granulites can only be seen where strain was at its lowest. There the original granoblastic texture is preserved, and pseudomorphed, by recrystallized aggregates of hornblende and quartz (which are sometimes poikilotopic). Otherwise, the granulites have a streaked appearance, with larger crystals becoming refined via grain boundary granulation. In the case of plagioclase, internal kink-bands produce disjointed subidioblastic crystals which often deflect the foliation. Biotite is common in clusters around opaques.

Within the shear zone the rocks pass from granulite, to amphibolite gneiss, to amphibole mica schists. Discrete shears and mylonite zones are common (the aphanitic ground mass of the mylonite being littered with rounded and angular crystals and rocks)

3.3.1.7 Laxfordian granite vein (NC 227 479) (Fig. 3.7 and 3.10c)

The granite sheet can be found at Laxford Bay, on a West facing cliff, East of the Laxford Bridge to Durness road. The coarse grained sheet is mostly discordant, cutting the axial plane of a Laxfordian F_2 fold. Minor offshoots run concordantly to banding. Near the contact the gneiss appears to be migmatized.

The granite is coarse grained and rich in K-feldspar, which is strongly perthitic. Much of the feldspar is cracked along kink-bands. At the contact, the gneiss has a high percentage of K-feldspar. Epidote is also abundant, and plagioclase is partly altered. Further away the rock is still rich in perthitic K-feldspar (indicating a slow cooling rate). Feldspars show variable alteration to sericite, and epidotes are strained and intergrown with vermicular quartz. The idioblastic epidote overgrowths formed as a result of thermal overprinting by the granite vein. Away from the vein K-feldspar is absent, and must have been metasomatically introduced into the country rock gneisses around the vein.

3.3.1.8 Laxfordian pegmatite vein (NC 233 465) (Fig. 3.8 and 3.10b)

A discordant pegmatite vein, part of a larger system cutting hornblende biotite gneiss, can be found South of the Laxford Bridge junction, in an East facing roadcut.

The pegmatite is coarse and milky white, consisting of plagioclase, quartz, orthoclase, and biotite. The biotites, which are numerous at the margin of the vein, may mark a margin parallel flow texture. The gneisses are granular, with equant polygonal grains and a strong foliation parallel to banding. Numerous small pegmatitic off shoots penetrate the country rock.

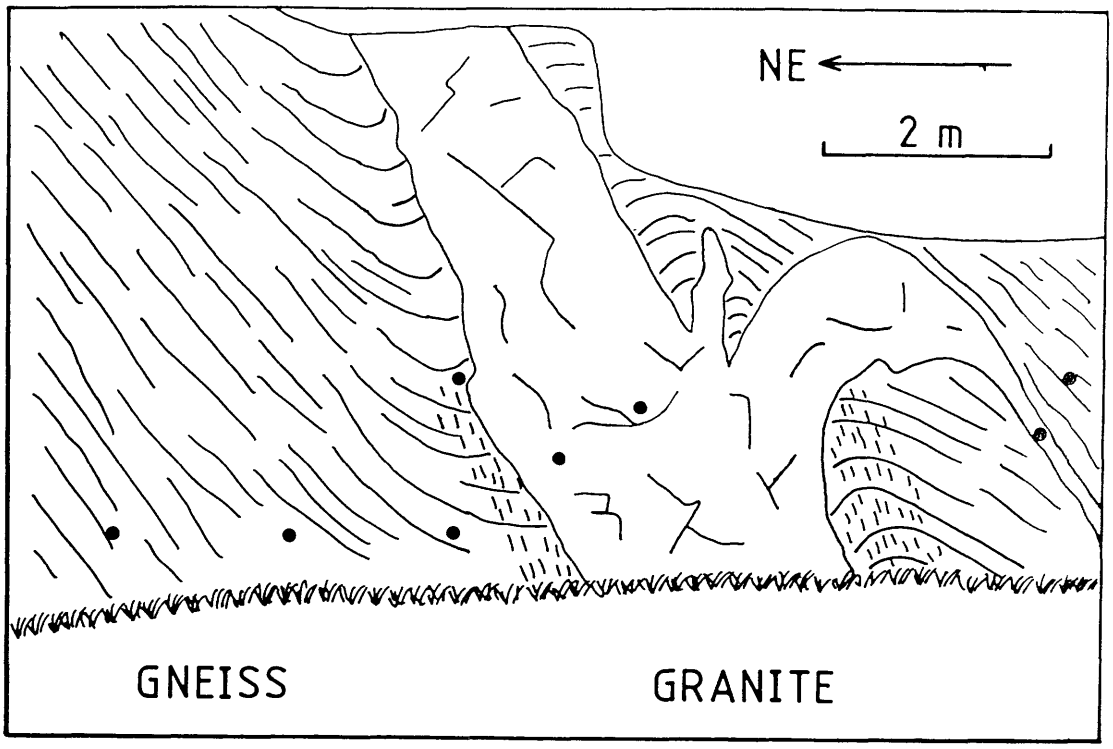

Figure 3.7 Field sketch of the Laxfordian granite vein at Laxford Bay (prefix-G). Grid reference NC 227 479. ● = sample point.

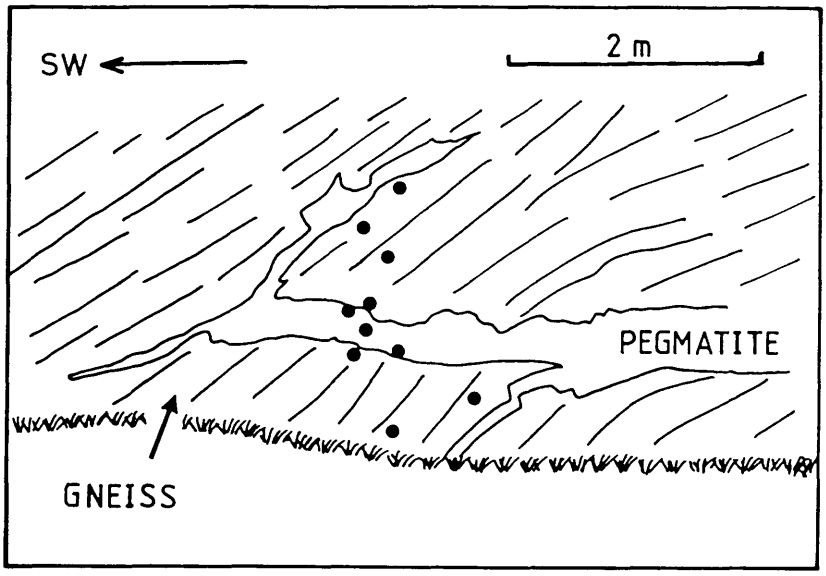

Figure 3.8 Field sketch of the Laxfordian pegmatite vein at Laxford Bridge (prefix-PE). Grid reference NC 233 465. ● = sample point.

3.3.2 Basement sample sites (specific sampling)

3.3.2.1 Ultrabasic body (NC 160 427) (Fig. 3.10d)

A peridotite-serpentinite body, by the road side to Upper Badcall, was sampled with a field drill specifically to obtain samples of sealed fractures. The body is of limited outcrop size and is heavily altered along joints. Olivine was the only constituent of this peridotite, which it is now totally altered to serpentine pseudomorphs.

3.3.2.2 Scourie dyke at Lochinver (NC 096 232) (Fig. 3.9d)

The outcrop studied occurs to the North of the River Inver, where the Lochinver to Skiag Bridge road crosses the river.

The dyke is some 20m wide, vertical, and possesses a NW trend. The margins are fine grained and sheared, giving way to a coarse grained ophitic dolerite-gabbro in the centre. The dyke is highly diapthorized throughout, with amphibole pseudomorphing pyroxene. The retrogression of the country rock gneisses, and the diapthoresis of the dyke are, assumed to be similar to the Scourie dyke described from Scourie. Sampling was specific coring of large sealed fractures and joints.

3.3.2.3 Laxfordian gneiss (NC 440 657) and (NC 272 537) (Figs. 3.9e and 3.9f)

Laxfordian gneiss was sampled at two locations within the northern region. Both in quartzo-feldspathic gneisses: at Rispond Beach car park; and North of Rhiconich, at Creag Gharbh Mhor. At both locations visible sealed fractures werecored with a field drill.

3.4 Basement petrology: a summary

The pyroxene granulites of the Kylesku Group are, on the whole, composed of a coarse granulomorphic polygonal mosaic of quartz, andesine, hypersthene and augite. Ilmenite and magnetite occupy the inter-polygonal crystal boundaries. In many cases the pyroxenes are lightly altered to biotite or hornblende.

Toward the shear zones, deformation and hydration increase. The pyroxenes first become mantled by fibrous hornblende and actinolite rims, and plagioclase shows slight to heavy sericitization. When actinolite forms, pyroxene is usually in contact with plagioclase (which is subidioblastic and partly digested). This indicates the interaction of pyroxene and plagioclase to produce actinolite. Crystals then become refined with marginal granulation of plagioclase and pyroxene occurring. Eventually recrystallization and hydration progress to completion leaving a fine grained mosaic of hornblende and quartz.

This reaction can be explained by the following equations:

$$Opx + Cpx + Plag + H_20 = Hb + Qtz; \text{ and}$$

$$Plag = Alb + Epi + Ca^{2+} .$$

The excess calcium produced by this reaction is seen in sphene coronas around ilmenite. In the Laxfordian shear zones, there is a noticeable increase in biotite (which is absent in the Inverian structures). This can be explained in terms of

$$Opx + Cpx + Plag + H_2O_{(k^+rich)} = Hb + Bio + Qtz.$$

The potassium required for the biotite is introduced via potassium rich fluid moving along the shear zone. In both Laxfordian and Inverian shear zones, the fine quartz and hornblende mosaics become recrystallized into poikilotopic hornblende with quartz inclusions. This is evidence for a post-shearing thermal high within the zones. In some Inverian zones deformed poikilotopic hornblendes show evidence for Laxfordian reworking. Similarly, the presence of biotite indicates Laxfordian metamorphism.

The Scourie dyke suite consists of coarse dolerites. These are heavily diapthorized outside the usual marginal zone of shearing. Pyroxenes are altered to, and pseudomorphed to, hornblende and actinolite, while plagioclase maintains its original igneous lath form. Thus, the original igneous texture of the dolerite is retained.

The granite and pegmatite veins sampled occur within the 2 km wide Laxford Shear Zone, bounding the northern and central Lewisian regions. Here the rocks are of greenschist to lower-amphibolite facies. The veins intrude along the banding planes and the Laxfordian F_2 axial planes. The granites have migmatized the adjacent wall-rock . K-feldspar has been introduced, and subidiomorphic epidotes now possess idiomorphic thermal overgrowths.

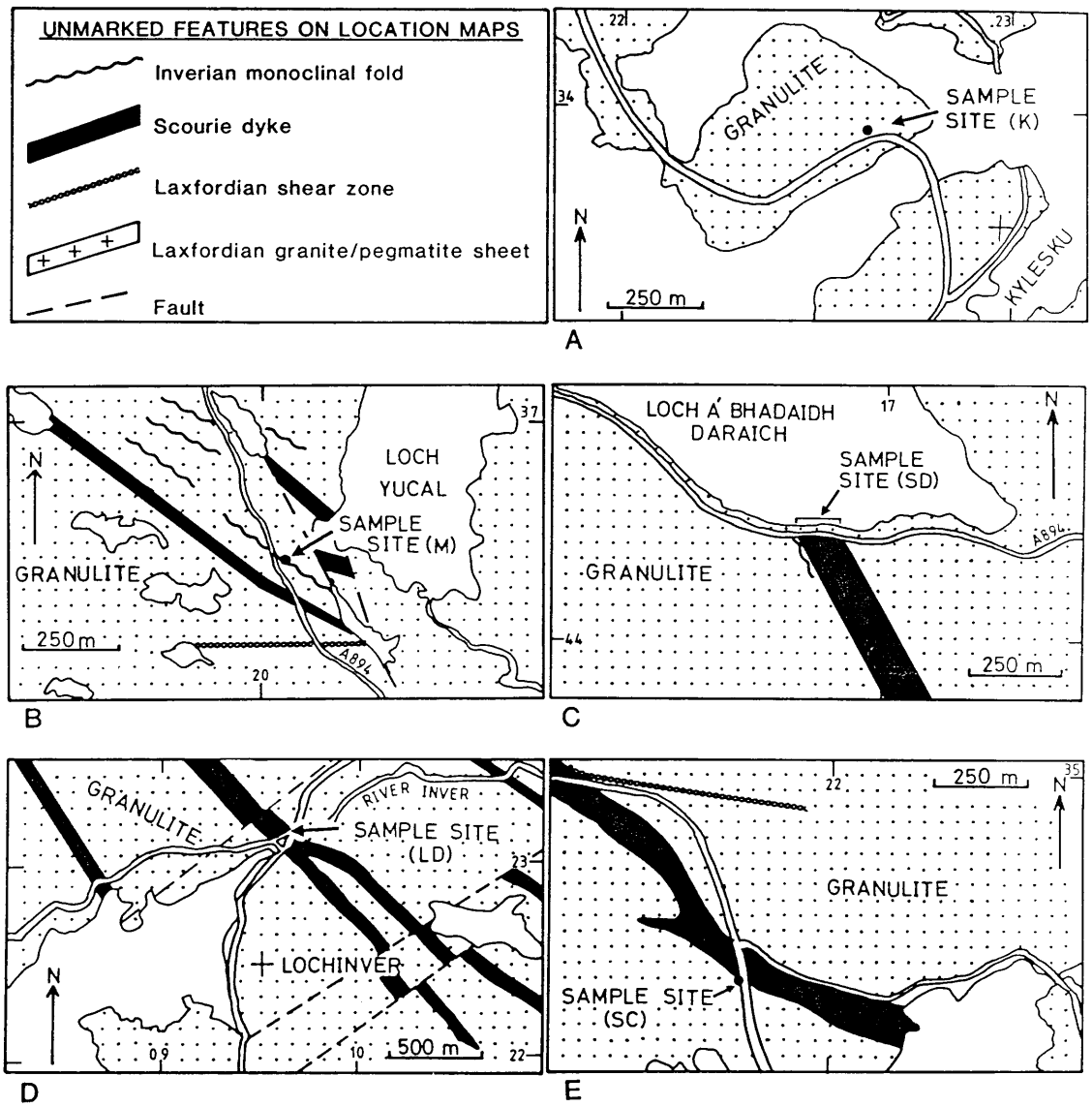

Figure 3.9 Location maps for basement sample sites.

A = Kylesku Group granulite at Kylesku Bridge (sample site K). Geology from Khoury (1968).
B = Inverian monoclinal fold belt at Duartmore Forest (sample site M). Geology from Khoury (1968).
C = Scourie dyke at Scourie (sample site SD). Geology from 1: 63,360 Geological Survey sheet # 107.
D = Scourie dyke at Lochinver (sample site LD). Geology from 1: 63,360 Geological Survey sheet # 107 .
E = Sheared Scourie dyke margin at Kylestrome (sample site SC). Geology from Khoury (1968).

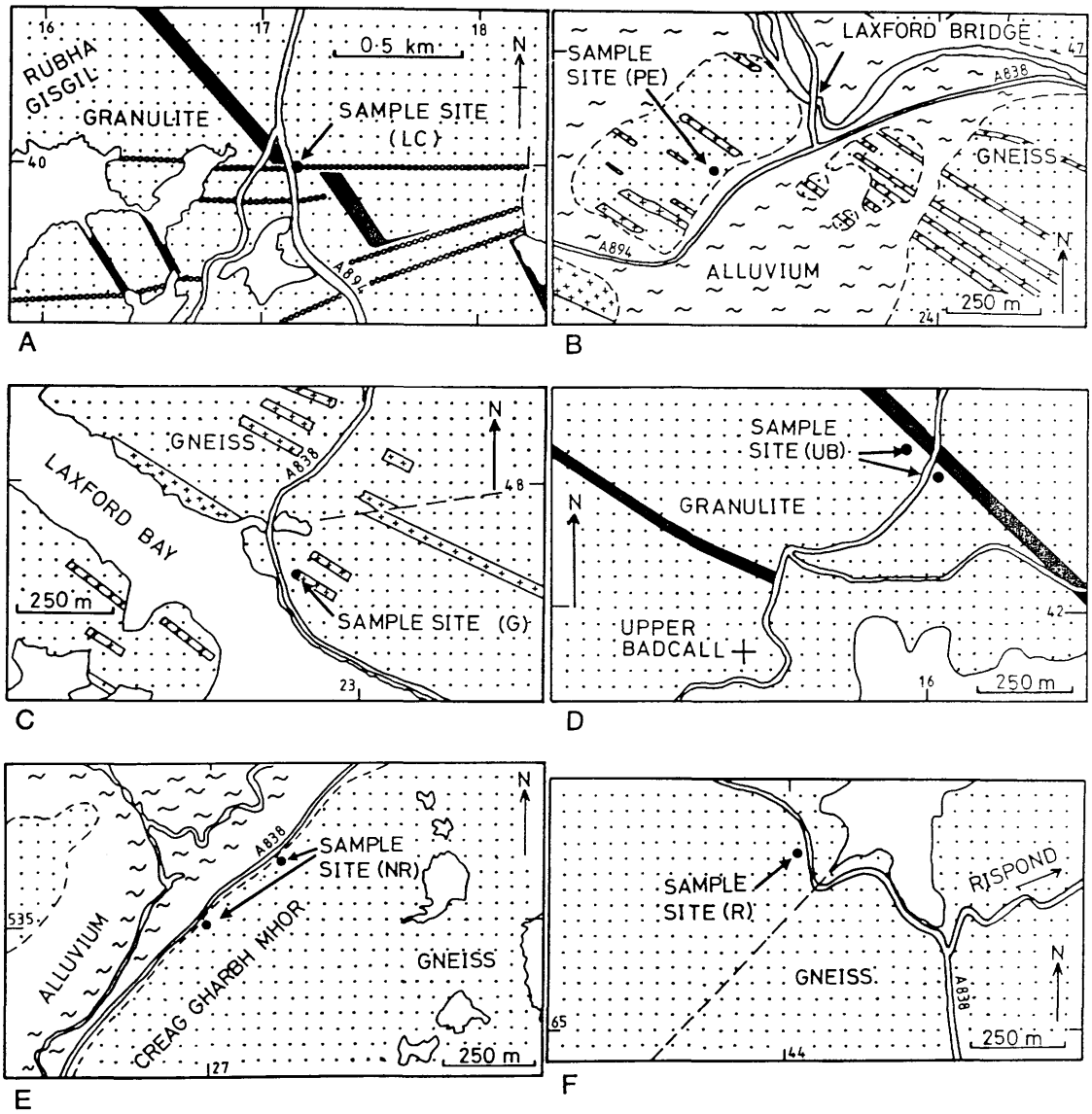

Figure 3.10 Location maps for basement sample sites.

A = Laxfordian shear zone near Geisgeil (sample site LC). Geology from Khoury (1968).
B = Laxfordian pegmatite vein at Laxford Bridge (sample site PE). Geology from Gillen (1975).
C = Laxfordian granite sheet at Laxford Bay (sample site G). Geology from Gillen (1975).
D = Badcallian ultrabasic rock near Upper Badcall (sample site UB). Geology from 1: 63,360 Geological Survey sheet # 107.
E = Laxfordian gneiss North of Rhiconich (sample site NR). Geology from 1: 63,360 Geological Survey sheet # 113.
F = Laxfordian gneiss at Rispond (sample site R). Geology from 1: 63,360 Geological Survey sheet # 113.

3.5 Unconformity sample sites

Sampling of the Torridonian and Cambrian unconformities, above the Lewisian basement, took place within both the northern and central regions of the Lewisian. It was designed to identify any relationship of fracture sealing to the unconformities, and thus provide a time tie to the age of fracture sealing (as well as attempting to delimit the nature of the geological event responsible for the hydrothermal fracture sealing).

3.5.1 Torridonian unconformity sample sites

3.5.1.1 Clachtoll (NC 041 267) (Fig. 3.11a)

South of Clachtoll Bay vertical Lewisian gneiss is overlain by Torridonian Stoer Group conglomerates and fine grained purplish-red sandstones. The conglomerates are composed of, rounded and angular, clasts and blocks of gneiss. They are preserved offlap fans upon the original Lewisian topographic highs.

The Lewisian is cut by sand-dykes which usually follow the foliation or joint directions, and penetrate the basement for a visible 10-15 meters.

Sampling of visible sealed cracks was done with a field drill.

3.5.1.2 Rubh' a' Choin (NC 03 14) (Fig. 3.11b)

The Torridonian outcrops of Rubh' a' Choin have been studied previously by Gracie & Stewart (1967), and represent one of the classical localities within the region. Here the Stoer Group and Applecross Formation unconformities can be seen, in relation to one another, and in relation to the Lewisian.

The unconformity to the Stoer Group is exposed both on the shore of Enard Bay and on the hill side above the Rubh' a' Choin peninsula. The basal conglomerates are composed of locally derived, rounded and angular, clasts and blocks of gneiss. Many of the clasts are rich in pumpellyite, often as a whole rock alteration of plagioclase. On the hill exposures of basement gneiss massive veins of pumpellyite are developed along joint surfaces. Areas of gneiss, up to 30 cm across are altered to pumpellyite. Sand-dykes penetrate the gneisses and in places both veining and sand-dykes appear contemporaneous. Brown sandstone gives way to siliceous green pumpellyite sand, and discrete pumpellyite veins crosscut the sand-dykes.

The conglomerates have an arkosic matrix, consisting of angular quartz, feldspar, and lithic fragments. Aggregates of epidote or pumpellyite are common, as is haematite cement. The epidote appears to be both detrital and authigenic in nature.

Sampling at Rubh' a' Choin was confined to the Stoer Group, specifically to the large veins, sand-dykes and the basal Stoer conglomerate. The Applecross Formation overlies the Stoer Group with an angular unconformity of 30-35° and does not contain the large amounts of epidote found in the Stoer Group below. In depth stratigraphy and lithological descriptions of this location are given in Gracie & Stewart (1967).

3.5.1.3 Loch Assynt (NC 215 252) (Fig 3.11c)

On the North shore of Loch Assynt, some two miles West of Skiag Bridge, the Torridonian unconformity with the Lewisian is exposed in road cuttings. Here the unconformity is essentially planar, with Lewisian overlain by the Applecross formation (which is about 600 metres thick, as exposed on Quinag directly above the sample site).

In places the Lewisian gneiss is deeply weathered to a palaeosol, in which the structures of the gneiss are preserved. The gneisses are well jointed. To the West the outcrop weathering disappears and the joint planes are sealed by pumpellyite.

The gneisses are heavily reddened by haematite which must have moved down from the Torridonian above. Neither sealed cracks nor joints are seen to continue into the Torridonian, and the red haematite staining is cross-cut by the pumpellyite sealed cracks. The implication is that the staining is due to the Stoer Group (which is now not present in this location), with the pumpellyite mineralization occurring after the deposition of the Stoer Group and prior to the deposition of the Applecross Formation.

Sampling was specific to the sealed cracks and was carried out using a drill.

3.5.1.4 Gruinard Bay (NG 951 898) (Fig. 3.11d)

In the SE corner of Gruinard Bay the Stoer Group conglomerates outcrop by the roadside in a small cutting. These conglomerates contain well rounded clasts of Lewisian gneiss, granites and fine grained amphibolites. The outcrop is cross cut by joints, and the vertical ones are sealed by pumpellyite. Sampling was specific to the sealed joints.

3.5.1.5 Dorman (NC 185 593) (Fig. 3.11e)

The Applecross formation directly overlies the Lewisian gneiss of the northern region at Dorman harbour. The unconformity itself is not seen, but can be placed to within one or two metres. Sampling was by traverse across the unconformity.

The Lewisian gneiss is a slightly weathered quartzo-feldspathic, coarse grained, biotite gneiss and is cross cut by Laxfordian pegmatites. The gneiss is coarse and granoblastic, with irregular ameboid grains. Quartz is polycrystalline and feldspar is usually weathered along lattice cleavages. Biotite exists in clusters, is poorly aligned, and

is often poikilotopic with quartz.

The Torridonian consists of a medium coarse basal conglomeratic grit, overlain by arkosic sandstones. The sediments are cross-bedded and interlayered with fine lenses of siltstone. The pebbles in the grits are well rounded and, amongst others, consist of quartzite and jasper. There are no obvious Lewisian clasts. The basal unit is grain supported, and cemented by both calcite and haematite cements. The haematite cements form thin horizontal bands. The matrix also contains rounded epidote, quartz and feldspar.

3.5.1.6 Sheigra (NC 183 607) (Fig. 3.11e and Plate 4.11d)

The Applecross Formation also overlies the Lewisian at the sea cliffs NW of Sheigra. This locality has been investigated and described by Williams (1968). The unconformity is subplanar, and the underlying gneisses weathered to a depth of about 4 metres . Although the structure of the gneisses are perfectly preserved, the mafic minerals are altered to chlorite. Granite veins cross cutting the gneisses are not weathered.

The gneisses are composed of quartz, plagioclase and biotite. They possess an inequigranular interlobate texture with spaced biotite picking out a weak foliation. The feldspars are heavily altered to sericite and fractured. Haematite sealed fractures traverse the rock, and chlorite replaces biotite.

The unconformity is marked by a thin (20 cm) layer of fine red and green sandstone-siltstone, succeeded by coarse conglomeratic grits. The basal siltstone is well sorted and grain supported. Comprising of subrounded and rounded quartz and feldspar, with lenses of biotite, muscovite and epidote. These grains are surrounded by a radial micaceous matrix which grows fibrously into the pore space. Haematite cement occurs in distinctive horizontal bands and is syndepositional. The overlying grits have no haematite bands, being more calcareous. Sampling was by traverse across the unconformity.

3.5.2 Cambrian unconformity

The Cambrian Eriboll sandstone oversteps the Torridonian to lie directly upon the Lewisian basement in the region of Rispond. The basement gneiss was sampled at two localities, the Radio Station NW of Loch Sian (NC 443 639), and on the exhumed unconformity (NC 437 643). Both of which show identical geology (Fig. 3.11f).

The unconformity is planar and dips at about 10° to the East, parallel to the regional dip of the Cambrian succession.

The Lewisian consists of coarse grained quartzo-feldspathic Laxfordian gneisses with amphibolite and pegmatite bands. The feldspars show a ubiquitous alteration to clay

minerals and mica, to form agalmatolite (see Allison and Russell 1985, and earlier discussion of the Cambro-Ordovician). Alteration is common along joints and on the surface of the unconformity (once the Cambrian sea floor), with large-growths of green micro-crystals after orthoclase. Sampling was specific to areas of agalmatolite development within the Laxfordian gneisses.

3.6 Summary

1. The Lewisian is old and dry, therefore allowing easy identification of permeable zones.The structures under study all preserve evidence of mineral hydration, or fluid flow, during some period of the Lewisian's history. The range of basement sites chosen was intended to maximize the possibility of finding evidence of fluid flow events specific to tectonic events (and therefore time), as well as providing a wide geographical coverage.

2. Many of the sample sites are highly fractured and are therefore likely to be good sites for the study of microcracks. Concentrated evidence of any fluid flow event that may have affected the Lewisian during its history should be preserved there in the form of sealed cracks. A detailed knowledge of the geology of the sample sites will be critical to the understanding of the processes in operation during, and associated with, fracture sealing.

3. Similar to the basement sample sites, the unconformities of the Torridonian and Cambrian are sites where waters are known to have been in contact with the Lewisian basement. The range of u nconformity sites chosen was intended to maximize the possibility of finding evidence for fluid flow events specific to periods of sedimentation as well as providing time markers for fracture sealing. Sealed cracks are visibly present at some of these sites.

4. Sampling of the chosen sites between Gruiniard Bay and Rispond was carried out on either, or both, of two levels:
   (a) as traverse sampling across sites; or
   (b) as specific core sampling of visible sealed cracks.

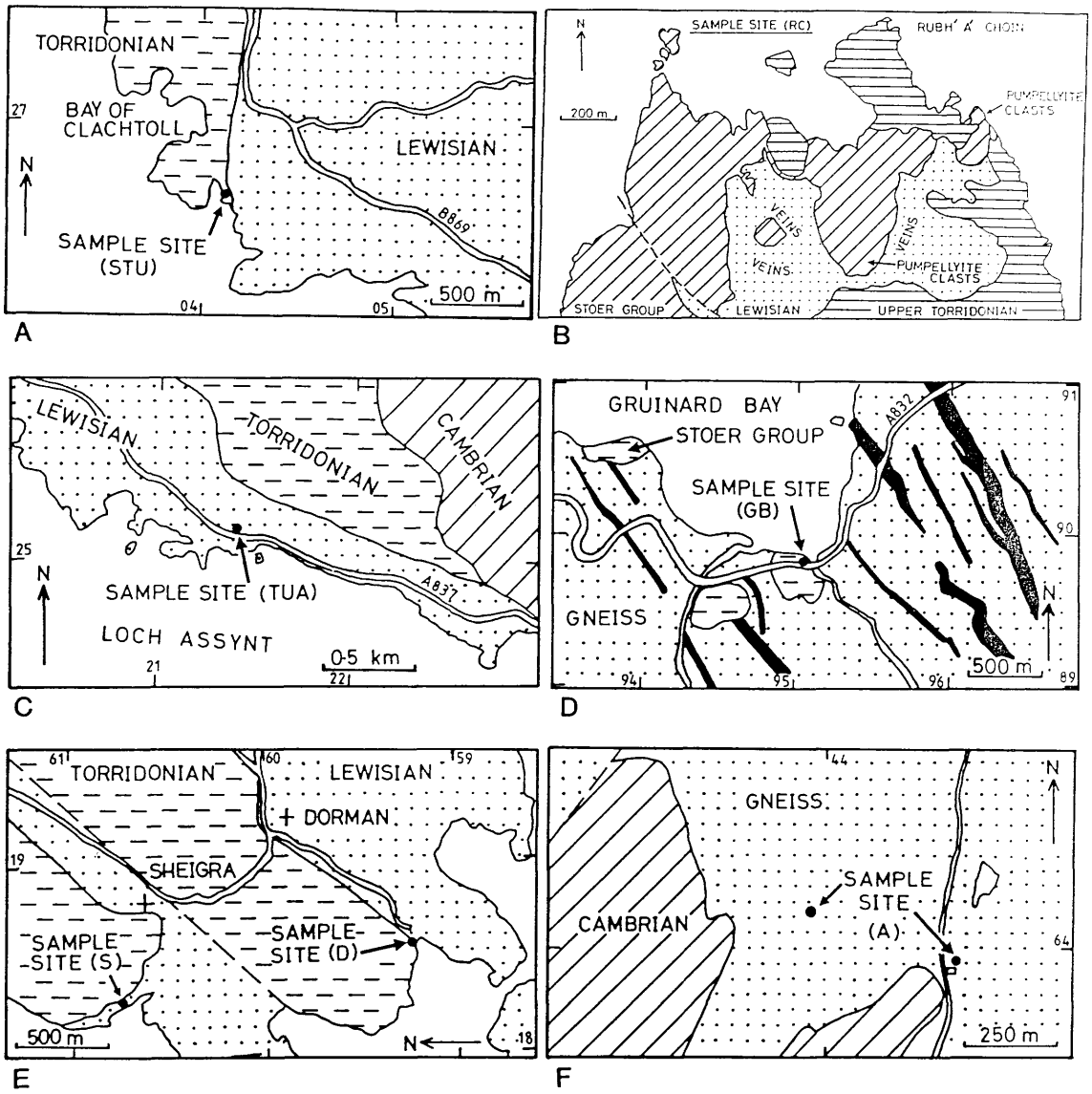

Figure 3.11 Location maps for unconformity sample sites.

A = Stoer Group unconformity at Clachtoll (sample site STU). Geology from 1: 63,360 Geological Survey sheet # 107.

B = Map of Rubh' a' Choin showing location of main features. (sample site RC). Geology from Gracie & Stewart (1967).

C = Applecross Formation unconformity at Loch Assynt (sample site TUA). Geology from 1: 253,440 Geological Survey sheet # 107.

D = Stoer Group unconformity at Gruinard Bay (sample site GB). Geology from 1: 63,360 Geological Survey sheet # 92.

E = Applecross Formation unconformities at Dorman (sample site D), and Sheigra (sample site S). Geology from 1: 63,360 Geological Survey sheet # 113.

F = Cambrian unconformity near Rispond (sample site A). Geology from 1: 63,360 Geological Survey sheet # 113.

CHAPTER 4

CHARACTERIZATION OF THE LEWISIAN MICROCRACKS

4.1 Techniques applied to microcrack investigation[1]

The microcracks were studied using both optical techniques and scanning electron microscopy. Samples were prepared as both, or either, standard thin sections and thick polished sections (crack sections). The mineralogy of the sealed cracks was studied with the use of E.D.X.S. systems at Massachusetts Institute of Technology and Memorial University of Newfoundland.

4.2 Open microcracks

Three principal open microcrack sets are present within the Lewisian rocks. They are intergranular cracks, grain boundary cracks and intragranular cracks (including cleavage cracks). Also found is open porosity, preserved by micropores and other cavities, which may have a solution origin. These fractures have been imaged on the SEM, and fracture widths measured for permeability estimation. No measurement, or statistical analysis, of the lengths and aspect ratios of these cracks have been carried out.

4.2.1 Intergranular cracks

Intergranular cracks are numerically the least common open crack. They are typically thin, being in the order of 3 - 10 μm wide. On the occasions, where more than one is visible in the section, they are either subparallel, or at a high angle, to each other. Those exhibiting subparallelism lie in echelon systems (Plate 4.1a). Plate 4.1a also illustrates that these microcracks possess sharp crack tips, indicative of tensional splitting. When as thin as 3 - 5 μm the microcracks often show the influences of pre-established discontinuities on the direction of microcrack propagation. In Plate 4.1b, the influences of feldspar cleavage, on the local propagation direction, can be seen. The steps, or 90° changes in direction, relate to the mineral's cleavage intersections. Plate 4.1c demonstrates the influence of grain boundaries, between K-feldspar and albite, on the local propagation of intergranular cracks. In both plates 4.1b and 4.1c the overall direction of crack propagation is constant.

---

[1] A full description of sample preparation, microscopy, SEM operating conditions, and the photographic techniques used in the study of the microcracks is provided in Appendix 1.

These fractures are formed in response to mechanical stress, most likely tensional, and can be classified as stress induced cracks. The open intergranular cracks are not always open along all of their lengths. Plates 4.1e and 4.1f illustrate mineral bridges within open cracks. In these photographs the bridges are due to mineral seals. Along with touching asperities, and loose material, these will help to prop open a crack.

4.2.2 Grain boundary cracks

Open grain boundary cracks are almost exclusively found around quartz. As mentioned in Chapter 1, this may relate to the thermodynamic properties quartz. Observations show that other minerals, such as biotite, do not allow grain boundary cracks to form (Plate 4.1d). Here it is found that microcracks around quartz end abruptly against the biotite, and do not continue along the quartz - biotite grain boundary.

One of the best examples of open grain boundary cracks can be seen in Plate 4.1g. Here every quartz and feldspar crystal is surrounded by a crack. Most are open but others appear to be closed allowing mineral - mineral contact. In closer detail, grain boundary cracks are found to have irregular walls, and occasional mineral bridges exist across the crack (Plate 4.1h). This would allow the existence, and preservation, of open porosity even under compression. With the irregularities, bridges and asperities preventing full closure. In Plate 4.2a, a triple point junction between three quartz crystals can be seen to preserve open porosity. Assuming this is continuous for the length of the crystal edges, this will represent a pipe system, as opposed to the flat grain boundary crack found between crystal faces. The pipe system would be difficult, if not impossible, to close under compression, and open porosity in such positions could remain under most crustal conditions.

A grain boundary crack formed as a result of differential contraction between adjacent minerals is shown in Plate 4.2b. Here, a single, concentric, grain boundary crack exists between sphene, and the adjacent quartz and feldspar.

The widths of the open grainboundary cracks fall in the broad range of 1 - 10 μm (Fig. 4.1), and their lengths will relate to the size of the crystal around which they form. The methods for the formation of grain boundary cracks are many (see Chapter 1), but a principal control appears to be a favourable host mineralogy.

SYMBOLS USED IN PLATES

A = actinolite; **AL** = albite; **Ba** = barite;
BI = biotite; **C** = calcite; **CPX** = clinopyroxene
H = hornblende; **KF** = K-feldspar; **M** = magnetite;
PF = plagioclase feldspar; **PR** = prehnite; **PU** = pumpellyite;
PY = pyrite; **Q** = quartz; **S** = sphene;
ST = stilpnomelane.

Plate 4.1a Echelon crack tips of an open intergranular crack (slide G-1).

Plate 4.1b Feldspar cleavage controls the local propagation path of intergranular crack tips (slide G-1).

Plate 4.1c Grain boundaries control the local propagation of an intergranular crack system (slide G-5).

Plate 4.1d Grain boundary cracks specific to quartz (slide PE-1).

Plate 4.1e Mineral bridge within an open intergranular crack (slide LC-6) .

Plate 4.1f Mineral sealing bridge within an open intergranular crack (slide LC-6).

Plate 4.1g A mosaic of grain boundary cracks surrounding quartz (slide DM-12).

Plate 4.1h Irregular walls of grain boundary cracks (slide DM-10).

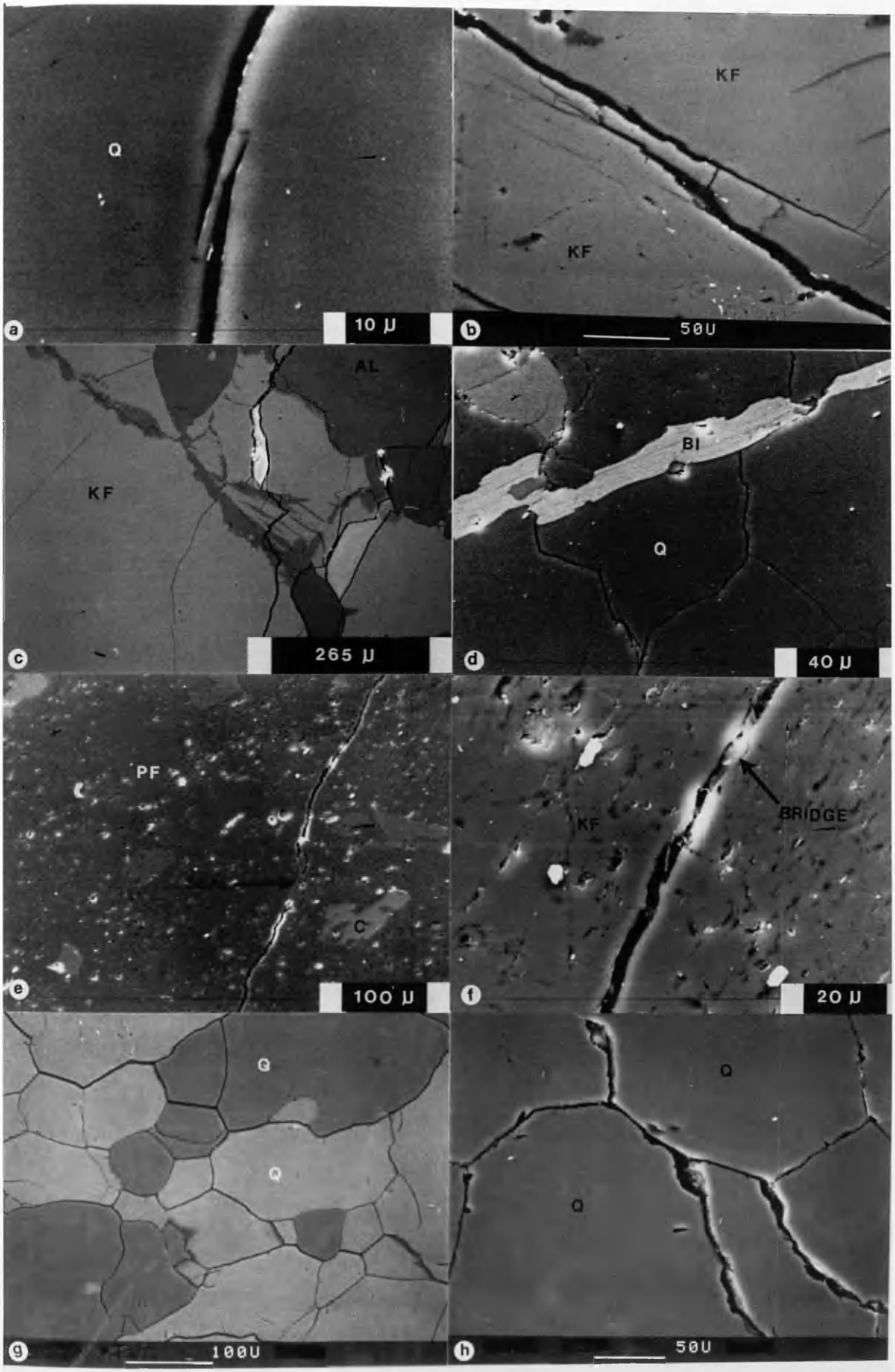
Q
10 µ
a
KF
KF
50U
b
AL
KF
265 µ
c
BI
Q
40 µ
d
PF
C
100 µ
e
KF
BRIDGE
20 µ
f
Q
Q
100U
g
Q
Q
50U
h

PLATE (4.1)

4.2.3 Intragranular cracks

Mineralogy again appears an important factor in the formation of open intragranular cracks, although more minerals favour the formation of these in comparison with grain boundary cracks. These microcracks have been observed in quartz, feldspar, pyroxene, biotite and stilpnomelane. Their orientations often being controlled by a combination of stress and cleavage.

Plate 4.2c and 4.2d show intragranular cracks in pyroxene, and Plate 4.2e intragranular cracks in biotite. Similarly, Plate 4.2f illustrates an intragranular crack in K-feldspar. Here cleavage planes, as marked by exsolved albite, are the sites for microcracks. Stress controlled cracks are illustrated in Plates 4.2g and 4.2h and 4.3a.

Plate 4.2g illustrates an interesting set of open microcracks through a stilpnomelane sealed crack. The tensional open microcracks run parallel to the stilpnomelane crystals (across the sealed crack), and have an element of mineral control. They also have an element of stress control, running parallel to the sealed microcrack, and appear to relate to shrinkage of the stilpnomelane. Direct interaction, between a stress induced intragranular crack and a mineral cleavage crack, can be found in Plate 4.2h. Here differential shear movement along the intersecting cleavage crack has allowed only part of the echelon intragranular system to open, with the other half remaining closed.

Plate 4.3a shows a stress controlled intragranular crack through quartz. This microcrack is one of an array of stress induced, parallel, intragranular cracks, which only form in the competent quartz bands (note the microcrack does not travel through the small inclusion of material in the quartz, and does not continue into the adjacent minerals. Similar to Plate4.1d).

Less regular intragranular cracks also exist and their formation, in relationship to the factors of influence (stress and cleavage), is not easily explained. Plate 4.3b illustrates such a case. Here intragranular cracks in feldspar show neither obvious geometery nor obvious influence over their formation. These may be classified as cracks of unknown origin. The widths of the intergranular cracks appear broadly similar to those of the grain boundary cracks, ranging from about 1 - 10 μm (Fig. 4.1).

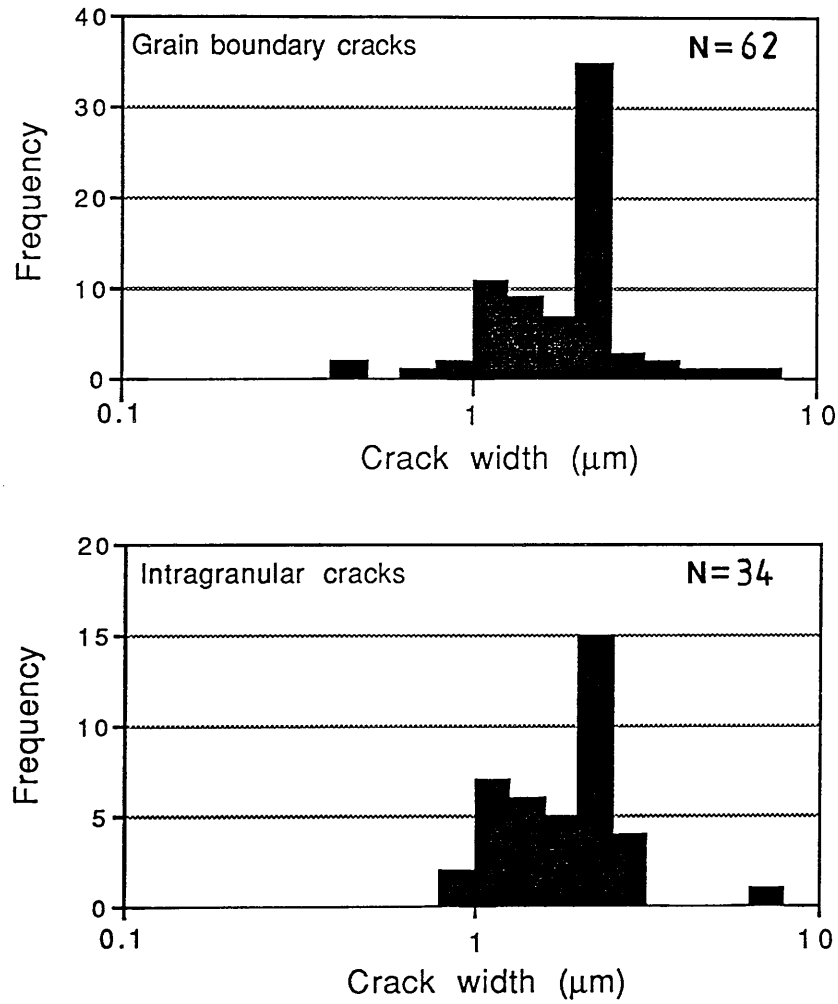

Figure 4.1 Open crack width histograms for grain boundary and intragranular cracks. Apparent widths, as measured from S.E.M. photographs.

Plate 4.2a Open grain boundary porosity at a quartz triple point junction (slide JH-330).

Plate 4.2b Thermally induced grain boundary cracks surrounding sphene (slide JH-330).

Plate 4.2c Intragranular cleavage cracks in clinopyroxene (slide JH-334).

Plate 4.2d Intragranular cleavage cracks in clinopyroxene (slide JH-334).

Plate 4.2e Intragranular cleavage cracks in biotite (slide JH-330).

Plate 4.2f Intragranular cleavage cracks in K-feldspar (Slide G-5) .

Plate 4.2g Intragranular cracks in stilpnomelane (slide SD-10).

Plate 4.2h Differential shear and extension along cracks of different orientations (slide JH-330).

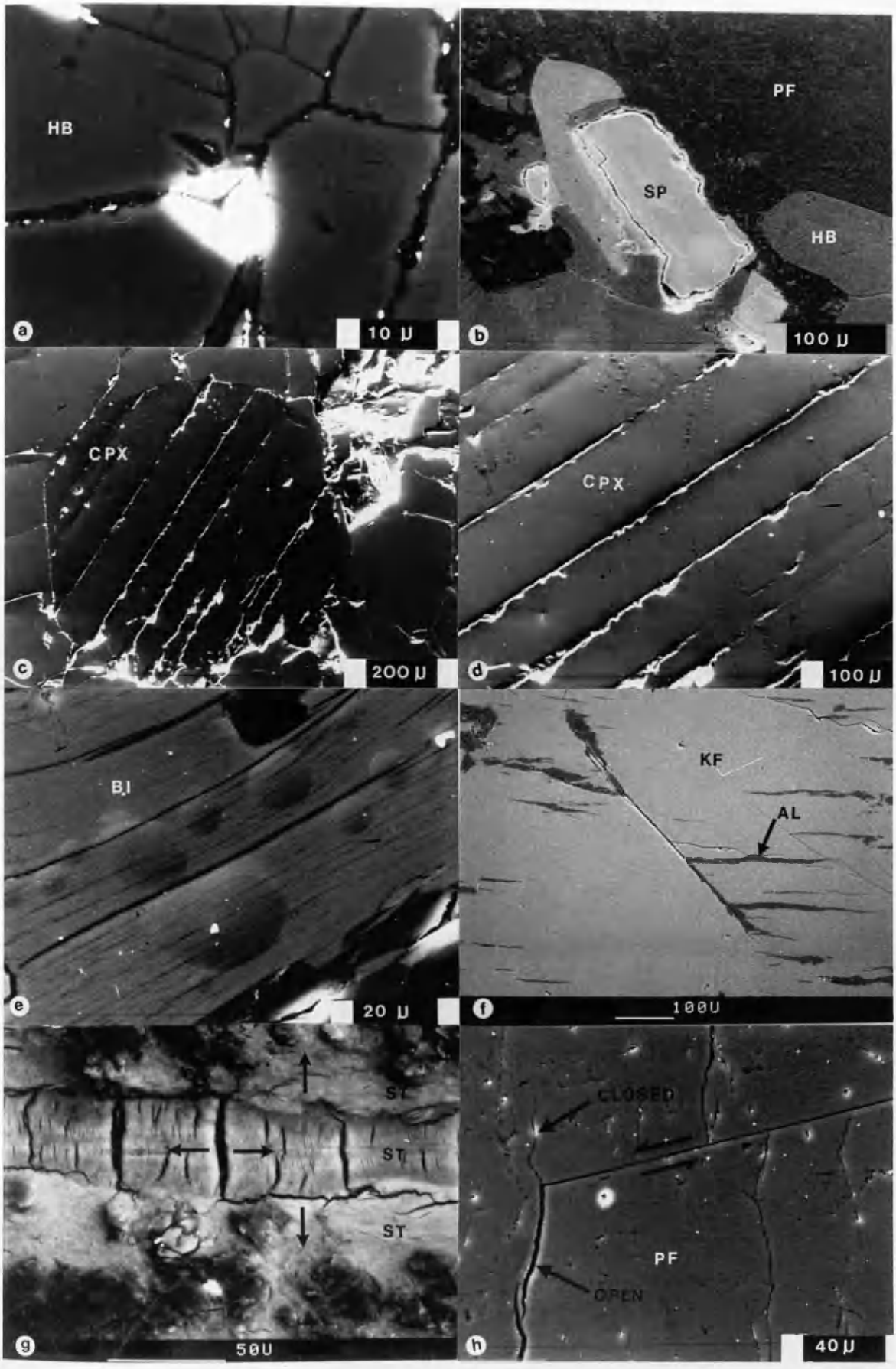
HB
a
10 µ
PF
SP
HB
b
100 µ
CPX
c
200 µ
CPX
d
100 µ
BI
e
20 µ
KF
AL
f
100U
ST
ST
ST
g
50U
CLOSED
PF
OPEN
h
40 µ

PLATE (4.2)

4.2.4 Micropores and irregular cracks

Micropores have been observed as forming due to the partial healing of microcracks. They can be identified as one of two types. Those preserved as fluid inclusion trails and larger pores in an intragranular position, as a result of the healing of either an intragranular or intergranular crack (Plates 4.3c and 4.3d). Or those preserved as partly healed grain boundary cracks, occupying a grain boundary position as illustrated in plates 4.3e and 4.3f. While these features maintain open porosity, it is doubtful if they will greatly contribute to permeability, as they may be isolated. However, if a change in physical conditions occurred while these pores were full of fluid, it is possible that they could become sites of fracture initiation.

The formation of irregular microcracks, such as those found in Plates 4.3b and 4.3d, is difficult to explain as having occurred by any method other than solution. The embayed nature of the wall in Plate 4.3d strongly suggests chemical dissolution in the formation of this pore system. Although the actual microcrack discontinuity, seen above and below the pore system, probably formed in another way, perhaps as a primary cleavage plane.

4.3 Sealed microcracks

As with open microcracks, grain boundary cracks, intragranular cracks (including cleavage cracks) and intergranular cracks are the three main sealed microcrack types which were found to exist within the rock suite. Also present are sealed micropores and sealed joints. The sealed microcracks have been analysed in more depth than the open microcracks.

4.3.1 Grain boundary cracks

Sealed grain boundary cracks, as with the open grain boundary cracks, occur most commonly adjacent to quartz. However, they are also found surrounding hornblende. Plates 4.3g and 4.3h show pumpellyite sealed grain boundary cracks surrounding quartz. As with the open grain boundary cracks, the sealed grain boundary cracks may almost isolate individual crystals within the rock fabric. Plates 4.1g and 4.1h illustrated that open microcracks could exist in this fashion, so theoretically it is possible that all the microcracks in Plates 4.3g and 4.3h were open simultaneously. In closer detail, Plate 4.3h reveals that many of these sealed microcracks have embayed walls. This suggests solution had an influence on the present widths and shapes of these microcracks. However, It is unlikely that pumpellyite would form as a replacement of quartz. This implies that at one point an open space existed which the pumpellyite now seals. From Plates 4.3g and 4.3h,

Plate 4.3a Intragranular stress controlled crack in a competent quartz layer (slide LC-6).

Plate 4.3b Irregular intragranular cracks (slide JH-330).

Plate 4.3c Intragranular micropores, formed as fluid inclusions (slide JH-330).

Plate 4.3d Irregular intragranular micropore formed as a result of solution (slide JH-330).

Plate 4.3e Grain boundary micropore between quartz crystals (slide JH-330).

Plate 4.3f Partly healed grain boundary crack (slide JH-330).

Plate 4.3g Grain boundary cracks sealed by pumpellyite surround a quartz mosaic (slide M-3/2).

Plate 4.3h Irregular walls of sealed grain boundary cracks indicating solution (slide M-3/2).

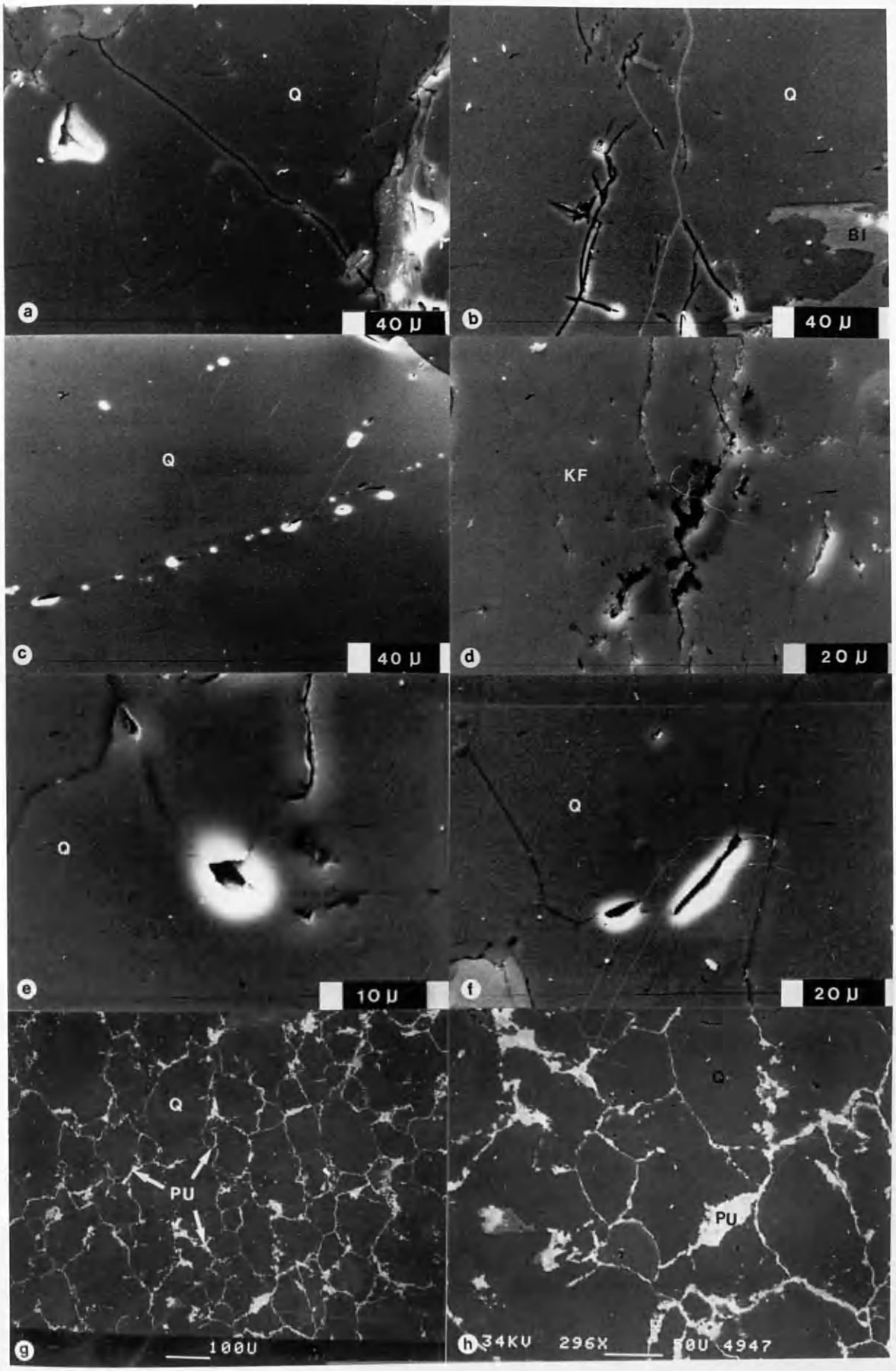
a
Q
40 µ
b
Q
Bi
40 µ
c
Q
40 µ
d
KF
20 µ
e
Q
10 µ
f
Q
20 µ
g
Q
PU
100U
h
Q
PU
34KU 296X 50U 4947

PLATE (4.3)

the sealed microcracks may either run continuously for the whole length of a crystal face, or be partially healed, resulting in discontinuous lenses of sealing mineral along the crystal face. These imply the model of Watson & Breenan (1987) did not operate.

The ability of fluids to permeate along flat microcracks associated with the crystal face is evident. It can also be seen that crystal edges act as conduits as shown by mineral precipitation along triple edge pipe systems (as illustrated in Plate 4.4a). Here a triple point junction between three quartz crystals is sealed by stilpnomelane, while the grain boundary cracks along the crystal faces are closed, and presumably healed.

The composition of the sealing mineral, preserved within the grain boundary crack, is found to be either independent, or dependent, on the adjacent host mineralogy. The sealed grain boundary cracks with quartz as a host mineral show no relationship between host and sealing mineralogy. Here the precipitation of pumpellyite and stilpnomelane can be considered to be independent of the wall-rock. However, those sealed grain boundary cracks surrounding hornblende do exhibit a dependence of sealing mineralogy on the host wall-rock mineralogy. They are always sealed by stilpnomelane (Plate 4.4b). Stilpnomelane has a very similar chemistry to hornblende (see Appendix 3) and it appears that the stilpnomelane is buffered by the wall-rock hornblende.

The role of solution, in the production of open grain boundary space, is further illustrated by the crack in Plate 4.4c. The solution of the quartz has produced large asperities, which touch, to prop open the crack. This crack was then been sealed with stilpnomelane.

It has been shown (Plates 4.1g and 4.1h) that open grain boundary cracks similar to the sealed grain boundary cracks represented in Plates 4.3g, 4.3h and 4.4b, can exist. However, doubt exists as to whether all the grain boundary cracks represented in Plates 4.3g, 4.3h and 4.4b, formed at the same time. Plate 4.4d shows that the grain boundary cracks around quartz may open at different times. This can result in open, and sealed, cracks in the same grain boundary system. Grain boundary porosity has been investigated by White & White (1981) and recently discussed by Watson & Breenan (1987). It is seen as the locus for most open porosity, and free fluid phase, at depth within crystalline rocks.

When fully developed, the size and orientation of grain boundary cracks must depend on the size and orientation of the adjacent crystal faces. Their presence is controlled by host mineralogy, and by the ability of the microcracks to remain open, either by wall mismatch or some form of crystal propping. Of those grain boundary cracks measured, lengths range between 80μm and 1200μm, and widths between 0.6μm and 8.6μm. True aspect ratios range between $1x10^{-4}$ and $5x10^{-2}$, with a mean value of $1x10^{-2}$ (Fig. 4.2).

4.3.2 Intragranular cracks

Within the Lewisian rocks, the sealed intragranular cracks are broadly similar in dimension to the sealed grain boundary cracks. Lengths range between 60μm and 4500μm with widths between 0.5μm and 25μm. True aspect ratios range between $1x10^{-4}$ and $1x10^{-1}$ (cracks with such high ratios are classed as pores), with an average aspect ratio of $2\ x10^{-2}$ (Fig. 4.3). As was the case with the open intragranular cracks, sealed intragranular cracks are found to be controlled by mineralogy and stress.

Quartz, biotite, feldspar and pyroxene are again the principal minerals to preserve intragranular cracks. Within biotite, feldspar and pyroxene, the mineral cleavage is usually the site for the sealed crack. Plates 4.4e, 4.4f and 4.4g illustrate such intragranular cracks within biotite, feldspar and pyroxene. In every case, sealed intragranular cracks found in quartz have been observed to have a stress related origin. Sets of aligned microcracks are confined to the more competent quarts bands, and run parallel to larger sealed intergranular cracks. This feature is illustrated in Plate 4.4h, by an array of pumpellyite sealed intragranular and intergranular cracks.

Unlike sealed grain boundary cracks, sealed intragranular cracks do not possess as much evidence for involvement of solution in their formation. Most have very planar straight walls (Plate 4.5a), with only occasional signs of mismatch. The lack of such solution features may indicate that the intragranular cracks have less fluid passing through them.

4.3.3 Intergranular cracks

The sealed intergranular cracks found within the Lewisian rocks can be subdivided into two kinds: those which show a component of shear displacement; and those which do not (i.e. show only extension). In every case, these cracks can be thought of as forming in response to an applied non-hydrostatic stress.

Shear cracks have only occasionally been found, and are generally marked by a thin line of gouge material. Very occasionally they are sealed by mineral phases, providing evidence of a fluid phase having passed along them. The shear cracks can be identified by mismatch between the wall on opposite sides of the crack. Plate 4.5b illustrates a sealed intergranular crack, with components of shear, and extension. Where present, the main microshears are linked together by arrays of anastomosing subshears. One example of this type of array is seen in Plate 4.5c. However, shear cracks are not found in significant abundance.

Plate 4.4a Stilpnomelane sealed quartz triple point junction (slide M-2).

Plate 4.4b Stilpnomelane sealed grain boundary cracks around hornblende (slide M-16/2).

Plate 4.4c Irregular walled grain boundary crack sealed with stilpnomelane (slide SD-4).

Plate 4.4d Partly sealed grain boundary system (slide JH-330).

Plate 4.4e Intragranular cleavage cracks in biotite sealed by magnetite (slide PE-4).

Plate 4.4f Intragranular cleavage cracks inK-feldspar sealed by magnetite (slide G-4).

Plate 4.4g Intragranular and grain boundary cracks in clinopyroxene sealed by magnetite (slide K-1).

Plate 4.4h Stress controlled inter- and intragranular cracks sealed by pumpellyite (slide SC-10).

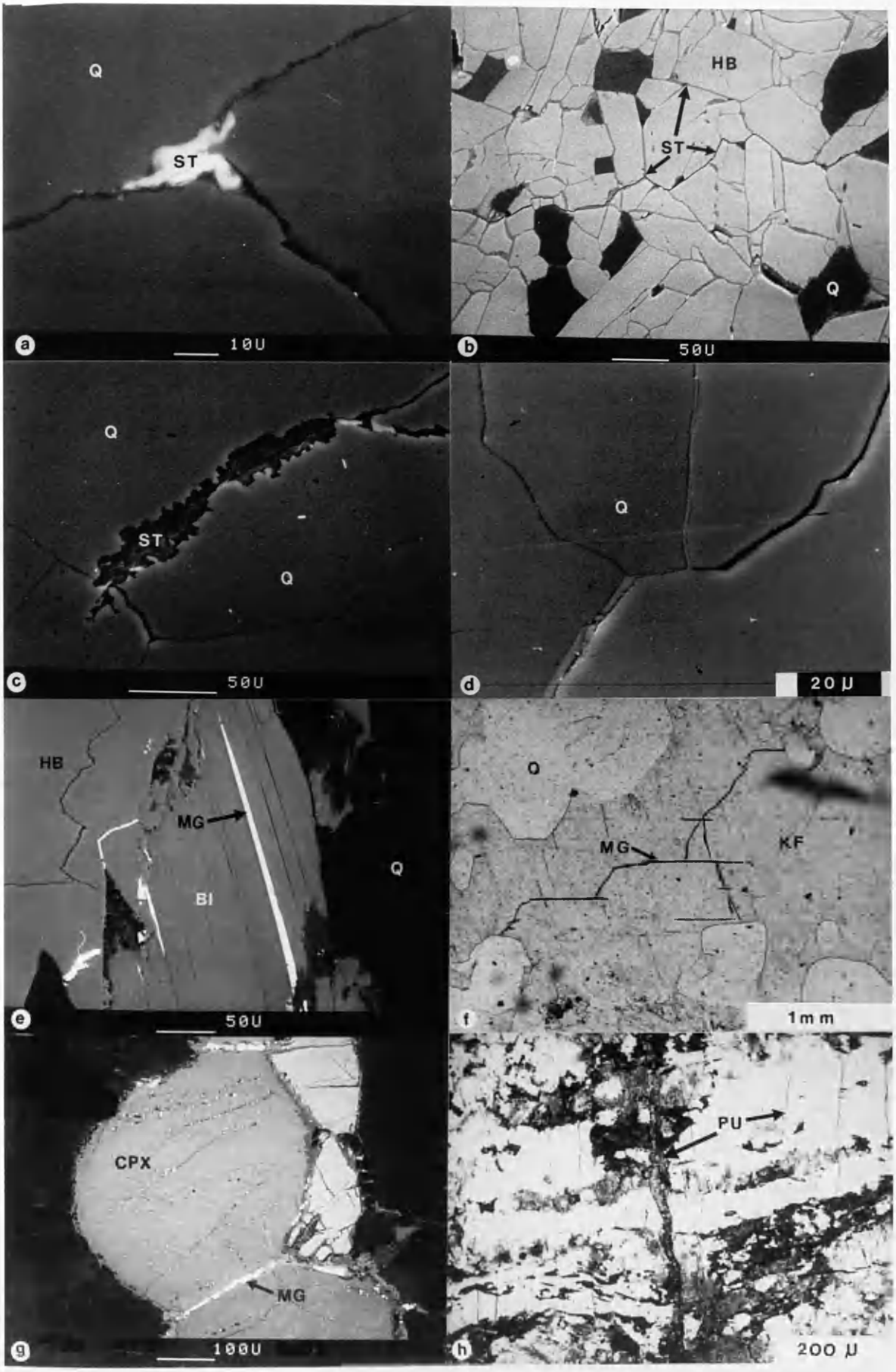
Q
ST
a
10U
HB
ST
Q
b
50U
Q
ST
Q
c
50U
Q
d
20 µ
HB
MG
Q
Bi
e
50U
Q
MG
KF
f
1mm
CPX
MG
g
100U
PU
h
200 µ

PLATE (4.4)

Sealed extensional cracks are more abundant than shear cracks. Thus they appear to be, and have been, much more important as conduits for fluid flow. As with open intergranular cracks, the sealed extensional intragranular cracks lie in subparallel en-echelon arrays (Plate 4.5d). They often intersect one another, and are usually sealed by mineral phases. The extensional intergranular cracks are the largest of the sealed microcracks measured. Lengths measured (limited by section size) range from 100μm to 25mm . Widths vary between 1μm and 200μm, although larger crack widths of up to 1500μm have been measured for microcracks which exceed the section size in length. Veins of up to 15 cm wide have been recorded in the field. The true aspect ratios of the intergranular cracks range between 4 $x10^{-4}$ and $5x10^{-2}$, with a mean value of 7 $x10^{-3}$ (Fig. 4.4)(more elongate than the two other microcrack types).

A log-log relationship between the length and width of the sealed microcracks exists and is presented in Fig. 4.5. These plots are combined data for all types of sealed crack encountered, and relate to true dimensions measured from thin sections. This relationship allows the estimation of crack length from a measurement of crack width. This is particularly useful when dealing with intergranular cracks, which often exceed section size in length, and will be used in Chapter 6.

The larger sealed veins, which can be seen on outcrops and are continuous for lengths of several meters, are parallel to the open joint sets within the rock. Plate 4.5e shows a joint surface within the Kylesku Group granulites covered by pumpellyite. Plates 4.5f , 4.5g and 4.5h illustrate that many of the sealed cracks visible in the field were originally open joints. Plate 4.5f shows a calcite sealed joint, whereas plates 4.5g and 4.5h show open joints running parallel to prehnite sealed joints of the same set . These sealed joints are present throughout the Lewisian, and were in existence prior to the permeating events as open joints. It is highly likely these long and wide (in comparison to the microcracks) joints represent the primary conduits for post-Laxfordian fluid flow through the crystalline Lewisian complex.

The intergranular crack arrays of a single generation are parallel to each other, and their orientations must relate to rock palaeostresses. The local inhomogeneities of the rock, such as crystal lattices or crystal boundaries, may impose localized variations in propagation path (Plate 4.6a). This was also found with the open intragranular cracks. These variations in propagation path are most obvious when the microcracks are thin.

The microcrack tips of the sealed intragranular cracks are usually sharp, indicating tensional splitting. The sealed intragranular cracks end in three ways: at an intragranular site (Plate 4.6b); as an array of splaying microcracks leading off the major microcrack

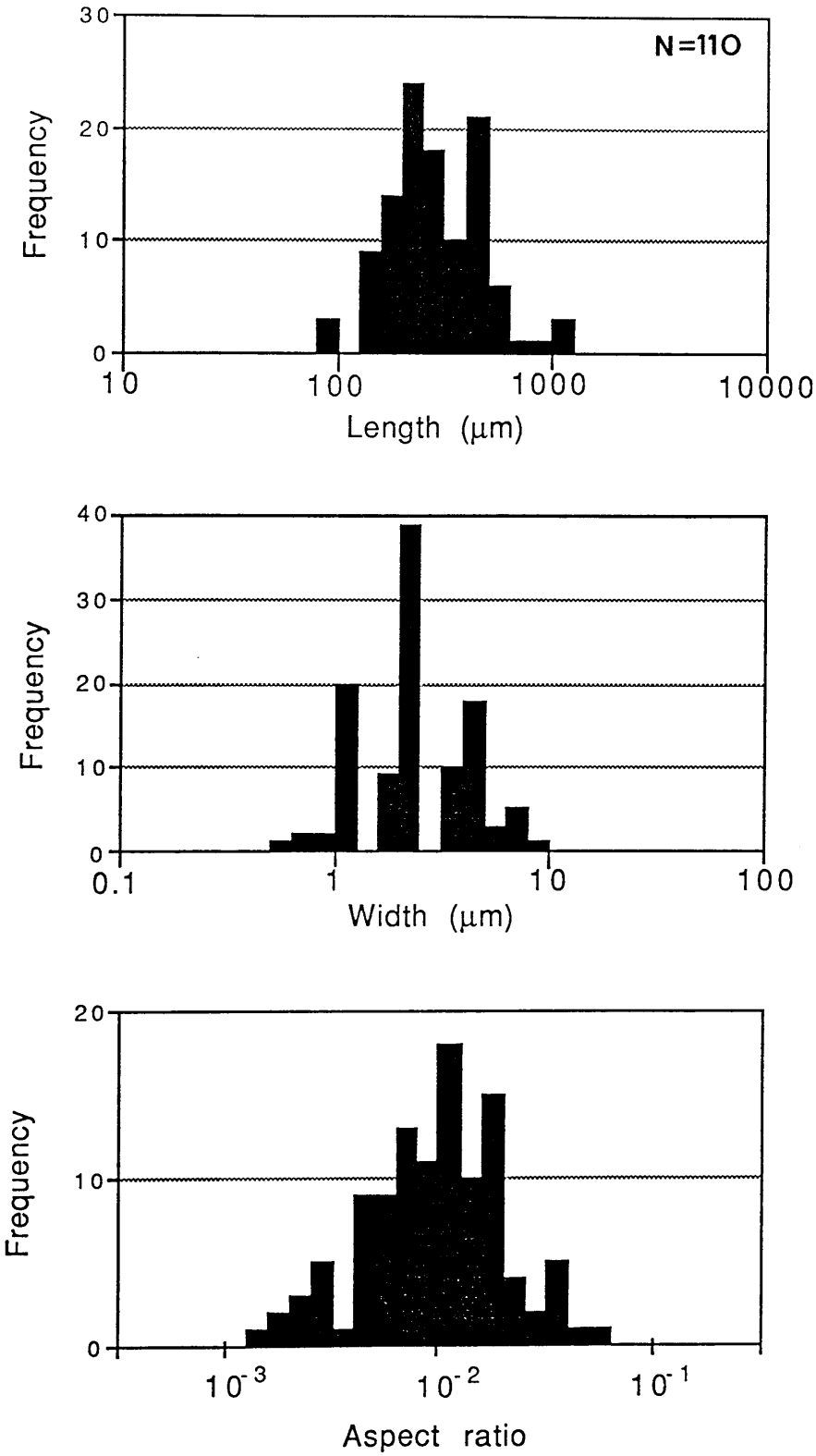

Figure 4.2 Length, width and aspect ratio histograms for sealed grain boundary cracks. True sizes, as measured directly from thin sections.

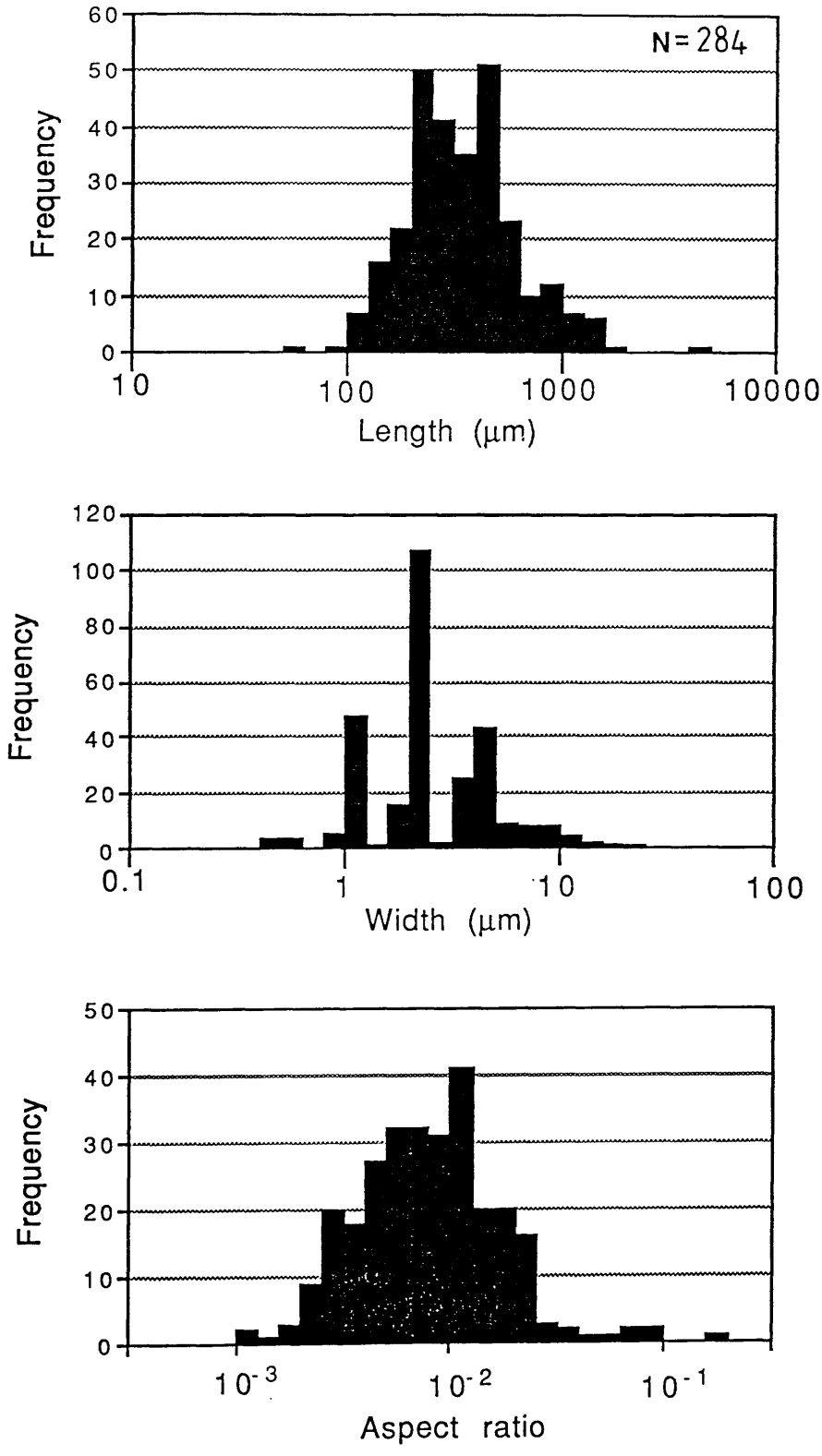

Figure 4.3 Length, width and aspect ratio histograms for sealed intragranular cracks. True sizes, as measured directly from thin sections.

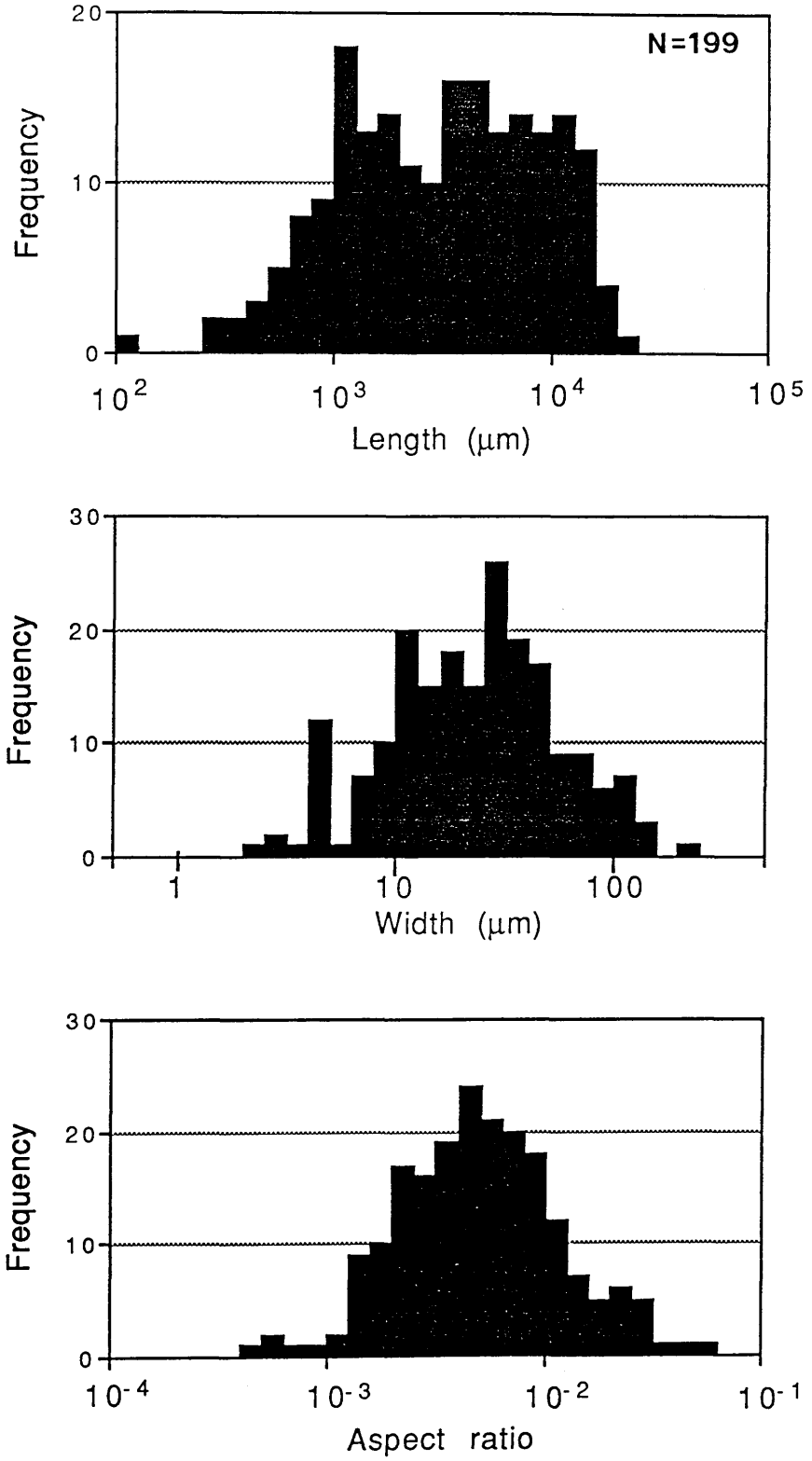

Figure 4.4 Length, width and aspect ratio histograms for sealed intergranular cracks. True sizes, as measured directly from thin sections.

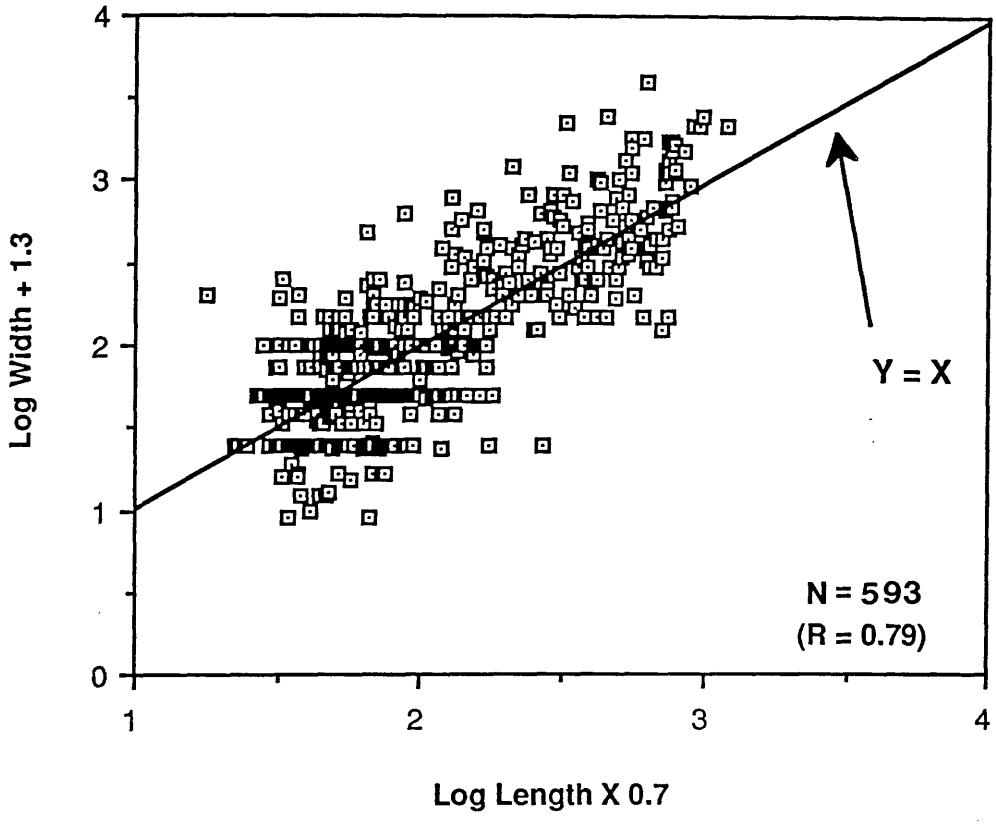

Figure 4.5 The relationship between length and width of the sealed cracks, measured from thin sections. R = correlation coefficient of regression line.

Plate 4.5a Smooth walled intragranular crack in quartz (slide LC-1).

Plate 4.5b Sealed intergranular crack preserving evidence of both shear and extension (slide M-14).

Plate 4.5c Array of small shear cracks (slide M-14).

Plate 4.5d En-echelon sealed intergranular cracks (slide SC-3).

Plate 4.5e Joint surface within Kylesku granulites at Kylestrome, covered with pumpellyite.

Plate 4.5f Joint in the Scourie dyke at Scourie, sealed by calcite.

Plate 4.5g Prehnite sealed crack/joint running parallel to an open joint within a Scourie dyke at Lochinver.

Plate 4.5h Prehnite sealed cracks/joints running parallel to open joint system within a Scourie dyke at Lochinver.

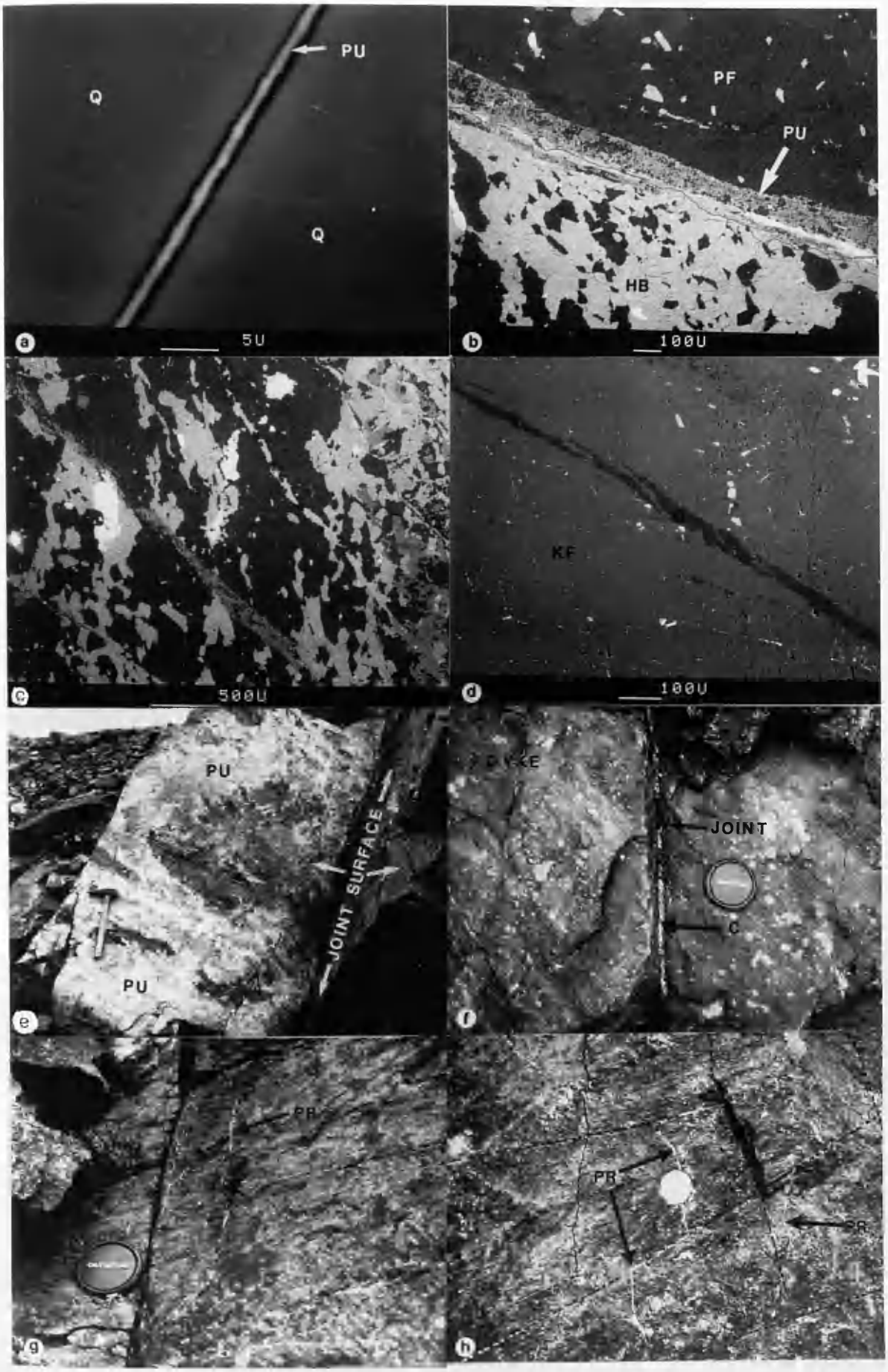
PU
Q
Q
5U
PF
PU
HB
100U
500U
KF
100U
PU
JOINT SURFACE
PU
DYKE
JOINT
C
PR
PR
PR

PLATE (4.5)

(Plate 4. 6c); or, most commonly, at a grain boundary location. There the microcrack thins, and exploits the weaker crystal edge discontinuities, as the energy at the microcrack tip decreases. Intergranular crack systems, being the largest, are likely to have been more permeable than the smaller grain boundary crack and intragranular crack systems. They would have carried more fluid, similar to open intergranular systems (Brace *et al.* 1968, Brace 1977) . Most of the information gained during this study comes from the sealed extensional intergranular cracks.

4.3.4 Micropores

Micropores, similar to the open micropores, are preserved as sealed cracks. Partly healed grain boundary cracks, once open, are often found sealed (Plate 4.4c); as are partly healed Intragranular cracks. These healed intragranular cracks are preserved as inclusion trails (Plate 4.6d). Other larger sealed pores, such as those open ones shown in Plates 4.4e and 4.4f, probably exist within the Lewisian samples, but are not easily seen.

4.4 The nature of the sealing minerals

The presence of mineral phases within the three types of microcrack shows that fluids do exploit open fractures, and that even small fractures a few tens of microns in size play a part in allowing fluid to permeate through crystalline rock. By analysing the textures of mineral seals within the cracks, evidence of fluid processes that occur in situ within the crust can be found.

Incremental opening of microcracks, following the "crack-seal" method of rock deformation (Ramsay 1980), can be seen in Plate 4.6e. Here the sealing of the microcrack has kept pace with its opening, resulting in a fibrous crystal sealing phase. No alteration of the wall-rock is seen, although interaction with the fluid phase is likely to have occurred, with the wall-rock hornblende buffering the stilpnomelane. The stilpnomelane nucleates on all wall-rock minerals and is not a simple replacement of hornblende.

However, the majority of microcracks do not show this style of sealing, and are sealed by blocky crystal formations. In many cases interaction of the fluid phase with the wall-rock can be seen, by the specific, and often orientated, nucleation of one sealing mineral on a certain wall-rock mineral. There are many examples of this present within the microcracks found in the Lewisian. Fibrous actinolite is found to grow from hornblende, in optical continuity with the hornblende lattice, using the crystal's lattice and surface as a seed (Plates 4.6f and 4.6g). Plagioclase is another sealing mineral found to be selective in

Plate 4.6a Differential movement along a sealed intergranular crack due to the influence of crystal cleavage on propagation direction of the crack (slide SD-6).

Plate 4.6b Intergranular crack sealed with stilpnomelane ends at an intragranular site (slide M-6).

Plate 4.6c Intergranular crack ends as a splaying array of smaller cracks (slide SD-6).

Plate 4.6d Sealed micropores. An inclusion trail sealed with magnetite (slide K-1).

Plate 4.6e Intragranular crack sealed with stilpnomelane, via the crack seal method of mineral growth (slide SC-9).

Plate 4.6f Interaction of wall rock and fluid to produce mineral growth (slide DM-1/2).

Plate 4.6g Actinolite growing from a hornblende wall rock (slide DM-1/2).

Plate 4.6h Albite grows next to K-feldspar, calcite next to hornblende (slide SD-11/2).

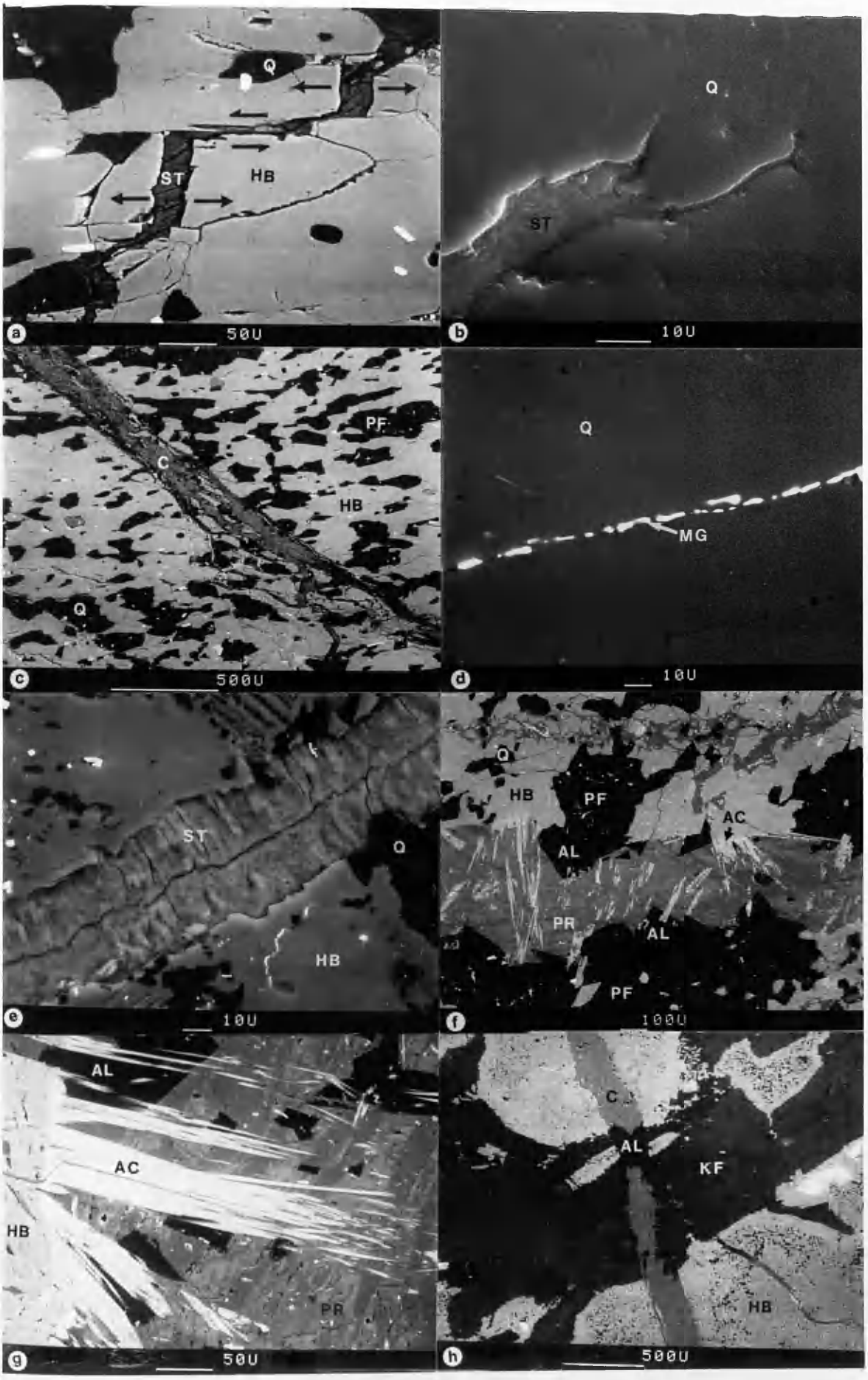
Q
ST
HB
a
50U
Q
ST
b
10U
PF
C
HB
Q
c
500U
Q
MG
d
10U
ST
Q
HB
e
10U
Q
HB
PF
AC
AL
PR
AL
PF
f
100U
AL
AC
HB
PR
g
50U
C
AL
KF
HB
h
500U

PLATE (4.6)

its growth position, nearly always growing from feldspar. This is illustrated in Plates 4.6f, 4.6h and 4.7a, where plagioclase is seen to nucleate on either wall-rock plagioclase (Plates 4.6f and 4.7a) or K-feldspar (Plate 4.6h). Other common examples are the growth of sphene on ilmenite, or the buffering of stilpnomelane by hornblende (Plates 4.4b and 4.7b).

Occasionally metasomatic alteration of the wall-rock by the fluid phase, prior to sealing, can be seen (Plate 4.7c), Here plagioclase has been metasomatically altered to prehnite by the fluid. These interactive reactions between the fluid and the wall-rock require a continual, slow moving, supply of fluid along the crack. For such alteration the microcrack must remain open for a period long enough for interaction to take place.

The random nucleation of prehnite on the fracture wall-rock, progressing to selective orientated crystal growth, is typical of mineral growth into fluid space. This texture is illustrated in Plate 4.7d, and requires an open space for its formation.

The mechanisms allowing a fracture to remain open have been discussed before (Chapter 1), and evidence supporting these mechanisms was found in the open cracks and the sealed grain boundary cracks. Sealed intragranular cracks also preserve evidence for these mechanisims in their wall-rock, and sealing mineral, characteristics. Crystal propping occurs in several ways within the sealed intragranular cracks. These are:

(a) fracturing with wall-rock spalling resulting in crystal wedging;

(b) mineral dissolution; and

(c) inhomogeneous mineral precipitation and crack healing.

Spalling of the wall-rock on fracture, resulting in crystal wedging, is shown in Plate 4.7e. Crystals of hornblende have fallen into the crack on fracturing, and prevented closure by wedging open the crack. The removal of material from the wall-rock, by spalling, has also created uneven walls to this microcrack. These touch in places, also preventing closure. Inhomogeneous mineral precipitation is illustrated in Plate 4.7f. Here plagioclase growth from opposite sides of the crack wall have produced a mineral bridge, which would enable the microcrack to remain open. Mineral bridges are also present in Plates 4.1e and 4.1f. Here crack healing has partly closed an open microcrack, with the bridges preventing closure. It is likely that the formation of uneven walls, or asperities, by solution and crystal spalling,are, along with crystal wedging, the principal methods of microcrack propping. With inhomogeneous mineral precipitation, and crack healing, being formed as a result of the microcrack being propped open by touching asperities or spalled crystal wedges. Similar to the open cracks, crack healing is also found to have occurred. Plate 4.8d illustrates amphibole bridges, crossing a crack sealed by calcite and K-felsdspar.

Plate 4.7a Albite grows next to plagioclase, calcite next to hornblende (slide M-4).

Plate 4.7b Stilpnomelane is buffered by hornblende (slide M-16/2).

Plate 4.7c Prehnite produced as a result of the fluid-wall rock interaction (slide SD-25).

Plate 4.7d Growth of prehnite from the wall rock into an open space (slide LD-C14).

Plate 4.7e Asperities and debris within a sealed crack (slide SD-7).

Plate 4.7f Asperities grown across a sealed crack so preventing closure (slide DM-1/2).

Plate 4.7g Calcite/K-feldspar sealed crack resplit and sealed with stilpnomelane (slide LC-4).

Plate 4.7h Three sealing periods within one sealed crack (slide M-16/2).

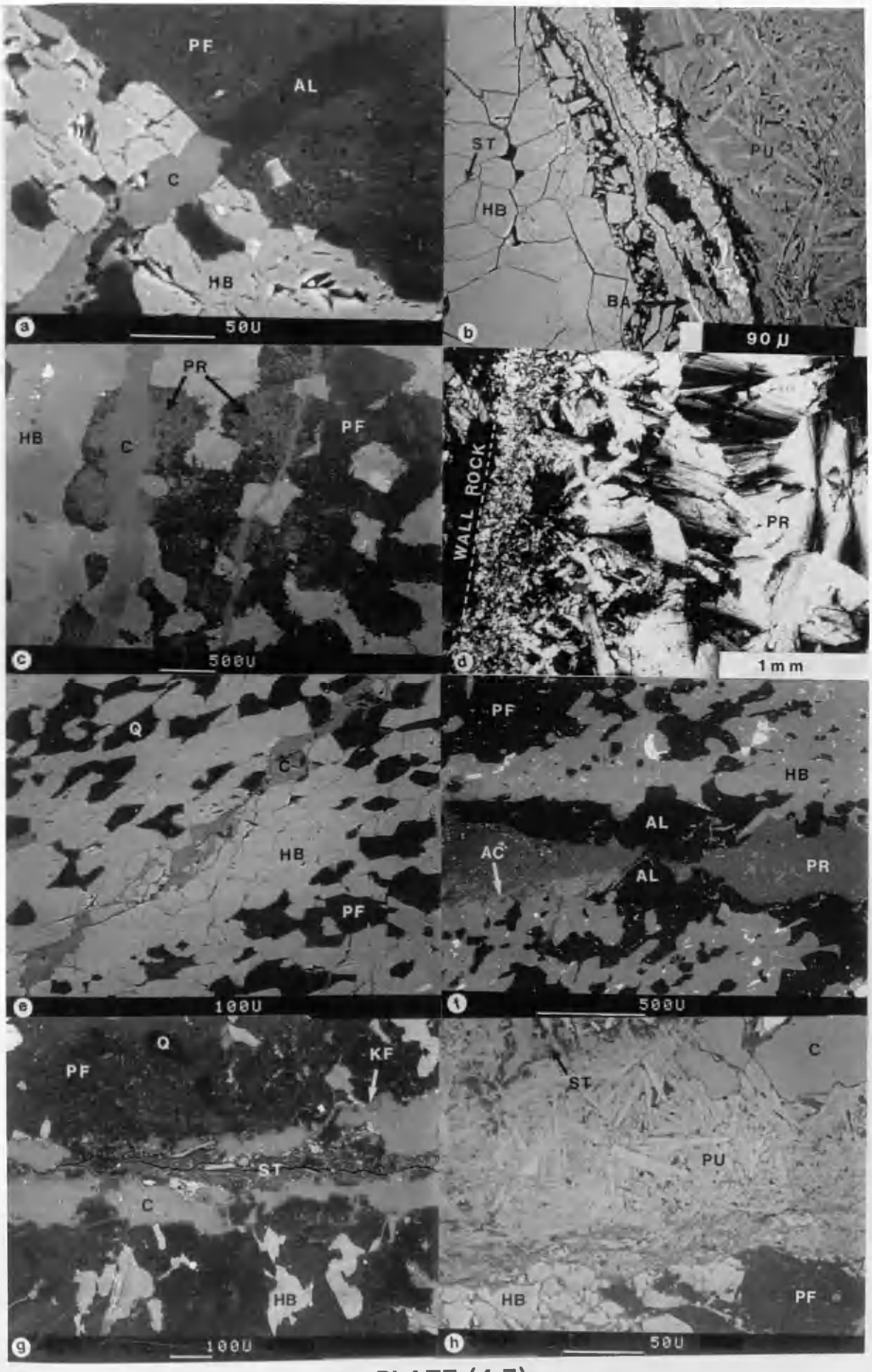
PF
AL
C
HB
a
50U
ST
ST
PU
HB
BA
b
90 µ
PR
HB
C
PF
c
500U
WALL ROCK
PR
d
1 m m
Q
C
HB
PF
e
100U
PF
HB
AL
AC
AL
PR
f
500U
Q
PF
KF
ST
C
HB
g
100U
C
ST
PU
HB
PF
h
50U

PLATE (4.7)

Textural relationships between minerals in some cracks suggest that they have carried fluid more than once in their histories. Three methods have been observed to occur.

(a) Refracturing of an already existing sealed intergranular crack is a commonly observed feature. Plate 4.7g illustrates a microcrack sealed by calcite and K-feldspar to have been split, and resealed at a later time by stilpnomelane, which itself is split to produce an open microcrack network.

(b) Solution of one sealing mineral and precipitation of another is also found to occur. This is often the case with calcite sealed intergranular cracks, as shown in Plate 4.7h. Calcite and K-feldspar is embayed along the crystal boundaries and microcrack edges. With the areas dissolved now sealed by prehnite, albite and actinolite.

(c) As a result of the preservation of open porosity between microcrack sealing minerals. Between the radiating pumpellyite in Plate 4.7c there are open spaces. Along the edges of the microcrack the voids are sealed by stilpnomelane, apparently having been precipitated by a later fluid percolating along the inter-pumpellyite porosity.

Plates 4.8a and 4.8b are examples where the inter-pumpellyite porosity has been sealed by later barite, which grows as poikilotopic crystals through the pumpellyite sealed crack.

Evidence of an evolving fluid passing along a crack can also be found in the Lewisian samples. In plate 4.8c the growth of prehnite has given way to precipitation of calcite. In such prehnite-calcite sealed cracks, calcite is invariably preserved at the centre of the crack. A change in some physical condition, or fluid composition, might allow this feature to develop.

The preservation of these many these features indicate that microcracks may be permeable during several fluid flow events. Vaughan *et al.* (1986) discovered that passing water at 300 °C through microcracks in granite for a period of two weeks led to a reduction in permeability of 96%, whereas the calculated porosity was reduced by only 10% over the same period. This may indicate a preference for material to be precipitated inhomogeneously throughout a crack, with the choking of microcrack intersections or critical narrows. It would be quite possible for porosity in microcracks to remain present between permeation events. Or, for a later fluid flow event, or change in the physio-chemical conditions of the fluid, to create a secondary porosity. This would enable pre-existing sealed microcracks to act as recurring fluid pathways. Secondary porosity is found on many occasions within the microcracks where calcite has been preferentially dissolved. The concentration of fracturing and fluid flow along already existing sealed cracks is to be expected, as the sealed cracks are likely to be weak zones within the rock.

4.5 The crack sealing mineral assemblages and their relative ages

The mineralogical textures associated with equilibrium and disequilibrium mineral sealing phases, as well as microcrack intersections, can allow the establishment of a sealing mineral crystallisation history (Caruso & Simmons 1985). Evidence of successive permeation phases can be seen when one distinct set of sealed microcracks is crosscut by a later different set (Richter & Simmons 1977). Intersection may either be at a high angle to the first microcrack or parallel, where the latest microcrack propagates along the centre of the earlier one.

Several distinct sets of microcracks have been recognised within the Lewisian, by their different mineral sealing assemblages. Their relative ages have been discerned using crack set intersection rules, augmented with equilibrium / disequilibrium textural evidence from S.E.M. photomicrographs of the microcracks. This has allowed the creation of a crack sealing sequence for the microcracks found within the sampled zones listed in Chapter 3. Omitted from this sequence are mineral phases, such as prehnite (Plate 4.7c), which are not crack seal minerals but replacements of the wall rock. Spalled wall-rock (Plate 4.7e) is also omitted, as it possesses no relationship to the crack sealing minerals. The crack sealing assemblages found within the Lewisian, from oldest to youngest, are presented in Table 4.1. Each assemblage is interpreted as having been formed under separate physiochemical conditions experienced during a permeation event. It is likely that there is more than one permeation event represented in this sequence.

Table 4.1 Post-Laxfordian mineral assemblages found within the sealed cracks. Minerals in brackets may or may not be present and are mostly due to wall-rock buffering. The assemblages are compiled from observations on 97 thin sections and 56 polished sections taken from the sample sites listed in Table 4.9, 598 S.E.M. photomicrographs and 980 E.D.X.S. analysis (Alb = albite, All = allanite, Act = actinolite, Epi = epidote, K-fel = K-feldspar, Qtz = quartz, Sph = sphene, Stilp = stilpnomelane).

Crack sealing mineral assemblages	
Pyrite	**YOUNG**
Barite	
Stilpnomelane (+ Qtz)	
Quartz	
K-feldspar	
Pumpellyite + Calcite + Quartz (+ K-fel + Act + All + Stilp)	
Calcite + Quartz (+ Act)	
Prehnite + Calcite + Albite (+ Act + Sph + K-fel + Qtz + Stilp)	
Quartz	
Calcite + K-feldspar (+ Alb + Epi + Sph)	**OLD**

Plate 4.8a Poikilotopic barite grown through pumpellyite laths (slide M-18).

Plate 4.8b Poikilotopic barite grown through pumpellyite laths (slide M-18).

Plate 4.8c Prehnite growth gives way to calcite towards the center of a sealed crack (slide LD-C2).

Plate 4.8d Intergranular quartz and calcite sealed crack partly healed and bridged by wall -rock hornblende (slide ?).

Plate 4.8e Calcite / K-feldspar sealed crack cut by pumpellyite sealed crack (slide SD-6).

Plate 4.8f Calcite / K-feldspar sealed crack cut by stilpnomelane sealed crack (slide LC-4).

Plate 4.8g Prehnite sealed crack cut by pumpellyite sealed crack (slide LC-7).

Plate 4.8h Prehnite sealed crack cut by pumpellyite sealed crack (slide LC-7).

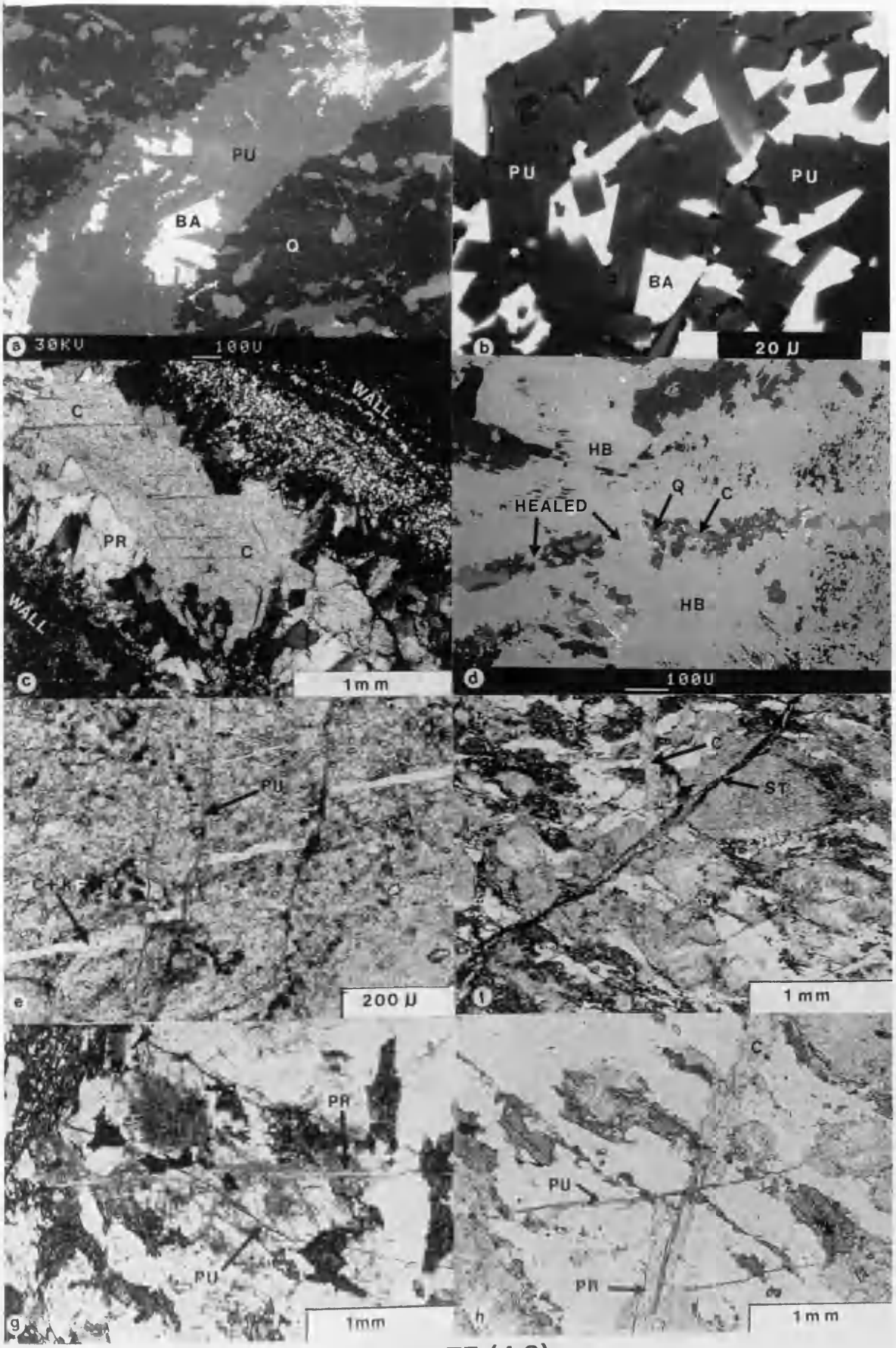
PU
BA
Q
a 30KV 100U
PU
PU
BA
b 20 µ
C
WALL
PR
C
WALL
c 1mm
HB
HEALED
Q
C
HB
d 100U
PU
C+K
e 200 µ
C
ST
f 1 mm
PR
PU
g 1mm
C
PU
PR
h 1mm

PLATE (4.8)

Tables 4.2 to 4.8 show the relative ages of the mineral sealing phases, for every analysed thin section from the traverse sample sites, within the Lewisian central region. The assumption is made that any intersection relation seen in a thin section, will be consistent for the sample location that the thin section came from. This allows the construction of the sequences presented in Table 4.1. Table 4.9 is a summary of the relative ages of the crack sealing mineral assemblages, from each of the traverse sample sites, within the Lewisian central region. This was derived from Tables 4.2 to 4.8, and results in an overall regional, relative crack sealing, stratigraphy.

There are still some discrepancies, noticeably in defining relative ages when no intersections are present. Although there are variations across the region due to localized seals, such as magnetite within the Laxfordian granites, the sequential development of the major crack sealing phases across the area is relatively consistent. Four main post metamorphic phases dominate: early calcite + K-feldspar; prehnite + calcite + albite; pumpellyite + calcite + quartz; and finally stilpnomelane (Table 4.9).

To simplify Tables 4.2 - 4.9, mineral phases which are in equilibrium with the named mineral sealing phases, but are of lesser abundance (i.e. actinolite in Plates 4.6f and 4.7f) have been omitted from the legend. These phases are due mainly to wall-rock buffering and may or may not be present. Full mineral assemblages are given in Table 4.1.

The monomineralic mineral assemblages within Tables 4.1 are often of local development, occurring in only one or two thin sections, or one or two traverse sample localities. These localized events within the sequence, while occurring in similar order, may not be the same event from location to location. Their obvious numerical scarcity, and localization, make any regional correlations between these sealed cracks impossible.

Cracks often show multiple sealing episodes of stilpnomelane following the crack seal method (Ramsay 1980). These are interpreted as a multiple phases of microcrack opening under the same physical conditions, during a single permeation event.

Plate 4.9a Calcite / quartz sealed crack cut by pumpellyite sealed crack (slide SD-7).

Plate 4.9b Prehnite sealed crack cut by pumpellyite sealed crack cut by quartz sealed crack (slide LC-7).

Plate 4.9c Pumpellyite sealed crack cut by K-feldspar sealed crack (slide SD-5).

Plate 4.9d Pumpellyite sealed crack cut by quartz sealed crack (slide SD-1).

Plate 4.9e Quartz sealed crack cut by stilpnomelane sealed crack (slide LC-7).

Plate 4.9f Pumpellyite sealed crack cut by stilpnomelane sealed crack (slide SC-14).

Plate 4.9g Stilpnomelane sealed crack cut by barite sealed crack (slide M-14).

Plate 4.9h Stilpnomelane sealed crack cut by pyrite sealed crack (slide SD-6).

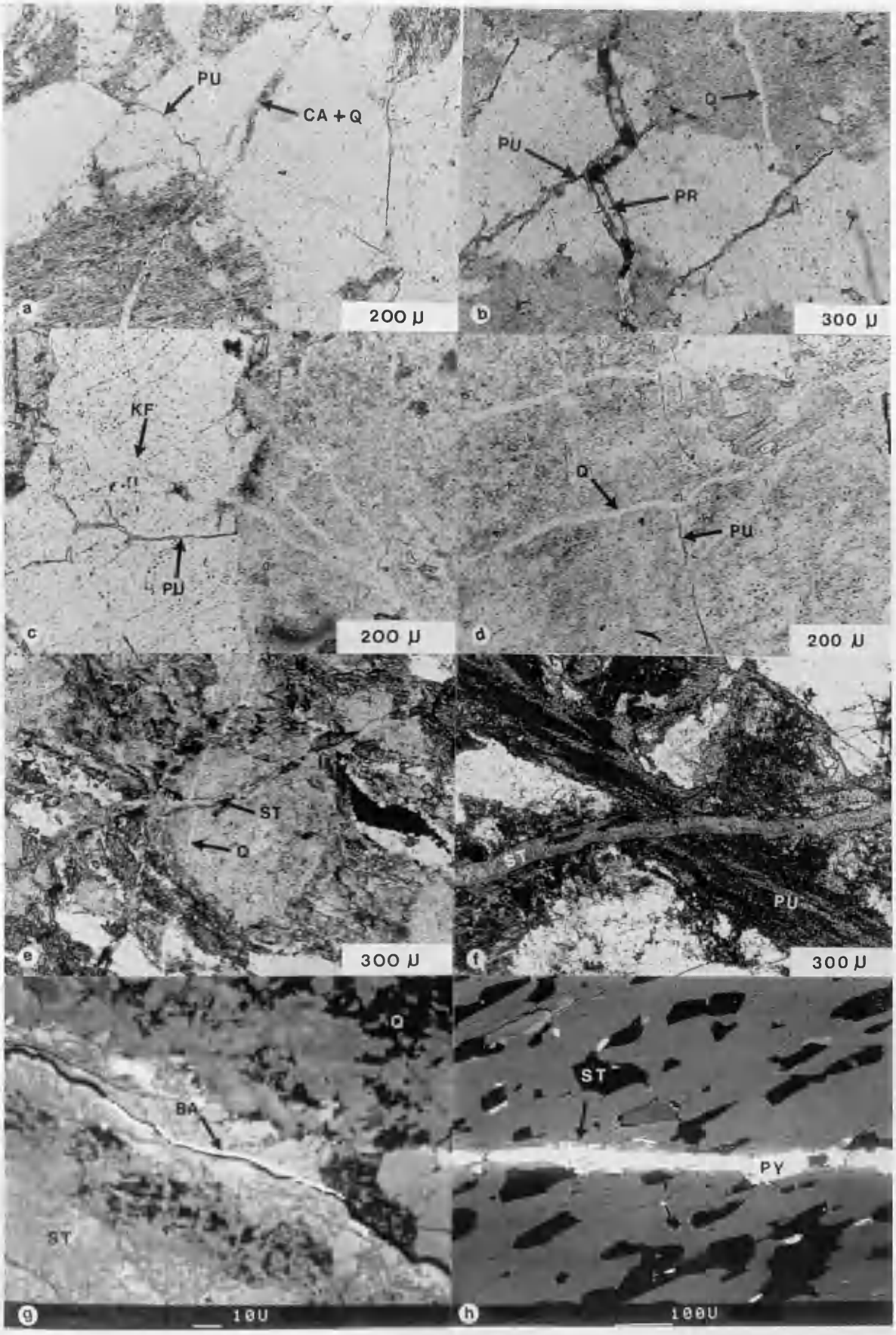
PU
CA + Q
a
200 µ
Q
PU
PR
b
300 µ
KF
PU
c
200 µ
Q
PU
d
200 µ
ST
Q
e
300 µ
ST
PU
f
300 µ
Q
BA
ST
g
100
ST
PY
h
100

PLATE (4.9)

Table 4.2 Relative ages of sealed cracks found in sample site **M**, the Inverian monoclinal fold belt at Duartmore.
Numbers show the relative ages of the crack sealing assemblages present in each thin section analysed. The lowest number represents the oldest assemblage seen. ★ indicates the relative age is unknown due to no intersecting relationships. ★? indicates that due to no intersecting relationships the assemblage present is uncertain (p after the section number indicates a polished section).

	THIN SECTION NUMBER																				
Sealing minerals	1	2	2p	3	3/2ap	3/2bp	4	4p	5	6	6p	7	8	8p	14p	16/2ap	16/2ap	16/2cp	18	18p	18/2bp	18/2cp
Pyrite			3																			
Barite															4	3	2			2		4
Stilpnomelane		2	2								2		2					3			3	3
Quartz	★?			★?										★								
K-feldspar															3							
Pu + Cal + Qtz		1			1	3	★		★	★		★			2	2						
Cal + Qtz				★																		
Pr + Cal + Alb										★	1	★		★		1	1	2	2	1	2	2
Quartz	★?			★?		2			★													
Cal + K-feld			1			1	★	1		★		★	1	★	1			1	1		1	1
Magnetite (Badcallian)	1																					

Table 4.3 Relative ages of sealed cracks found in sample site **SD**, the Scourie dyke near Scourie. (Symbols as with Table 4.2).

Sealing minerals	THIN SECTION NUMBER																				
	1	1p	2/2p	3	4	4p	5	5p	6	6p	7	7p	8	8p	9	9p	10	10p	11	11p	11/2p	25p
Pyrite										3												
Barite			3																			
Stilpnomelane		★	2			★				2		3			2	2	1	2	1	1		
Quartz	2				★?																	
Pu + Cal + Qtz	1			1	★		★	2	3		3	2	1	1	1	1						
Cal + Qtz		★?									2					★		1				
Pr + Cal + Alb	★		1		★		★	1	2	1	1										1	1
Quartz					★?																	
Cal + K-feld		★				★			1			1				★						
Magnetite (Badcallian)		1																				

Table 4.4 Relative ages of sealed cracks found in sample site **DM**, the Scourie dyke emplaced along an Inverian monoclinal fold at Loch'a Mhinidh. (Symbols as with Table 4.2).

	THIN SECTION NUMBER															
Sealing minerals	1	1/2ap	1/2bp	1/2cp	2	2p	3	3p	5	6	7	8	10	10p	12	12p
Stilpnomelane	2															1
Albite						1										
Quartz							★?		★?							
Pu + Cal + Qtz					1						2		1		1	
Cal + Qtz																
Pr + Cal + Alb	1	1	1	1							1					
Quartz							★?		★							

Table 4.5 Relative ages of sealed cracks found in sample site **SC**, the sheared Scourie dyke margin at Kylestrome. (Symbols as with Table 4.2).

Sealing minerals	THIN SECTION NUMBER											
	3	3p	5	5p	7	9	9p	10	10p	11	12p	14
Stilpnomelane		2		★		3	2					2
Pu + Cal + Qtz			★					1	1	1	★	1
Cal + Qtz	★?	★?					★?					
Pr + Cal + Alb			★		1	2					★	
Cal + K-feld	★?	★?		★			★?					
Magnetite (Scourie dyke)						1						

Table 4.6 Relative ages of sealed cracks found in sample site **LC**, the Laxfordian shear zone at Geisgeil. (Symbols as with Table 4.2).

Sealing minerals	THIN SECTION NUMBER											
	1	1p	2p	4	4p	5	6	7	8	9	14p	14p
Stilpnomelane				3			★	5			1	1
Quartz								4				
Pu + Cal + Qtz	1	2	1	2	1	1	★	3	2			
Pr + Cal + Alb					2		★	2	1	1		
Quartz								1				
Cal + K-feld				1								
Magnetite (Laxfordian)		1										

Table 4.7 Relative ages of sealed cracks found in sample site G, the Laxfordian granite sheet at Laxford Bay. (Symbols as with Table 4.2).

Sealing minerals	THIN SECTION NUMBER										
	1	1p	2	3	4	4p	5	5p	6	6p	7
Stilpnomelane						★				★	
Quartz				★?	★?						
K-feldspar						★		2		★	
Pu + Cal + Qtz							1		1		1
Cal + Qtz				★?	★?						
Quartz				★?	★?						
Magnetite (Lax. granite)	1	1	1					1		1	

Table 4.8 Relative ages of sealed cracks found in sample site PE, the Laxfordian pegmatite vein at Laxford bridge. (Symbols as with Table 4.2)

Sealing minerals	THIN SECTION NUMBER										
	1	1p	2	2p	3	3p	4	4p	5	6	6p
Stilpnomelane		★	1	2				2			
K-feldspar		★									
Pu + Cal + Qtz						1	1				
Magnetite (Laxfordian)				1				1			

Table 4.9 A summary of the relative ages of sealed cracks found the sample sites. Symbols as with Table 4.2, except for + which implies that the barite and pyrite assemblages are younger than the stilpnomelane but do not intersect one another.

	STRUCTURE SAMPLED								
Sealing minerals	Kylesku Granulite	Inverian monoclinal fold	Scourie Dyke	Scourie dyke along monocline	Laxfordian shear zone	Sheared Scourie dyke contact	Granite vein	Pegmatite vein	overall relative age order
Pyrite		+	+						+
Barite		+	+						+
Stilpnomelane	★	6	7	3	7	3	★	2	1 2
Quartz		★	6	★?	6		★?		1 1
K-feldspar		5					2	★	1 0
Pu + Cal + Qtz	★	4	5	2	5	★	★	★	9
Cal + Qtz		★?	4			★	★?		8
Pr + Cal + Alb		3	3	1	4	2			7
Quartz		★?	★?	★?	3		★?		6
Cal + K-feld		2	2		2	★			5
Magnetite (Granite vein)							1		4
Magnetite (Laxfordian)					1			1	3
Magnetite (Scourie dyke)						1			2
Magnetite (Badcallian)	1	1	1						1

Table 4.10 Sealed cracks found at other sample sites not represented in Table 4.9.

Sample site	Sealed crack mineral assemblages
Basement	
UB	Chrisotile
LD	Prehnite + Calcite : Pumpellyite + Quartz
NR	K-feldspar + Calcite : Haematite
R	Pumpellyite
Unconformity	
TUA	Pumpellyite + Quartz + Calcite : Haematite
STU	Calcite + K-feldspar : Haematite
RC	Pumpellyite + Calcite
GB	Pumpellyite + Calcite
D	None
S	Haematite
A	None

Using the techniques mentioned previously, only one set of "prehnite", "pumpellyite", and "stilpnomelane" sealed microcracks have been identified. Plates 4.8e to 4.9h illustrate some of the post-Laxfordian intersecting relationships between the different sealed microcrack sets from the central region sample sites. The sealed crack sets, present at the locations sampled by specific drilling of larger sealed cracks and joints, are summarized in Table 4.10.

4.6 The orientations of the sealed microcracks and joints

The orientations of visible open, and sealed, extensional microcracks and joints, present within the traversed sampled sites of the central region between Kylesku and Loch Laxford, were measured in the field. This was done in an attempt to relate the sealed microcracks and joints to the direction of extension associated with the fracture, sealing and hence the permeation events in operation.

The orientation data[2], for both open and sealed cracks from each of the measured localities, are presented in figs 4.6 to 4.13 as:

(a) equal area stereographic projections of the poles to the fractures; and

(b) computer drawn percentage contour plots of the poles to the fractures.

From these diagrams several conclusions can be drawn about the orientations of the fractures present within the studied central region locations. In most cases, for the poles to

[2] The orientation plots were generated using the SODS routine installed by Dr. C. Farrow on the VAX 11/750 in the Department of Geology, Glasgow University.

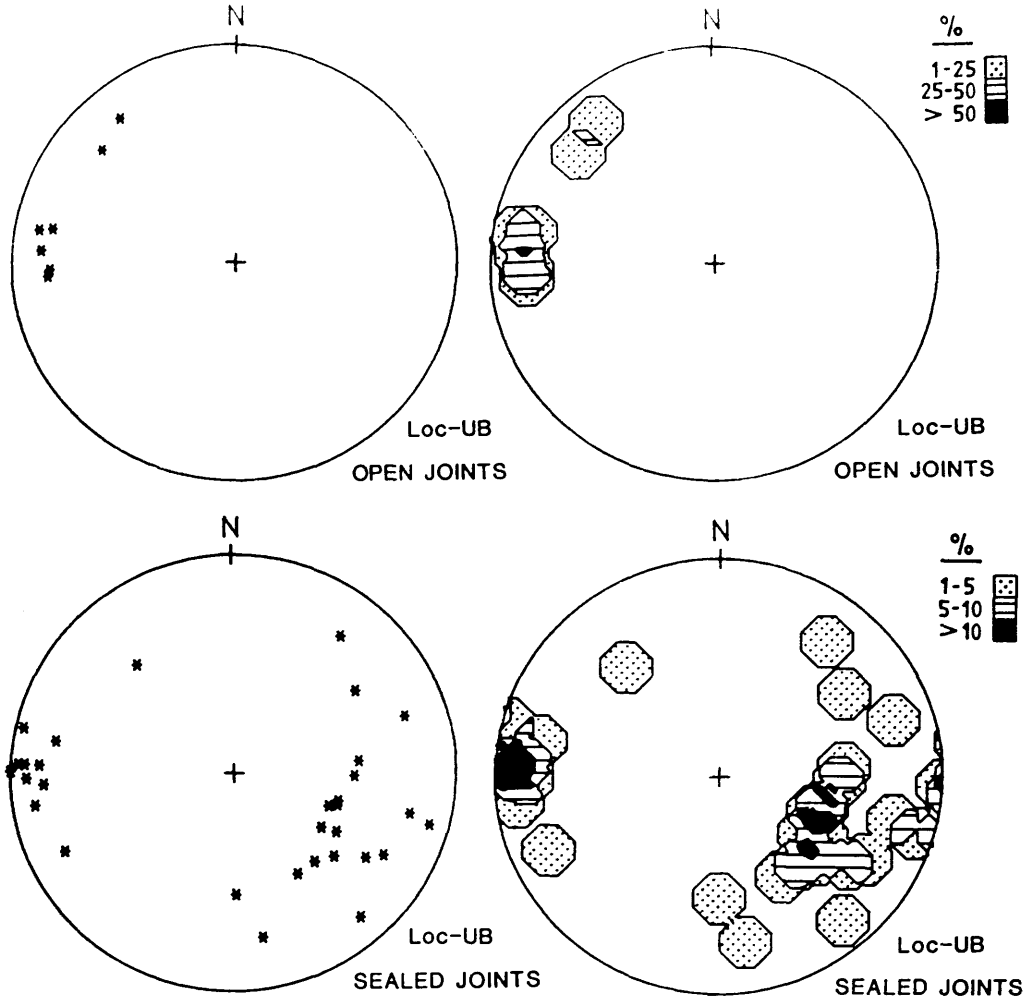

Figure 4.6 Orientation of open and sealed joints and cracks from sample site UB, the Badcallian ultrabasic rock. Plots are equal area, stereographic projections, of poles to the open and sealed joints. Illustrated are an actual , and a percentage contoured, plot of the data. The poles to the sealed cracks represent the direction extension prior sealing.

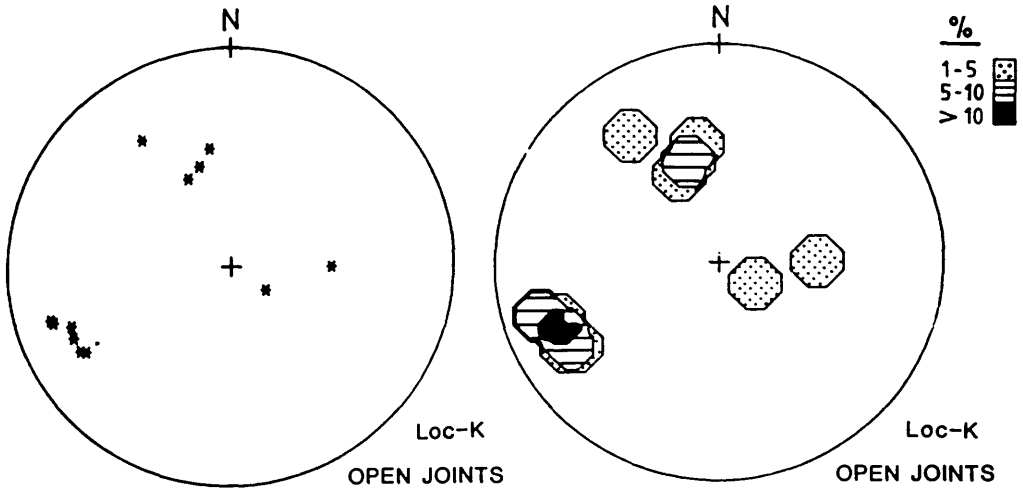

Figure 4.7 Orientation of open joints from sample site K. Plots are equal area stereographic projections of poles to the open joints. Illustrated are an actual, and a percentage contoured, plot of the data.

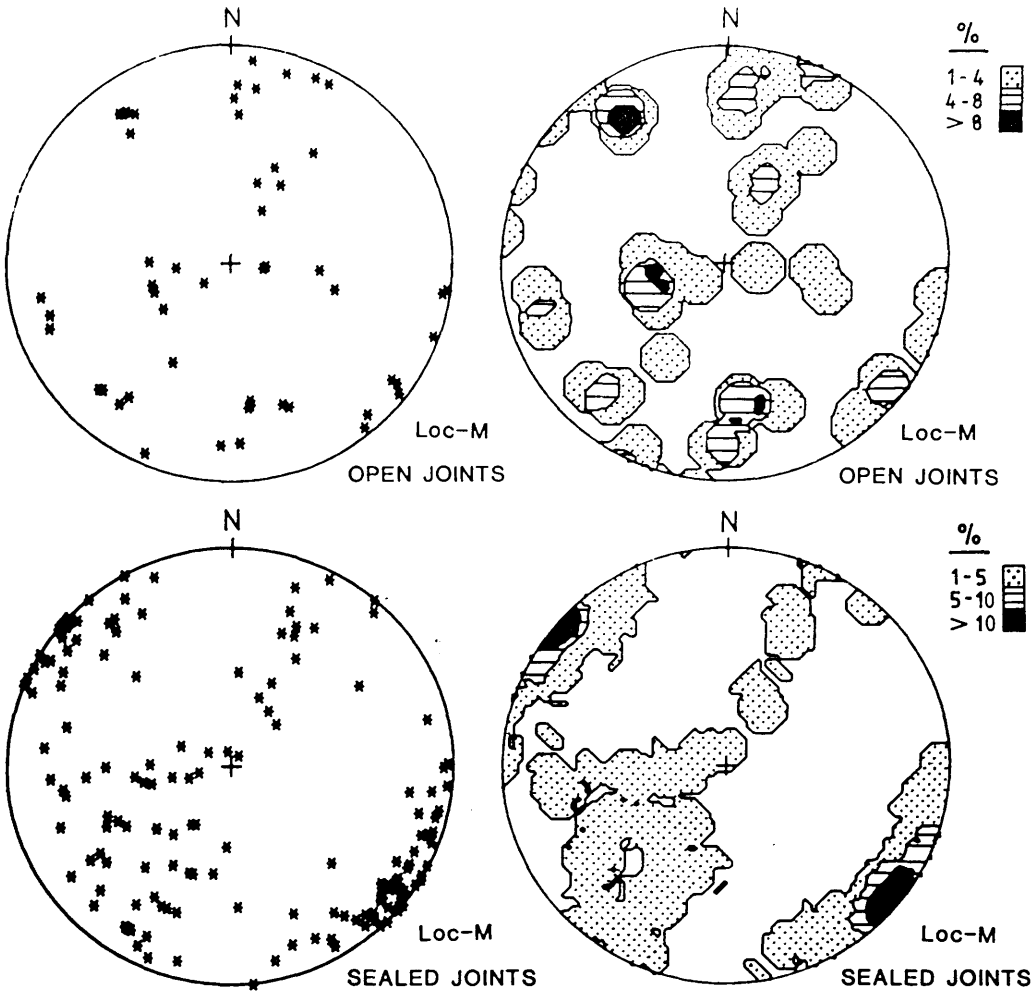

Figure 4.8 Orientation of open and sealed joints from sample site M, the Inverian monoclinal fold. Plots are as with Figure 4.6.

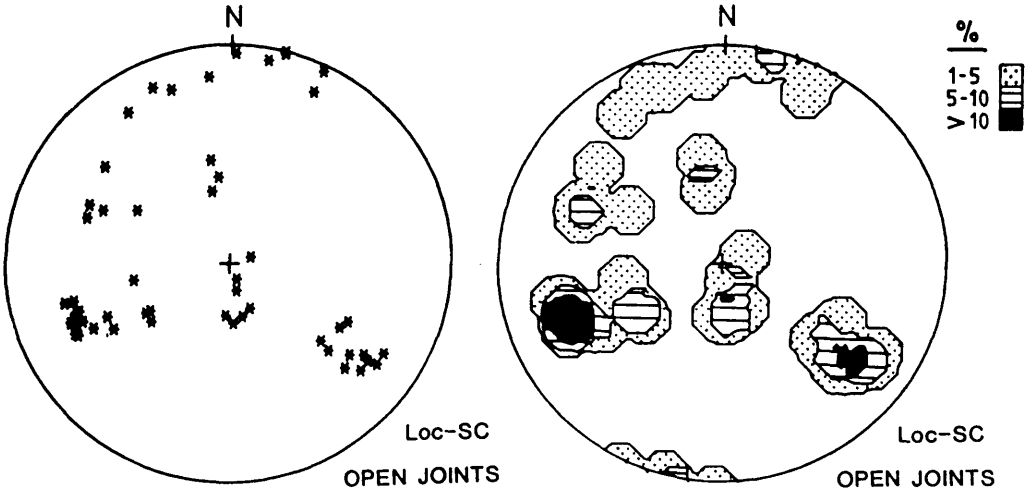

Figure 4.9 Orientation of open joints from sample site SC, the sheared Scourie dyke margin. Plots are as with Figure 4.7.

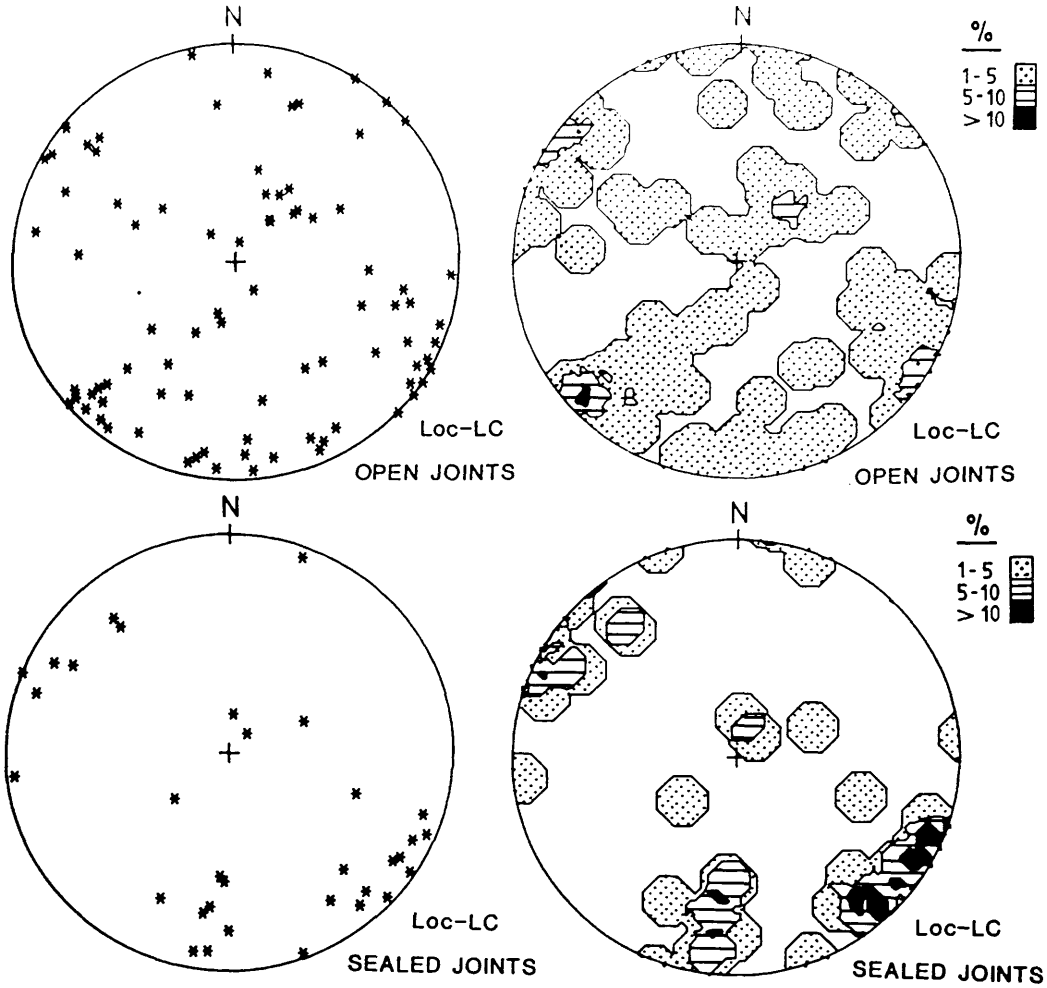

Figure 4.10 Orientation of open and sealed joints from sample site LC, the Laxfordian shear zone. Plots are as with Figure 4.6.

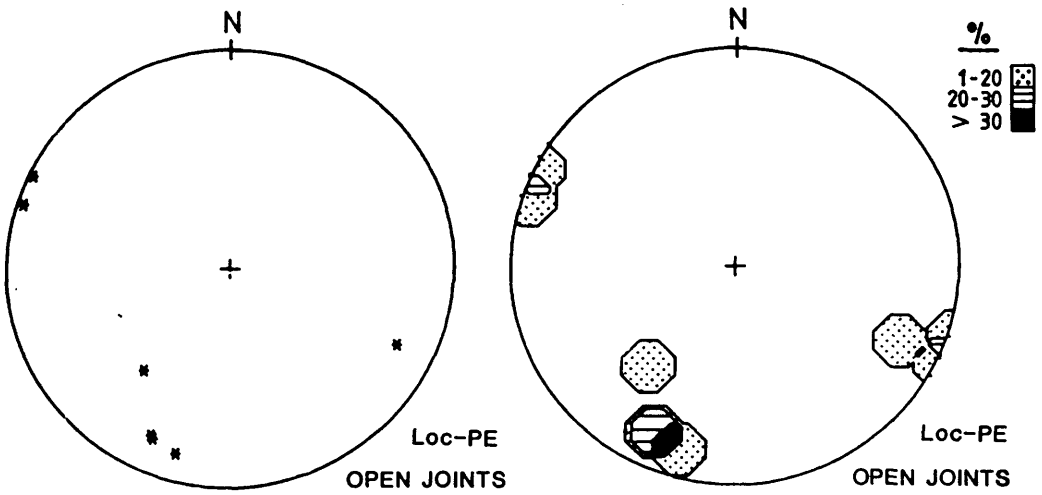

Figure 4.11 Orientation of open joints from sample site PE, the Laxfordian pegmatite vein. Plots are as with Figure 4.7.

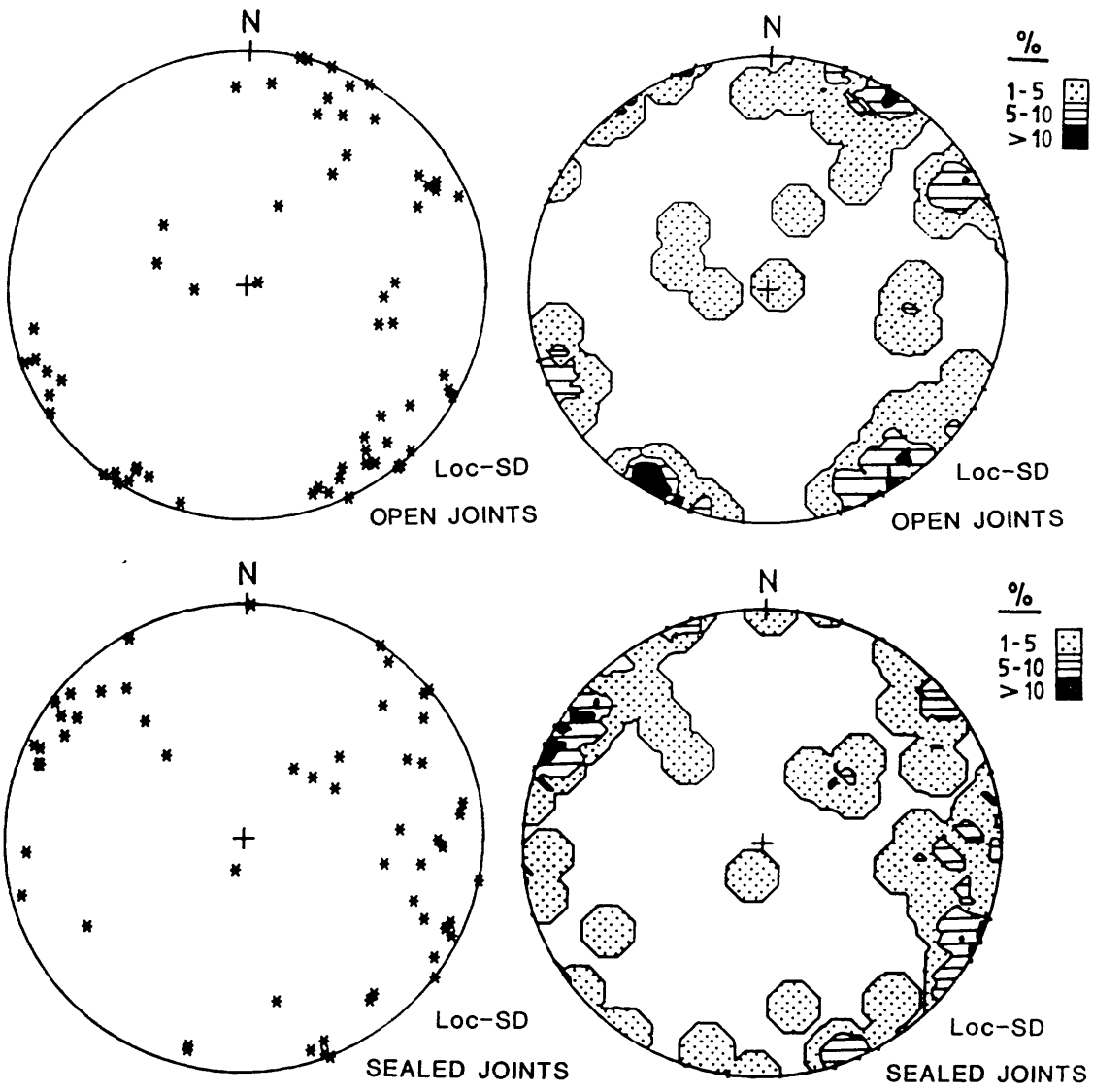

Figure 4.12 Orientation of open and sealed joints from sample site SD, the Scourie dyke. Plots are as with Figure 4.6.

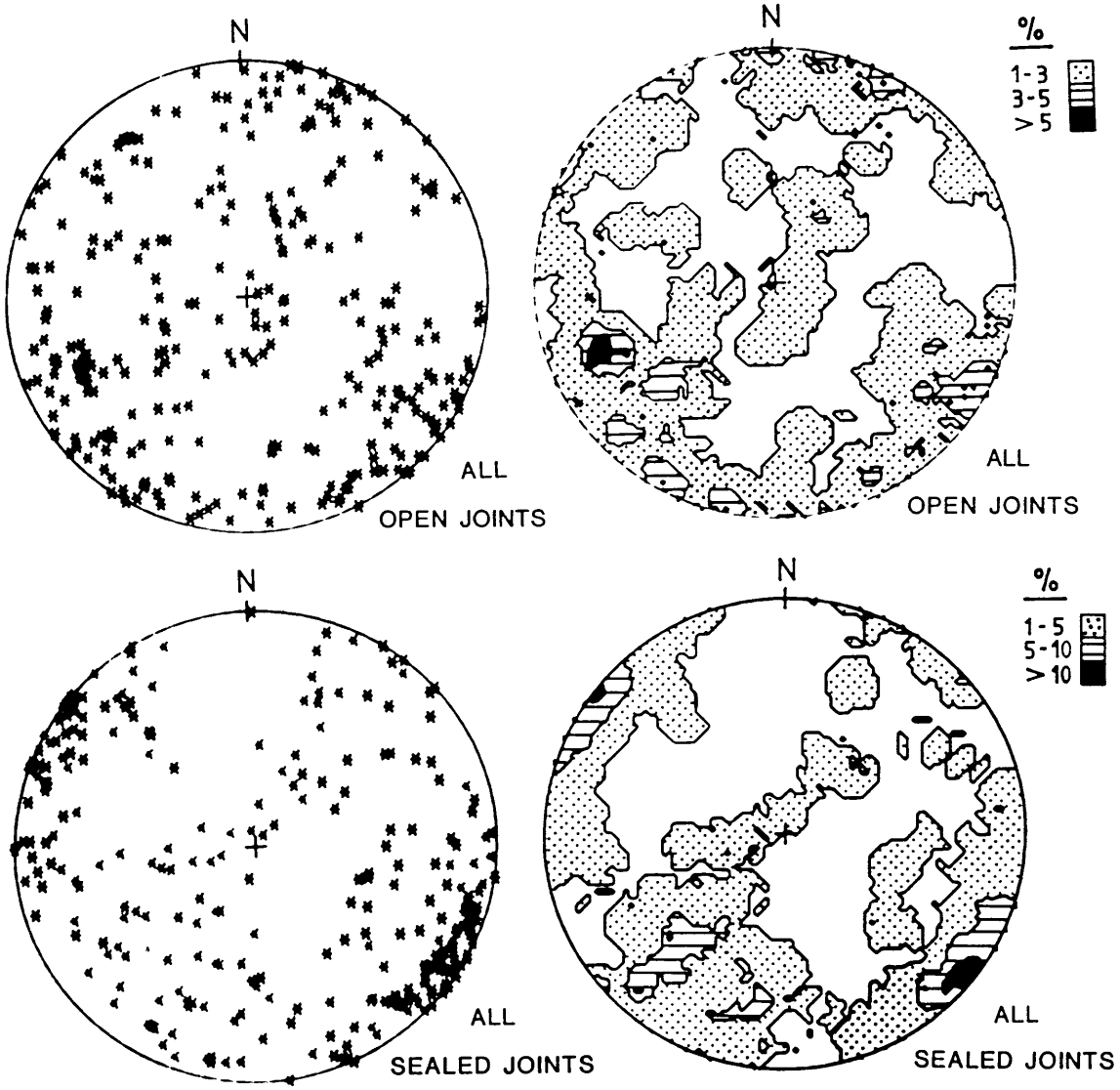

Figure 4.13 Orientation of open and sealed joints from all sample sites. Plots are as with Figure 4.6.

open joints of individual structures, and for the poles to open fractures as a whole, an even distribution in terms of azimuth and plunge is found.

This contrasts with the poles to the sealed fractures. For individual structures, and as a whole, a strong concentration of fractures exist whose orientations are predominantly near vertical (dipping steeply either to the NW or the SE) and strike NE-SW. This indicates that the fractures undergoing extension during the period of fluid permeation were of a NE-SW strike and steeply dipping, as a result of NW-SE extensional stresses at the time of fracture dilation and sealing.

The concentrations of sealed fractures, within localities, often closely correspond to concentrations of open joints. This indicates that the large sealed fractures visible in the field probably originated as joints. These would have formed in response to tectonic stresses active during the Scourian, Inverian and Laxfordian.

4.7 Likely ages and possible sources of fluids causing microcrack sealing

The consistency of the main mineral sealing phases, and their relative ages over the region of the traverse (some 22 km across the granulite terrain), irrespective of location, implies that the four major sealed crack assemblages are the result of a regional pattern of fluid flow events. These differ from the lesser assemblages, some of which appear to be due to events specific to sample locations.

There are five main geological events in post-Laxfordian times that may be responsible, either partly or wholly, for the permeating events. These are:

(a) uplift of the Lewisian terrain with fracturing upon unroofing, due to the expansion of trapped fluid, between 1700 ma and 1000 ma at the onset of the Torridonian sedimentation;

(b) downward permeating surface fluids during the Proterozoic Torridonian rifting;

(c) the Cambrian marine transgression with downward permeating surface fluids;

(d) Caledonian thrusting; and

(e) post-Caledonian extension and uplift.

Although the main permeation events took place between the Laxfordian (1800 ma), and the present day, phases of crack sealing of an age prior to the Laxfordian are also found. Magnetite sealed microcracks occur within the Badcallian granulites (2700 ma), and the Scourie dyke dolerites (2400 ma), where magnetite occupies intragranular and grain boundary cracks associated with pyroxene. In the Laxfordian gneisses (1900-1700 ma), magnetite occurs as an exsolved phase along intragranular cracks in biotite. In the Laxfordian granites (1700 ma), magnetite, associated with the granites magmatisim, is

found sealing intergranular and intragranular cracks.

4.7.1 Early post-Laxfordian sealed cracks and their relation to the geology

Calcite and haematite sealed fractures, in the Lewisian gneiss below the Torridonian unconformity of northwest Scotland, have been attributed to Torridonian weathering (Williams 1968). Instances where ilmenite has been leached of iron along cleavage cracks, with haematite sealed microcracks emanating from the crystal, have been observed (J. Hall Pers. com. Plate 4.10a). This indicates the presence of oxidising fluids. Joint sets within the Lewisian, immediately beneath the Torridonian, are very often heavily stained, or sealed, by haematite.

Although haematite sealed microcracks have not been seen within the sampled structures of the Kylesku to Loch Laxford area, haematite sealed fractures cut the earliest calcite + K-feldspar assemblage (Plate 4.10b) below the Torridonian unconformity at Clachtoll. This indicates an earliest-, or pre-, Torridonian age for this assemblage. The haematite also indicates that fluid was able to flow downwards into the basement.

The pumpellyite + quartz + calcite suite of crack sealing is clearly post-Laxfordian. At Loch Assynt, reddened gneiss below the Torridonian unconformity is cut by pumpellyite veins. These do not continue into the Upper Torridon Group directly above the gneiss. This suggests that the reddening of the gneiss, and the pumpellyite veining, took place at an earlier time than the deposition of the Upper Torridon Group. Implying that the reddening was a result of Stoer Group weathering which preceded the pumpellyite veining. In this area the Stoer Group must have been eroded prior to the deposition of the Upper Torridon Applecross Group.

At Rubh' a' Choin, North of Achiltibuie, joint sets in the Lewisian gneiss, directly below the Torridonian, are sealed by bright green pumpellyite. Here the veins within the gneiss are up to 15 cm wide (Plate 4.10d), and the gneiss on the exposed unconformity surface is partly altered to pumpellyite. Locally derived Torridonian conglomerates of the Stoer Group at Rubh' a' Choin contain clasts of green pumpellyite, and altered "pumpellyitized" gneiss. However, veining is found to continue into the Stoer conglomerates, indicating that pumpellyite mineralization occurred both before, and after, the deposition of the Stoer Group. Outcrops of Stoer Group conglomerate at Gruinard Bay also possess cross-cutting pumpellyite sealed joints (Plate 4.10e).

Epidotic grits are present above the unconformity within the Torridonian, at Kishorn (Peach *et al.* 1907), and on Skye (Sutton & Watson 1960). The detrital pumpellyites within the Stoer conglomerate of Rubh' a' Choin have pumpellyite or epidote overgrowths, and form localized areas of epidotic grit (Plate 4.10f). "Epidotized" gneiss has also been

Plate 4.10a Haematite sealed cracks radiate from a magnetite-ilmenite crystal (slide JH-330).

Plate 4.10b Haematite crack cuts a Calcite/K-feldspar crack (slide STU-2).

Plate 4.10c Clast of pumpellyitized gneiss in Stoer Group conglomerate with a pumpellyite matrix (slide RC-13).

Plate 4.10d Large pumpellyite vein on Torridonian unconformity surface at Rubh 'a Choin.

Plate 4.10e Pumpellyite vein cuts the Stoer conglomerate at Gruinard Bay.

Plate 4.10f Stoer conglomerate matrix, consisting of pumpellyite, Rubh 'a Choin.

Plate 4.10g Plagioclase altered to pumpellyite within a pumpellyitized clast from the Stoer Group, Rubh 'a Choin.

Plate 4.10h Intergrowth of prehnite and pumpellyite (slide M-18).

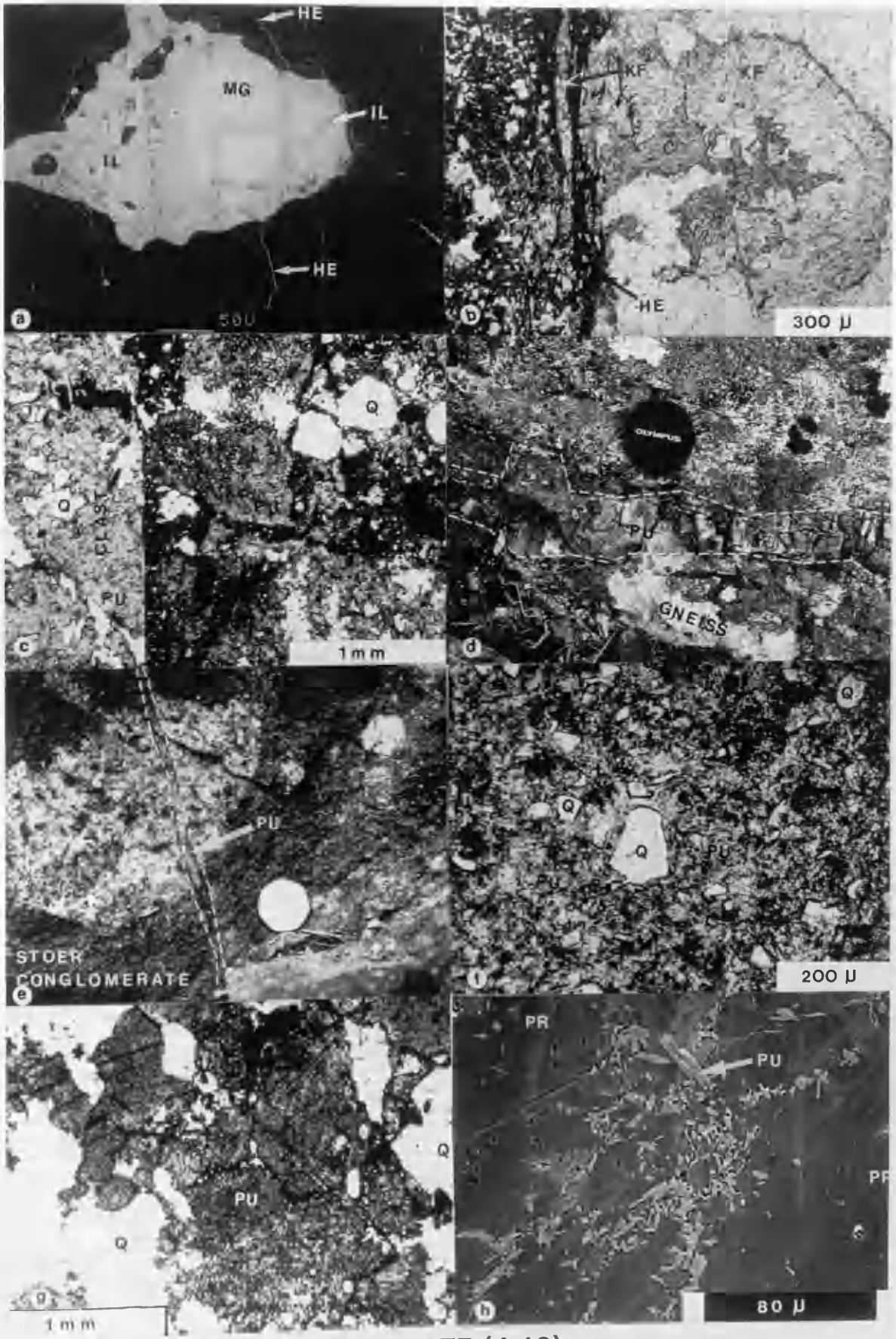
HE
MG
IL
IL
HE
a
500
KF
KF
HE
b
300 µ
Q
Q
PU
c
1 mm
PU
GNEISS
d
Q
Q
Q
PU
PU
STOER
CONGLOMERATE
e
f
200 µ
PR
PU
PR
Q
PU
Q
g
1 mm
h
80 µ

PLATE (4.10)

reported below the unconformity to the East of Suilven, and NW of Cul Mor (Peach *et al.* 1907). The earlier pumpellyite clasts, found within the Stoer Group conglomerates, are likely to be a result of post-Laxfordian retrogression. The alteration of plagioclase, to pumpellyite pseudomorphs (Plate 4.10g), suggests this event was a more pervasive phase than the later, discrete, sealed cracks. The close association of "prehnite" and "pumpellyite" sealed cracks within the sequence, and the occasional occurrence of prehnite and pumpellyite together (Plate 4.10h), may imply they are closely related in real time.

Within the gneisses, the prehnite and pumpellyite minerals are largely confined to the fractures, and are not found as tectono-metamorphic retrogressive phases throughout the gneisses. This indicates that although the geothermal gradient across the region appears to have been fairly constant (indicated by the presence of the prehnite-pumpellyite crack sealing phases from Achiltibuie to Rispond), the fluid phase was confined to the fractures. Therefore suggesting a hydrothermal system, rather than a widespread, post-Laxfordian, period of retrogressive metamorphism.

The Torridonian basin is interpreted as forming via rifting (Stewart 1982). There was ample opportunity for waters to percolate to depth during the Torridonian, as indicated by NE trending, rift parallel, sand-dykes (Peach *et al.* 1907), and the penetration of haematite into the Lewisian gneisses. The sand-dykes (Plate 4.11a) may be up to 5 m wide, and extend down for 600 m or more into the Lewisian (Jones *et al.* 1987). The source for the haematite, found within the sealed cracks, is almost certainly the Torridonian. Plates 4.11b and 4.11c show that the Torridonian sediments and sand-dykes are both rich in haematite.

4.7.2 Later post-pumpellyite sealing events and their significance

The Cambrian marked a transgression of the Lewisian foreland by the Cambrian potassic sea (Ronov & Migdijov 1971, Allison & Russell 1985). It was a time of extension in the Dalradian Basin to the SE, and marine transgression over the northwest highlands. In places, the seabed lay directly above the Lewisian outcrops. Alkaline weathering of the Lewisian, below the Cambrian unconformity, can be seen in the development of agalmatolite (Russell & Allison 1985). This is a form of alteration, traceable for some metres, along joint planes below the unconformity. Authigenic K-feldspar is a major constituent of the early-Cambrian Fucoid Beds, a member that also contains anhydrite nodules occasionally rimmed with barite (Allison & Russell 1985).

Early-Cambrian seawater, or fluids passing through the Cambrian sequence at a later date, could have exploited these same joints and percolated to depth into the Lewisian. The

Plate 4.11a Sand dyke in Lewisian below the Stoer Group, Clachtoll beach.

Plate 4.11b Haematite matrix of the Stoer Group sediments, (slide S-5).

Plate 4.11c Section through a Torridonian sand dyke (slide STU-7).

Plate 4.11d Upper Torridonian unconformity at Sheigra.

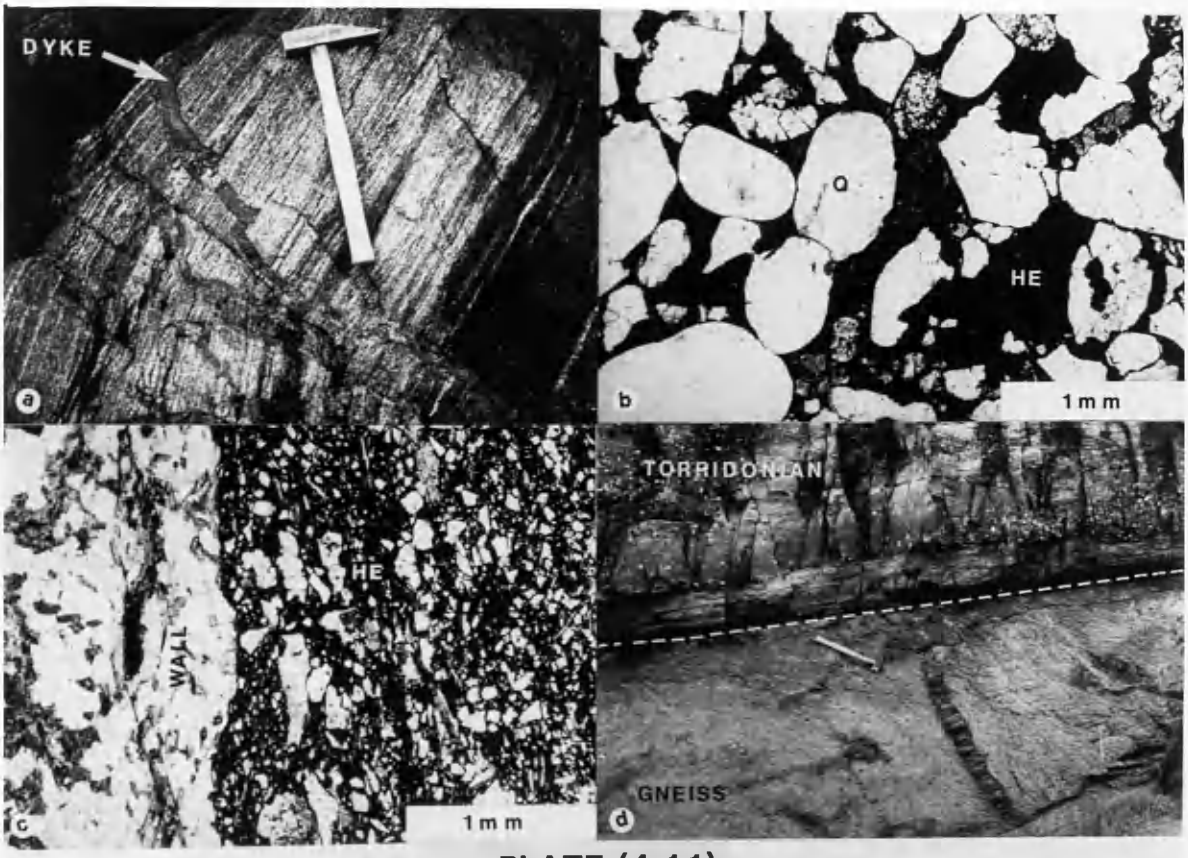

PLATE (4.11)

later, and often more locally developed, K-feldspar, albite, stilpnomelane, barite and pyrite assemblages could be a result of an early-Cambrian episode of hydrothermal convection involving seawater, with high activities of K^+, Na^+ and SO_4^{2-} (see Bischoff *et al.* 1981).

This model is obviously speculative, and the association of stilpnomelane with prehnite-pumpellyite assemblages is common (Zen 1974), perhaps indicating an affinity to the earlier hydrothermal system. However, an early-Cambrian age for these assemblages, carries the implication that the δ^{34} S, of the barite in the fractures, will lie between +30 and +35 ‰ (Claypool *et al.* 1980)

4.7.3 Possible later events of influence

Johnson *et al.* (1985), investigating illite crystallinity below the Moine Thrust, and within the Lewisian foreland, concluded that the thrusting had resulted in a regional thermal high of ~ 275 °C. Allied with tectonic stresses, it may be possible that some of the post-pumpellyite crack forming, and sealing, events were a result of this episode. Post-Caledonian extension, during North Atlantic opening, may also account for some of the later sealed fractures.

No direct evidence to support a role by these post-Cambrian events has been found but their possible influence on the later sealing assemblages is not ruled out.

At this stage, a tentative association of sealed fracture set and geological process can be made (see Fig. 4.14). In the following Chapter, the possible ages and sources of the fluids are investigated further, using mineral assemblage PTX considerations, fluid inclusions, stable and unstable isotopes.

4.8 Summary

1. The open cracks, found within the Lewisian gneiss, preserve features which indicate they were formed by both mechanical and thermal stresses. Shear and dilation, within open crack arrays, are seen to depend upon the cracks orientation relative to the principal stress directions. Mineral bridges, and wall-rock asperities, are found within the open cracks. These would allow preservation of open porosity under compression.

2. The sealed cracks, preserved in the Lewisian, are morphologically similar to the open cracks found in the Lewisian. It can be inferred that they formed by similar

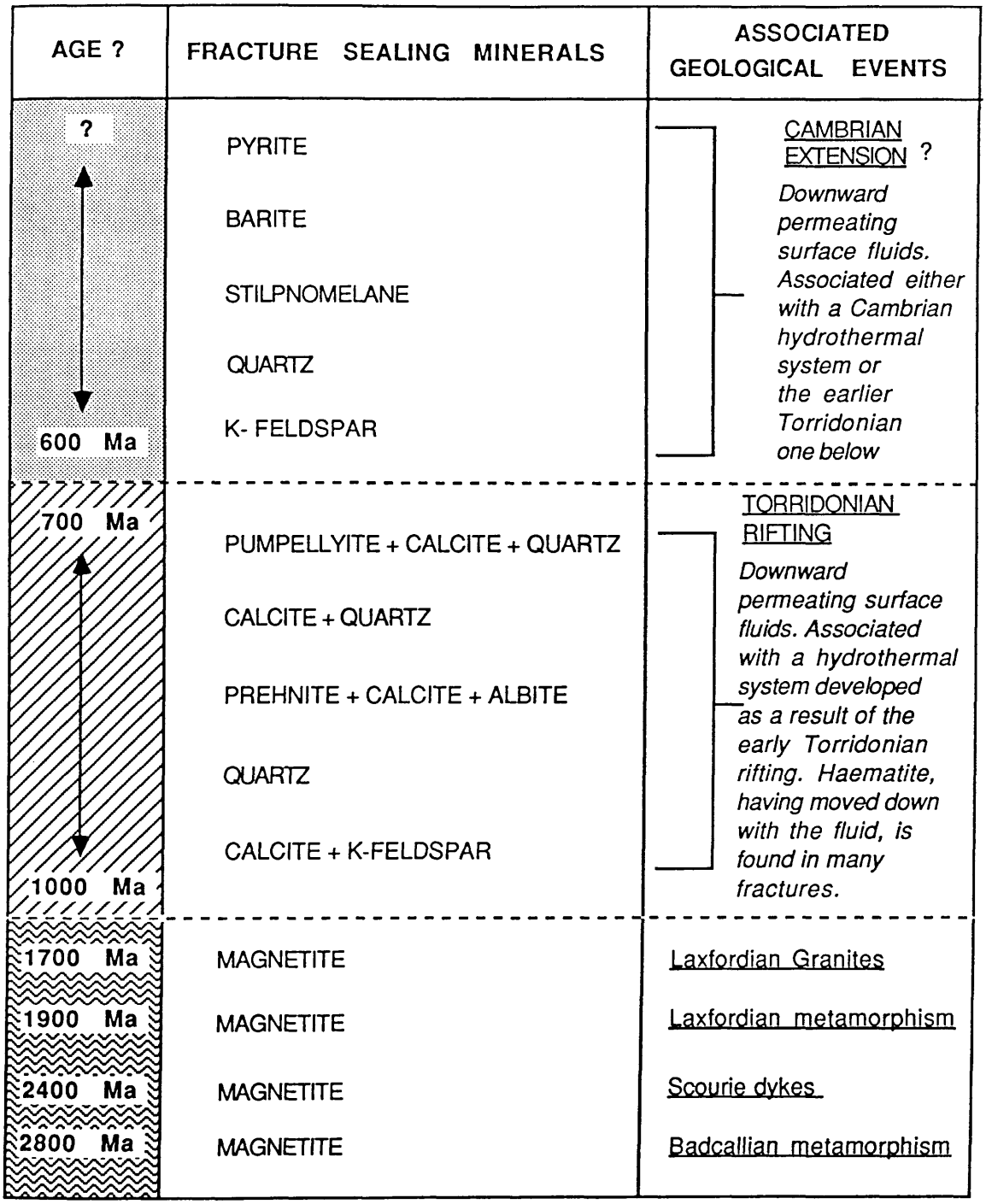

Figure 4.14 The association of sealed cracks to geological events within the northwest highlands. Derived from the observations reported in Chapter 4.

processes. The principal factors influencing their formation were likely to have been tectono-thermal stresses. Although, as with the open cracks, mineralogy and mineral solution are also important factors.

3. Microcracks are the crystal scale fluid conduits and preserve evidence, by way of their sealing mineral phases, of aqueous fluid flow events within the crust. This study has illustrated that many of the sealed microcracks remained open, allowing fluid to permeate along them and interact with the wall-rock. Visible wall-rock alteration is infrequent, and confined to the crystals directly adjacent to the microcrack, but buffering of the mineral sealing phase within the crack is common. Many mineral phases are formed by this interaction with the wall-rock.

4. Many of the microcracks have acted as recurring fluid pathways, and open porosity can be maintained by crystal propping. Evidence, from mineralogical textures, suggests that the sequence of mineral sealing within a fracture preserves a record of the changing fluid conditions.

5. The primary conduits for fluids through the Lewisian basement were joints. Many of the visible sealed cracks are sealed joints, running parallel to open joint systems.

6. The sealed fractures within the Lewisian retain evidence of both localized and regional fluid flow events. From geological relationships, these can be constrained as having developed over a period of some 2 billion years. From the Badcallian to the Torridonian, and perhaps the Cambrian.

7. The early magnetite crack sealing phases relate directly to geological episodes associated with the Lewisian's tectonic cycles during the Archaean and Proterozoic. They are specific to certain structures and lithologies. Post-Laxfordian crack sealing also relates to specific geological events. The sequences containing prehnite and pumpellyite appear to relate to a period of regional fluid permeation. This developed after the deposition of the Stoer Group, but prior to deposition of the Applecross Formation. These sealed cracks formed during episodes of NW-SE extension, perhaps associated with downward percolating surface fluids, during Proterozoic rifting and the formation of the Torridonian basin.

CHAPTER 5

SEALED CRACKS: THE RECORD OF A HYDROTHERMAL SYSTEM

5.1 PTX considerations from mineral assemblages

The depth of the suspected hydrothermal system now exposed on the exhumed unconformity is uncertain due to the uneven nature of the Lewisian - Torridonian unconformity and the unknown depth of Torridonian basin subsidence. Temperatures of the fluid associated with the sealed crack formation are also unknown, but the model for a maturing and deepening hydrothermal system (Russell 1978) suggests that the earliest crack sealing minerals found should relate to a hotter regime than the later sets.

Prehnite occurs mainly with calcite, albite and actinolite. The later pumpellyite occurs principally with calcite and quartz. The temperature at which pumpellyite forms in natural water/rock reactions is not well constrained. Several experimental studies (Plyusina & Ivanov 1978, Liou 1979, Schiffman & Liou 1980, 1983) have shown pumpellyite stability to depend on the interaction of several factors: the equilibrium mineral phases present; temperature, fluid pressure (P_{H_2O}); mol. fraction of CO_2 in the fluid (X_{CO_2}); and the oxygen fugacity (fO_2). Fe-pumpellyite is stable at lower temperatures than Mg-pumpellyite (Liou 1979, Schiffman & Liou 1980) (pure Mg-pumpellyite does not occur naturally). FO_2 interacts with temperature and fluid pressure (where $P_{fluid} = P_{H_2O}$) to affect mineral stability. In an fO_2 buffered system, Mg-pumpellyite was stable between 350 -400 °C, where P_{H_2O} varied from 2-8 kb respectively (Schiffman & Liou 1980). Under similar conditions, Fe-pumpellyite was stable between 200 - 240 °C, between P_{H_2O} of 1-5 kb (Liou 1979).

Plyusina & Ivanov (1978) concluded that prehnite - pumpellyite assemblages are stable over a range of 260-350 °C and pressures of 1-4 kb. However as the mol. fraction of CO_2 in the fluid increases, the pressures at which pumpellyite may be stable is decreased (being stable at 1, 2 and 3 kbars where X_{CO_2} is < 0.2, < 0.05 and < 0.005 respectively). The temperatures of stability for prehnite -pumpellyite assemblages may or may not be independent of X_{CO_2}. This depends on the mineral assemblages present (Glassley 1974). However, for most reactions at a constant pressure, an increase in X_{CO_2} will lead to a higher temperature of stability for the mineral assemblages (see Glassley 1974, Figs.3-5). It is possible to progress from prehnite bearing assemblages, to prehnite-pumpellyite, and then pumpellyite alone by altering one or any combination of the aforementioned parameters which control the minerals synthesis.

The occasional occurrence within the Lewisian of assemblages in which prehnite and pumpellyite appear to have formed together within a single vein, would represent a position on a univariant line between the stability fields of prehnite and pumpellyite. Natural pumpellyite occurrences have been estimated as forming between 100 -150 °C in Franciscan greywackes, by comparison with vitrinite reflectance measurements (Bostick 1974). Sigvaldson (1963) has estimated pumpellyite to be stable at temperatures between 180 - 230 °C in Icelandic geothermal systems. A pumpellyite + quartz + calcite suite falls within the "pumpellyite zone", of the upper part of the ophiolitic volcanic member from the Del Puerto ophiolite, and may have formed at temperatures between 125 - 225 °C (Evarts & Schiffman 1983). This was estimated from assemblages characterized by pumpellyite+ albite +quartz + sphene + haematite + calcite, where pumpellyite is an Fe-rich variety. Calcite veins are also common, indicating X_{CO_2} may have been relatively high. Calcite is common within the northwest highland fractures and therefore X_{CO_2} was also likely to have been high here. In the case of pumpellyite, similar values to those of Evarts & Schiffman (1983) may be likely (that is in the region of 125 - 225 °C), as temperatures are derived from mineral assemblages similar to those present within the Lewisian sealed cracks.

The prehnite suite was developed before the pumpellyite suite in the northwest highlands. Prehnite-bearing fracture sequences have been estimated as forming at temperatures of between 150 - 275 °C from prehnite/laumonite assemblages (Costain *et al.* 1987). The assemblage prehnite + actinolite + albite occurs within the "amphibole zone" of Evarts & Schiffman (1983), at temperatures estimated from metamorphic assemblages as being above 350 °C. The abundance of calcite within the prehnite veins suggests X_{CO_2} was high. Therefore, the formation temperature of the prehnite assemblage may lie around 300 - 350 °C, which is within the upper regions of the prehnite-pumpellyite stability (Plyusina & Ivanov 1978).

Both prehnite and pumpellyite are now found at the same level (therefore at similar pressures). This appears to be consistent with a cooling hydrothermal system. Here, temperature may have interacted with X_{CO_2}, at constant pressure, to affect the stability of the prehnite and pumpellyite: prehnite forming earlier at greater temperatures, and pumpellyite succeeding as temperatures dropped (Glassley 1974). Assemblages with prehnite and pumpellyite may represent intermediates within this sequence.

5.2 Stable isotope systematics relevant to this work

5.2.1 Stable Isotopes, terminology and the δ notation

Isotopes are atoms of an element of atomic number (Z) (equal to number of protons in the nucleus) with different atomic mass (A). The difference in mass is due to differences in the number of neutrons (N) in the atom's nucleus (electrons have negligible weight).

For example, hydrogen has two isotopes, ^{1}H and ^{2}H (deuterium), with atomic masses of 1 and 2 respectively. Both isotopes have 1 proton (Z=1), but deuterium also has one neutron and therefore, $A = Z+N = 2$.

Stable isotopes fractionate during the natural processes involved in geology. Their investigation, measurement and interpretation provide information on the geological processes in operation. The stable isotopes used in this study are those of hydrogen, carbon, oxygen and sulphur, and the approximate relative abundances of the isotopes measured is outlined in Table 5.1.

Table 5.1 The stable isotope ratios measured, and the relative abundance of each isotope.

	Ratio Measured	Relative Abundance (normalized)	
Hydrogen	D/H	^{1}H	(99.985%)
		D	(0.015%)
Carbon	$^{13}C/^{12}C$	^{12}C	(98.89%)
		^{13}C	(1.11%)
Oxygen	$^{18}O/^{16}O$	^{16}O	(99.756%)
		^{18}O	(0.205%)
Sulphur	$^{34}S/^{32}S$	^{32}S	(95.02%)
		^{34}S	(4.21%)

These isotopic ratios are measured relative to a standard on a mass spectrometer to produce a δ value.

The δ notation is defined as:

$$\delta_{sample} = \frac{R_{SAMP} - R_{STD}}{R_{STD}} \times 10^{3} \quad (‰), \qquad 5.1$$

where R is the ratio of the heavy/light isotope, SAMP is the unknown sample and STD is

the calibrated standard. This δ value is reported as parts per thousand (‰), or 'per mil'. An enrichment in the heavy isotope, within the sample relative to the standard, will therefore produce a +ve value. Similarly a depletion in the heavy isotope, within the sample relative to the standard, will give a -ve value. The standards used have recently been summarized by O'Neil (1986 a). For hydrogen and oxygen the standard is V-SMOW (Vienna-Standard Mean Ocean Water), and for carbon V-PDB (Vienna-Peedee Belemnite) (these are the same as the original SMOW and PDB standards). Sulphur is reported relative to the CDT standard (Canyon Diablo Troilite from the Canyon Diablo meteorite).

In most cases the standards used are not those mentioned above but other laboratory standards, whose δ values, relative to the original standards, are known. In the following sections, the aspects of stable isotopes relevant to this study are summarized.

5.2.2 The fractionation factor (α) and its relationship to δ

The isotopic difference (or fractionation) between two substances A and B is defined as

$$\alpha_{A-B} = \frac{R_A}{R_B} \quad . \qquad 5.2$$

From equations 5.1 and 5.2, α can be related to δ by the following equation,

$$\alpha_{A-B} = \frac{1+\delta_A / 1000}{1+\delta_B / 1000} \quad ,$$

or

$$\alpha_{A-B} = \frac{1000+\delta_A}{1000+\delta_B} \quad .$$

Values of α are all close to unity, typically 1.00x.

5.2.3 The fractionation factor (α) and its relation to Δ

A more convenient number is available for analysis, because 10^3 ln (1.00x) is approximately equal to x. This is $10^3 \ln\alpha$, or the 'permil fractionation'. This is essentially a scaling factor which allows easier manipulation of α (e.g. if α = 1.002 then $10^3 \ln\alpha$ = 2.0). The permil fractionation can be approximated by the Δ notation, where the approximation

$$\Delta_{A-B} = \delta_A - \delta_b \approx 10^3 \ln\alpha_{A-B}$$

is found to hold (within analytical errors) when $\delta A - \delta B$ is less than 10. So, by subtracting the δ values of two mineral pairs a very good approximate to $10^3 \ln \alpha$ can be derived. Significance is added to this fact from experimental studies which show that $\ln\alpha$ is a function of the absolute temperature, where

$$\ln\alpha \propto \frac{1}{T^2},$$

so that graphs of $10^3 \ln\alpha$ against $\frac{1}{T^2}$ give straight lines (Bottinga & Javoy 1973).

5.2.4 Fractionation of isotopes

Fractionation within the isotopic systems studied can occur in two ways (See O'Neil 1986 b):

(a) kinetic fractionation; and

(b) equilibrium fractionation.

5.2.4.1 Kinetic fractionation

Kinetic isotope effects are associated with fast, incomplete or unidirectional processes such as evaporation, diffusion and dissociation reactions. Kinetic theory states that the average kinetic energy (K.E.) per molecule is the same for all ideal gases at a given temperature. That is,

$$KE = \frac{1}{2} mv^2 \qquad 5.3$$

Consider the isotopic molecules $^1H_2{}^{18}O$ and $^2H_2{}^{18}O$, of the molecular weights of 20 and 22 respectively. Solving equation 5.3, the ratios of the velocities of the light to heavy isotope species is $(22/20)^{\frac{1}{2}}$, or 1.049. Without considering temperature, the average velocity of $^1H_2{}^{18}O$ molecules is 4.9% greater than the average velocity of $^2H_2{}^{18}O$ molecules in the same system. Similarly, $^1H_2$ will travel 141.4% faster than $^2H_2$ in the same system.

Molecules containing heavier isotopes have stronger bond strengths, and higher

dissociation energies, making it easier to break the bonds of lighter isotopic molecules (such as $^{1}H_2O$, as opposed to $^{2}H_2O$). This is believed to be an important factor in low temperature processes, as opposed to the high temperature reactions involved in this study. In high temperature reactions, fractionation is frequently explained in terms of equilibrium fractionation.

5.2.4.2 Equilibrium fractionation

Equilibrium fractionation effects can be considered in terms of the effect of atomic mass on bond energy. Molecules containing heavy isotopes are more stable (and have greater binding energies), than molecules with the lighter isotope. The oxygen isotope exchange reaction between quartz and water can be written as

$$\tfrac{1}{2}\ Si^{16}O_2 + H_2{}^{18}O \leftrightarrow \tfrac{1}{2}Si^{18}O_2 + H_2{}^{16}O\ .$$

At equilibrium, the equilibrium constant K for this reaction can be written as

$$K = \frac{\left(Si^{18}O_2\right)^{\frac{1}{2}}\left(H_2{}^{16}O\right)}{\left(Si^{16}O_2\right)^{\frac{1}{2}}\left(H_2{}^{18}O\right)}\ .$$

Take, for example, the fractionation of oxygen isotopes between quartz and water. The fractionation between quartz and water at different temperatures is known (Matsuhisa *et al.* 1979) and $10^3 \ln\alpha = 4.06$ for 400°C, and thus $\alpha = 1.00407$. As $K = \alpha$ when one atom is exchanged, K for this reaction is equal to 1.00407 at 400°C.

Four influences on equilibrium fractionation may occur (see O'Neil 1986 b). These are temperature, pressure, chemical composition (of both mineral and fluid) and crystal structure.

5.2.5 Influences on fractionation (Δ)

The greatest single influence on the isotopic fractionation (Δ) between two substances is temperature. Experimental studies have shown for most geological substances, and within geological temperatures, Δ varies linearly with T^{-2} (where temperature is degrees Kelvin). Near absolute zero, the isotopic fractionation between substances will approach a

maximum. As the temperature increases, the value of Δ usually decreases, and at high, or infinite, temperature it will approach zero ($\alpha = 1$, or, $10^3 \ln \alpha = 0$).

In some cases, fractionation is thought to be temperature independent. One example is the hydrogen isotope fractionation between clinozoisite and water (Graham *et al.* 1980). Exceptions to the linear T^{-2} relationship are inflections, as found in the magnetite-water ^{18}O fractionation or the hydrogen fractionation in the kaolinite / muscovite-water of Suzuoki & Epstein (1976). Crossovers, where $10^3 \ln\alpha$ changes sign as the temperature changes, also occur. For example, the ^{18}O fractionation between zoisite and water (Matthews *et al.* 1983). The possible implications of these exceptions to geothermometery are great.

Pressure effects on fractionation of oxygen isotopes were related to temperature and Δ by Clayton *et al.* (1975). Under experimental conditions, pressure effects on Δ were found to be negligible for oxygen isotopes (i.e. less than experimental error/ reproducability). No detailed work on hydrogen isotopes presently exists, and the effects of pressure are assumed to be negligible.

Both oxygen and hydrogen isotope fractionations between minerals are influenced by chemistry. Bonds to ions with a high ionic potential (high charge and a low atomic mass) will have the greatest vibration frequency, and thus the highest energy. Therefore, preferential incorporation of a heavier isotope, by energetic bonds, will minimize the energy of the system. The ions Si^{4+}, Al^{3+} and Fe^{2+} show a decrease in ionic potential and charge, and an increase in mass. It is found that in equilibrium assemblages, the $\delta^{18}O$ values for minerals involving these ions decrease in the same order. The substitution of one ion for another in the crystal lattice, will therefore result in a variation in fractionation. Taylor & O'Neil (1977) showed that a fractionation occurred between grossular and andradite due to the substitution of Fe^{3+} for Al^{3+}. Similarly, the substitution of Al^{3+} by Fe^{3+} in epidotes is thought to result in a difference in fractionation (Matthews & Schliestedt 1984).

Suzuoki & Epstein (1976) showed experimentally determined hydrogen isotope fractionations, between various hydroxyl bearing minerals relative to water, were influenced by the mineral chemistry following the equation

$$10^3 \ln\alpha_{\text{min-}H_2O} = -22(10^6 T^{-2}) + (2X_{Al} - 4X_{Mg} - 68X_{Fe}) + 28.2$$

(where X is the mol. fraction of the cation in the octahedral (X) site). Other systems, such as epidote - H_2O, do not show varying fractionation due to the differing cation chemistry with the hydrogen system (Graham *et al.* 1980).

The composition of the fluid, with which the forming minerals are in equilibrium, has been demonstrated as having influence on the fractionation between those minerals and water.

Graham & Sheppard (1980) experimentally derived the hydrogen isotope fractionation of the epidote-water system in pure water and salt solutions. They concluded, that over a temperature range of 250-400°C, saline solutions concentrated hydrogen relative to pure water.

The final factor which may affect the fractionation in a system, is crystal structure of the mineral. These effects are believed to be minor (O'Neil 1986 b), but one aspect relevant to this work concerns hydrogen bonding. Graham *et al.* (1980) showed hydrogen-bonded epidote and AlO(OH) minerals had much more negative mineral-water fractionation factors than non-hydrogen bonded minerals. Similarly, Suzuoki & Epstein (1976) showed that the difference between muscovite-water and boehmite-water fractionations at 400°C is about 50‰, and attributed this to boehmite possessing hydrogen bonds. It would be expected, therefore, that minerals possessing hydrogen bonds would have highly negative hydrogen mineral - water fractionations.

5.2.6 Stable isotope palaeothermometry.

The estimation of palaeotemperatures using mineral-water oxygen isotope fractionations was suggested by Urey (1947) for the system calcite-water. The oxygen isotope fractionation of the calcite-water system has, along with many others, been experimentally derived. As α is proportional to T^{-2}, the fractionation between any two materials is precisely controlled by temperature. This can be expressed in the general form as

$$\Delta_{min - H_2O} = A+\beta\ (10^6\ T^{-2}) + B\ ,$$

where β is the mol. fraction of cation substitution present for that system. The fractionation between calcite and water is given by the equation of O'Neil *et al.* (1969) as

$$\Delta_{cal-H_2O} = 2.78\ (10^6\ T^{-2}) - 3.40\ . \qquad 5.4$$

The system magnetite-water has been calculated by Bottinga & Javoy (1973) and is given as

$$\Delta_{mag\text{-}H_2O} = -1.47\ (10^6\ T^{-2}) - 3.70\ . \qquad 5.5$$

From either of these equations, it can be seen that if the isotopic values for both mineral and water is known, it is possible to solve the equation to define the temperature.

In geological systems, the isotopic composition of the fluid is rarely known. However, as the mineral-water equations define straight lines it is easy to subtract one from the other removing the common term (water). This results in mineral-mineral equations. For example, subtracting equation 5.5 from 5.4 gives

$$\Delta_{cal\text{-}mag} = 4.25\ (10^6\ T^{-2}) + 0.30\ .$$

Thus it is possible to derive temperatures of formation by the separation of coexisting mineral phases (presumed to be in equilibrium with each other).

Problems exist in this approach. It has already been shown that salinity of the original fluid may have an influence on Δ. One possible explanation to account for ambiguous fractionation factors, between workers, for mineral-H_2O reactions. This may be due to the use of different reaction fluids. Therefore, inaccuracies are inherent in the method. The errors and assumptions have been summarized by Jenkin (1988) as follows. The major assumptions are:

(a) the attainment of equilibrium between the phases present;

(b) equilibrium should be attained at a geologically recognizable time; and

(c) equilibrium has been preserved since that time.

The magnitude of uncertainty in temperatures, based on errors in fractionation factor and isotope analysis, may be as high as ±50°C. The magnitude will also depend on the value of A (i.e. how temperature dependent the mineral-mineral curve is). The higher the A value the less the error. This is an important problem to which there is, as yet, no rigorous solution.

Similar to oxygen isotopes, experimentally determined fractionation equations exist for hydrogen isotopes. Unfortunately major isotopic variations exist due to complex mineral structure and chemistry. Therefore, the use of hydrogen isotope min-H_2O curves, to produce mineral-mineral curves and temperature estimates, is difficult. An up to date summary of fractionation equations and stable isotope thermometry can be found in O'Neil (1986b).

5.2.7 Estimation of fluid composition

Naturally occurring fluids can be defined by their δD and $\delta^{18}O$ values relative to SMOW, and waters involved in natural systems fall within well defined $\delta^{18}O/\delta D$ fields (Fig. 5.1). The δD and $\delta^{18}O$ values of the fluid in equilibrium with the mineral phases, can be estimated from the experimental fractionation factors, if the δD and $\delta^{18}O$ value of the mineral is known and the temperature constrained (either by isotope or fluid inclusion methods). Natural fluids, on interaction with rock, usually become more +ve in oxygen as interaction with positive $\delta^{18}O$ minerals occurs. Oxygen evolution is more noticeable than hydrogen as oxygen is more abundant in rocks than hydrogen, with the hydrogen in the system being dominated by the fluid phase. The variations of isotopes in natural waters have recently been summarized by Sheppard (1986).

5.2.8 The isotopes of carbon and sulphur

Carbon isotopes within minerals may fractionate relative to either CO_2 in the atmosphere, or to bicarbonate, HCO^{3-}, in aqueous solutions. Experimentally determined $\delta^{13}C$ fractionation factors exist for these systems as was the case with oxygen and hydrogen isotopes.

The $\delta^{13}C$ value for CO_2 in the atmosphere is about -7 ‰ $_{(PDB)}$, and dissolved carbonate in sea water lies near 0 ‰ $_{(PDB)}$ representing an equilibrium fractionation with atmospheric CO_2. Fresh water is more enriched in ^{12}C, thus producing negative values, as a result of dissolved organic carbon (Faure 1977). The evolution of $\delta^{13}C$ of sea water through time is fairly well constrained from variations in the $\delta^{13}C$ values of marine limestones (Veizer *et al.* 1980).

Similarly, the $\delta^{34}S$ isotope ratios of seawater are well constrained (Holser & Kaplan 1966, Claypool *et al.* 1980) and have varied from +10 to +35 ‰ $_{(CDT)}$. Temperature dependent fractionation occurs between co-existing sulphide minerals. The large effects with time are primarally due to partitioning of ^{32}S into sulphides, and burial in reduced sediments. Subsequent exhumation, and weathering, returns ^{32}S to the oceans.

5.3 Fractionation factors involved in this study

5.3.1 Oxygen Isotopes

Four minerals were analysed for their oxygen isotope ratio: prehnite, pumpellyite, calcite and K-feldspar. The published experimental and theoretical oxygen isotope fractionation factors used in this study were:

$\Delta_{Quartz\text{-}Epidote} = 1.56 + 1.92\beta\ (10^6\ T^{-2})$, Matthews & Schliestedt (1984)

$\Delta_{Quartz\ -\ H_2O} = 3.38\ (10^6\ T^{-2}) - 3.4$, Clayton *et al.* (1972)

$\Delta_{Calcite\ -\ H_2O} = 2.78\ (10^6\ T^{-2}) - 3.4$, O'Neil *et al.* (1969)

$\Delta_{K\text{-}spar\text{-}\ H_2O} = 2.91\ (10^6\ T^{-2}) - 3.41$. O'Neil & Taylor (1967)

In the equation for epidote, the β value (or mol. % pistacite) relates to the amount of Fe^{3+} cation substitution for Al^{3+} in the mineral lattice. This is calculated by

$$mol\%pistacite\ (\beta) = \left(\frac{mol\%Fe^{3+}}{mol\%Fe^{3+} + mol\%Al^{3+}} \right) .$$

Pistacite is the pure Fe^{3+} epidote end member (clinozoisite is the pure Al^{3+} end member). As explained in section 5.2.5, Fe^{3+} has a stronger affinity for the heavy ^{18}O isotope than Al^{3+}. So, all other conditions being equal, more positive $\delta^{18}O$ values are produced with greater Al^{3+}- Fe^{3+} substitution. From these equations listed above, by subtraction, the following equations can be derived:

$\Delta_{Cal\text{-}Epidote} = 0.96 + 1.92\beta\ (10^6\ T^{-2})$;

$\Delta_{Epidote\text{-}H_2O} = 1.82 + 1.92\beta\ (10^6\ T^{-2})$; and

$\Delta_{K\text{-}spar\ -\ Calcite} = 0.13\ (10^6\ T^{-2}) - 0.01$.

The oxygen isotope mineral-water and mineral-mineral curves, useful to the crack sealing minerals, are illustrated in Figures 5.2 and 5.11.

5.3.2 Hydrogen isotopes

Hydrogen isotope compositions of prehnite and pumpellyite have been analysed. No experimental or theoretical curves exist for these minerals, but pumpellyite is like epidote and the following curve equation can therefore be used.

$\Delta_{Epidote\ -\ H_2O} = 29.2\ (10^6\ T^{-2}) - 138.8$ Graham *et al.* (1980).

or $= 35{\cdot}9 \pm 2{\cdot}5 \quad > 250^{\circ}C$

This curve was demonstrated to be independent of composition. Bowers & Taylor (1985) suggested prehnite would display hydrogen isotope fractionation, following the muscovite-

kaolinite curve of Suzuoki & Epstein (1976), and Liu & Epstein (1984) (Fig. 5.3). However, the basis for this selection is conjectural. Therefore, a curve has been derived from prehnite hydrogen isotope values given for the Franciscan complex by Magaritz & Taylor (1976) and Boylestone quarry, near Glasgow, (T. Fallick pers. comm.)(Fig. 5.4). Both these studies have a good control on the δD composition of the fluid from which the prehnite precipitated, and the temperature of the fluid at the time of prehnite formation. It is found that the δD v's temperature positions for these samples lies close to the boehmite curve of Graham *et al.* (1980). There,

$\Delta_{Boehmite - H_2O} = -55.5 \pm 2$, (380-280°C),
or $= - 36.5 \pm 2$, (<200°C)

This is the closest approximation available at the present time, and substantially different from that suggested by Bowers & Taylor (1985). The hydrogen isotope mineral-water fractionation curves used in this study are shown in Fig. 5.4.

5.3.3 Carbon isotopes

Similar to oxygen and hydrogen, the fractionation equations relating carbon dioxide ($CO_{2\ gas}$), to calcite ($CaCO_{3\ solid}$), and to bicarbonate ($H_2CO_{3\ aqueous}$) have been derived (Deines *et al.* 1974), where

$\Delta_{Cal\ (s) - CO_{2(g)}} = 1.194 \quad (10^6\ T^{-2}) \ -3.63$, Deines *et al.* (1974), and
$\Delta_{H_2CO_{3(aq.)} - CO_{2(g)}} = 0.0063\ (10^6\ T^{-2}) \ -0.19.$ Deines *et al.* (1974).

By subtraction, it is possible to derive the equation for $\delta^{13}C$ calcite-bicarbonate fractionation as

$\Delta_{CaCO_{3(S)} - H_2CO_{3(aq.)}} = 1.1877\ (10^6\ T^{-2}) \ -4.54.$

this curve is illustrated in Fig. 5.5.

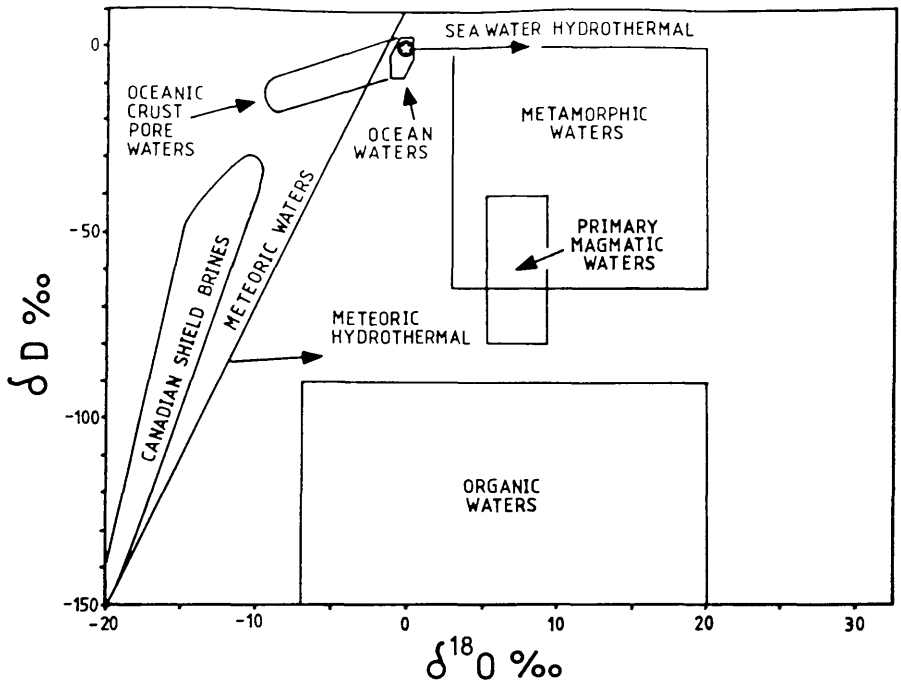

Figure 5.1 $\delta^{18}O_{(SMOW)}$ and $\delta D_{(SMOW)}$ fields for naturally occurring waters. From data provided in Sheppard (1986).

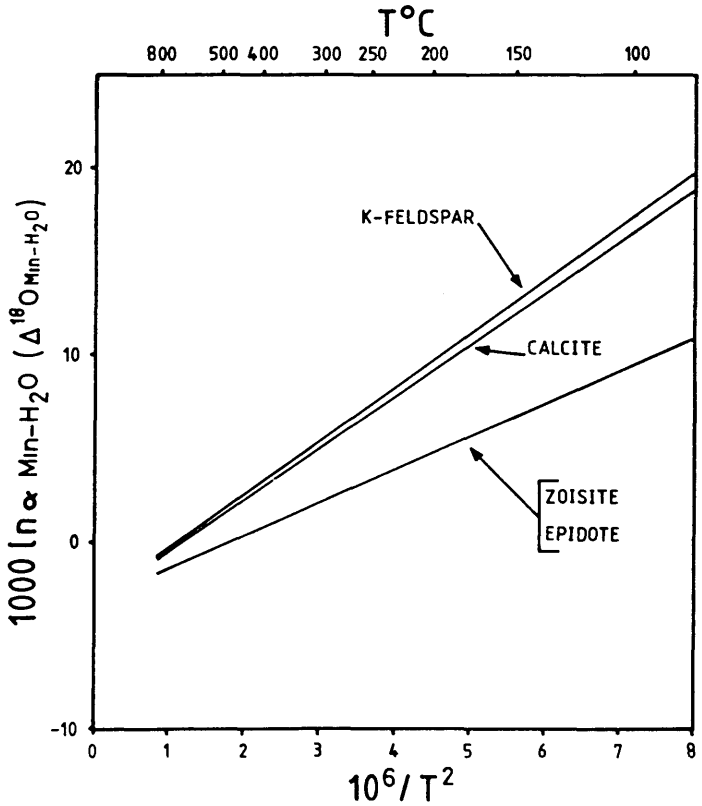

Figure 5.2 $\Delta^{18}O_{min\text{-}water}$ temperature fractionation curves useful to this study. Drawn using the fractionation equations reported in the text.

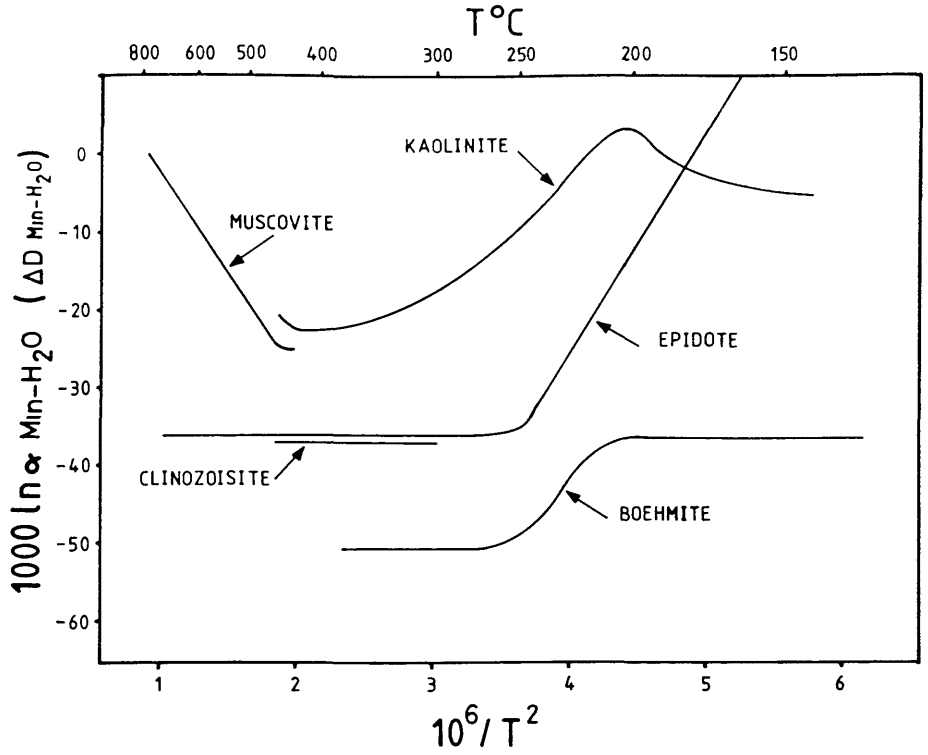

Figure 5.3 $\Delta D_{\text{min-water}}$ temperature fractionation curves useful to this study. Drawn using the fractionation equations of Graham *et al.* (1980), Lui & Epstein (1984) and Suzuoki & Epstein (1976).

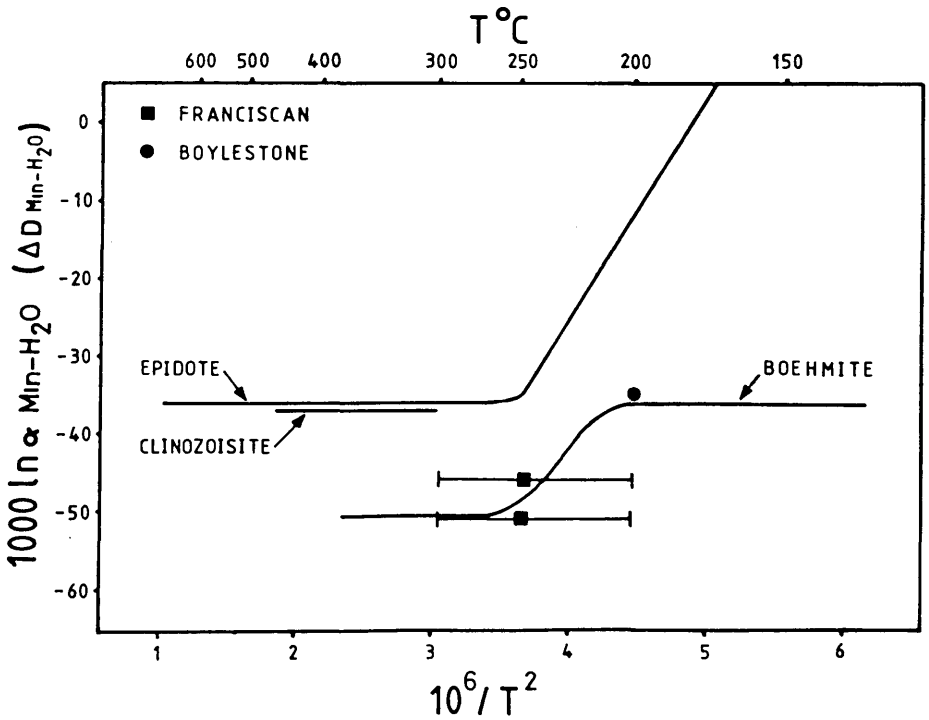

Figure 5.4 Assumed $\Delta D_{\text{min-water}}$ temperature fractionation curve for prehnite. Derived using the Franciscan complex data of Magaritz & Taylor (1976) and the Boylestone Quarry data of Fallick (pers. comm.).

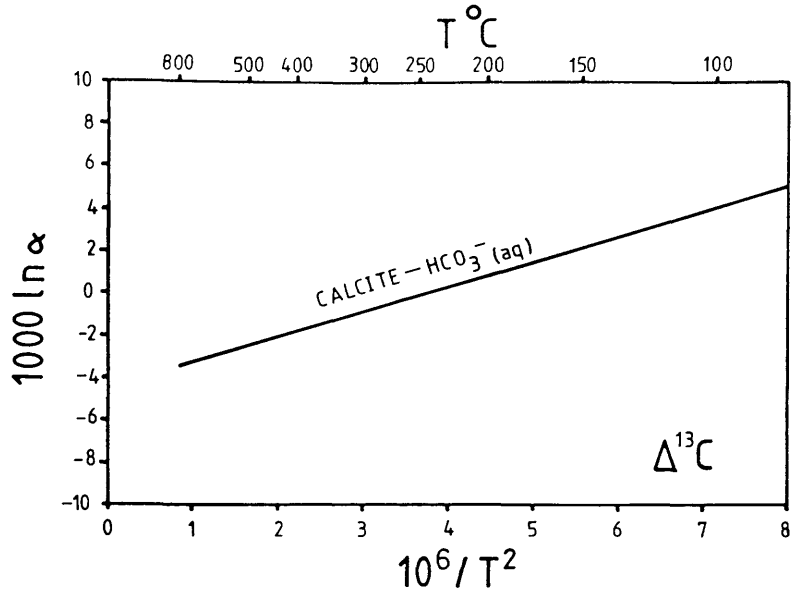

Figure 5.5 $\Delta CaCO_{3\,(aq)} - H_2CO_{3\,(aq)}$ temperature fractionation curve for $\delta^{13}C$. Drawn using the fractionation equation of Deines *et al.* (1974), reported in the text.

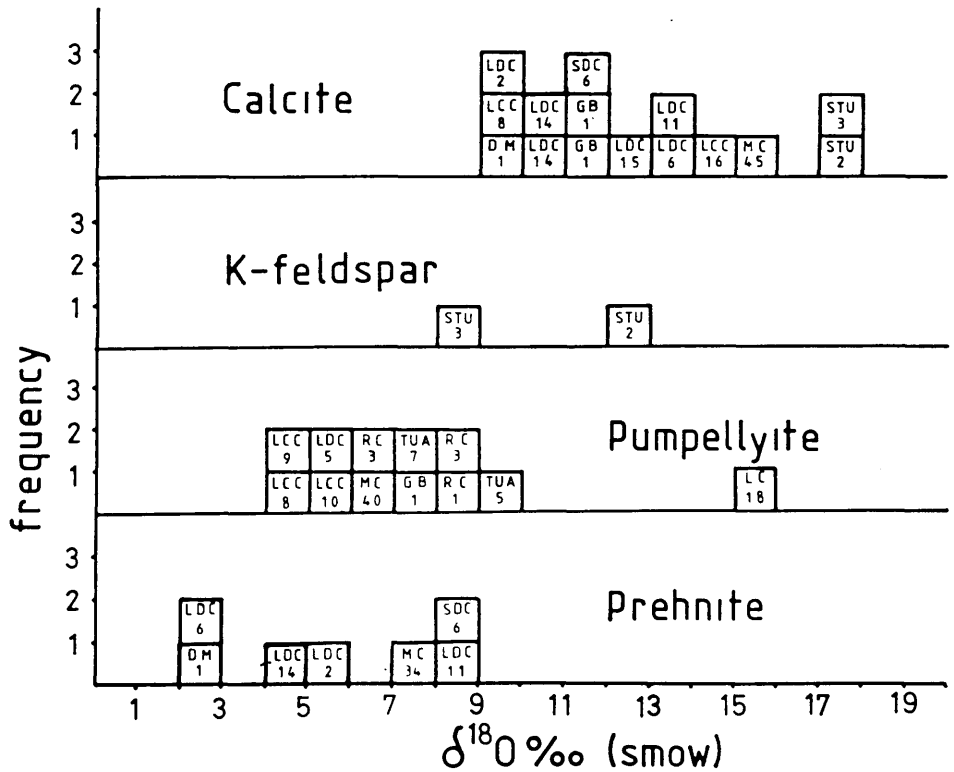

Figure 5.6 $\delta^{18}O_{(SMOW)}$ values for the crack sealing minerals analysed during this study.

5.4 The stable isotope ratios of the crack sealing minerals

5.4.1 Oxygen isotopes

The $\delta^{18}O$ values for prehnite, pumpellyite, calcite and K-feldspar, separated from the sealed cracks, were measured at SURRC using the procedure outlined in Appendix 4 (measured $\delta^{18}O$ values are also given in Appendix 4). Fig. 5.6 is a plot of $\delta^{18}O$, against frequency of occurrence, for prehnite, pumpellyite, calcite and K-feldspar from the sealed cracks. Where possible more than one mineral was separated from the cracks to allow isotope palaeothermometry. To check accuracy, samples were occasionally analysed twice. Precision with calcite was to $\pm$ 0.2 ‰, with the one silicate re-run being $\pm$ 0.8‰.

From Fig. 5.6, it is found there is a range of $\delta^{18}O$ values between minerals. This is not unexpected as different minerals fractionate oxygen isotopes relative to one another, and preserve different $\delta^{18}O$ values under similar conditions. Theoretical fractionation curves for calcite, K-feldspar, prehnite and pumpellyite (see 5.3.1 and Fig 5.2) suggest that, under similar formational temperatures and from the same water, calcite and K-feldspar should display a more positive $\delta^{18}O$ value than either prehnite or pumpellyite. This appears to be true for calcite and its coexisting prehnite or pumpellyite.

In the Lewisian samples, pumpellyite has slightly higher $\delta^{18}O$ values than prehnite. As prehnite and pumpellyite both display fractionation following the epidote curve, the difference in $\delta^{18}O$ values could be due to a difference in chemistry, temperature of formation, or original fluid composition.

The mol. % pistacite present in the prehnite and pumpellyite from the Lewisian sealed fractures is quite high (Fig. 5.7). Individual pumpellyite crystals are found to lie in the range 0.15 to 0.35 mol. % pistacite, with prehnite crystals lying between 0.0 and 0.55 mol. %. These large ranges reflect the occurrence of Fe rich and Fe poor varieties of these minerals. These variations are easily seen using back scattered electron imaging on the SEM and can be seen in Plates 4.7b and 4.6g. The samples prepared for isotope analysis made could make no distinction between iron rich and poor phases, and values have been taken at the average content of 0.25 mol. % for pumpellyite and 0.2 mol. % for prehnite.

From these values, it can be predicted that, under similar temperature conditions and similar fluids, pumpellyite should be more enriched in ^{18}O than prehnite, and therefore have a more positive $\delta^{18}O$ value. This is what is found for the Lewisian sealed crack samples.

From the PTX considerations and the sealed crack-crack relationships, it appears likely that both the prehnite assemblage and the pumpellyite assemblage sealed cracks did

not form under identical conditions. The differences in the values between these mineral sets are therefore likely to be influenced by the combination of aforementioned factors, rather than any one factor alone.

The $\delta^{18}O$ of prehnite lies between +2.3 and +8.8 ‰ relative to SMOW, a range of 6.5‰. Similarly, $\delta^{18}O$ values of pumpellyite lie between +4.6 and +9.9‰ relative to SMOW, a range of 5.3‰ (excluding sample LC-18, which has a value of +15.8‰ relative to SMOW). The two K-feldspars analysed possess $\delta^{18}O$ values which lie between +8.9 and +12.4 ‰ relative to SMOW, a range of 3.5‰. Calcite has a larger range, some 8.1‰, between +9.3 and +17.4‰ relative to SMOW.

For any mineral, if conditions of fluid composition, temperature, mineral chemistry and mineral assemblages are similar, the $\delta^{18}O$ value of the samples within a single mineral group should be identical (assuming equilibrium has been reached). This is not the case for the Lewisian sealed fracture minerals.

If $\Delta^{18}O_{min - min}$ equilibrium existed, fractures sealed under the same conditions should show identical Δ values. Although it is known from geological observations that the K-feldspar, prehnite, and pumpellyite assemblages each appear representative of a single period of permeation (in terms of PT conditions and time), it would be less than sensible to assume that identical conditions prevailed at each location and at each time. To establish if oxygen isotope equilibrium exists, it would be best to use mineral triplets from a sealed crack, and to look for $\Delta_{min - min}$ concordance between all mineral pairs in the triplet. This is not possible for the samples from the sealed cracks, as the most mineral separates from any single crack was two. Therefore, it would be best to look at multiple analyses of identical mineral pairs from different cracks at a single location.

This has been done for the K-feldspar-calcite cracks at Clachtoll (sample prefix STU). In Fig 5.6 and Appendix 4, it can be seen that STU2 and 3 have similar $\delta^{18}O$ calcite values (namely, +17.1 and + 17.4 ‰ relative to SMOW) whereas K-feldspars from the same samples have values of +12.4 and +8.9 ‰ relative to SMOW. This provides two $\Delta_{Kspar - cal}$ values of 4.7 and 8.5 respectively. It is possible that these two samples could have equilibrated oxygen isotopes at different temperatures, but from Fig. 5.10 the temperatures suggested by these Δ values are too low, and Indicate that this assemblage is out of oxygen isotope equilibrium.

Similarly $\Delta_{preh-cal}$ values for fractures in the Scourie dyke at Lochinver (prefix LD) lie over a range from 10.42 to 3.72. This again suggests that some of the pairs did not equilibrate oxygen isotopes at the same temperature, or are out of oxygen isotope equilibrium.

This type of analysis, under the circumstances, provides the best possible indication

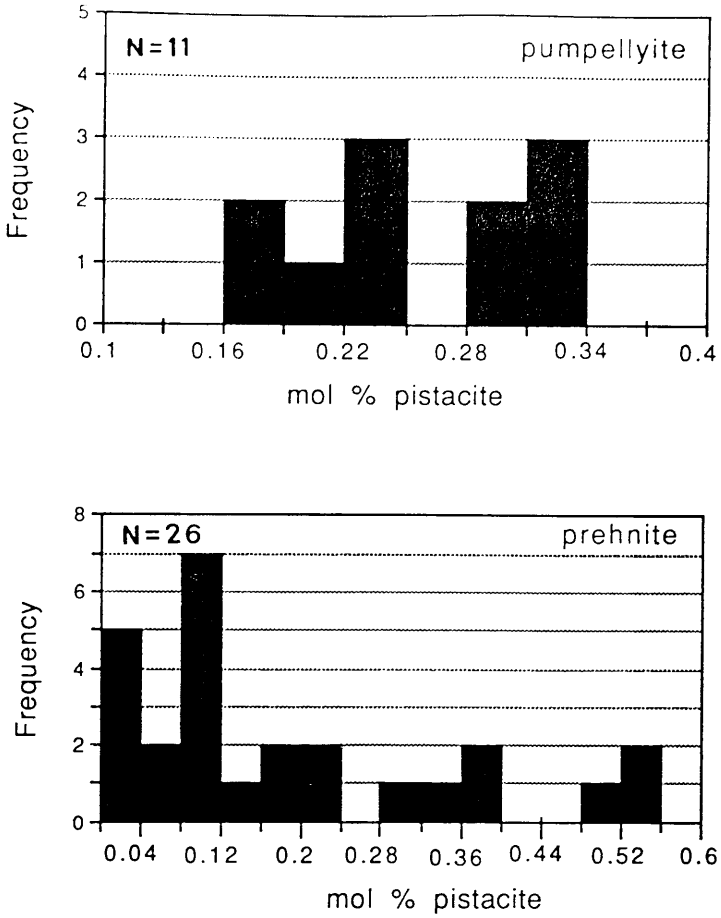

Figure 5.7 Mol % pistacite present in prehnite and pumpellyite. Measured using E.D.X.S. Values are given in Appendix 3.

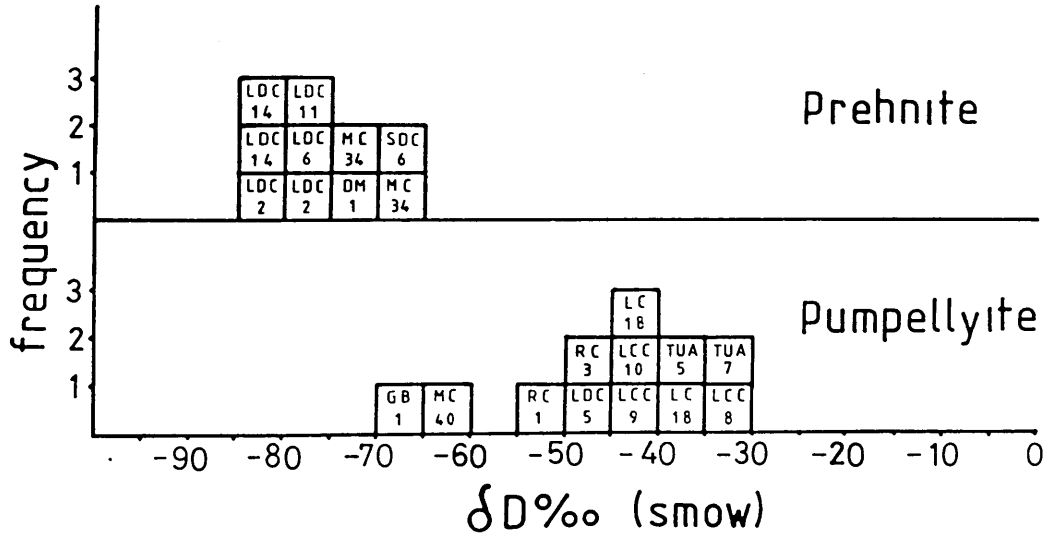

Figure 5.8 $\delta D_{(SMOW)}$ values for the crack sealing prehnite and pumpellyite analysed during this study.

as to the likelihood of oxygen isotope equilibrium assemblages being present. In both cases it appears that assemblages may be out of oxygen isotope equilibrium, and estimations of palaeotemperature using these assemblages may be worthless. This does not discount the fact that one of the fractures may be preserving an oxygen isotope equilibrium assemblage, and, although any "sensible" temperatures derived from such a case can be considered no more than an estimates, it is considered worthwhile calculating them (see section 5.6).

5.4.2 Hydrogen isotopes

Hydrogen isotope analysis was carried out on the OH-bearing prehnite and pumpellyite at SURRC following the procedure outlined in Appendix 4 (values of δD for the prehnite and pumpellyite are also given in Appendix 4). Fig. 5.8 is a plot of δD, against frequency of occurrence, for prehnite and pumpellyite from the sealed cracks. To check precision samples were occasionally analysed twice, the repeated analysis gave results varying at $\pm$ 2‰.

Fig. 5.8 indicates that prehnite from the sealed cracks possess δD values ranging from -80 ‰ to -65 ‰ relative to SMOW. This contrasts with pumpellyite which possesses δD values of -30 ‰ to -66‰ relative to SMOW. The average δD value for prehnite is -75 ‰ relative to SMOW, and the average for pumpellyite being -46 ‰ relative to SMOW.

The extremely light δD values for the prehnite can be explained by hydrogen bonding within the prehnite (see section 5.2.5). Pumpellyite does not possess hydrogen bonding, and as a result heavier δD values are expected, and found. This fact reinforces the use of the boehmite-water fractionation curve of Graham *et al.* (1980), as suggested by published natural prehnite-water fractionations (Fig 5.3). Boehmite possesses hydrogen bonding, which produces a more negative min-water fractionation curve than for epidote-water or, for muscovite/ kaolinite-water.

Similar spreads lie in the hydrogen data as lie in the oxygen data (15 ‰ for prehnite and 36 ‰ for pumpellyite). The likely reason for these spreads are variations in fluid chemistry and temperature. The larger range in the pumpellyite may be due to the epidote-water curve being temperature dependent for part of its course. Whereas the boehmite-water curve is largely temperature independent (Fig. 5.4).

5.4.3 Carbon isotopes

The $\delta^{13}C$ values of calcite were analysed following the procedure outlined in Appendix 4 (the recorded values are also listed in Appendix 4). Again, occasional multiple analyses were carried out to check precision of analyses. Repeat analyses were found to be reproducible to $\pm$ 0.3‰

Fig. 5.9 shows a plot of $\delta^{13}C$ against frequency of occurrence for the calcite $\delta^{13}C$ analysis. From this two principal groupings are found. The first has $\delta^{13}C$ values ranging from -1.2 to -0.8 ‰ relative to PDB (a range of 0.4 ‰). This group consists of samples prefixed GB and STU. The second has a slightly larger range of $\delta^{13}C$ values, between -7.4 and -4.5 ‰ relative to PDB (a range of 2.9 ‰). It is interesting to note that the heavier samples, GB and STU, are from localities where fractures are associated with the Torridonian Stoer Group. The isotopically lighter samples all originate from fractures within the basement Lewisian gneisses (Fig 5.10). It is possible that these two groups represent different fluids. This will be discussed later.

The very light sample DM-1 is so different it is difficult to explain in geological terms. The locality this sample came from was a shallow lochan, low in water. The sample, was on the surface and would normally have been just under the water surface. A possibility exists that perhaps some contamination was present within the sample, or that the calcite had recrystallized, to lower the $\delta^{13}C$ value.

5.5 Temperature and pressure constraints on the sealed crack sets

5.5.1 Mineral pair isotope thermometry

Separation of minerals from the fracture sets have produced three groups of mineral pairs: prehnite and calcite; pumpellyite and calcite; and K-feldspar and calcite.

The theoretically derived mineral-mineral fractionation curves for calcite-epidote or zoisite (β = 0), and K-feldspar-calcite (as listed in section 5.3.1) are shown in Fig.5.11. The requirements for a mineral-mineral fractionation curve to provide an effective thermometer have already been discussed in section 5.2.6. From Fig. 5.11 it is found that the K-feldspar-calcite fractionation curve lies very close to $10^3 \ln\alpha = 0$. In actual fact, the factor A in the fractionation equation equals 0.13. This implies that the fractionation of oxygen isotopes between equilibrium assemblages of K-feldspar and calcite will be very nearly temperature independent and the choice of this mineral pair is not to be recommended as the slightest inaccuracies in the determination of Δ will lead to huge variations in temperature.

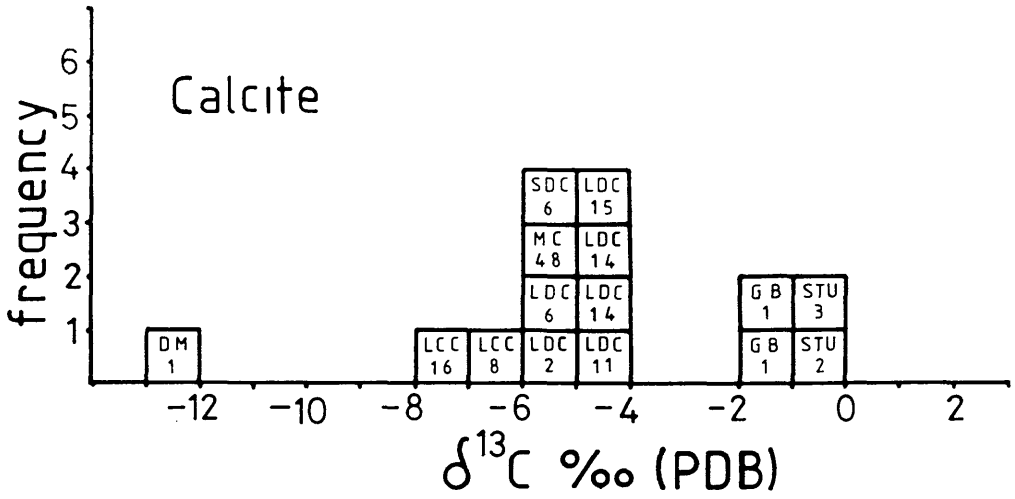

Figure 5.9 $\delta^{13}C_{(PDB)}$ values for the crack sealing calcite analysed during this study.

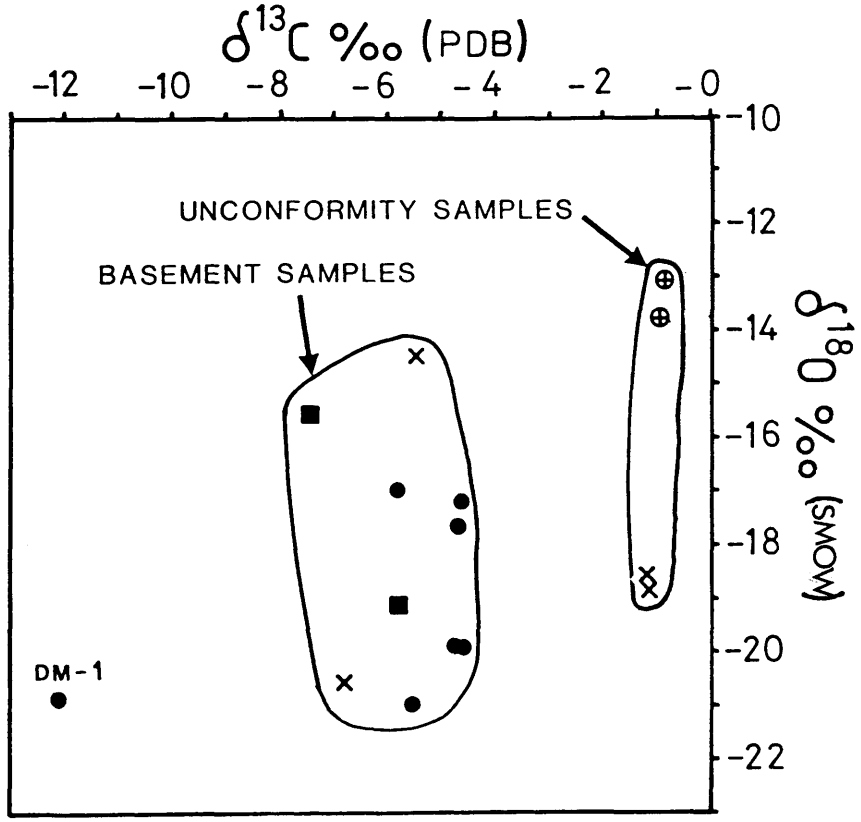

Figure 5.10 Plot of $\delta^{13}C_{(PDB)}$ vs $\delta^{18}O_{(SMOW)}$ for crack sealing calcite.

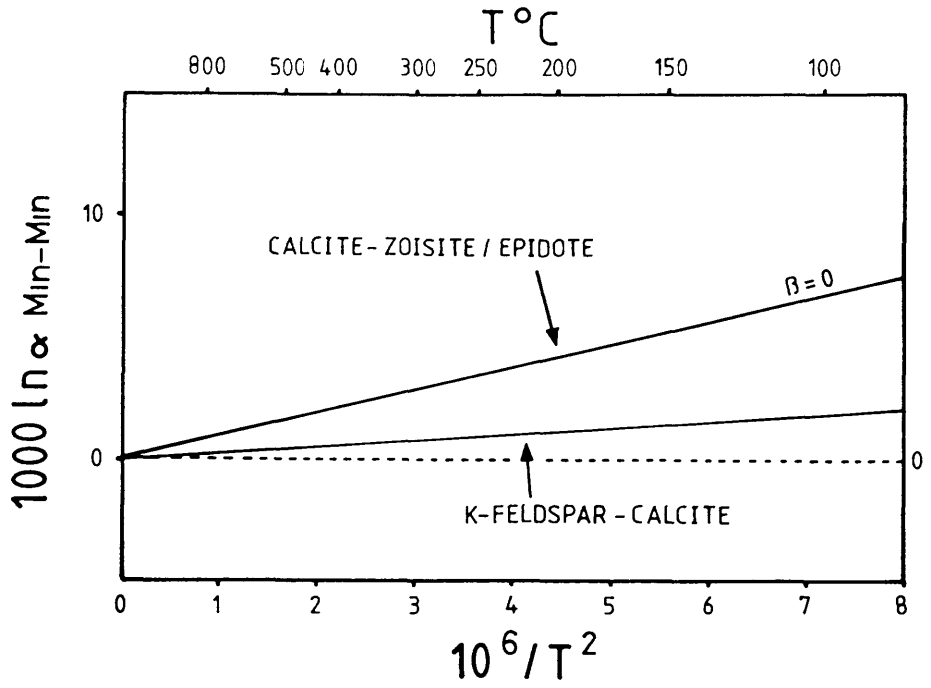

Figure 5.11 Derived $\Delta^{18}O_{min\text{-}min}$ temperature fractionation curves useful to this study. Calculated from the fractionation equations reported in the text.

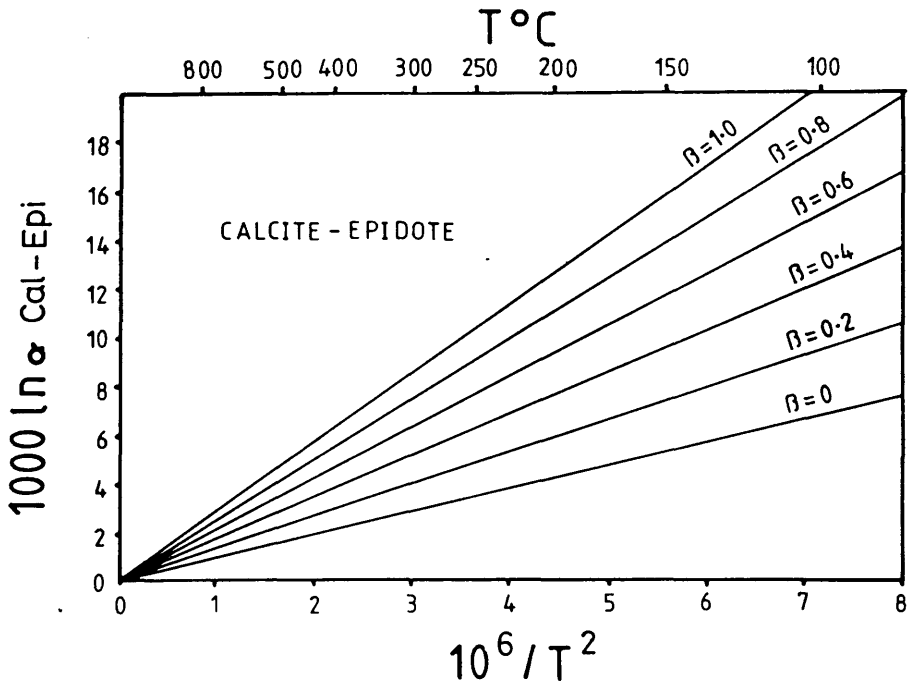

Figure 5.12 Influence of β (mol % pistacite) on the $\delta^{18}O$ temperature fractionation curve between calcite and epidote. Calculated using the derived equation reported in the text.

The fractionation between calcite and both prehnite and pumpellyite (as represented by the calcite-epidote curve in Fig. 5.11) is slightly more temperature dependent ($A = 0.96 + 1.92\beta$). The curve shown in Fig. 5.11 is for the condition of $\beta = 0$ (i.e. no substitution of Al^{3+} by Fe^{3+}). For this condition A = 0.96. As substitution of Al^{3+} by Fe^{3+} increases, the β factor increases, so increasing the value of A. The effect of this on the calcite-epidote curve is shown in Fig. 5.12 and it is found that as β increases, the temperature dependence of the curve increases, thus a better thermometer is produced.

The palaeotemperatures calculated from the Δ values of the calcite-prehnite and calcite-pumpellyite mineral pairs, (at averaged β compositions), are listed in Table 5.2.

Table 5.2 Calculated temperatures for oxygen isotope mineral pairs

Sample #	Mineral	$\Delta^{18}O_{cal\text{-}min}$	Temp °C
LC-C8	PUMP	5.09	**259**
GB-1	PUMP	4.17	314
GB-1	PUMP	4.47	**294**
LD-C2	PREH	3.72	**328**
LD-C6	PREH	10.42	75
LD-C11	PREH	4.36	**282**
LD-C14	PREH	5.67	214
SD-C6	PREH	2.4	475
DM-1	PREH	7.1	162

From these calculated temperatures, it is seen that a range exists for both minerals. By comparison with the expected temperatures of formation derived, from PTX considerations (section 5.1), it is possible to eliminate some of the values and to select the more "sensible" ones (underlined).

PTX considerations suggest that the prehnite assemblage present should have formed at around 300 °C, with the pumpellyite assemblage forming at slightly lower temperatures, in the region of 200 °C. From the calculated temperatures (and removing those that provide very different temperatures than those expected), the following range of temperatures for the formation of prehnite and pumpellyite is derived.

Prehnite-calcite-albite = **305** °C ± 25 °C ,

Pumpellyite-calcite-quartz = **280** °C ± 30 °C .

These temperatures are not rigorous, and are only an indication. Besides disequilibrium

assemblages (as is certainly the case for the exceptionally high and low Δ value samples LD-C6, SD-C6 and DM-1), one of the problems is the β factor calculation. Fig. 5.12 illustrated how β influenced the temperature at which a certain fractionation will occur. As average values of β have been used (due to the samples containing a mixture of high and low mol% pistacite crystals), inaccuracies will exist in the temperature calculations. Fig. 5.12 indicates that in the region of fractionation interest (Δ = 3.5-5.5), and the average range of β values found (2.0 to 2.5 mol. % pistacite), an inaccuracy of 0.1 mol.% pistacite will change the calculated temperature by as much as ± 50 °C. This could account for sample LD-C14 being only slightly lower than expected, and the pumpellyite samples being slightly higher than expected in comparison to PTX considerations.

5.5.2 Fluid inclusion homogenization temperatures

Fluid inclusion homogenization temperatures for the K-feldspar-calcite, prehnite-calcite, and pumpellyite-calcite sealed crack sets were measured following the procedure outlined in Appendix 5. Freezing temperatures were also measured to estimate the salinity, and these will be discussed later (measured fluid inclusion data are also given in Appendix 5). The fluid inclusion homogenization data is presented in Fig 5.13. All the fluid inclusions analysed were two phase liquid-vapour inclusions. They ranged in size from ~ 100μm to 20μm in diameter. As best as possible, only primary inclusions were measured. Care was taken to avoid inclusions trails and long elongate inclusions. Both of these may be healed cracks and so would be of a younger age than the sealing mineral. All the fluid inclusions measured homogenized in the liquid phase.

The oldest of the sealed crack sets sampled, the K-feldspar-calcite suite, was found to possess a large range of homogenization temperatures (T_h) (some 153 °C between a minimum of 203 and a maximum of 356°C). The dataset gives a mean temperature of 279 °C, with one standard deviation (σ_{n-1}) of ± 35°C.

The prehnite-calcite assemblage is the next oldest in terms of stratigraphic sealed crack set relationships. Again T_h values provided a large range (99 °C) with a minimum of 182 and maximum of 281 °C. Mean temperature was 235 °C, and in this case one standard deviation (σ_{n-1}) is ± 24 °C.

The youngest of the sealed crack sets analysed was the pumpellyite-calcite suite. Here the data set is quite small and may not be statistically representative. However, the T_h data obtained are significantly lower than the other two sets, averaging at 195 °C. The suite has a homogenization range of 84 °C, with a minimum value of 155 °C and a maximum of 239 °C. One standard deviation (σ_{n-1}) is ± 27 °C.

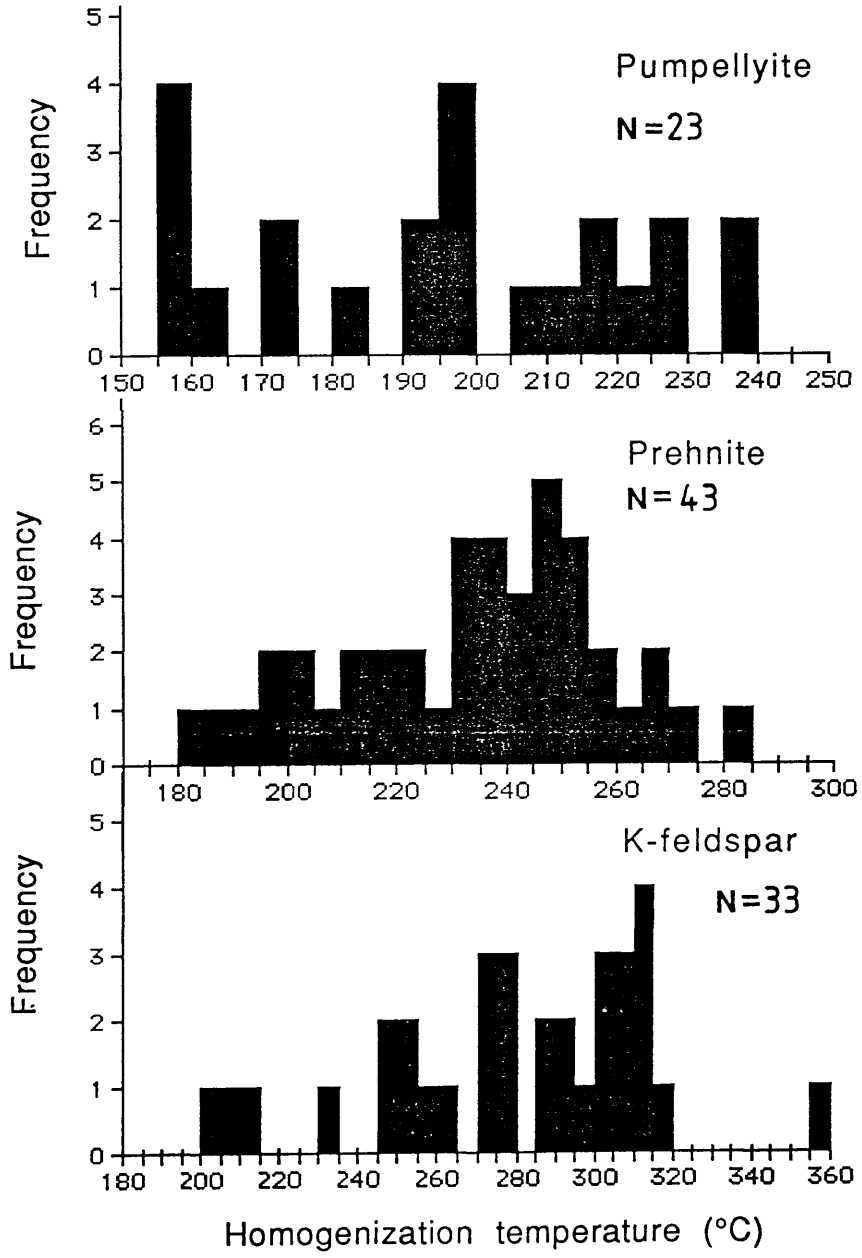

Figure 5.13 Fluid inclusion homogenization temperatures for K-feldspar, prehnite and pumpellyite sealed crack assemblages.

The fluid inclusions indicate that as the crack sealing sequence progressed through time the temperatures of formation decreased, indicating a cooling system. Although a large range exists for the homogenization temperatures (probably due to secondary inclusions within the dataset), the temperatures of formation of the three sets are:

K-feldspar-calcite	T_h = **279** °C ± 35 °C ;
Prehnite-calcite-albite	T_h = **235** °C ± 24 °C ; and
Pumpellyite-calcite-quartz	T_h = **195** °C ± 27 °C .

Errors are reported as one standard deviation or σ_{n-1}.

These temperatures have no pressure correction, as is required for fluid inclusions. This pressure correction depends on the conditions of formation and fluid salinity. These pressure corrections are only precisely appropriate if:

(a) the inclusion contains only pure NaCl;

(b) the salinity of the fluid is correctly known;

(c) the estimate of pressure is correct; and

(d) the inclusion homogenized in the vapour state.

The fluid inclusion homogenization temperatures for the prehnite and for the pumpellyite sealed cracks are lower than the estimated mineral pair isotope formation temperatures (Fig. 5.14). The differences between mean temperatures are 85 °C for pumpellyite, and 70 °C for prehnite. If the range of isotope derived temperatures, are correct, then the need for a temperature correction of 85 °C and 70 °C (with ± a combined uncertainty of 57 °C and 49 °C respectively) is suggested.

5.5.3 Inclusion temperature correction and pressure of formation

The relationship between T_h and the salinity of a fluid inclusion (in wt% NaCl equivalent) has been calibrated for pressure of formation, to allow the derivation of the temperature correction required for that inclusion (Potter 1977). It follows that if the temperature of homogenization, the true temperature of formation, and the salinity of the inclusion are all known, the pressure of formation can be calculated (within the errors of the other three factors).

Salinity of the fluid inclusions has been measured using the technique outlined in Appendix 5, and gives average values of about 10 wt% NaCl equivalent. This is accurate enough for this technique as calibrated graphs only exist for 5 wt% intervals, and there is not a great deal of difference over ± 5 wt% equivalent.

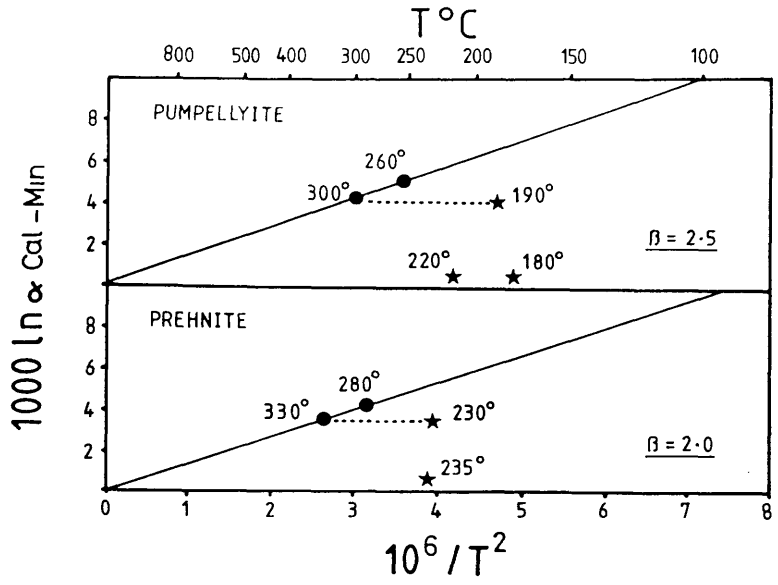

Figure 5.14 Comparison between calculated oxygen isotope, and measured fluid inclusion, temperatures of crack sealing for the prehnite and pumpellyite assemblages. ● = oxygen isotope temperature, ★ = fluid inclusion homogenization temperature. Tied points indicate the same sample.

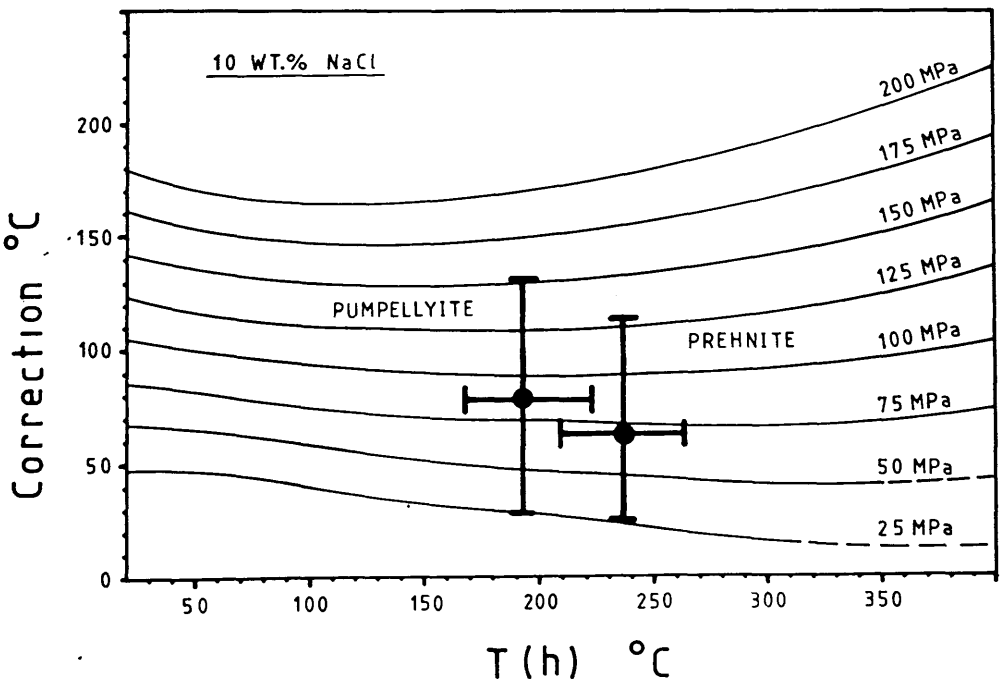

Figure 5.15 Estimated pressures at which prehnite and pumpellyite crack sealing took place. Derived from the differences between oxygen isotope, and fluid inclusion homogenization, temperatures. Plotted on the 10 wt% NaCl equivalent graph from Potter (1977). Errors represent the uncertainty in pressure, calculated from the combined uncertainty in temperature estimates.

For a salinity of 10 wt% NaCl equivalent (assuming formation temperatures within the ranges given in section 5.5.1, and corrections in accordance to the differences between inclusion and isotope temperature ranges), the pressure at formation for the sealed fracture sets are:

Prehnite+calcite+albite	= **70 MPa** ± 50 MPa ; and
Pumpellyite+calcite +quartz	= **90 MPa** ± 65 Mpa .

This relationship is illustrated in Fig. 5.15. The error bars are maximum and minimum possible cases and were calculated as a combined error of the Isotope temperature uncertainty plus the Inclusion T_h uncertainty (as given in sections 5.5.2).

Although this pressure is hydrostatic pressure, as opposed to lithostatic, the components producing the pressure will provide an indication as to the depth at which the inclusions formed. Roedder & Bodnar (1980) summarized the range of possible pressure conditions acting upon an inclusion. They are essentially one of two cases. Either:

(a) pressure is truly hydrostatic, where it represents the weight of the free standing column of water in the open fissure at the depth of inclusion formation; or

(b) the pressure can be a variable sum of hydrostatic components and lithostatic components, where the fracture is not open to the surface.

The Lewisian sealed cracks are so small that it would be nearly impossible for them to have been open to the surface, so a component of lithostatic pressure is suggested. However, they opened as tension cracks, and the pressure in the cracks must have been less than lithostatic pressure. Pressures of 70 and 90 MPa are equal to 0.7 and 0.9Kb respectively, and as a consequence in a system of only lithostatic pressure these would represent crustal depths of about 2.1 to 2.8 km. As the system in operation must have been less than lithostatic pressure, these depths can be considered as minimum values (with prehnite forming earlier and possibly at shallower depth than pumpellyite).The possible errors on the depths , estimated from the possible errors in pressure calculation, are ± 1.5 and 1.9 km respectively

Considering the geology of the region and the likely location of the fractures being sealed, these appear to be reasonable estimates. The Torridonian sequence is some 7km thick from the lowermost to uppermost parts of the sequence. However, much of the Stoer Group was removed in the gap of some 200 Ma prior to the deposition of the Upper Torridonian, and the sequence is nowhere complete. As a consequence, the depth and thickness of the Stoer Group, and the depth of Lewisian complex at the time of fracture

sealing is not known. It seems likely it would have been near these limits, perhaps about 3 km.

5.6 Isotopic and fluid inclusion constraints on the fluids

5.6.1 $\delta^{18}O$ and δD

For oxygen and hydrogen, the experimentally derived mineral-water fractionation curves (section 5.3.2) allow the calculation of the $\delta^{18}O$ and δD compositions of the fluid originally in equilibrium with the mineral when it formed. The assumption can only be correct where the mineral actually was in equilibrium with the fluid, and where the mineral has remained a closed system to oxygen and hydrogen since its formation.

Knowing the temperature and the isotopic composition of the mineral, it is a straight forward step to calculate the composition of the original fluid. The calculated $\delta^{18}O$ and δD compositions for both the prehnite and pumpellyite from the sealed cracks are shown in Fig 5.16. The error bars represent the possible range in fluid compositions, due to the uncertainty in the temperature estimates of the minerals formation. The temperature ranges of 305 °C ± 25 °C for prehnite, and 280 °C ± 30 °C for pumpellyite, were used in the calculation of these values.

From Fig 5.16, it can be seen that the values for prehnite and pumpellyite lie in a field between values found for surface waters and those found for metamorphic waters. The high δD and low $\delta^{18}O$ values strongly suggest that the fluids precipitating the prehnite and pumpellyite were surface derived. It is common for hydrothermal fluids to possess δD - $\delta^{18}O$ trends of this nature. Progressing from isotopically light oxygen values, to isotopically heavier values, as interaction between surface derived fluids and the rocks take place. Interaction is known to have taken place, evidence of fluid wall rock interaction has been seen in the sealed microcracks and reported in Chapter 4.

The calculated $\delta^{18}O_{H_2O}$ value of the fluids, in equilibrium with the prehnite and pumpellyite at the considered temperatures, range from -0.3 ‰ to +6.0 ‰ relative to SMOW (one value of +12.3 ‰ is recorded). Likewise, the range of δD_{H_2O} for the same minerals is between 5.4 ‰ to -30.3 ‰ relative to SMOW. The complete list of values is given in Table 5.3.

These calculations give a large range in δD_{H_2O} for the fluid. Prehnite is, on the whole formed from an isotopically lighter δD fluid (-14 to -28 ‰ relative to SMOW) than the pumpellyite (+5 to -15 ‰ relative to SMOW). Two pumpellyite analysis provide δD_{H_2O} values within the prehnite field (GB-1 and M-C40). The older prehnite minerals (and

two pumpellyites) were therefore in equilibrium with an isotopically lighter δD fluid than the other younger pumpellyites. This indicates that the fluid may have changed from isotopically light to isotopically heavy δD with time. This is a common occurrence in natural waters where the δD composition of the fluid progresses from -ve to +ve. Such a sequence can be explained by three processes: a lowering of latitude; a lowering of elevation; and evaporation of fluid from a restricted basin (Faure 1977). Two conditions may apply to the Torridonian to explain the δD shift with time. The Torridonian was deposited in a rift system and the elevation was likely to decrease as time progressed, and the rift deepened. There also records of ephemeral lakes within the Torridonian suggesting, like the East African rift system, the basin was restricted.

Table 5.3 Calculated $\delta^{18}O$ and δD compositions for the fluid in equilibrium with prehnite and pumpellyite.

Sample #	Mineral	Temp (°C)	$\delta^{18}O_{(H_2O)}$	$\delta D_{(H_2O)}$
TUA-5	PUMP	280±30	**6.0**±0.9	**-3.2** ± 2.5
TUA-7	PUMP	280±30	**3.7** ±0.9	**5.4** ± 2.5
LC-C8	PUMP	280±30	**0.8** ±0.9	**-1.3** ± 2.5
LC-C9	PUMP	280±30	**0.6** ±0.9	**-5.3** ± 2.5
LC-C10	PUMP	280±30	**1.2** ±0.9	**-6.7** ± 2.5
LC-18	PUMP	280±30	**12.3** ±0.9	**-4.5** ± 2.5
RC-1	PUMP	280±30	**4.6** ±0.9	**-15.5** ± 2.5
R-C3	PUMP	280±30	**3.4** ±0.9	**-11.9** ± 2.5
GB-1	PUMP	280±30	**3.4** ±0.9	**-30.3** ± 2.5
LD-C5	PUMP	280±30	**1.4** ±0.9	**-13.9** ± 2.5
M-C40	PUMP	280±30	**2.5** ±0.9	**-26.6** ± 2.5
LD-C2	PREH	305±25	**2.4** ±0.6	**-28.0** ± 2.0
LD-C6	PREH	305±25	**-0.2** ±0.6	**-23.9** ± 2.0
LD-C11	PREH	305±25	**5.7** ±0.6	**-26.3** ± 2.0
LD-C14	PREH	305±25	**1.5** ±0.6	**-29.0** ± 2.0
SD-C6	PREH	305±25	**5.6** ±0.6	**-14.0** ± 2.0
DM-1	PREH	305±25	**-0.3** ±0.6	**-19.2** ± 2.0
M-C34	PREH	305±25	**4.3** ±0.6	**-18.1** ± 2.0

(‰ relative to SMOW)

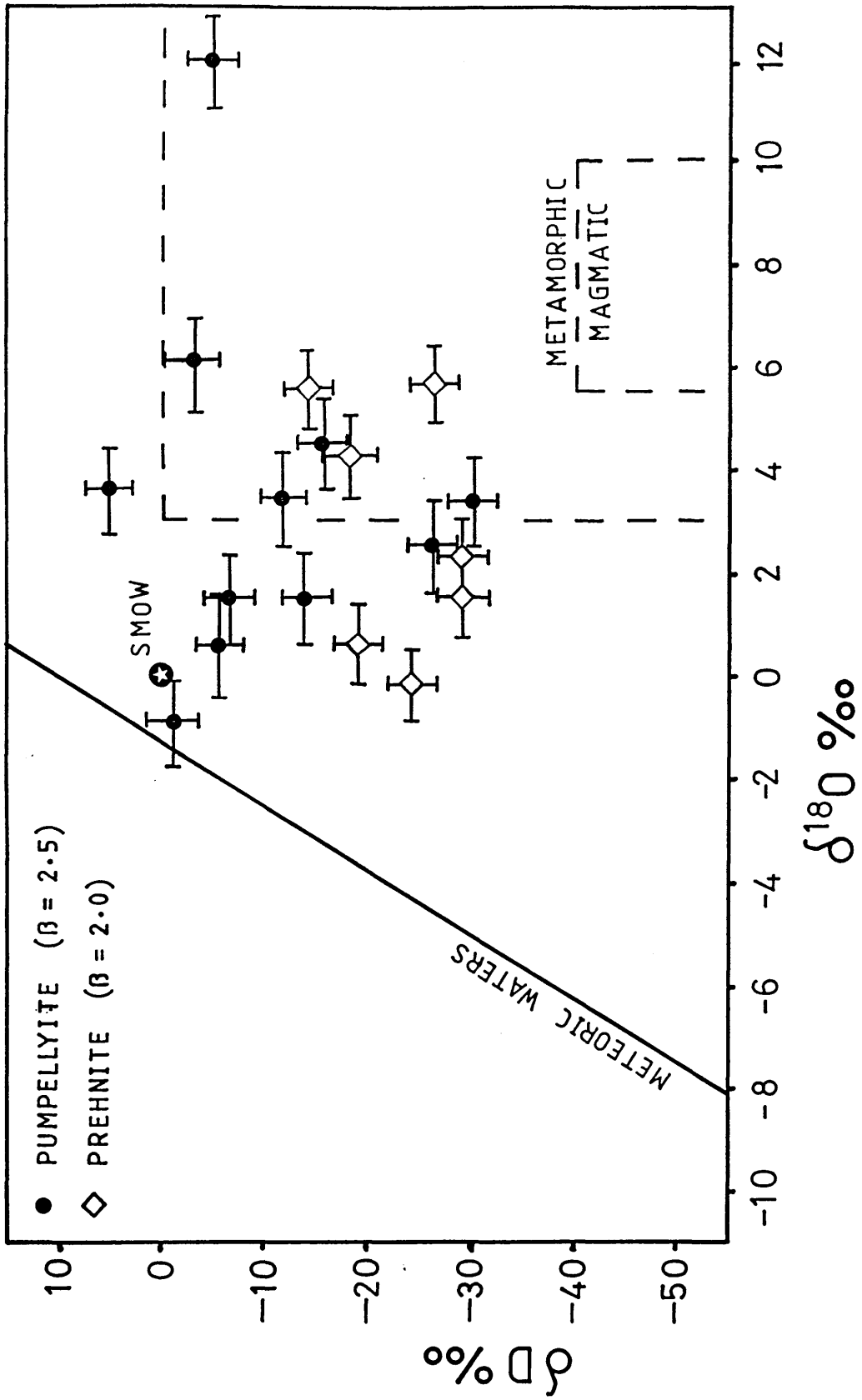

Figure 5.16 $\delta^{18}0$ (SMOW) and δD (SMOW) fields for the fluid in equilibrium with crack sealing prehnite and pumpellyite. Derived using the mineral-water fractionation curves reported in the text. Errors represent the uncertainty in fluid composition, calculated from the uncertainty in the temperature of formation.

5.6.2 $\delta^{13}C$ and $\delta^{34}S$

Whether CO_2 retains its $\delta^{13}C$ signature during the processes involved in the formation of mineral deposits, depends on the rate of isotopic exchange between the fluid and the forming solid. If the rate is slow, they may retain the original value, that is

$$\delta^{13}C_{(i)\Sigma CO_2} = \delta^{13}C_{(f)\Sigma CO_2} ,$$

where (i) and (f) indicate initial and final values, and Σ implies sum (Ohmoto 1986). It is possible that the $\delta^{13}C$ value of ΣCO_2 may be diagnostic of its source. The $\delta^{13}C$ value of ΣCO_2 can be calculated using:

(a) the fractionation factors between the mineral and $H_2CO_3^*$, (where $H_2CO_3^*$ is H_2CO_3 and $CO_{2aq.}$) or HCO_3^{-*} ; and

(2) the relative abundance of $H_2CO_3^*$ and HCO_3^{-*} in the fluid.

To determine carbonate speciation, pH and temperature must be known. However in geological fluids above 100 °C the amount of HCO_3^- is negligible in comparison to the amount of $H_2CO_3^*$ (Ohmoto 1986). And the approximation can be made that:

$$\delta^{13}C_{\Sigma CO_2} = \delta^{13}C_{calcite} - \Delta_{calcite - H_2CO_3^*} .$$

The fractionation factors of Deines *et al.* (1974) (given in section 5.4.1) can be used to derive the above fractionation equation. Thereby relating $\delta^{13}C$ of solid calcite to $\delta^{13}C$ of aqueous bicarbonate at a specific temperature.

Applying this fractionation over the ranges of temperatures thought to be correct, the values for $\delta^{13}C_{\Sigma CO_2}$ of the fluid in equilibrium, with the calcite from prehnite and pumpellyite bearing fractures, is given in Table 5.4.

Table 5.4 $\delta^{13}C_{\Sigma CO_2}$ values of the fluid, in equilibrium with the calcite, from prehnite and pumpellyite bearing fractures.

SAMPLE #	$\delta^{13}C_{(calcite)}$	Temp (°C)	$\delta^{13}C_{\Sigma CO_2}$
DM-1	-12.09	305±25	-11.13 ± 0.30
LD-C2	-5.05	305±25	-4.09 ± 0.30
LD-C6	-5.81	305±25	-4.85 ± 0.30
LD-C11	-4.66	305±25	-3.70 ± 0.30
LD-C14	-4. 54	305±25	-3.58 ± 0.30
LD-C14	-4.66	305±25	-3.70 ± 0.30
LD-C15	-4.86	305±25	-3.72 ± 0.30
SD-C6	-5.47	305±25	-4.78 ± 0.30
GB-I	-1.13	280±30	-0.51 ± 0.42
GB-1	-1.19	280±30	-0.57 ± 0.42
LC-C8	-6.75	280±30	-6.13 ± 0.42

The fractionation of ^{13}C between calcite and the fluid at the temperatures of interest is small, usually about 1‰. It can be seen that the separate groups identified in Fig. 5.10 are representative of fluids with separate $\delta^{13}C$ values. This suggests there have been two distinct fluids permeating through the cracks. One with a $\delta^{13}C$ value of about 0 ‰ (relative to PDB), and the other with a value of between -6 and -3‰ (relative to PDB). The samples preserving a record of the isotopically heavy $\delta^{13}C$ fluid occur at the Lewisian - Torridonian Stoer Group unconformity. The lighter $\delta^{13}C$ fluids are found in basement samples. This suggests a distinctly different fluid chemistry above and below the unconformity surface. The upper fluid possessing surface values, perhaps similar to Torridonian diagenetic cements or surface waters, and the lower fluid possessing more negative values due to prolonged wall-rock interaction with metamorphic carbonates from the Lewisian gneiss (which would be expected to be more negative).

The $\delta^{34}S$ composition of a single separate of barite cutting a pumpellyite-calcite-quartz sealed crack (M-C40) has been determined. Sulphur in barite exhibits temperature independent fractionation with SO_4^{2-} (Section 5.3). It follows that the preserved $\delta^{34}S$ composition of the barite will be the same as the $\delta^{34}S$ composition of the fluid with which it was in equilibrium. As mentioned in Chapters 2 and 4, the $\delta^{34}S$ composition of Cambrian sea waters was in the region of +30 to +34 ‰ relative to CDT. This is a very distinctive value, the highest value for sea water to have occurred. Authigenic anhydrite from the Cambrian succession in the northwest highlands have

already yielded $\delta^{34}S$ values of +31‰ (Allison & Russell 1985), and such values from the sealed cracks would indicate a Cambrian sea water component within the fluids.

However, the $\delta^{34}S$ value for the barite from the sealed crack was +8.3 ‰ relative to CDT. The implication of this is that the postulated Cambrian influence, as suggested in Chapter 4 and by Hay *et al.* (1988), cannot be substantiated.

5.7 Radiometric isotopes

5.7.1 Rb-Sr determinations

A set of six samples, consisting of four pumpellyites and two prehnites, were analysed for their Rb-Sr concentrations by isotope dilution analysis. Their Rb-Sr isotopic composition was measured by mass spectrometry at SURRC. The theory behind isotope dilution analysis, and a full account of the experimental and analytical procedure involved, is given in Appendix 6. The measured concentrations of Rb and Sr, as well as the values for the isotopic ratios of $^{87}Rb/^{86}Sr$ and $^{87}Sr/^{86}Sr$, present within the samples are also reported in Appendix 6.

A feature of the samples is their very low levels of Rb. This is not surprising, as there is no element within prehnite or pumpellyite that would allow Rb to be held in the lattice. Sr, on the other hand, exists in reasonable levels because it can be preserved in the lattice instead of calcium.

The very low levels of ^{87}Rb have resulted in very little shift in the value of the $^{87}Sr/^{86}Sr$ ratio with time. This can be seen in Table 5.5, where the present $^{87}Sr/^{86}Sr$ ratio ($^{87}Sr/^{86}Sr_{(t)}$) has been back calculated to a model age of 1000 Ma ($^{87}Sr/^{86}Sr_{(o)}$). This is probably slightly older than that inferred by the geological relationships.

Table 5.5 $^{87}Sr/^{86}Sr$ ratios for prehnites and pumpellyites at present and at 1000ma. (Calculated with $\lambda = 1.42 \times 10^{-11}\ Y^{-1}$).

SAMPLE #	MINERAL	$^{87}Sr/^{86}Sr_{(t)}$	$^{87}Sr/^{86}Sr_{(o)}$
TUA-5	PUMPELLYITE	0.7060596	0.7060578
M-C34	PUMPELLYITE	0.7030475	0.7030287
RC-1	PUMPELLYITE	0.7069726	0.7069718
LC-C10	PUMPELLYITE	0.7069450	0.7068986
DM-1	PREHNITE	0.7066850	0.7033322
LD-C11	PREHNITE	0.7059140	0.7052879

The errors involved in the calculation of the ratios (listed in Appendix 6) were of the order of 10^{-5} for $^{87}Sr/^{86}Sr$. That is, affecting the last three figures listed above. For all samples of pumpellyite and prehnite, and within the errors, the $^{87}Sr/^{86}Sr$ is effectively the initial ratio at the time of formation. As a result, it proved impossible to fit an isochron age to the data.

There are likely to be two factors influencing the $^{87}Sr/^{86}Sr_{(o)}$ ratios within the prehnite and pumpellyite from the sealed cracks, they will be:

(a) the $^{87}Sr/^{86}Sr$ ratio of the fluid in equilibrium with the minerals at the time of formation; and

(b) the $^{87}Sr/^{86}Sr$ ratio of the host rock at the time of mineral formation.

If the fluid had a marine origin, the $^{87}Sr/^{86}Sr$ ratios of the fluid should dominate the system, because the concentrations of strontium are likely to be higher in the fluid than rock. But, if it was meteoric, the Sr content may have been highly variable. Interaction between the wall rock and the sealing minerals of the cracks is known to have occurred , and there may be a component of $^{87}Sr/^{86}Sr$ from the host lithology.

The $^{87}Sr/^{86}Sr$ ratios of seawater throughout time, from the Cambrian to the present day, are fairly well constrained (Burke *et al.* 1982), the Precambrian is not so well constrained. Veizer (1976) estimated that the $^{87}Sr/^{86}Sr$ ratios between 1000 ma and 800 ma would vary from 0.707 to 0.708 (with ratios of 0.705 to 0.707 between 1500 ma and 1000 ma). Moorbath (1969) estimated that seawater, over the period of Torridonian deposition (1000 ma - 800 ma), would have an $^{87}Sr/^{86}Sr$ ratio of about 0.705 to 0.706.

There is much published data concerning the Rb-Sr ratios and ages of the northwest Highland lithologies. Rb-Sr data exist on most lithologies from the Lewisian complex as well as from the Torridonian. Using the data found in the literature, it is possible to calculate and plot the evolution of the $^{87}Sr/^{86}Sr$ ratios, found within the different lithologies, with time to establish if any of the lithologies had $^{87}Sr/^{86}Sr$ ratios similar to the vein minerals. Fig. 5.17 shows the calculated evolution of the Lewisian and Torridonian lithologies, and the projected evolution of the $^{87}Sr/^{86}Sr$ ratio for seawater, with time. Also shown are the $^{87}Sr/^{86}Sr$ ratios of the prehnite and pumpellyite, which correspond to their $^{87}Sr/^{86}Sr$ initial ratios.

From Fig. 5.17, it can be seen that most Lewisian lithologies had too high $^{87}Sr/^{86}Sr$ ratios to be responsible for the $^{87}Sr/^{86}Sr$ ratios in the prehnite and pumpellyite within the time constraints produced by the geology. Only the Scourie dykes and the Torridonian Stoer Group have $^{87}Sr/^{86}Sr$ ratios approaching the correct values. From the study on the

microcracks, solution is seen to be common, and it is possible that a low $^{87}Sr/^{86}Sr$ fluid permeating down through the Stoer Group above could inherit the required signature. On the other hand, the estimated $^{87}Sr/^{86}Sr$ compositions of Precambrian seawater for such times encompass the range of $^{87}Sr/^{86}Sr$ ratios found in the crack sealing minerals. From the fluid inclusion studies, salinity was within the region of 10 wt % NaCl equivalent. This is a low value for geothermal brines which can be up to 25 wt % NaCl equivalent, but within the upper limits of epithermal ore fluids which are usually about 5 wt % (but can be up to 10 wt % NaCl equivalent) (Roedder 1985). The δD and $\delta^{18}O$ compositions for the fluid, expected to be in equilibrium with the prehnite and pumpellyite assemblages, suggested a surface derived meteoric fluid. Therefore, from the data presently available, it seems most likely that the $^{87}Sr/^{86}Sr$ ratios preserved in the prehnite and pumpellyite were inherited from a surface meteoric fluid which had undergone interaction with the Torridonian Stoer Group.

As far as ages of formation, the best estimates are still between those of Moorbath (1969), with precipitation of the prehnite and pumpellyite to seal the cracks occurring between about 1000 ma and 800 ma.

5.7.2 K-Ar determination

One K-Ar analysis of K-feldspar was carried out at SURRC, on sample NR-C4 from Rhiconich. The Ar concentration and isotopic ratio was carried out by isotope dilution and mass spectrometry. The K concentration was measured by flame photometry. The theory behind the K-Ar method of age dating is discussed in Appendix 7, where the analytical results are also given.

Using the K-Ar method it is possible to derive a date since blocking from a single analysis. The K-feldspar (from a K-feldspar-calcite sealed crack) was believed to belong to the earliest post-Laxfordian crack sealing set, and showed evidence of haematitic staining. This is believed to be derived from the Torridonian as was the case in the other cracks belonging to this set. Using the constants listed in Appendix 7, a single age of 345 ± 7 ma was calculated for this K-feldspar. This is a post-Caledonian Carboniferous age, and perhaps not too much should be read into this "one-off" analysis. However, if the sealed crack is Precambrian in its age of formation, then this may indicate the influence of a later event which has reset or disrupted the isotopic system. Considering the isolation of this analysis, to speculate would be unwise.

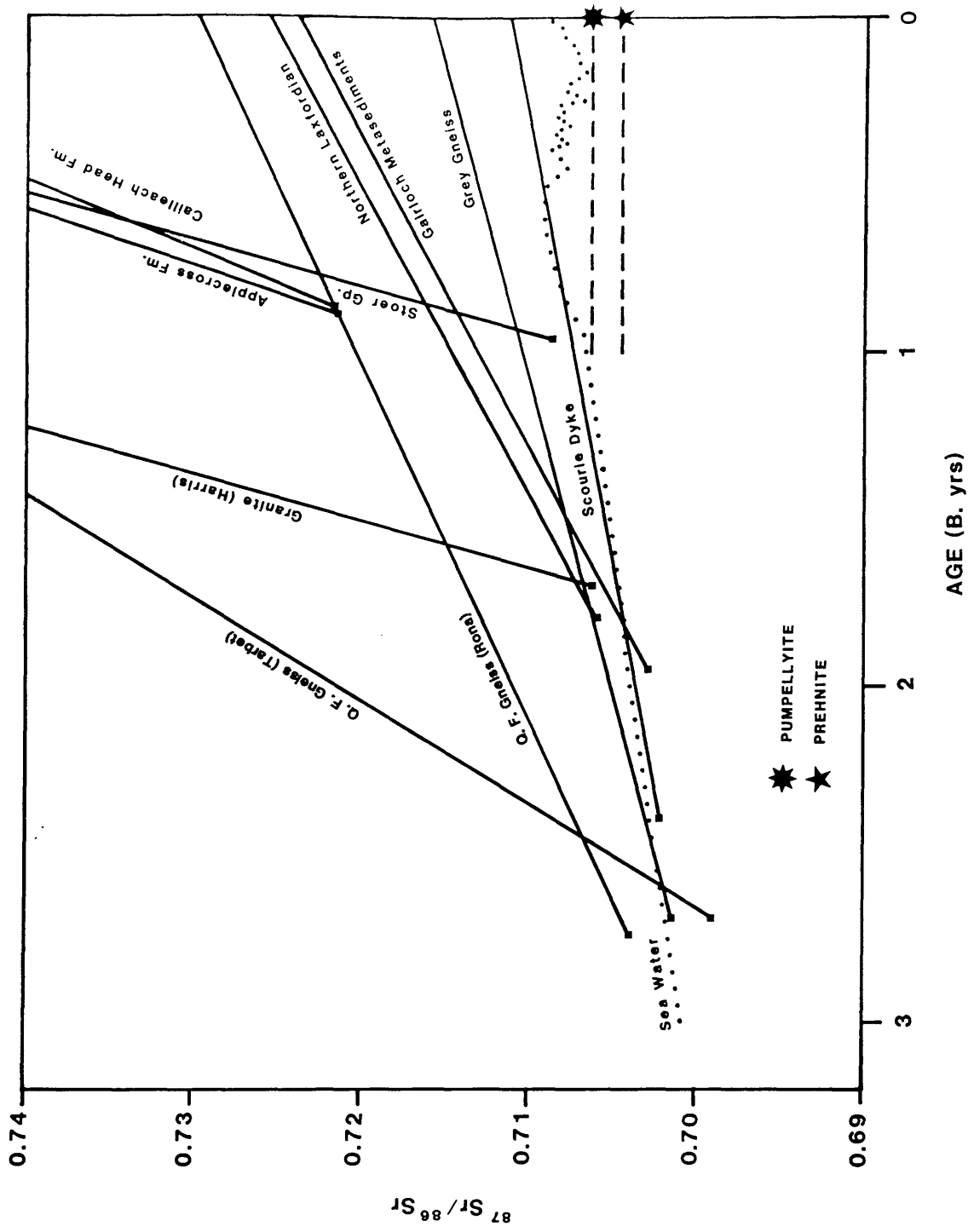

Figure 5.17 $^{87}Sr/^{86}Sr$ ratios of main lithologies, crack sealing prehnite and pumpellyite, and sea water through time. Calculated using $\lambda = 1.42 \times 10^{-11}$ Y^{-1}. Rb-Sr data for the lithologies were obtained from the following sources: quartzofeldspathic gneiss (Rona) and quartzofeldspathic gneiss (Tarbet) from Lyon (1973); grey gneiss from Moorbath *et al.* (1975); Scourie dyke from Chapman (1979); Gairloch metasediments from Bickerman *et al.* (1975); northern Laxfordian gneiss from Lambert & Holland (1972); Laxfordian granite (Harris) from van Breemen *et al.* (1971); Torridonian Stoer Group, Applecross Formation and Cailleach Head Formation from Moorbath (1969); and Sea water from Moorbath (1969), Veizer (1976) and Burke *et al.* (1982).

5.8 Summary

1. Mineralogical and isotopical analysis of the the sealed fractures, preserved within the Lewisian complex, have allowed the establishment of certain constraints upon the nature and development of a period of hydrothermal activity within the Lewisian basement. The fluids involved in the hydrothermal event are isotopically characterised by their δD, $\delta^{18}O$, $\delta^{13}C$, $\delta^{34}S$ and $^{87}Sr/^{86}Sr$ compositions. Within the constraints and limits of the methods employed, separate mineralogical assemblages sealing the microcracks and joints are believed to represent different PTX conditions within an evolving hydrothermal system.

2. Despite large oxygen isotope disequilibrium existing between coexisting minerals appearing to have formed at a similar time in the fractures, the PTX considerations, fluid inclusions and isotope palaeothermometry all suggest that the crack sealing assemblages represent a cooling sequence. The temperatures regressing from somewhere around 350°C, estimated for the earliest K-feldspar assemblage, to 330 - 280°C preserving a prehnite assemblage, with a cooler 300-250°C preserving a pumpellyite assemblage.

3. Broad estimates of the pressure at the time of fluid inclusion formation suggest that these cracks were sealed within the top 5 km of the crust, probably at depths between 2 and 3 km. These sealed cracks were not formed in the deep crust.

4. Possible reasons for the oxygen isotope disequilibrium may be that the cracks did not seal quickly, and the calcite was precipitated from an isotopically different fluid at a different temperature; or that the calcite may have partially re-equilibrated at a later time.

5. The calculated δD and $\delta^{18}O$ compositions of the fluids in equilibrium with prehnite and pumpellyite, suggest that the fluid was surface derived. A δD composition of -30 to -20 ‰ relative to SMOW is suggested for the earlier hotter prehnite assemblage (with some pumpellyite). This gives way to an isotopically heavier δD fluid of between -20 and 0 ‰ relative to SMOW, which was preserved in cracks sealed by a cooler pumpellyite assemblage. The $\delta^{18}O$ compositions indicate that the fluid varied between 0 and +6 ‰ relative to SMOW over its history. The variations in the δD and $\delta^{18}O$ composition of the fluid can be explained as a result of an evolving fluid, with

the $\delta^{18}O$ compositions becoming more +ve with time due to interaction between the fluid and the wall rock. The δD values, becoming more +ve with time, can be accounted for by a combination of reduction in elevation, and the development of a restricted rift basin, during the development of the Torridonian rift.

6. Two separate fluid compositions are also supported by the calculated $\delta^{13}C_{\Sigma CO_2}$ compositions of the fluid in equilibrium with the calcites. One, preserved primarily by the prehnite assemblage ranges from -6 to -3 ‰ relative to PDB, whereas the other, preserved by the K-feldspar and the pumpellyite assemblages have values of 0 ‰ relative to PDB. The reason for these two groups may be a function of location. The isotopically heavier calcites all come from samples associated with the Torridonian unconformity. The lighter samples are all from within the gneiss complex. It may be that the fluids inherit their $\delta^{13}C$ values from the $\delta^{13}C$ values present within the host rock through fluid wall-rock interaction. The Torridonian may be about 0 ‰, in equilibrium with surface fluid whereas the gneisses might be expected to have more negative $\delta^{13}C$ values, typical of metamorphic rocks.

7. $\delta^{34}S$ analysis of barite produced a value of +8.3 ‰, relative to CDT, for the fluid in equilibrium with the barite. This suggests there is little or no influence of the Cambrian seawater sulphate within the fluids operating in the hydrothermal system.

8. The $^{87}Sr/^{86}Sr$ initial ratios of between 0.703 and 0.706 for the prehnite and pumpellyites support this conclusion. The $^{87}Sr/^{86}Sr$ ratio in Cambrian seawater was about 0.708-0.709. The $^{87}Sr/^{86}Sr$ values found in the sealed crack minerals, suggest that the minerals inherited their $^{87}Sr/^{86}Sr$ ratio from a combination of Proterozoic meteoric waters interacting with the Torridonian Stoer group. Fluid inclusion salinities suggest this was likely to have been a mixed salt, brine which contained NaCl, $MgCl_2$ and $CaCl_2$ (with salinities of around 10 wt% NaCl equivalent). δD and $\delta^{18}O$ values of the fluids suggest a meteoric origin with the salinities, developing during the hydrothermal process, as a result of dissolution of elements from the wall rock into the fluid.

9. The Rb-Sr ratios of prehnite and pumpellyite were unable to provide isochron ages of the sealed cracks. The K-Ar dating provided an age of 345 ± 7 ma which does not fit with the geologically defined age expected for the sealed cracks. This may either be a cooling age, or may indicate that the isotopic system was disrupted at a later date.

CHAPTER 6

POROSITY AND PERMEABILITY OF THE LEWISIAN GNEISS: AT PRESENT AND IN THE PAST

6.1 Background to porosity - permeability work and the samples used

Previous descriptions of sealed fractures from the Lewisian complex have indicated that the sealed fractures, now preserved at the surface, are wider than open fractures found in surface exposures of Lewisian gneiss today (Hall 1986, 1987). Porosities and permeabilities, associated with such sealed fractures, are expected to have been larger than those presently accounted for by open fractures. Present day surface Lewisian gneiss has a porosity of usually less than 1%, and may average about 0.5% (Hall 1986). Corresponding present day permeabilities are as high as 30 $x10^{-18}$ m^2 (30 microdarcies), reducing to values of 10^{-21} m^2 (1 nannodarcy) at depths of 1 km. It was suggested that permeabilities associated with large sealed cracks, perhaps formed within the deep crust and now exposed at the surface, may have reached values as high as 1 darcy (10^{-12} m^2) (Hall 1986). It is believed such sealed fractures maybe associated with substantial groundwater flow (Costain *et al.* 1987).

Samples used for permeability and porosity measurement covered the main lithological divisions present within the Lewisian central and northern regions (Fig. 6.1). These samples were collected by Jeremy Hall.

6.2 Porosity and permeability measurements from core tests

6.2.1 Present day porosity

Porosity was measured by the vacuum saturation method, as outlined in Brown (1981). Measured cores were evacuated and then saturated under vacuum before being left under water and vacuum, for four days. Their wet and dry weights were measured using scales. Dry weight was calculated after four days evacuation at 105 °C in a vacuum oven. Samples were transferred to a dry sample jar and allowed to cool before weighing. Wet weights were measured for surface dry samples. Porosity (η) was calculated using the computer program PORE (see Appendix 10), and the equations:

$$B_{vol} = \left(\frac{\pi D}{4}\right) \times L \,, \qquad V_{vol} = W_{sat} - W_{dry} \,,$$

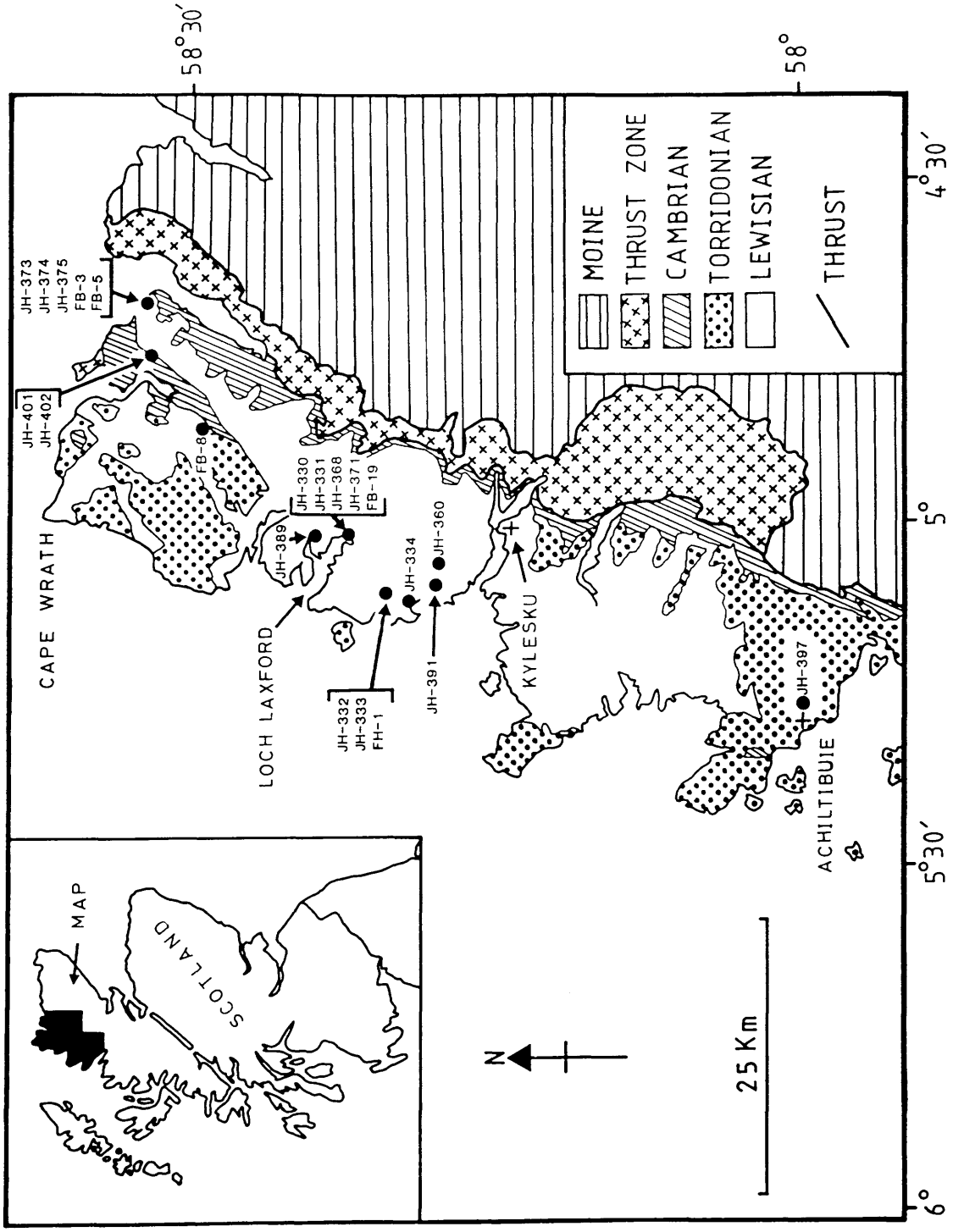

Figure 6.1 Location map for samples used in porosity and permeability core tests. Geology taken from 1:253,440 Geological Survey sheet # 5.
For list of samples, see Appendix 8.

and $$\eta = \left(\frac{V_{vol}}{B_{vol}} \right) \times 100 \quad .$$

Final readings (reported in Appendix 8) were the average values taken over four separate runs. Weights were measured to ±0.01g and core dimensions to ±0.02cm.

Fig. 6.2 shows a frequency histogram, of the average percentage porosity, for each sample within the suite of Lewisian rocks tested. It is seen that these rocks have low porosities typical of fresh crystalline rock (see Fig. 1.1). Lewisian values range from 0.2% to 1.6%, with a mean value of 0.8%.

When porosity is plotted against lithology, as illustrated in Fig. 6.3, apart from the sample of mafic granulite there is an overall decrease in the average porosity from the silica-rich granites to the basic, silica-poor Scourie dykes. A similar overall trend is apparent within the maximum and minimum values of porosity recorded for the lithologies. Large porosity ranges existing within some lithologies (up to1.5%) illustrate the presence of inhomogeneous pore space. Thus providing different cores with different values. The reason for this is due to some cores containing occasional larger intergranular cracks, with others containing only the smaller, but more abundant, intragranular and grain boundary cracks.

6.2.2 Present day permeability

Permeability was measured using a constant head permeameter, as described in Monicard (1980). The sample was housed in an ELE Hoek cell at the desired confining pressure. Pressured nitrogen was then passed through the core to be collected in a burette. The rate of gas passed (Q) can be related to permeability (K) by Darcy's Law, where

$$Q = \frac{A K}{\mu} \times \frac{\Delta P}{\Delta L} \quad . \qquad 6.1$$

Mass flow, (Q_m) in a porous tube, where the pressure difference is constant can be written

$$Q_m = Q\rho ,$$

where ρ is the gas density at a pressure P. Gas density is related to pressure by the equation

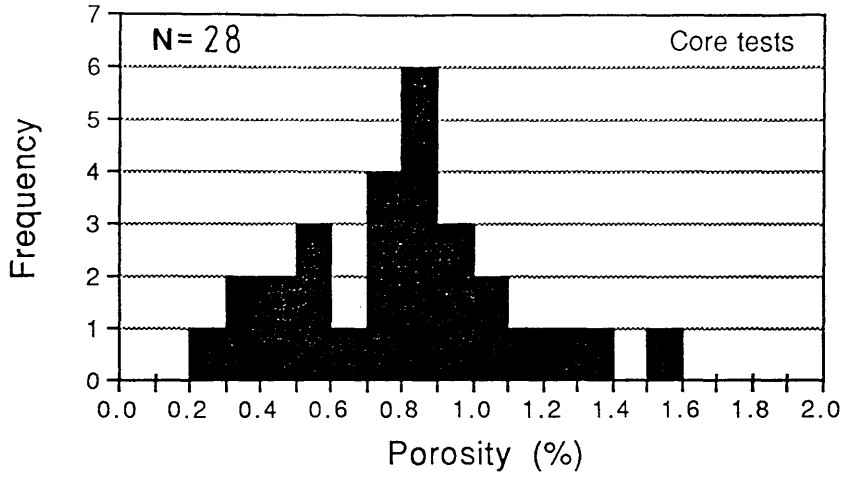

Figure 6.2 Porosity values obtained from core tests on Lewisian lithologies. Values used are the averages of four separate runs, and are given in Appendix 8.

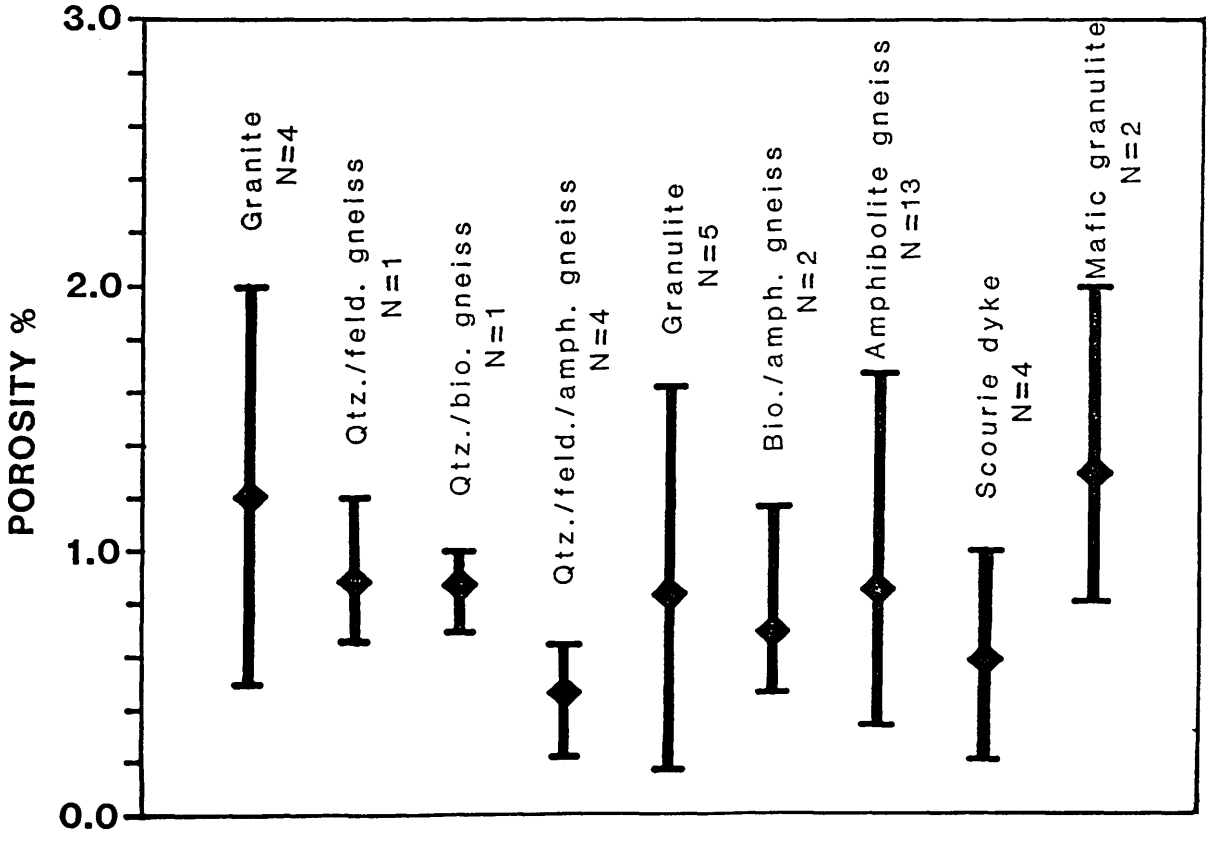

Figure 6.3 Range of porosities found in different Lewisian lithologies. Maximum, minimum and average values are shown.

$$\rho = B\,P \quad ,$$

where B is a constant [1]. Thus,

$$Q_m = Q \times B\,P \quad ,$$

which can be rewritten as

$$Q = \frac{1}{BP} \times Q_m \quad . \qquad 6.2$$

By combining equations 6.1 and 6.2,

$$(B\,P) \times \Delta P = \frac{\mu\, Q_m}{A\,K} \times \Delta L \quad .$$

This equation relates ΔP (pressure gradient) to ΔL (flow path gradient). After integrating for path length (L), the equation becomes

$$\frac{BP}{2} \times (Pa^2 - Px^2) = \frac{\mu\, Q_m}{A\,K} \times L \quad . \qquad 6.3$$

Measuring Q at pressure P, at the flow temperature, equation 6.2 holds. Combining equations 6.2 and 6.3 produces

---

[1] Klinkenberg related apparent permeability (K_a), measured for gas at an average pressure (P_m), to true permeability (K_t) by the equation

$$K_a = K_t \times \left(1 + \frac{B}{P_m}\right) \quad .$$

B depends on the average free movement (λ) of the gas at pressure P_m, and is defined as

$$B = \frac{4\,C' \times \lambda \times P_m}{r} \quad ,$$

where $C' = 1$, and r = channel width.

$$\frac{BP}{2} \times (Pa^2 - Px^2) = \frac{\mu Q BP}{A K} \times L .$$

This can be rewritten as

$$K = (\mu Q) \times \left(\frac{L}{A}\right) \times \left(\frac{2 Px}{Pa^2 - Px^2}\right) . \qquad 6.4$$

This is the equation used with the constant head permeameter.

Permeabilities of the Lewisian rocks were measured by two methods:

(a) permeability was measured at a constant confining pressure of 1 bar, while varying the gas pressure between 1 and 5 bars of excess pressure; and

(b) permeability was measured under a constant excess gas pressure of 5 bars, while varying the confining pressure between values ranging from 20 to 500 bars.

Samples were run in straight flow conditions only, with teflon or steel jacketed samples used for the variable gas pressure runs. Unjacketed samples were used for the variable confining pressure runs. The permeability response of the samples, to the changes in conditions, were monitored by the change in the rate of gas passed through the core. Permeabilities were calculated using the program PERM (see Appendix 10) with errors estimated from possible inaccuracies in the procedure. Conversion from nitrogen to effective water permeability was carried out using a multiplication factor for the differences in viscosity between the two fluids.

6.2.2.1 Permeability values for the Lewisian gneisses

Measured permeabilities for the Lewisian samples, at constant confining pressure and excess pressures of 1 to 5 bars, are illustrated in Fig.6.4. It can be seen that the permeabilities range over 5 orders of magnitude, from 1 nannodarcy (10^{-21} m^2) to 100 microdarcys (10^{-16} m^2). These are fairly typical values for core samples of fresh crystalline rock (Brace 1984). Fig. 6.4 also illustrates the variation in permeability between and within lithological types. Permeability between lithologies appears to be fairly similar, with mean and median values for all lithologies falling within a band between 100 nd to 10 µd. Those with the lowest recorded permeabilities (granulite, amphibolite gneiss and Scourie dyke dolerite) lie to the more basic end of the suite. Whereas, silica-rich rocks (granite, quartz-feldspar and quartz biotite gneisses) tend to

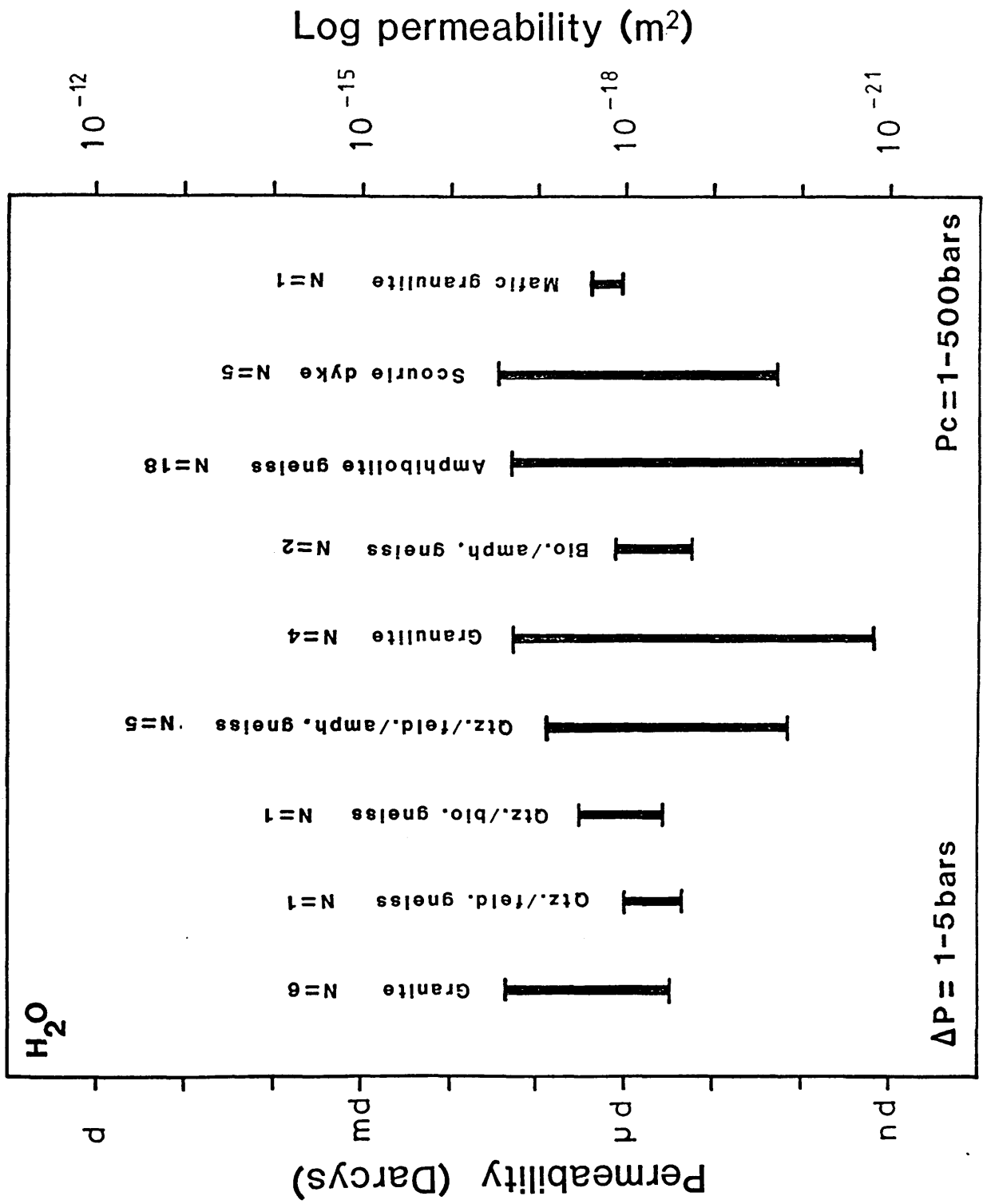

Figure 6.4 Range of permeabilities found in different lithologies. Maximum and minimum values over the conditions $\Delta P_{(H_2O)}$ = 1-5 bars and Pc = 1-500 bars. Values are given in Appendix 8.

have higher minimum permeabilities.

Large ranges within each lithology again may reflect the occurrence of occasional larger intergranular cracks within certain cores, in comparison to the ubiquitous smaller intragranular and grainboundary cracks present in every core. Values for the measured Lewisian permeabilities, and the errors involved, are given in Appendix 8.

6.2.2.2 Effects of increased head and confining pressures on permeability

Both Darcy's law, and the derived permeability equation used in this study, indicate that as the pressure head is increased, at a constant confining pressure, then permeability should drop. On analysis this is found to be the case. In Fig. 6.5, the permeability responses of the Lewisian rocks are shown, either plotted against the excess pressure head, or the confining pressure.

The response to an increase in pressure head can be illustrated by taking sample JH-330 as an example. From core to core and over the pressure conditions, the drop in permeability is found to be different, with size of this permeability drop dependent on the sample's permeability. However, within all the samples, the permeability drop is always between 10 - 20% of the order of magnitude within which the rock lies (i.e. from 300-100 μd or from 3 - 1 μd). The rate of permeability reduction decreases as pressure increases. This change in the rate of permeability decrease is due to the pressure component of equation 6.4 obeying an inverse power law, relative to permeability.

Upon an increase of confining pressure, relative to a constant pressure head, the permeability equation provided in Chapter 1.7.1 states that the permeability will decrease. Studies show this to be true, with permeability possessing an inverse cube law with regard to the natural log. of the effective pressure (Morrow *et al.* 1986, Bernabe 1987). In the Lewisian samples, all tests of this nature indicate that as the confining pressure is increased so the permeability decreases, by as much as an order of magnitude. This is also shown in Fig. 6.5. The graph for sample JH-368Y illustrates a half pressure cycle, where confining pressure is increased from 100 to 500 bars. As a result, permeability is seen to drop from 800 nd to 400 nd. The reason for this permeability drop is the compression of the sample and closure of the open cracks which allowed the fluid to permeate. The graph for sample JH-368Z illustrates a complete pressure cycle. Here, after the initial increase to 500 bars, the pressure has been relaxed back to 100 bars. On relaxation of the confining pressure the permeability does not fully recover to its original level. This indicates that a non-elastic deformation occurs to the rocks on compression.

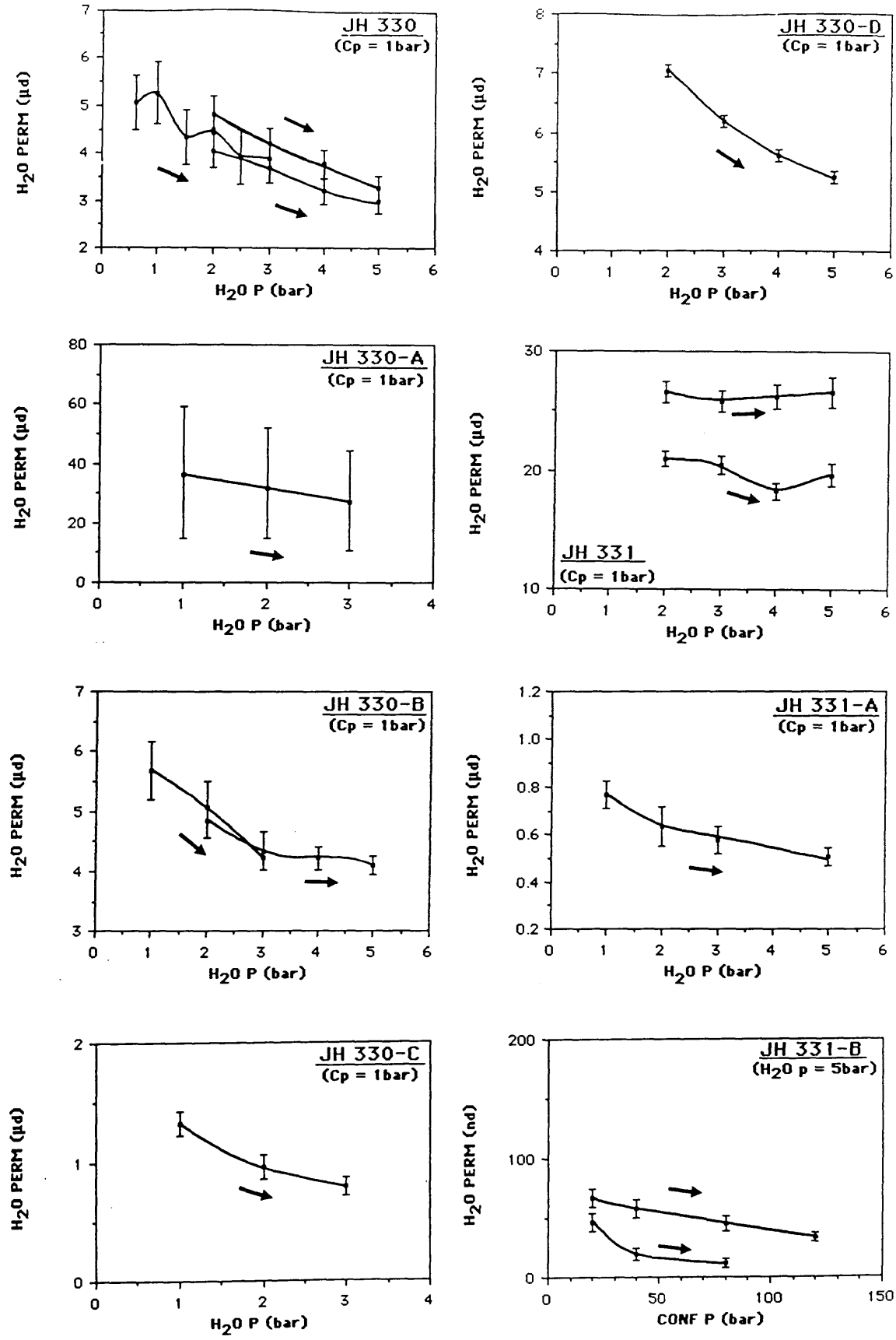

Figure 6.5 Response of permeability to increases in differential pressure head H_2O P, and confining pressure CONF P (or Cp). Values for the permeabilities and errors are given in Appendix 8. Measured with Nitrogen as the fluid and recalculated to water. A, B, C and D represent cores of the same sample. X, Y and Z represent cores of the same sample taken in the X, Y and Z tectonic fabric directions.

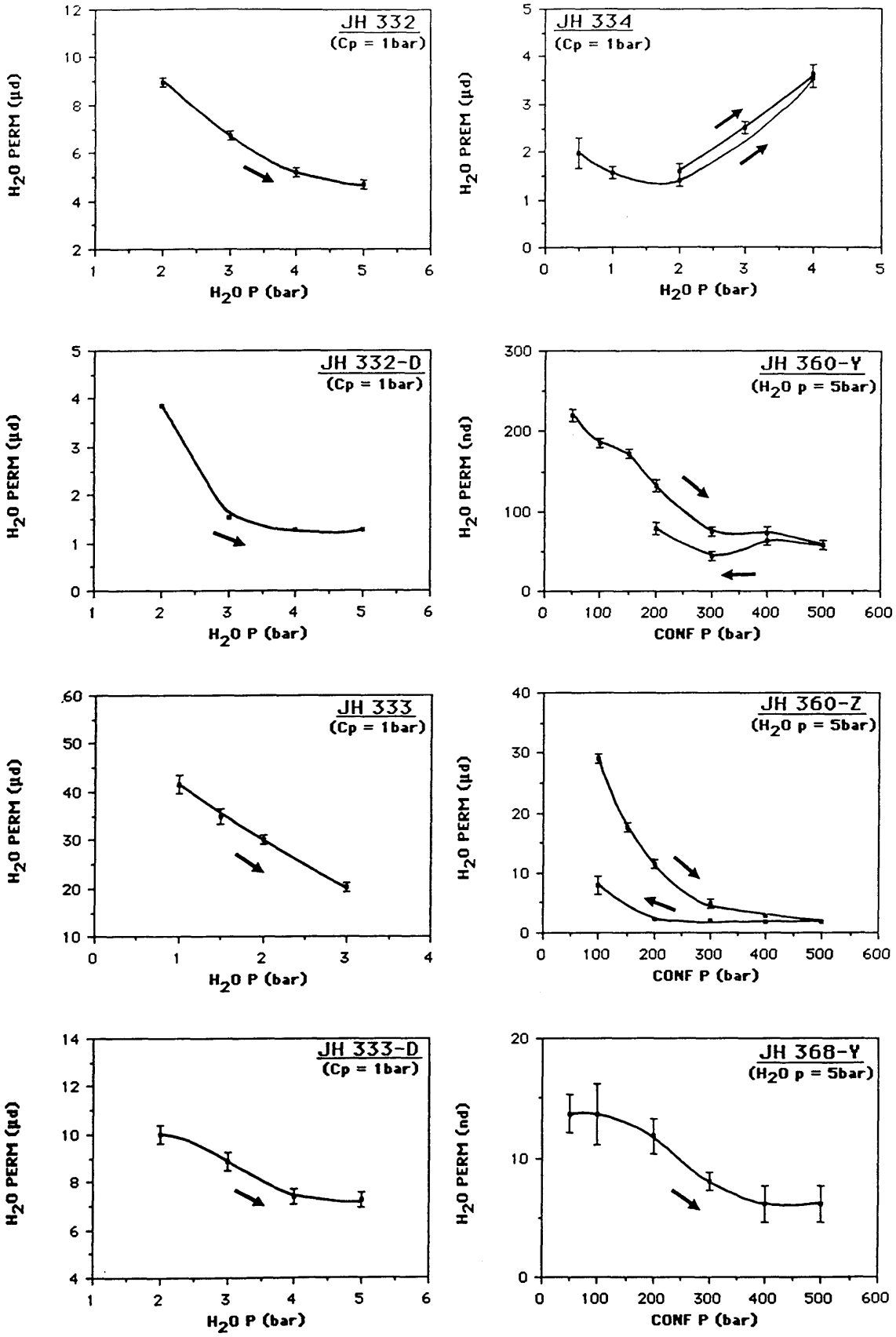

Figure 6.5 Continued.....

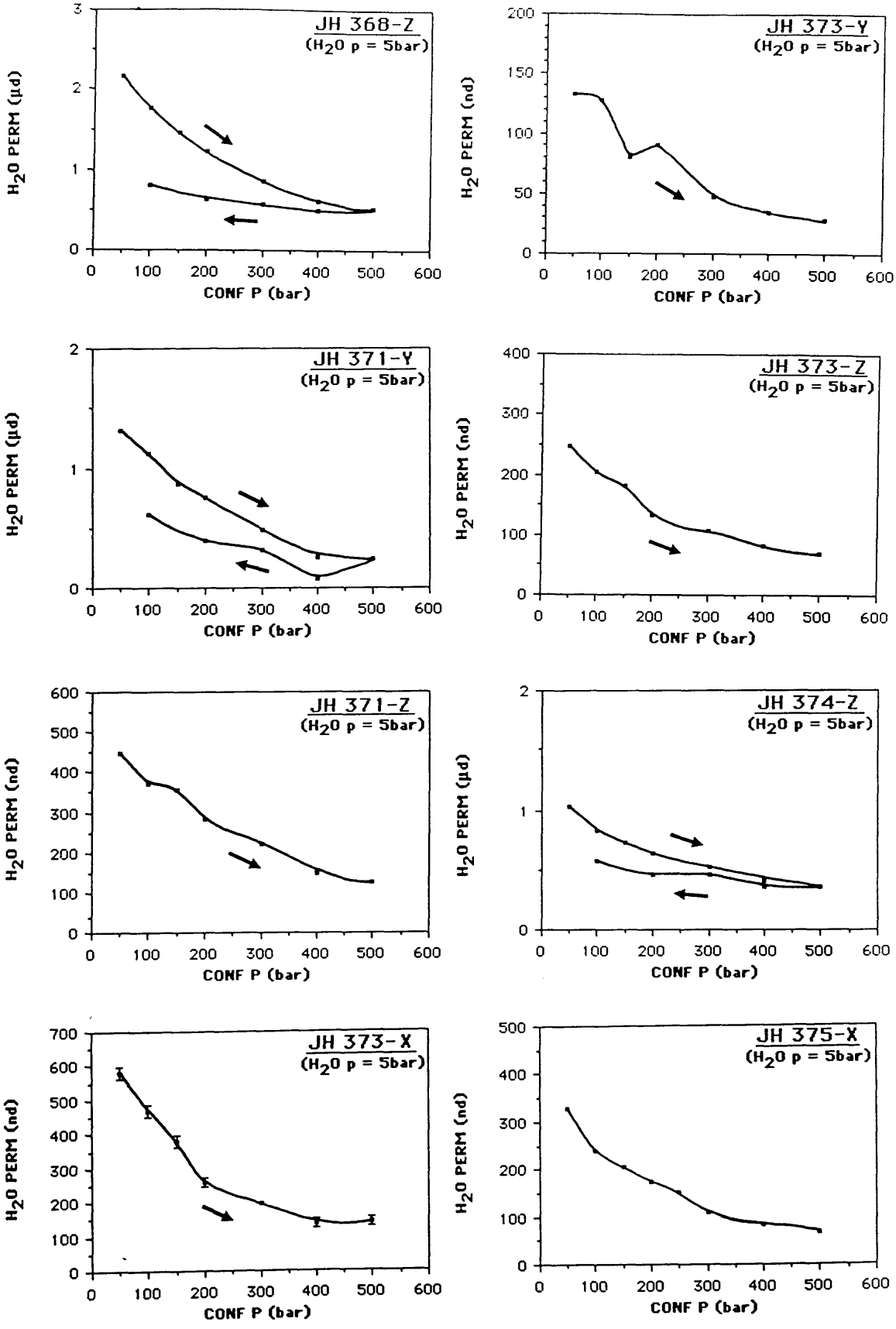

Figure 6.5 Continued.....

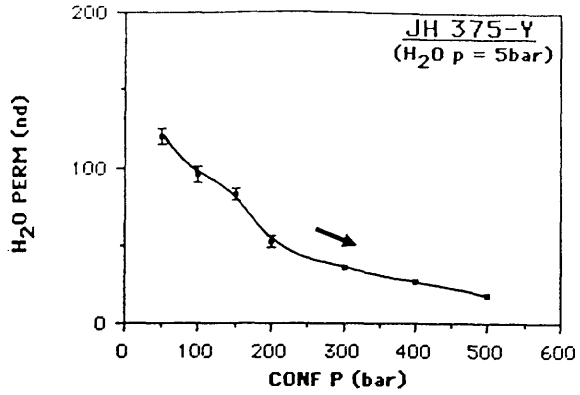

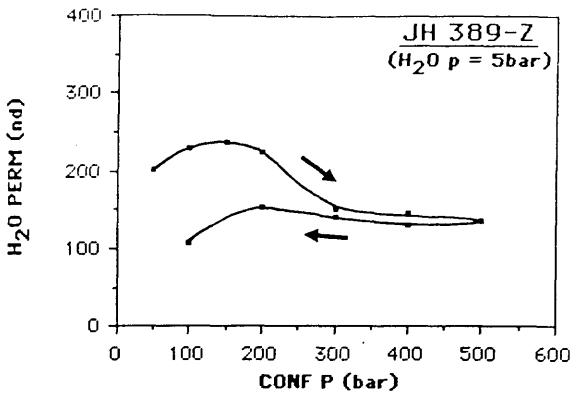

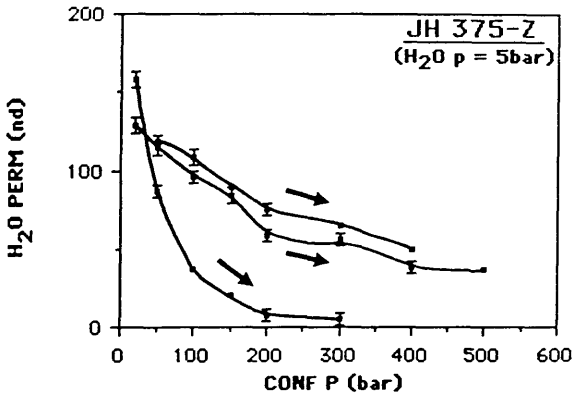

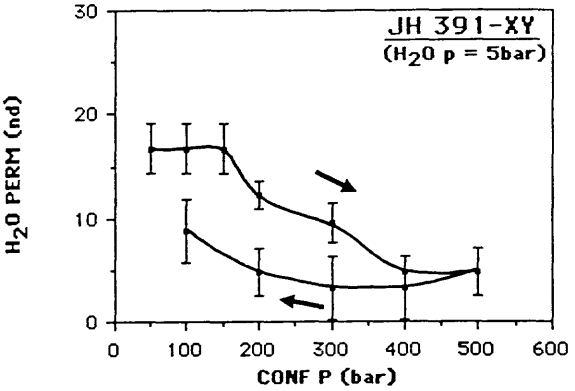

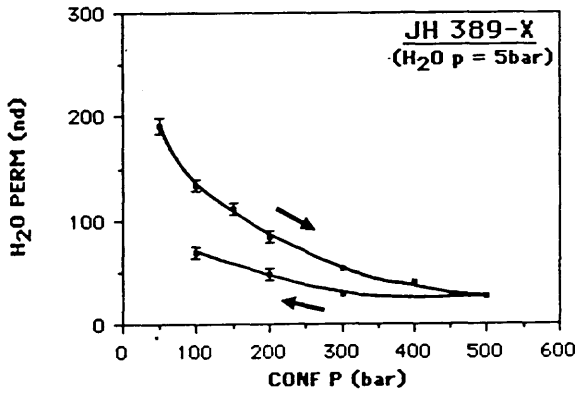

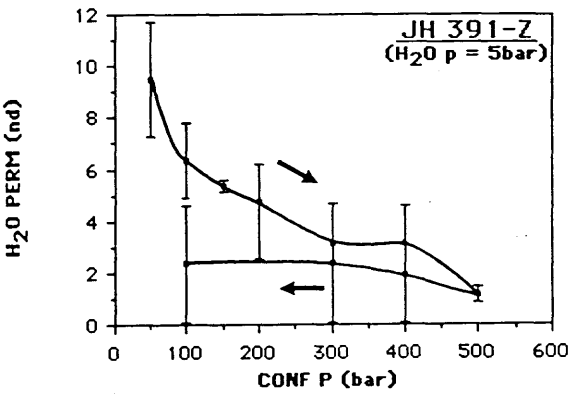

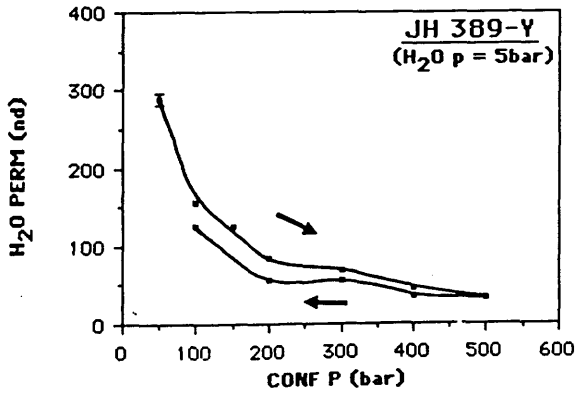

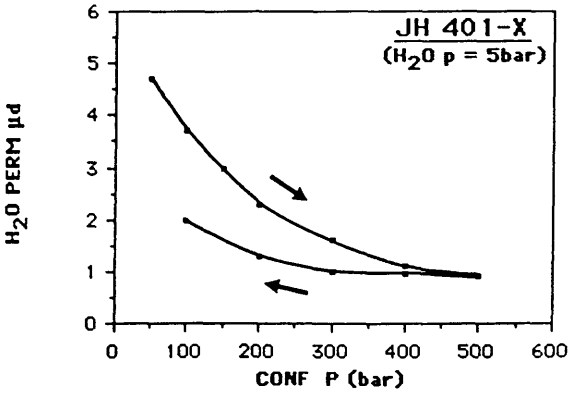

Figure 6.5 Continued.....

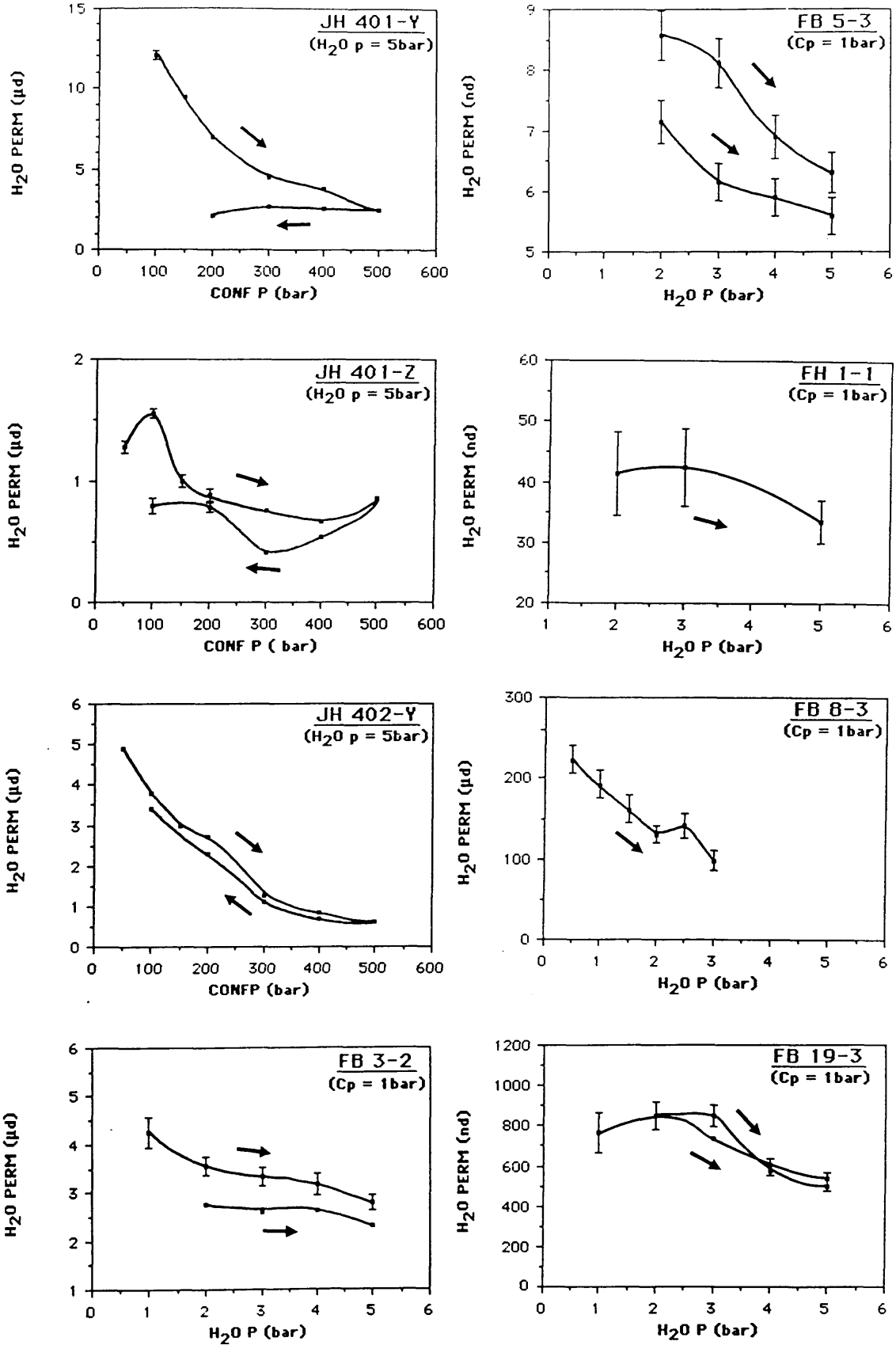

Figure 6.5 Continued.....

Also seen from these graphs, and the others in Fig. 6.5, are variations in the permeability of multiple cores from the same sample. Cores taken in the Y and Z tectonic directions for JH-368 show permeability to be strongly directional, being two orders of magnitude greater in the Y direction than the Z direction. This can perhaps be explained by the directional nature of intergranular cracks within the Lewisian, and suggests that permeability is not homogeneous within these rocks.

In many cases the permeability v's compression curves obtained during the core tests were irregular. Often different responses were exhibited for cores of different orientation. On some occasions, over parts of the curves, permeability increased as confining pressure increased (e.g. JH-389Z and JH-401Z). This may illustrate crack dilatancy with increasing confining pressure, before showing the more typical permeability decrease at higher pressures. This may be due to either the presence of fractures at a high angle to the direction of compression, or to the interaction of crack arrays, with compression along one producing dilation along another. Other curves, such as JH-391, while showing a permeability reduction with confining pressure, are stepped. Such curves indicate periods of crack closure once a threshold confining pressure has been reached. This response can be thought of as the crushing of asperities on the crack wall, or debris in the crack, allowing the cracks to close once the yield strength of the material has been exceeded.

6.3 Estimation of porosity and permeability by S.E.M. analysis

6.3.1 Present day porosity

Open crack porosity was estimated by direct measurement of open cracks from secondary electron image S.E.M. photographs, enlarged to approximately x500. Magnifications of x400 are considered adequate to measure all cracks (Hadley 1976). The photographs used for each rock sample were in the form of a consecutive linear mosaic of between 20 and 40 photographs. The mosaic of photographs was carefully orientated to be perpendicular to any directional intergranular crack. A grid system was adopted to measure the relative proportion of open void-rock. This consisted of two sets of five lines, crossing the S.E.M. image, perpendicular to one another. The linear proportion of open void-rock, along each of the ten lines, was then measured using a ruler. The sum of the two sets of lines were then added, and the total divided by ten to calculate the average void-rock ratio for that picture. Similar calculations were carried out to establish the average linear fracture density, or the number of crack traces per unit length. Individually, the two sets of lines

would allow the comparison of porosity and fracture density perpendicular, as well as parallel, to any intergranular array.

The average values for open porosity, as measured from the Lewisian samples, are illustrated in Fig 6.6, and listed in Appendix 9. It is found that the S.E.M. porosity estimates lie within the range of values found from the core tests, between 0.2 and 0.8%. These values lie to the lower half of the core test data and may be underestimations, due either to missing small pore space or to inhomogeneous porosity within the samples. However, it appears that average porosity can be fairly well estimated from a S.E.M. image. Crack densities were variable, and a range of values between 0.5 and 7 cracks per mm were found (crack densities are also listed in Appendix 9). Most of this relates to open grain boundary and intragranular cracks which are more abundant than open intergranular cracks. Due to their infrequent occurrence, no detailed figures were collected for open intergranular crack densities. For all samples analysed, the porosities and crack densities of the two perpendicular sets measured by the grid system, were broadly similar.

On a more detailed scale, the individual photographs from a mosaic indicate that the porosity of a crystalline rock can be divided into two components. That due to intragranular cracks and grain boundary cracks (a background porosity), and that due to intergranular cracks. The background porosity is constant, and can be found in every sample. The intergranular porosity is much more localized. Although this distribution is present in the Lewisian rocks, the best graphical example was found in a sample of Chelmsford granite (JH-340), analysed during this study. This is illustrated in Fig 6.7a. The porosity graph shows three peaks, where porosity jumps from the background value of less than 1% to 2-3%. In two cases (the right hand peaks) this increase in porosity can be tied in to an increase in intragranular and grain boundary (background) crack density (from less than 5 per mm to between 7 and 10 per mm). The left hand peak, on the other hand, has no corresponding increase in crack density, despite a 3% increase in porosity. This is due to the occurrence of a single intergranular crack in this picture. Fig. 6.7 also illustrates the distribution and relationship of open crack porosity and density for the other samples analysed with the SEM. These graphs all show a correlation between porosity and crack density due to background cracks. Background values for porosity and crack density are given in Table 4.1. It is concluded that crystalline rock porosity consists of, and can be divided up into:

(a) background porosity of fairly constant levels of less than 1%, at a constant background crack density. This is due to intragranular and grain boundary cracks; and

(b) intergranular porosity, which is localized and can be recognised by increases in

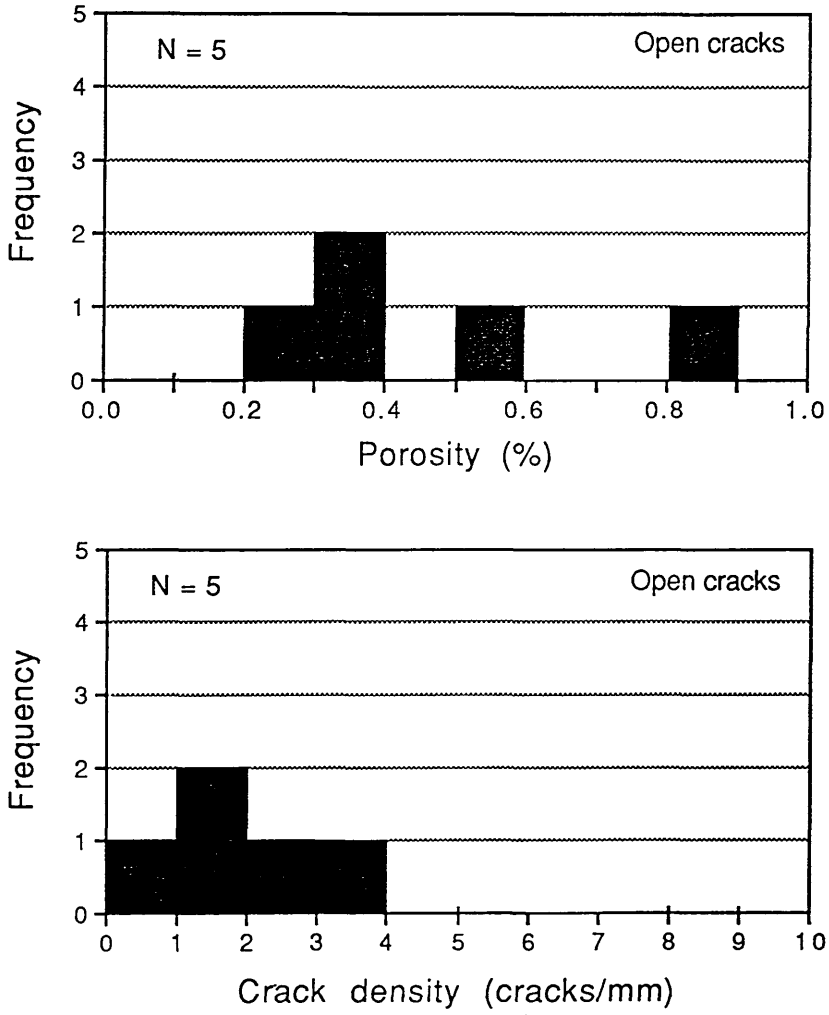

Figure 6.6 Open crack porosity and crack density as measured from S.E.M. photographs. Values are given in Appendix 9.

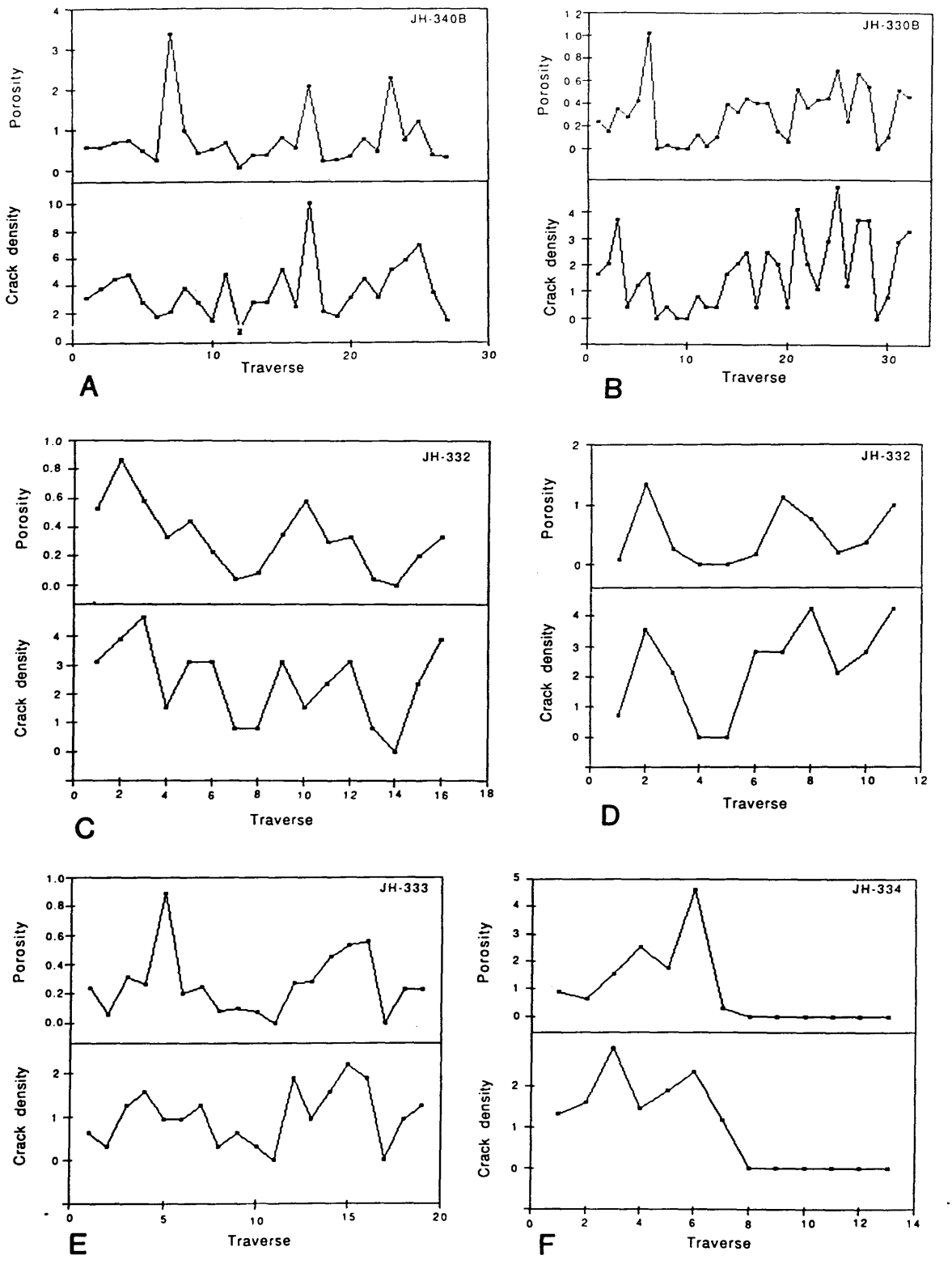

Figure 6.7 Relationship between open crack porosity and crack density

A = Chelmsford granite (JH-340). From 27 photographs across the slide.

B = Laxfordian granite (JH-330B). From 32 photographs across the slide.

C = Scourie dyke amphibolite (JH-332). From 16 photographs across the slide.

D = Scourie dyke amphibolite (JH-332). From 11 photographs across the slide.

E = Scourie dyke amphibolite(JH-333). From 19 photographs across the slide.

F = Badcallian mafic granulite (JH-334). From 13 photographs across the slide.

porosity at constant crack densities. This is due to intergranular cracks.

6.3.2 Present day permeability

It should be possible to estimate the present day permeability of a crystalline rock from the size and spacing of the cracks within the rock (using the permeability laws described in Chapter 1). In the following section, the calculation of rock permeability, using crack sizes and crack densities measured from S.E.M. images, is attempted. These are then directly compared to the permeability core tests of the same samples.

The cubic law for fracture permeability, as derived by Witherspoon et al. (1980), relates flow rate through a single fracture to pressure head, fracture size and the character of the asperities (see Chapter 1.6). As the cracks are not seen in three dimensions it must be assumed they are penny-shaped, that is equidimensional in two dimensions, such that $l_o = l_p$. Thus the cubic-law reduces to

$$\frac{Q}{\Delta h} = \frac{\left(\frac{\rho g}{12\mu}\right)}{\left[1+6.0\left(\frac{E}{2b}\right)^{1.5}\right]} \times (2b)^3 .$$

Therefore, the ratio $Q/\Delta h$ can be calculated for a specific fluid by establishing the width of a crack, and the height of the crack wall asperities. If pressure heads of specific values are assumed (e.g. 1-5 bars as used in the core tests), it is possible to calculate the flow rate at differential pressure head values of 1-5 bars by the simple equation

$$Q = \frac{Q}{\Delta h} \times \Delta h .$$

Having established the flow rate at specific pressure, it is now possible to calculate the permeability of the fracture at a specific pressure, using the equation for a constant head permeameter,

$$K = (\mu Q) \times \left(\frac{L}{A}\right) \times \left(\frac{2Px}{Pa^2 - Px^2}\right) .$$

For this equation, the dimensions of the sample are required. As the sample is to be compared to an actual core of the same rock, then the dimensions of the core can be used.

This allows the calculation of the permeability due to a single fracture through an imaginary core, with the same surface area and thickness as the core test equivalent. This allows direct comparison between the core test and the calculated fracture permeability .

As previously mentioned, the cracks can be split into intergranular cracks and background cracks. The crack-system permeability (i.e. the component of permeability within the rock due to a certain crack type) will be the sum of the permeabilities for each individual crack of that type occurring in the core sized sample. To calculate this, the number of cracks of each type occurring in the core sized sample must be calculated.

For the straight and parallel intergranular cracks, the number of cracks (NC) can be well approximated by a function of the linear intergranular cracks density (n_i), and the core diameter (D), where

$$NC = n_i \times D \ .$$

For background cracks, which are not straight and parallel, tending to form largely around grain boundaries, the number of cracks will be equal to a function of the linear background crack density (n_b) and the core surface area (A). Here the number of cracks (NC) can be approximated by the equation

$$NC = A \times 2 \left(n_b \times n_b - 1 \right) \ .$$

For these background cracks, the flow path through the core is not going to be as straight as was the case for the intergranular cracks. The flow path length (or core length) (L) must therefore be multiplied by a flow path tortuosity factor. Assuming that the grain boundaries are a unit size (l) long (the length of the background cracks), and the crystals to be cubic, then the tortuosity factor (T) required for the background crack system in a core of length (L) will be

$$T = \left(\frac{L}{l}\right) \times \left(\sqrt{l^2 + l^2}\right) \ .$$

In cases where the crack length cannot be directly seen, it can be accurately predicted using the relationship of crack width to length as derived in Chapter 4 (Fig. 4.5), where

$$\ln(l) = \frac{\ln(2b) + 1.3}{0.7} \ .$$

The total permeability for the rock (or the total system permeability), can be calculated

as the sum of the individual background crack permeabilities plus the individual intergranular crack permeabilities. These calculations were carried out using the program MODEL (Appendix 10).

Figs. 6.8 to 6.13 are plots of permeability against pressure head for samples analysed for open cracks. The plots each show three curves representing:

(a) the core test results;

(b) the calculated permeability, using the average measured crack widths and crack densities for that sample; and

(c) the best fit permeability curve, modelled by altering the crack widths and/or crack densities.

From Figs. 6. 8 to 6. 13 it can be seen that the calculated permeabilities, for the average crack widths and densities consistantly lie below the actual core derived data. The two curves average about one order of magnitude from each other. The closest calculated curve (JH-332D) is only 4 microdarcies less than the core test curve.

The visual best fit curves are achieved with changes to either the average crack densities or the average crack widths. The crack densities (cracks/mm) and widths (μm) used in these diagrams are summarized in Table 6.1. This table lists the average values as measured from the S.E.M., and the maximum limits for these parameters to allow calculation of the best fit curves. The best fit curves could be produced by many combinations of crack density and crack width between these limits.

Table 6.1 Measured and best fit data for crack widths (μm) and crack densities (cracks/mm). The best fit data is obtained by altering one variable, while using the average measured value for the other variable. These represent maximum limits.

	Measured average values		Best fit curve	
Core	Crack density	Crack width	Crack density	Crack width
JH-330	1.80	2.30	5.0	5.5
JH-330B	1.80	2.30	5.6	5.2
JH-332A	2.75	1.38	16.0	4.4
JH-332D	2.75	1.38	8.0	3.0
JH-333D	1.10	2.26	8.5	8.85

The cracks present in these samples were of a background nature, and there were no intergranular cracks present within these thin sections. These curves are also for smooth walled cracks, that is, there are no asperities included in the calculation.

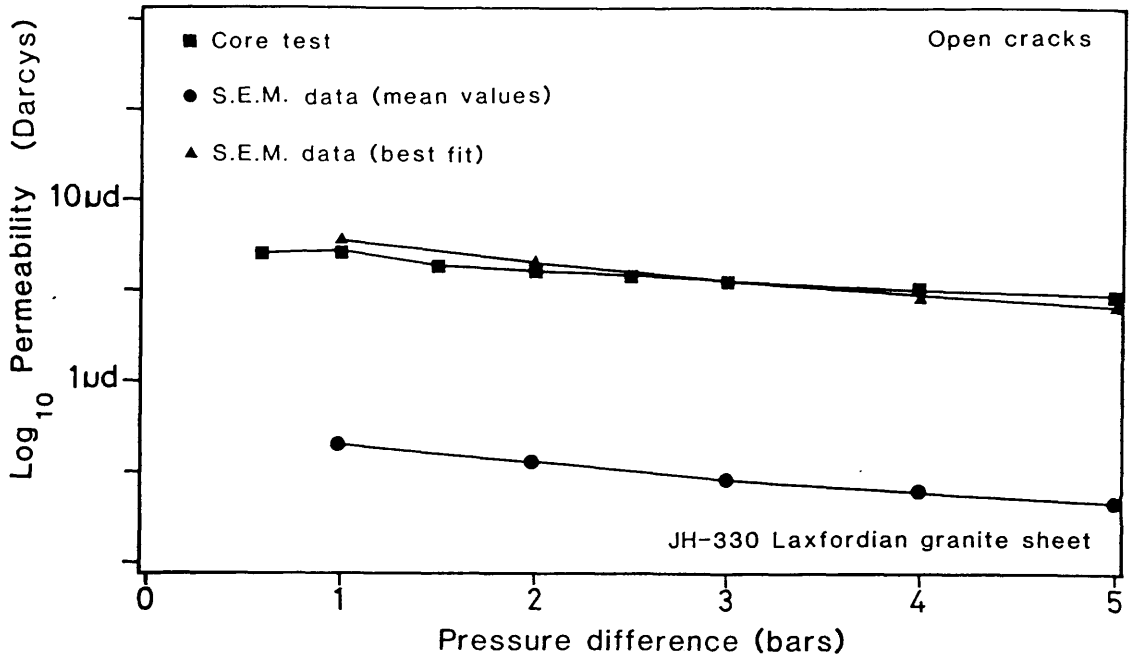

Figure 6.8 Calculated and modelled open permeability of Laxfordian granite (slide JH-330) from S.E.M. photograph data. Plotted with the observed permeability, measured from core JH-330.

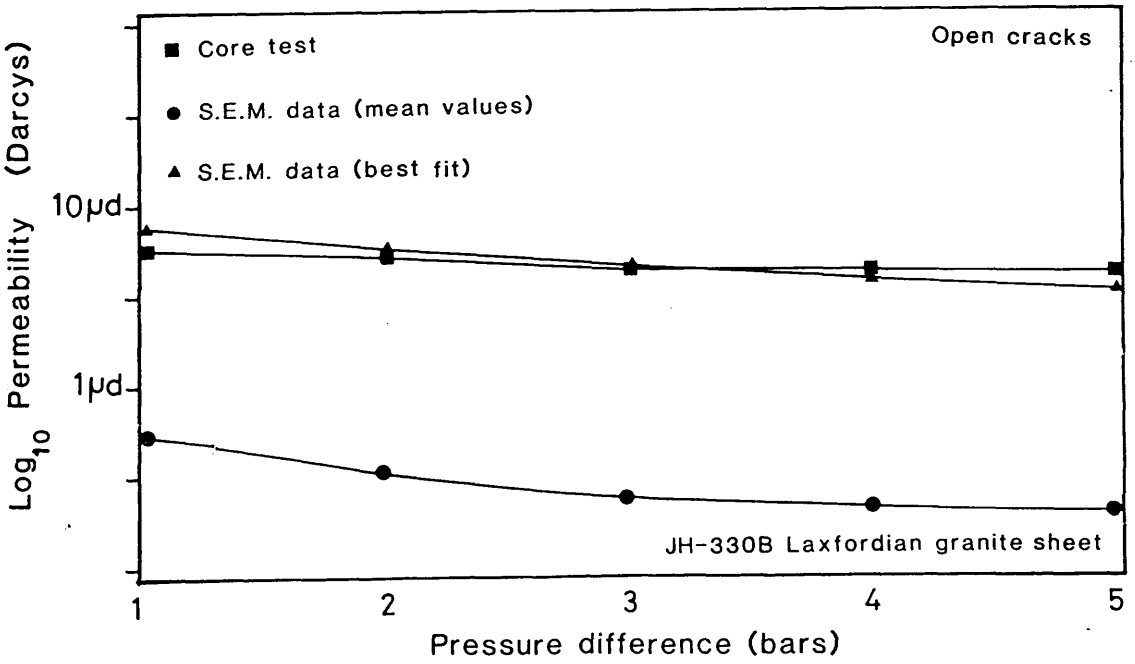

Figure 6.9 Calculated and modelled open permeability of Laxfordian granite (slide JH-330) from S.E.M. photograph data. Plotted with the observed permeability, measured from core JH-330B.

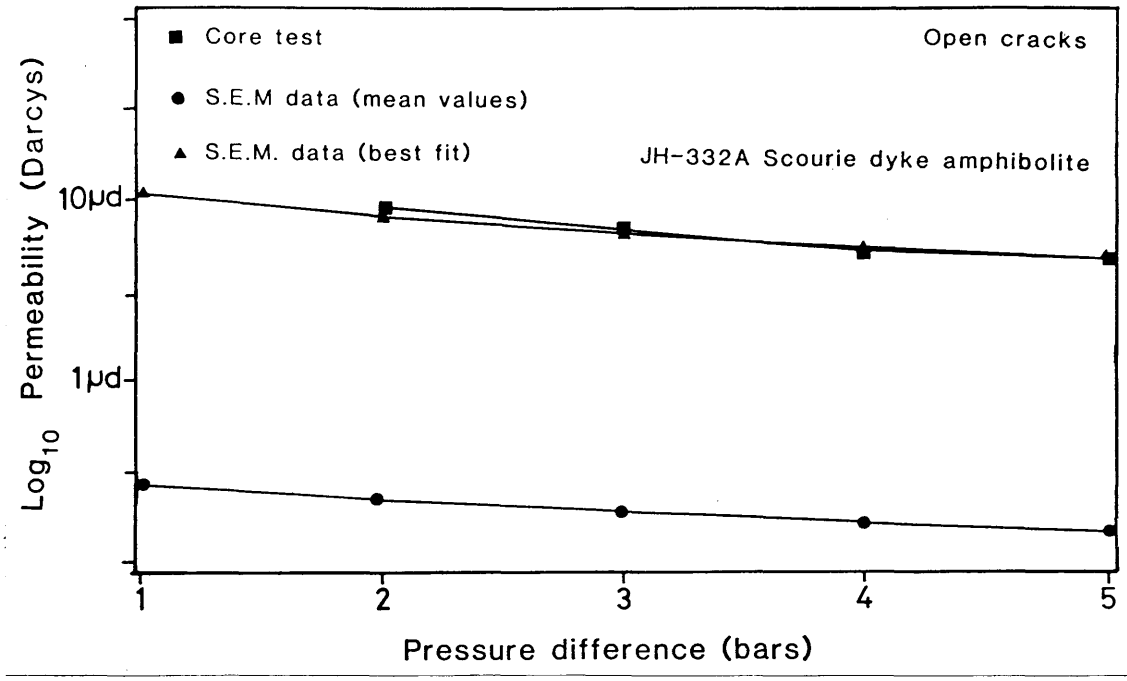

Figure 6.10 Calculated and modelled open permeability of Scourie dyke amphibolite (slide JH-332) from S.E.M. photograph data. Plotted with the observed permeability, measured from core JH-332A.

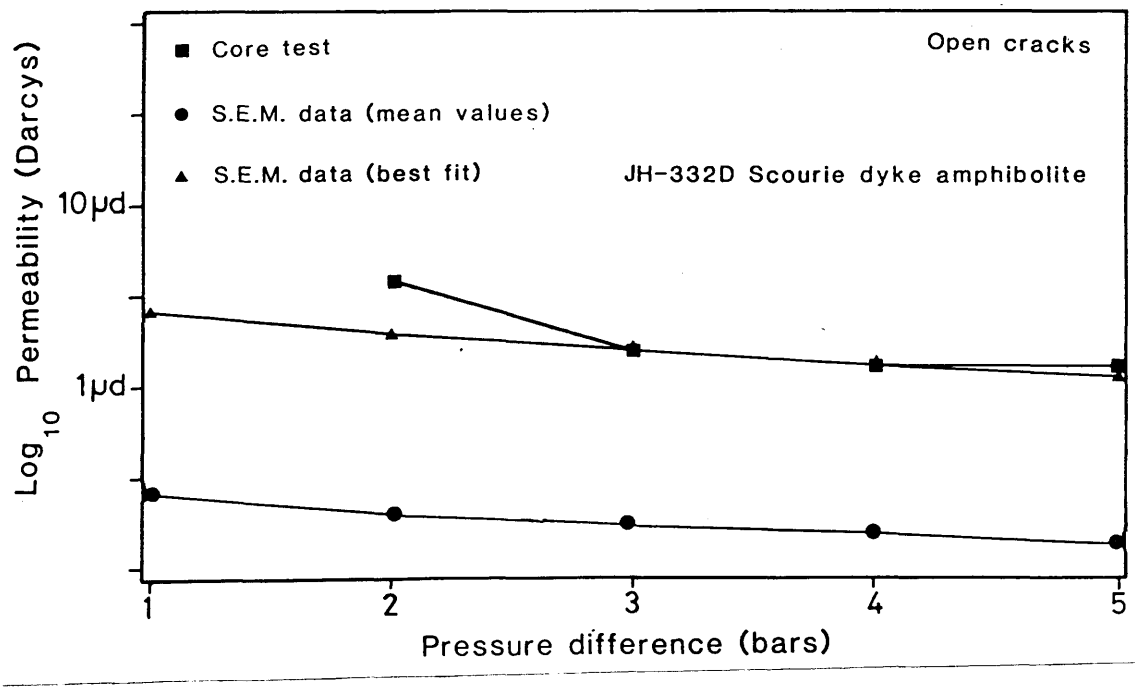

Figure 6.11 Calculated and modelled open permeability of Scourie dyke amphibolite (slide JH-332) from S.E.M. photograph data. Plotted with the observed permeability, measured from core JH-332D.

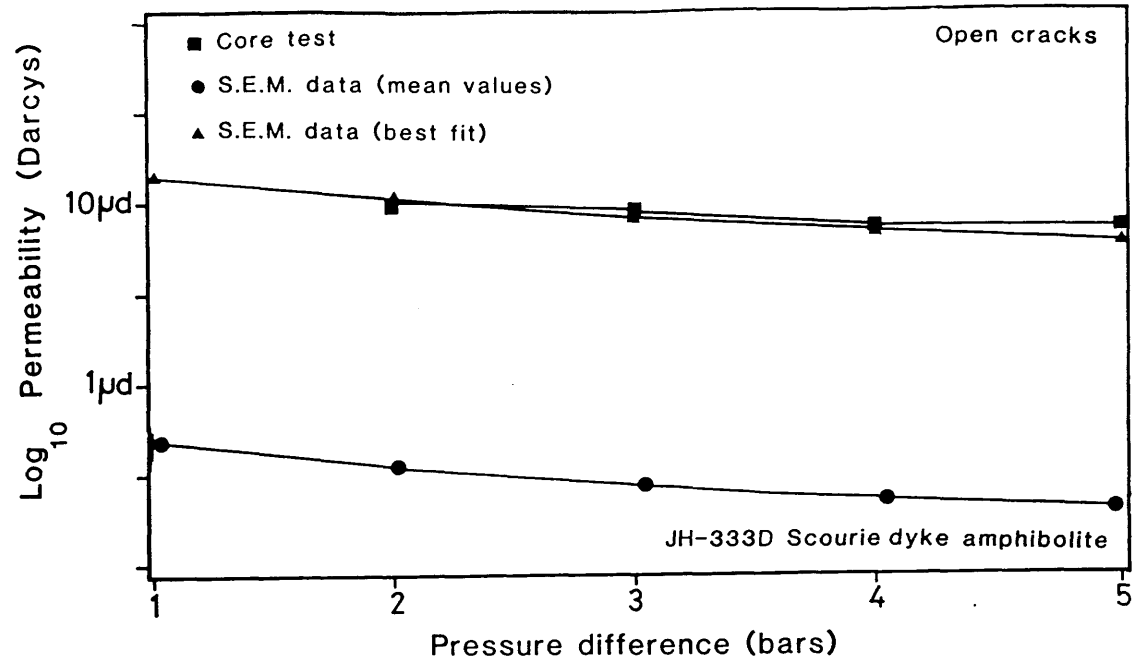

Figure 6.12 Calculated and modelled open permeability of Scourie dyke amphibolite (slide JH-333) from S.E.M. photograph data. Plotted with the observed permeability, measured from core JH-333D.

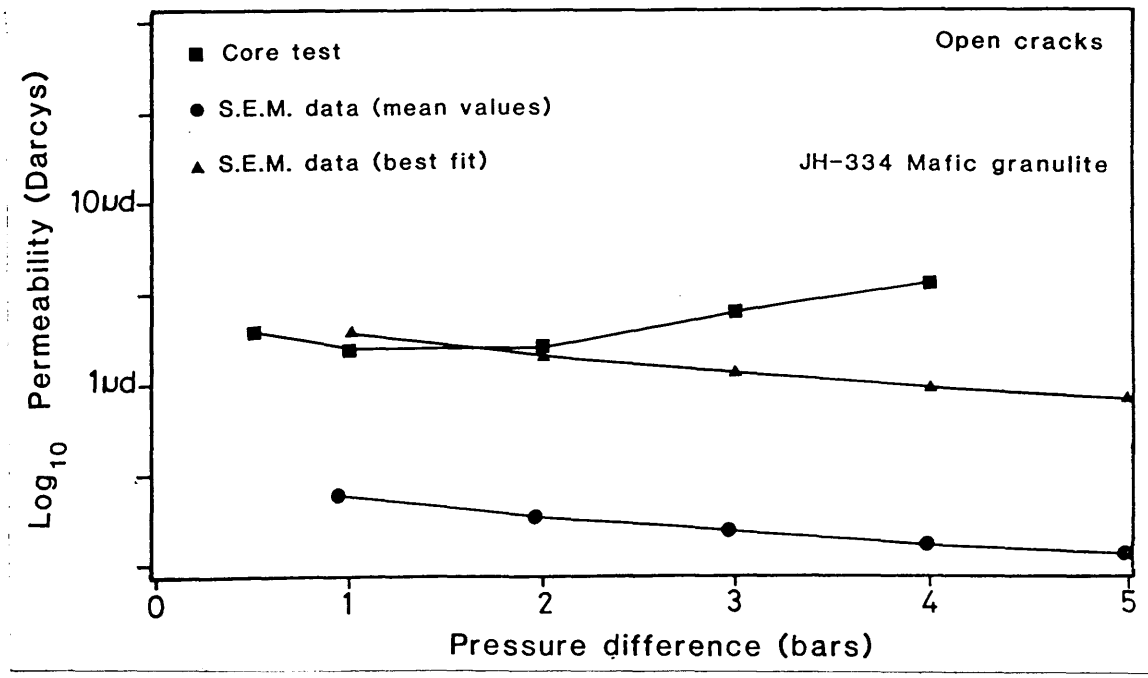

Figure 6.13 Calculated and modelled open permeability of Badcallian mafic granulite (slide JH-334) from S.E.M. photograph data. Plotted with the observed permeability, measured from core JH-334.

The calculation of permeability for the background system appears to give estimates close to the actual measured permeability for the Lewisian samples. If it is assumed that the background permeability as measured is correct, then for those which have lower calculated curves, the difference between the calculated curve and the core test curve may be due to spaced intergranular cracks present within the core (but not seen in the thin section). All graphs, except JH-332D, show that the "average value" calculated permeability is slightly smaller than the observed core test permeability. The influence of intergranular cracks may be the cause of this.

Using the average background measurements, and modelling the difference by a single intergranular crack cross cutting the core, the best fit curves can be achieved when the values for the intergranular crack width in Table 6.2 are used:

Table 6.2 Modelled crack widths (μm) for single intergranular crack cross-cutting the cores(Crack density is in cracks/mm).

	modelled intergranular crack dimensions	
Core	Crack density	Crack width
JH-330	0.044	90.0
JH-330B	0.044	92.0
JH-332A	0.044	110.0
JH-332D	0.044	110.0
JH-333D	0.044	110.0

Cracks of between 90 and 110 μm have never been found as yet in any of the cores. The most probable reason for the discrepancy between the core test and the average calculated curve is an error in the estimation of the background parameters. Within the limits presented in Table 6.1, there are many combinations of crack density and crack width which could account for the differences between the average and core test curves. Table 6.3 contains only one of the many possible combination of background crack density and width which may be used to calculate the best fit curve for each sample. However, this serves to illustrate that only slight errors in the measured S.E.M. values could result in the differences between the average value and core test curves. Errors of about 1 μm and 1 crack/mm for averaged crack width and density can account for the discrepancies between the cores and the S.E.M. data. When one considers, however, the sensitivity of permeability to the width of the cracks the process of averaging the crack width, as carried out in the modelling, will also lead to underestimates in permeability.

Table 6.3 Some of the many possible combinations of crack width (μm) and crack density (cracks/mm) which can result in the best fit curves.

	Measured average values		Best fit curve	
Core	Crack density	Crack width	Crack density	Crack width
JH-330	1.80	2.30	3.5	3.0
JH-330B	1.80	2.30	3.55	3.1
JH-332A	2.75	1.38	3.5	3.3
JH-332D	2.75	1.38	3.0	2.5
JH-333D	1.10	2.26	4.0	4.0

While samples JH-330 to JH-333 may possess only background cracks, JH-334 possessed both intergranular and background cracks. However, sample JH-334 gave a rather unusual permeability response to pressure head increase, showing increasing permeability with increasing head pressure (Fig 6.13). Although the reason for this is not clear, permeability lay within the range of 2-6 μd. On modelling with the "average variables", as listed below, the calculated permeability was found to lie slightly lower than the observed core test. This, as with the others, could be rectified by alterations in any of the average variables to produce the visual best fit line (Table 6.4).

Table 6.4 Measured (M) and modelled (m) crack densities (cracks/mm) and widths (μm) for JH-334. Best fit data are for individual crack types, which are calculated with the average measured other crack type. These represent maximum limits.

		Average background		Average intergranular	
		Crack density	Crack width	Crack density	Crack width
JH-334	(M)	0.99	2.35	0.04	4.50
		Best fit background		**Best fit intergranular**	
		Crack density	Crack width	Crack density	Crack width
JH-334	(m)	3.0	5.0	0.09	73.0

Modelling the difference between the curves (in Fig 6.13) by a single intergranular crack implies such crack is quite wide (73 μm). In this core there is a single large intergranular crack crossing the whole of the core, and this appears to be a reasonably accurate model, although the true situation could be one of many combination of values between the modelled end members presented in Table 6.4.

From these examples, it is seen for systems composed of either background cracks, or

both background and intergranular cracks, the permeability can be quite accurately estimated using the calculations and method adopted in the program MODEL (Appendix 10).

It is also interesting to note that quite large permeabilities, in the region of 1-10 μd, can be accounted for by flow through background porosity alone.

6.4 Palaeoporosity and permeability estimates from the sealed cracks

It has been shown that the estimation of the present day porosity and permeability of a rock can be accurately carried out by calculations involving measurements of open cracks. Therefore, the opportunity arises to calculate the palaeoporosity and permeability of a rock, from measurements of sealed fractures.

Due to the presence of multiple phases of crack sealing within the Lewisian, the crack sealing history of the rocks must be known. This allows the identification (and elimination) of:

(a) cracks already sealed prior to the cracks of interest; and

(b) cracks formed and sealed after the cracks of interest.

The removal of these two groups is critical to accurate estimation, otherwise overestimates will almost certainly occur. The crack sealing history for these rocks has been derived, and is reported in Chapter 4. This allows the separation of different crack sets which may occur in a single rock. A major assumption present, in this line of investigation, is that all cracks of the same generation were open to their presently preserved sizes at the same time. This can never be proved, or disproved, but certain criteria can help to identify those which may have been.

(a) If the cracks are sealed by the same minerals, it may be valid to assume these cracks were in some way, and at some time, interconnected and formed part of a permeable network. However, if cracks sealed by the same minerals cross cut each other, then they were not open together and should not be used.

(b) Evidence of interaction between the wall rock and the fluid indicates that the crack represents a once open conduit which remained open for a period of time.

(c) Cracks which show evidence of either incremental opening, or compression after sealing, should not be used.

(d) For the least unambiguous results, only sections preserving a single generation of sealed cracks should be used.

The samples analysed for the sealed crack porosity and permeability were those considered as being closest to obeying all these criteria. In total nine sections were analysed. The procedure used to measure the sealed cracks was identical to that used to measure the open

cracks (see section 6.3.1). The only difference between the two methods is the sealed cracks were measured off back scattered electron images as opposed to the secondary electron images used for the open cracks.

6.4.1 Sealed crack porosity

The sealed crack porosity was more variable between samples than the open crack porosity (a histogram of the average porosity for each sample is shown in Fig. 6.14). Porosity is mainly found to lie within the limits of 0.1-4.3%, with one sample (DM-1) as high as 10.9%. Although some overlap occurs these porosity values are higher than both the core test and open crack values. As with the open cracks, it is possible to split the porosity into a background level and an intergranular level. This distinction is more marked with the sealed cracks.

Background levels of between 0 - 2 % porosity (Fig. 6.15) are found throughout every slide. This is due to sealed grain boundary and intragranular cracks. Higher levels of up to 100 % exist for individual photographs within the traverses. This is due to the occurrence of large sealed intergranular cracks which are not found as open cracks. Figures 6.16 and 6.17 show the variation of porosity and crack densities over the traverses. From these it can be seen that the same divisions of porosity hold for the sealed cracks as did for the open cracks, and the presence of intergranular porosity can be seen in the relationship between porosity and crack density, as was found for the Chelmsford granite (JH-340).

The background crack densities are mainly between 0 and 3.7 cracks per mm (Table 6.4). The exception was M-16 with background density of 12.0 cracks per mm. The average intergranular crack densities (as measured from the photographs) were in the region of 0 - 1 cracks per mm (Table 6.4).

6.4.1 Sealed crack permeability

The sealed crack permeability was modelled using the program MODEL, as was the case for the open cracks. The crack densities, crack widths and the height of any asperities were measured from the traverse photographs. As with the open cracks, the values from each photograph were averaged, and the average values (Table 6.4) were.used in the calculation of the permeability

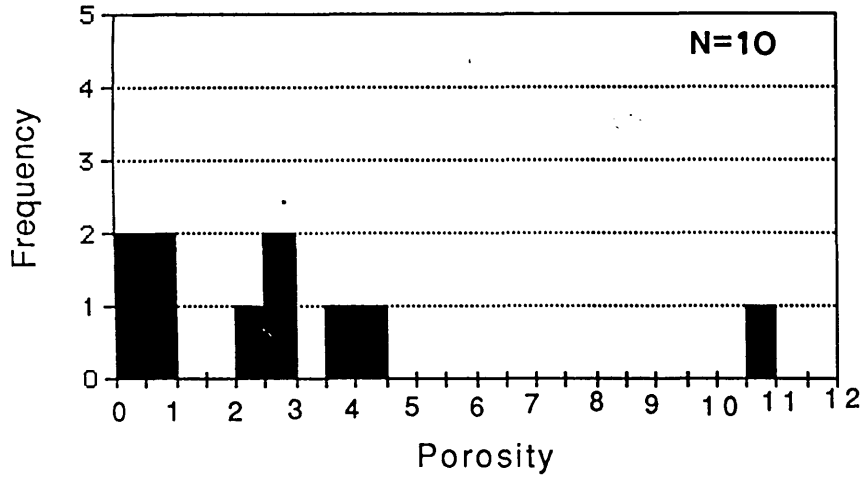

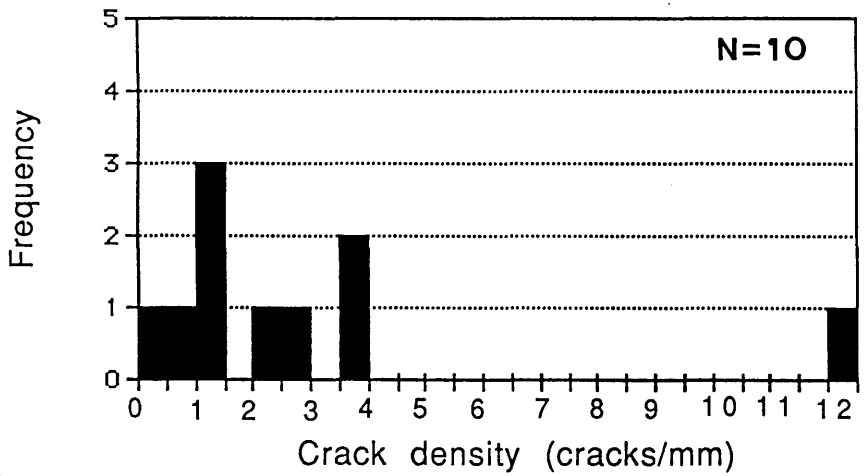

Figure 6.14

Sealed crack porosity and crack density as measured from S.E.M. photographs. Values are given in Appendix 9

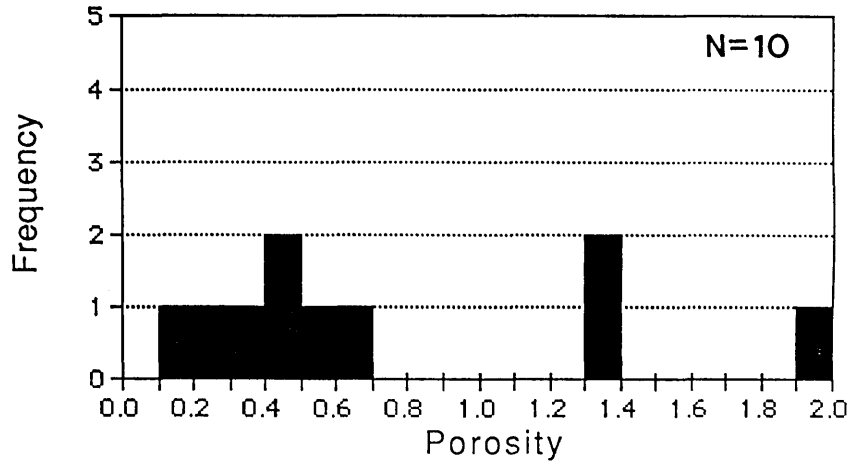

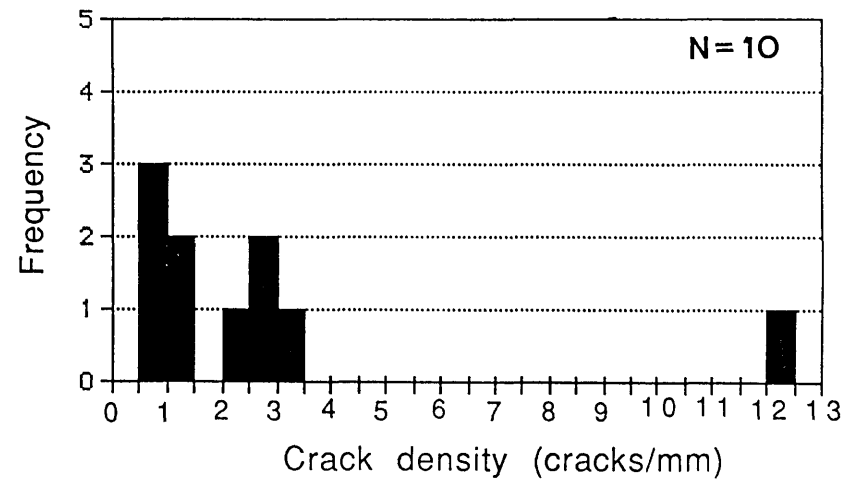

Figure 6.15

Sealed crack porosity and crack density due to background cracks, as measured from S.E.M. photographs with no intergranular cracks.

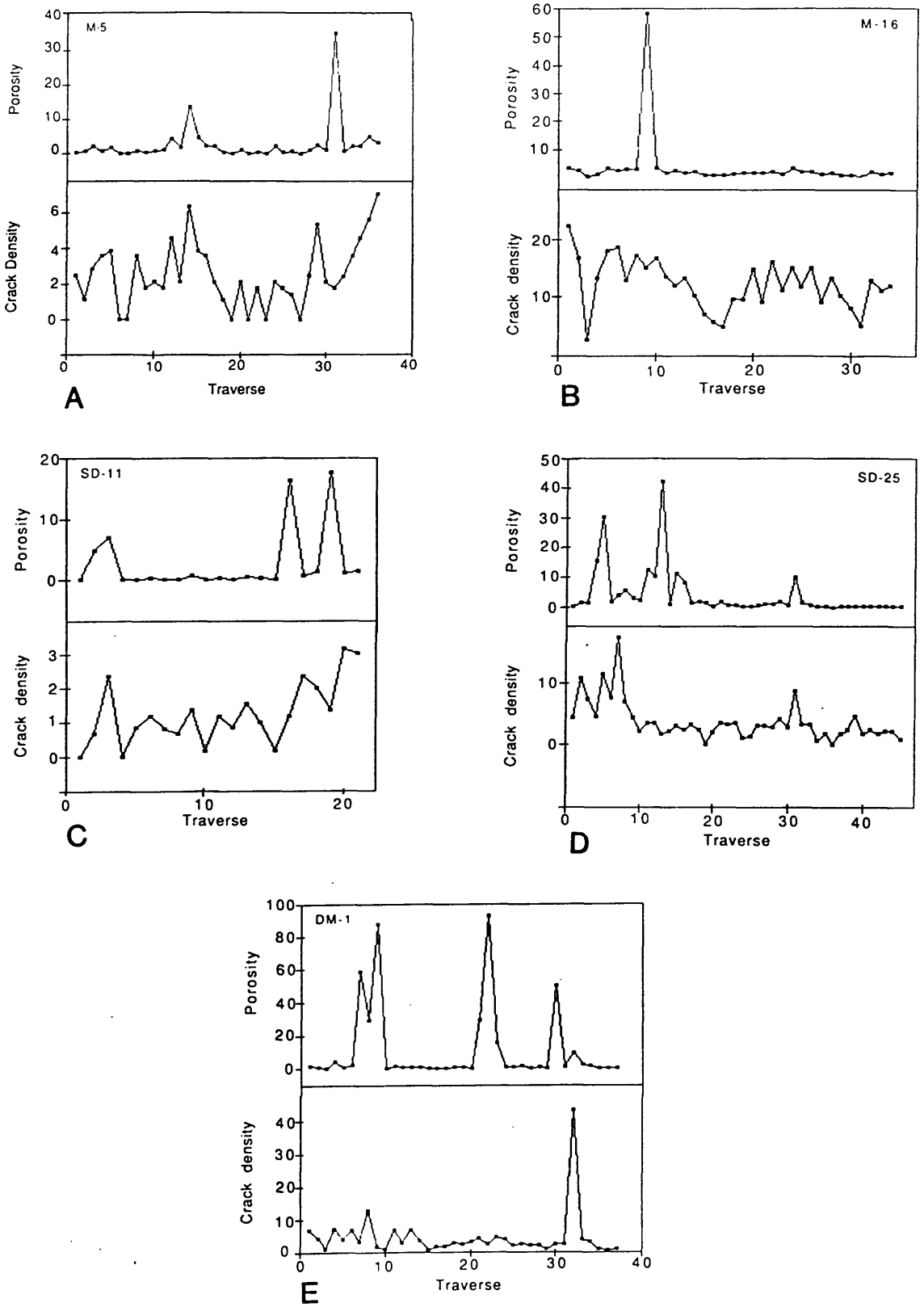

Figure 6.16 Relationship between sealed crack porosity and sealed crack density.

A = Inverian gneiss (M-5). From 36 photographs across the slide.

B = Inverian gneiss (M-16). From 13 photographs across the slide.

C = Scourie dyke amphibolite (SD-11). From 21 photographs across the slide.

D = Scourie dyke amphibolite (SD-25). From 45 photographs across the slide.

E = Scourie dyke amphibolite (DM-1). From 37 photographs across the slide.

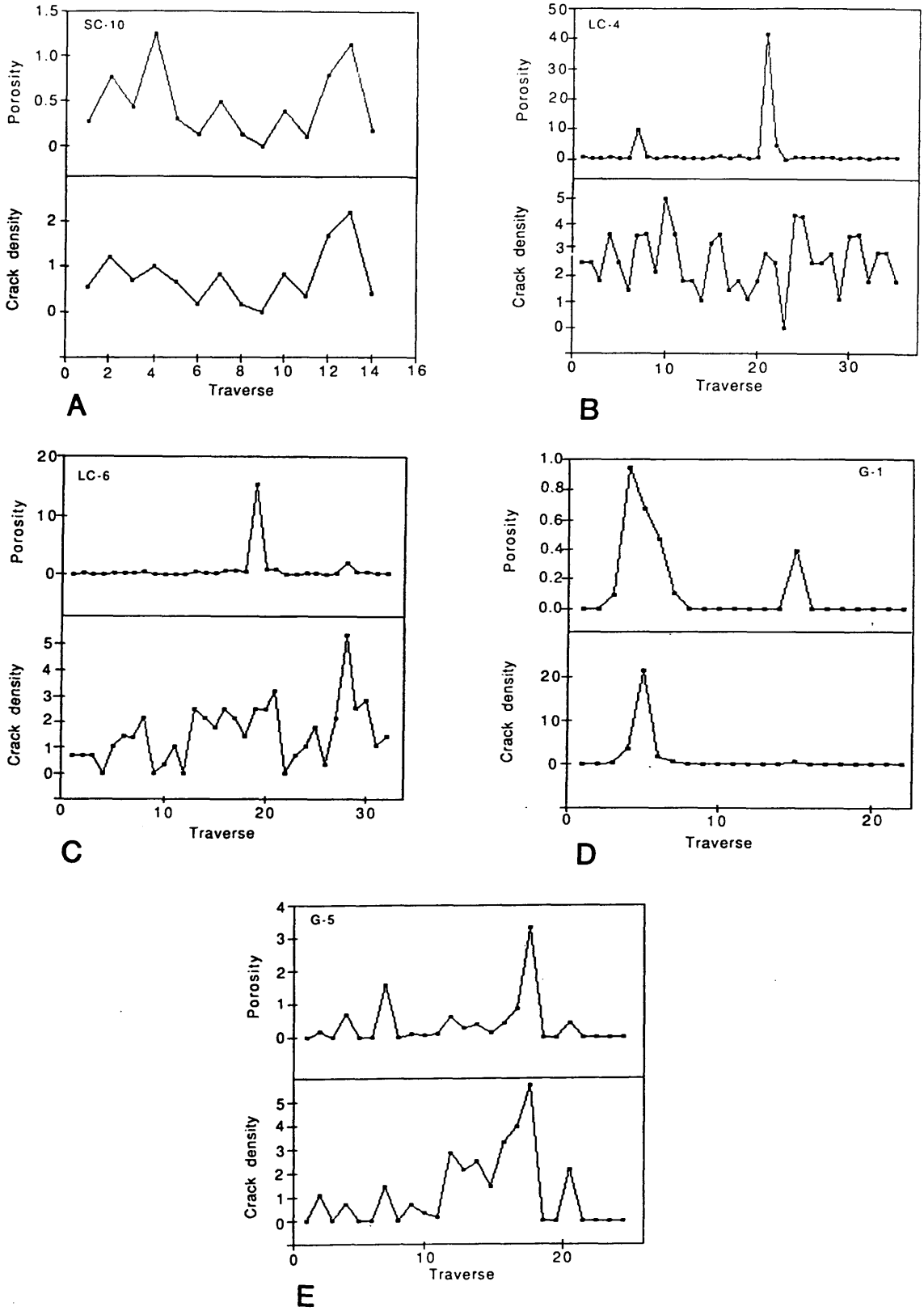

Figure 6.17 Relationship between sealed crack porosity and sealed crack density.
A = Kylesku granulite (SC-10). From 14 photographs across the slide.
B = Laxfordian gneiss (LC-4). From 35 photographs across the slide.
C = Laxfordian gneiss (LC-6). From 32 photographs across the slide.
D = Laxfordian granite (G-1). From 22 photographs across the slide.
E = Laxfordian granite (G-5). From 24 photographs across the slide.

Table 6.4 Average measured crack densities (cracks/mm), widths (μm) and height of crack-wall asperities (μm) for the sealed cracks.

	Sealed cracks - average values					
	Background cracks			Intergranular cracks		
sample	density	width	asperities	density	width	asperities
SD-25	3.7	1.63	0.0	0.32	74.0	8.3
SC-10	0.72	7.0	1.9	0.0	0.0	0.0
LC-4	2.7	1.97	0.0	0.12	123.0	21.6
G-5	1.1	2.55	0.0	0.32	5.4	0.0
DM-1	3.78	1.32	0.0	0.2	373.0	49.8
M-16	12.0	1.34	0.58	0.04	225.0	27.9
SD-11	1.03	2.31	0.8	0.2	71.4	17.57
LC-6	0.0	0.0	0.0	1.11	9.5	3.32
M-5	2.49	3.29	1.13	0.08	128.0	16.25

The calculated sealed crack permeabilities for these samples, at pressure heads of 1 - 5 bars, are shown in Fig. 6.18. All but one sample (DM-1) have palaeopermeabilities lying within the range 100 nd - 100 μd. A comparison between the calculated palaeopermeabilities, in Fig. 6.18, with the range of present permeabilities, in Fig. 6.4, shows the palaeopermeability estimates lie within, and exceed, the upper levels found for the open core tests. With the background crack sizes and densities being similar for these two sets of data, the reason for the increased palaeopermeability levels must be due to the presence of large, closely spaced, sealed intergranular cracks (the size and density of which have not been seen as open cracks).

From these calculations on sealed cracks, and assuming the criteria for their selection and modelling to be correct, it appears that crystalline rocks insitu may possess permeabilities only slightly higher than those found for surface exposed crystalline rocks today. For rocks undergoing fracture dilation and extension (as was the case when the sealed cracks were formed), it is not unreasonable that the preserved porosities and calculated permeabilities should be slightly higher than normally found. The likely permeability values appear to be between the limits of 100 nd and 1 md, with most between 1 and 10 μd. However, when one considers that:

(a) occasional inaccuracies of up to 1 order of magnitude in the calculated open crack permeability relative to the core test permeability for the same sample; and

(b) although all possible precautions have been taken, there may still be some doubt as to all the sealed cracks measured being open simultaneously to their full extent.

It might be suggested, for lab scale samples, there may be no major differences between

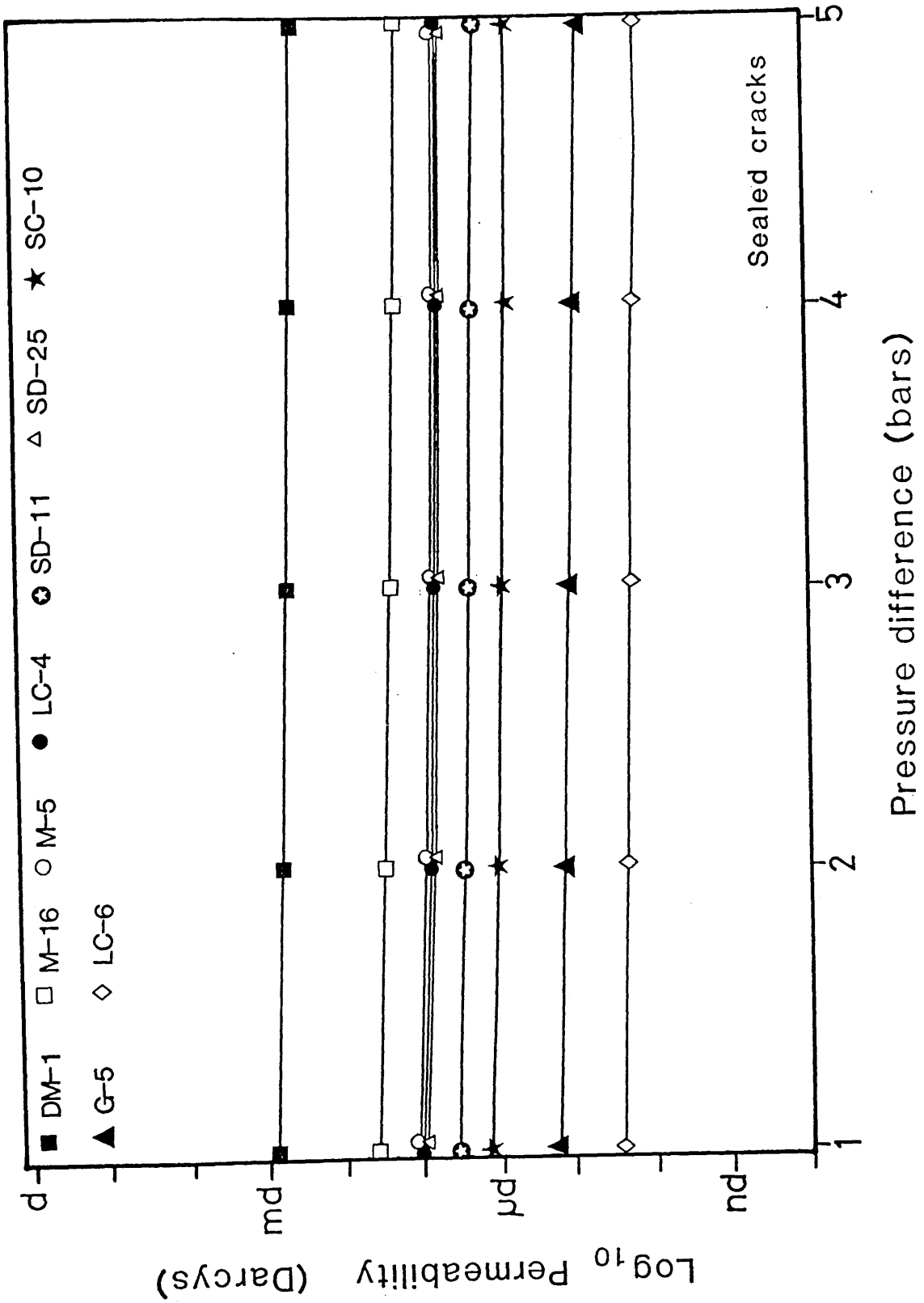

Figure 6.18 Modelled permeabilities for sealed crack arrays. Modelled using the parameters listed in Table 6.5.

the Lewisian permeabilities of today and the palaeopermeabilities that can be calculated from the Lewisian sealed cracks.

6.5 Summary

1. The porosity of Lewisian rocks was found to be low, typically in the range from 0.2% to 1.6%, with a mean value of 0.8%. An overall decrease in the average porosity occurs from the silica-rich granites to the basic, silica-poor Scourie dykes. Large porosity ranges exist within some lithologies (up to1.5%). This illustrates the presence of inhomogeneous pore space and may be is due to occasional larger intergranular cracks

2. Crystalline rock porosity consists of, and can be divided up into;
   (a) a background porosity of fairly constant levels of less than 1%, at a constant background crack density: due to intragranular and grainboundary cracks; and
   (b) intergranular porosity, which is localized, and is due to intergranular cracks.

3. S.E.M. image estimates of open porosity lie between 0.2 and 0.8%, within the range found for the core tests. These values may be underestimations due either to missing small pore space, or to inhomogeneous porosity within the samples. Open crack densities range between 0.5 and 7 cracks per mm.

4. Sealed crack porosity can be divided similarly. Sealed crack porosities range between 0.1 and 4.3% (exceeding the open crack and core test values) and sealed intergranular crack densities range between 0 and 1.1 cracks per mm. Background sealed crack porosity lies between 0 and 2% and background sealed crack densities of between 0.5 and 3.5 cracks per mm. These values are similar to the open cracks.

5. Measured permeabilities for the Lewisian samples range over 5 orders of magnitude, (from 1 nannodarcy ($10^{-21}m^2$) to 100 microdarcies ($10^{-16}m^2$)). These are fairly typical values for core samples of fresh crystalline rock. Permeability between lithologies appears to be fairly similar (with mean and median values for all lithologies falling within a band between 100 nd and 10 μd). Those with the lowest recorded permeabilities (granulite, amphibolite gneiss and Scourie dyke dolerite) lie to the more basic end of the suite. Whereas silica-rich rocks (granite, quartz-feldspar and quartz biotite gneisses) tended to have higher minimum permeabilities.

6. Permeability, as with porosity, is inhomogeneous. This is not a surprising feature given the strong directional nature of intergranular cracks within the Lewisian. In many cases the permeability versus compression curves derived during the core test were irregular, often exhibiting different responses for cores of different orientation. Other curves, while showing a permeability reduction with confining pressure, were stepped . This indicates periods of crack closure once a threshold confining pressure has been reached. This response can be thought of as a crushing of debris within the crack, or the crushing of asperities on the crack wall, once the yield strength of the material has been exceeded.

7. By applying the cubic law for fracture permeability to data taken from S.E.M. photographs, permeabilities can be closely estimated to the actual core derived permeability data. The measured and calculated curves are always within one order of magnitude of each other. The closest calculated curve being only .4 microdarcies less than the core test curve. Permeabilities in the region of 1-10 μd can be accounted for by flow through background porosity alone.

8. By analogy to sealed cracks, it appears that crystalline rocks insitu may possess permeabilities similar to, or slightly higher, than those found for surface exposed crystalline rocks today (and then only when the rock is undergoing dilation). The likely values appear to be between the limits of 100 nd and 1 md, with most between 1 and 10 μd. The reason for the slightly increased palaeopermeability levels is due to the presence of large, closely spaced, sealed intergranular cracks (the size and density of which have not been found as open cracks).

9. The permeability modelling with sealed cracks assumes all the cracks involved to have all been open simultaneously to their present size. While precautions in fracture choice can be taken to make this assumption more probable, it can never be proved. Therefore, the results of this type of study should be considered as maximum possible values.

CHAPTER 7

IMPLICATIONS OF THIS STUDY, WITH SUGGESTIONS FOR FURTHER WORK

7.1 Initial aims and approaches

At this point it is worth reiterating the original aims of the project. The principal objective was to establish the fracture permeability that crystalline rock might possess at depth. The depths of interest, from the seismic point of view, being in the region of 25 Km (within the middle to lower continental crust). It was hoped that this could be done by direct comparison between open and sealed cracks. The sealed cracks themselves presented an opportunity to investigate the possible characteristics of fluid flow within continental crustal basement. It was hoped that the period (or periods) of crack formation and sealing could be related to real geological events, whether that be dehydration reactions associated with metamorphism, fluid expulsion during igneous events, fluid movement associated with shear zones or uplift and erosion. The Lewisian was chosen because of its suitable geological nature, as well as the fact that the initial reconnaissance studies of Hall (1986, 1987) had shown sealed cracks to be present. It was hoped to tie in estimates of palaeo-permeability to present permeability work (which was being carried out at the time and was subsequently taken over by this study). To answer these questions, three main approaches were taken.

(a) The microcracks, both open and closed, were characterised in terms of their morphology, size and distribution; with the sealed cracks being further characterized by their sealing mineralogy and orientation. This part of the study relied heavily on the S.E.M., and is reported in Chapter 4.

(b) The causes of crack sealing were investigated to provide information about the time of sealing, the temperatures and pressures during that time, and the source of the fluids from which the minerals were precipitated. The study undertaken consisted of field observations, sealing mineral PTX considerations, isotopic and fluid inclusion analysis and is reported in Chapters 4 and 5.

(c) Porosity and permeability, both at present and in the past, was investigated using core test techniques, S.E.M. analysis and numerical modelling. This final part of the study is reported in Chapter 6.

The principal conclusions and inferences which can be drawn from these investigations are now discussed.

7.2 Discussion of the study

The discovery, during the course of this study, that fractures sealed by pumpellyite cross the Lewisian - Stoer Group unconformity has obvious implications to the initial suggestion that these sealed cracks formed while the Lewisian was in a deep crustal position. While it can now be proved that most of the post-Laxfordian sealed cracks relate to events occurring within the top 5 km of the crust, some sealed cracks were found which appeared to relate to fluid flow periods associated with tectono-metamorphic events. These magnetite sealed cracks are not common, and are nearly always grain boundary or intergranular cracks. Their distribution and characteristics suggest that they are associated with either dehydration reactions, or magmatic volatiles present during the history of their host lithology (some may even be due to exsolution). Another feature present, and perhaps associated with these events, are inclusion trails. These are very common in quartz. Not a lot can be done with these small early features, other than to note their presence and infer that fluids were present at some time during the Lewisian's period in the deep crust. The main body of sealed fractures preserved within the Lewisian, as mentioned above, relate to events occurring when the Lewisian complex was close to the surface. As it was these near surface sealed cracks which were subsequently investigated, the association with the deep crust cannot really be taken any further in this study.

Comparisons between the open and sealed cracks, found within the Lewisian complex and with the cracks described by Simmons & Richter (1976), indicated that both thermal and mechanical stress within the rocks resulted in fracturing. The processes involved in the formation of the sealed cracks appear to be identical to those envisaged for the open cracks. An interesting discovery was that many of the sealed cracks had been able to remain open within the rock, under pressures which may have over 1 kb. The mechanisms to allow this were seen in many instances, crystal propping by crack-wall asperities being the most common. The formation of the asperities was found to be the result of irregular crack opening, or mineral solution. Crystal spalling was also present, and together these mechanisms would all allow preservation of porosity under a confining pressure sufficient to close smooth walled cracks of a similar aspect ratio.

The precipitation of minerals within the cracks is evidence that they carried fluid at some time, and small cracks less than 1μm across are often seen sealed. The larger cracks provided more information on the processes in action within the cracks during sealing. Crack sealing was often seen to be inhomogeneous, with the preferred (and often orientated) growth of one mineral on another. Such fluid / wall-rock interaction with buffering of the sealing minerals was common. Also common was alteration of the crack

wall-rock. Feldspar was the mineral most often seen to be altered, to either pumpellyite or prehnite. It was observed on some occasions cracks appeared to have acted as conduits more than once in their history, either re-splitting to seal with later minerals, or any remaining open-void spaces being filled by later, unrelated, minerals. Such observations show that, on a small scale, fluids can completely permeate through rock via microcracks, with the interaction of the fluid and the wallrock occurring throughout. This is the type of fluid flow required to leach crystalline rocks of elements and form concentrated ore bodies. The primary conduits through the Lewisian complex, and the fractures taking the really big flow, are likely to have been the joints. Sealed joints, blocked by the same minerals which seal the microcracks, can be found throughout the region studied.

The timing of crack sealing is critical if the reasons for the hydrothermal event are to be discovered. The fracture-fracture intersections indicate that at least some of the crack sealing mineral assemblages represent a period of regional fluid permeation through the gneisses. The main assemblages are distinct in relative time, progressing from early calcite + K-feldspar, through prehnite + calcite + albite, then pumpellyite + calcite + quartz and finally stilpnomelane. This sequence formed the basis for subsequent investigation of the sealing minerals and is quite well constrained on both a local and a regional scale.

Geological relationships indicate that the Torridonian has a strong connection with the period of crack sealing. The prehnite and pumpellyite assemblages are likely to have been developed over the period between the deposition of the Stoer Group and the Applecross Formation. The orientation of the sealed cracks (predominantly the prehnite and pumpellyite assemblages were measured) indicate that the fluid permeation was largely taking place along NE-SW subvertical fractures undergoing a period if NW-SE dilatancy. The implications of these factors is that permeation took place in the late-Proterozoic, some time between 1000 ma and 800 ma, during a NW-SE extensional tectonic event. The most obvious connection with a NW-SE extensional event is to the supposed rifting during the formation of the Torridonian basin (Stewart 1982).

Stable isotopes and fluid inclusions suggest that the fluid in equilibrium with the prehnite and pumpellyite assemblages was surface derived; a meteoric hydrothermal system being suggested by the δD and $\delta^{18}O$ evolutionary trend of the fluid. The fluid appears to have been a complex brine with intermediate levels of salinity, progressing from an isotopically light to heavy δD and $\delta^{18}O$ signature with time. The salinity levels and the $\delta^{18}O$ shift of the fluid can be attributed to fluid/wall-rock interaction. The shift in the δD value of the fluid with time may be due to a change in surface fluid with time. The progression from -ve to +ve δD would be consistent with a reduction of land elevation, a

lowering of latitude, or the evaporation of fluid from a closed basin. A combination of elevation reduction during the formation of a restricted rift basin is the easiest model to envisage, given the geological controls, and can successfully account for the δD shift with time. This is similar to the situation found in the East African Rift Valley today. In light of the $\delta^{34}S$ value for crack sealing barite possessing values inconsistent with Cambrian sea water, it can be concluded that there is little, or no, Cambrian influence on the crack sealing sequence, and all the post-Laxfordian sealed cracks may be due to sub-Torridonian fluid permeation.

Fluid inclusion and stable isotope measurements on the crack sealing assemblages, although poorly constrained, suggest that the hydrothermal system was cooling with time. A progression from temperatures of around 350 °C to temperatures of 250 °C occurred between the formation of the calcite + K-feldspar cracks and the pumpellyite assemblage. This would be consistent with a deepening and cooling system, similar to that envisaged by Russell (1978). The fluid influx into the basement can be explained in terms of the imposition of hydrostatic pressure on extensional horizontal stress to overcome lithostatic pressure, so propagating fractures to depth. In light of pressure estimates, original depths of 2-4 km are suggested for the presently eroded level.

The driving force for the convection of the fluid is most likely to be due to an increased geothermal gradient during the period in question. There are two main possibilities to consider here; an increased regional geothermal gradient due to crustal thinning and underplating, or a localized increase, due to some form of high level intrusive igneous action. The evidence for igneous action within the Torridonian can be seen in the Stac Fada Member of the Stoer Group. The volcanic mud flow presents the possibility of convection as a result of high level igneous intrusion, but this unit is of limited outcrop whereas the sealed cracks occur on a regional scale, from Gruinard Bay to Rispond. This supports a regional increase in the geothermal gradient and suggests the driving force was an increased heat flow due to crustal thinning and underplating. Although hot-spots associated with high level activity, have not been found, their presence cannot be ruled out.

The discovery of a major period of hydrothermal circulation has obvious implications to the discovery of enriched ore bodies. With the later cracks being sealed by pyrite and barite, sulphides and sulphates have clearly been present within the mineralizing fluids, these phases however are not major. Crack sealing calcite often showed traces of nickel on the E.D.X.S spectra. Despite these occurrences, the Lewisian central region, where the majority of this study took place, is chemically depleted in RE and LIL elements.

Therefore, it is perhaps not the most likely place to get concentrations of economic elements preserved. Economic mineral accumulations do exist in the Lewisian's southern region near Gairloch. Assuming the period of hydrothermal circulation extended that far South, the Torridonian unconformity there may hold prospects.

Porosities and permeabilities of the Lewisian rocks are both inhomogeneous and low. Porosity averages about 0.8% with permeabilities any where from 100 nd to 10 μd. Since it has become clear that the sealed cracks of interest did not form and seal within the deep crust, the estimation of the palaeopermeability becomes of more general interest. It is known that cracks can stay open to the depths estimated for Lewisian crack sealing, and the important application for this part of the project is to establish whether permeability can be estimated from S.E.M. pictures and sealed cracks.

The recognition that porosity and crack density operate on two separate levels, and have separate configurations, was critical to being able to calculate the permeability with accuracy. The compared examples, of core test and S.E.M. estimate from the same rocks, suggest that using the calculations provided in Chapter 6 and the program MODEL in Appendix 10, the permeability of a crystalline rock can be accurately estimated from S.E.M. photographs. By the same reasoning if open cracks can provide accurate estimates so then can sealed cracks (assuming the criteria for selection are fulfilled). The study has shown that estimates for sealed cracks have similar values to those for open cracks and core tests. This is in contrast to the estimates of Hall (1986) which were as high as 1 darcy for a crack of 50 μm width. The calculations providing this value were for K_f only, that is fracture permeability alone. Taking account of the likely spacing between the cracks to calculate K_s (see Chapter 1), and the asperities on the crack-wall, values similar to the calculated sealed crack permeabilities of this study are derived (that is 3-4 orders of magnitude less.than those suggested by Hall (1986)).

From this work, although it cannot truly be analogous, it seems unlikely that permeability is any greater at depth than it is at the surface. These cracks may have been associated with substantial ground water flow, but no more substantial than rocks under similar conditions in the laboratory.

The implications of accurately being able to predict palaeopermeability are important, especially when considering petroleum migration. Source rock shale, although having greater porosity, is similar to crystalline rock in permeability terms. Little is known about primary migration from the source rock, except that it occurs, and is thought to occur along hydrofractures produced as a result of formational over pressure. Being able to predict the permeability that cracks sealed during this event afforded the rock, leads to the possibility of predicting the direction of migration and the volume of

petroleum expelled. This might allow better predictions of migration pathways and accumulation volumes, leading to reduction of development risk for new fields.

7.3 Suggestions for further work

There are several areas touched upon in this work which would benefit further study.

1. From the point of Lewisian geology, the Inverian deformation and metamorphism. is one of the few events not to be dated, and continues to be enigmatic.

2. The calibration of pumpellyite and prehnite (especially prehnite) for δD fractionation with water would benefit the study of hydrothermal systems, particularly because prehnite and pumpellyite are commonly found, they are index minerals and are present in many hydrothermal situations, not least sea floor hydrothermal systems. Considerable error probably exists within this work, due to these minerals not being calibrated.

3. Further study of the sealed cracks within the Lewisian would be of interest. Observations near the Lewisian- Torridonian unconformities are likely to be the most productive. There are many locations not covered by this study and there is scope to better define the hydrothermal event.

4. One area omitted from this study has been the Moine Thrust. Evidence suggests it was associated with a thermal anomaly across the region, and might have been associated with fracturing and possible hot fluids. This should be looked at as a serious candidate for some of the less well defined crack sealing episodes.

5. Application of permeability modelling to sealed cracks within petroleum source rocks could prove a very useful addition to the methods currently used in migration prediction.

6. Further study into the problem of reflective lower crust is obviously required, as this study has revealed nothing about that original problem, except that fracture permeability is unlikely to be any larger at depth than it presently is at the surface. How such research should be approached is not obvious. Deep drilling may be an option, although a very expensive one.

REFERENCES

ALI, M. 1983. Study of shear wave velocities in the Lewisian metamorphic complex of N.W. Scotland. *Unpublished Ph. D. Thesis*, Glasgow University.

ALLISON, I. & RUSSELL, M. J. 1985. Anhydrite discovered in the Fucoid Beds of N.W. Scotland. *Journal of Sedimentary Petrology*, **55**, 917-8.

ANDERSON, O. L. & GREW, P. C. 1977. Stress corrosion theory of crack propagation with application to geophysics. *Reviews in Geophysics and Space Physics*, **15**, 77-104.

BARNICOAT, A. C. 1983. Metamorphism of the Scourian complex, N.W. Scotland. *Journal of Metamorphic Geology*, **1**, 163-82.

BARNICOAT, A. C. 1987. The causes of high grade metamorphism of the Scourie complex, N.W. Scotland. In: PARK, R. G. & TARNEY, J. (eds), *Evolution of the Lewisian and comparable Precambrian high grade terrains. Geological Society Special Publication*, **27**, 73-9.

BARNICOAT, A. C. & O'HARA, M. J. 1979. High temperature pyroxenes from an ironstone at Scourie, Sutherland. *Mineralogical Magazine*, **43**, 371-5.

BATZLE, M., SIMMONS, G. & SIEGFRIED, R. W. 1980. Microcrack closure in rocks under stress: Part 1, direct observation. *Journal of Geophysical Research*, **85**, 7072 -90.

BEACH, A. 1973. The mineralogy of high temperature shear zones at Scourie, N. W. Scotland. *Journal of Petrology*, **14**, 231-48.

BEACH, A. 1975. The geometery of en-echelon vein arrays. *Tectonophysics*, **28**, 245-63.

BEACH, A. 1976. The interrelationships of fluid transport, deformation, geochemistry and heat flow in Early Proterozoic shear zones in the Lewisian complex. *Philosophical Transactions of the Royal Society of London*, **A280**, 569-604.

BEACH, A. 1980 a. Numerical models of hydraulic fracturing and the interpretation of syntectonic veins. *Journal of Structural Geology*, **2**, 425-38.

BEACH, A. 1980 b. Retrogressive metamorphic processes in shear zones with special reference to the Lewisian complex. *Journal of Structural Geology*, **1**, 275-63.

BEAMISH, D. & SMYTHE, D. K. 1986. Geophysical images of the deep crust: the Iapetus suture. *Journal of the Geological Society*,**143**, 489-97.

BERNABE, Y. 1987. The effective pressure law for permeability during pore pressure and confining pressure cycling of several crystalline rocks. *Journal of Geophysical Research*,**92**, 649-57.

BICKERMAN, M., BOWES, D. R. & van BREEMEN, O. 1975. Rb-Sr whole rock isotopic studies of the Lewisian metasediments and gneisses of the Loch Maree region, Ross-shire. *Journal of the Geological Society of London*, **131**, 237-54.

BIRCH, F. 1960. The velocity of compressional waves in rocks to 10 kbar, 1. *Journal of Geophysical Research*, **65**, 1083-102.

BISCHOFF, J. L., RADTKE, A. S. & ROSENBAUER, R. J. 1981. Hydrothermal alteration of greywacke by brine and seawater: roles of alteration and chloride complexing on metal solubilization at 200 °C and 350 °C. *Economic Geology*, **76**, 659-76.

BOIS, C., CAZES, M., DAMOTTE, B., GALDEANO, A., HIRN, A., MATTE, P., RAOULT, J. F. & TORREILLES, G. 1986. Deep seismic profiling of the crust in northern France: the ECORS project. In: BORAZANGI, M. & BROWN, L. (eds) *Reflection Seismology: A Global Perspective*. Geodynamics Series,**13**, 21-9. American Geophysical Union.

BORTHWICK, J. & HARMON, R. S. 1982. A note regarding ClF_3 as an alternative to BrF_5 for oxygen isotope analysis. *Geochemica et Cosmochimica Acta*, **46**, 1665-8.

BOSTICK, N. H. 1974. Phytoclasts as indicators of thermal metamorphism, Franciscan assemblage and Great Valley sequence (Upper Mesozoic), California. In: DUTCHER, R. R., HACQUEBARD, P. A., SCHOPF, J. M. & SIMON, J. A. (eds), *Geological Society of America Special Paper,* **153**, 1-17.

BOTTINGA, Y. & JAVOY, M. 1973. Comments on oxygen isotope geothermometery. *Earth and Planetary Sciences Letters,* **20**, 251-65.

BOWERS, T. S. & TAYLOR, H.P. 1985. An integrated chemical and stable-isotope model of the origin of mid-ocean ridge hot spring systems. *Journal of Geophysical Research,* **90**, 12583-606.

BOWES, D. R. 1968. An orogenic interpretation of the Lewisian of Scotland. *Proceedings of the 23rd International Geological Congress*, **4**, 225-36.

BOWES, D. R. 1972. Geochemistry of Precambrian crystalline rocks, northwest Highlands of Scotland. *Proceedings of the24th International Geology Congress*, **1**, 99-103.

BOWES, D. R. 1976. Archaean crustal history of north-western Britain. In: WINDLEY, B. F. (ed), *The early history of the Earth*, 469-79. Wiley.

BOWES, D. R. 1978. Shield formation in early Precambrian times: The Lewisian complex. In: BOWES, D. R. & LEAKE, B. E. (eds), *Crustal evolution in north-western Britain and adjacent regions. Geological Society Special Publication*, **10**, 39-80.

BOWES, D. R. & HOPGOOD, A. M. 1973. Framework of Precambrian crystalline complex of northwestern Scotland. In: PIDGEON, R. T., MACINTYRE, R. M., SHEPPARD, S. M. F. & van BREEMEN, O. (eds), *Geochronology and isotope geology of Scotland. 3rd European Congress of Geochronologists*, **A**1-14, East Kilbride.

BOWIE, S. H. U., DAWSON, J., GALLAGHER, M. J., OSTLE, D., LAMBERT, R. St. J. & LAWSON, R. I. 1966. Potassium-rich sediments in the Cambrian of northwest Scotland. *Transactions of the Institute of Mining and Metallurgy, (Section B: Applied earth science)*, **75**, 125-45.

BRACE, W. F. 1977. Permeability from resistivity and pore shape. *Journal of Geophysical Research*, **82**, 3343-9.

BRACE, W. F. 1984. Permeability of crystalline rocks: new insitu measurements. *Journal of Geophysical Research*, **89**, 4327-30.

BRACE, W. F., WALSH, J. B. & FRANGOS, W. T. 1968. Permeability of granite under high pressure. *Journal of Geophysical Research*, **73**, 2225-36.

BRANTLEY, S. L., CRERAR, D. A. & EVANS, B. 1986. Rates and mechanisms of porosity reduction in quartz: implications for fluid flow in rocks. *International Association of Geochemistry and Cosmochemistry. Fifth International Symposium on Water-Rock Interaction*, **(WRI-5)**, 79-82. Reykjavik, Iceland.

BROWN, E. T. 1981. *Rock characterization, testing and monitoring. ISRM Suggeted Methods*, 81-9, Pergamon Press.

BRUNER, W. M. 1979. Crack growth and the thermoelastic behaviour of rocks. *Journal of Geophysical Research*, **84**, 5578-90.

BURKE, W. H., DENISON, R. E., HETHERINGTON, E. A., KOEPNICK, R. B., NELSON, H. F. & OTTO, J. B. 1980. Variation of seawater $^{87}Sr/^{86}Sr$ throughout Phanerozoic time. *Geology*, **10**, 516-9.

CARTWRIGHT, I. 1988. Crystallization of melts, pegmatite intrusion and the Inverian retrogression of the Scourian complex, north-west Scotland. *Journal of Metamorphic geology*, **6**, 77-93.

CARUSO, L. & SIMMONS, G. 1985. Uranium and microcracks in a 1000-meter core, Redstone, New Hampshire. *Contributions to Mineralogy and Petrology*, **90**, 1-17.

CHAPMAN, H. J. 1979. 2,390 myr. Rb-Sr whole rock for the Scourie dykes of N. W. Scotland. *Nature*, **277**, 642-3.

CHAPMAN, H. J. & MOORBATH, S. 1977. Lead isotope measurements from the oldest recognised Lewisian gneisses of North West Scotland. *Nature*, **268**, 41-2.

CLAYPOOL, G. E., MOLSER, W. T., KAPLAN, I. R., SAKAI, M. & ZAK, I. 1980. The age curves of sulphur and oxygen isotopes in marine sulphate and their mutual interpretation. *Chemical Geology*, **28**, 199-260.

CLAYTON, R. N., O'NEIL, J. R. & MAYEDA, T. K. 1972. Oxygen isotope exchange between quartz and water. *Journal of Geophysical Research,* **77**, 3057-67.

CLAYTON, R. N.,GOLDSMITH, J. R., KAREL, K. J., MAYEDA, T. K. & NEWTON, R. C. 1975. Limits on the effect of pressure on isotopic fractionation. *Geochemica et Cosmochimica Acta,* **39**, 1197-201.

CLIFF, R. A., GRAY, C. M. and HUHMA, H. 1983. A Sm-Nd isotopic study of the South Harris igneous complex, the Outer Hebrides. *Contributions to Mineralogy and Petrology*, **82**, 91-8.

COLEMAN, M. L. & MOORE, M. P. 1978. Direct reduction of sulphates to sulphur dioxide for isotopic analysis. *Analytic Chemistry*, **50**, 1594-5.

COOMBS, D.S., NAKAMURA, Y., & VUAGNAT, M. 1976. Pumpellyite-actinolite facies schists of the Taveyanne Formation near Loeche, Valais, Switzerland. *Journal of Petrology,* **17**. 440-71.

CONNERNEY, J. E. P., NEKUT, A. & KUCKES, A. F. 1980. Deep crustal conductivity in the Adrionda cks. *Journal of Geophysical Research*, **85**, 2615-24.

COOPER, H. W. & SIMMONS, G. 1977. The effect of cracks on the thermal expansion of rocks. *Earth and Planetary Sciences Letters*, **36**, 402-12.

COSTAIN, J. K., BOLLINGER, J. & SPEER, J. A. 1987. Hydroseismicity - a hypothesis for the role of water in the generation of interplate seismicity. *Geology*, **15**, 618-21.

COWARD, M. P. & PARK, R. G. 1987. The role of mid-crustal shear zones in the Early Proterozoic evolution of the Lewisian. In: PARK, R. G. & TARNEY, J. (eds), *Evolution of the Lewisian and comparable Precambrian high grade terrains. Geological Society Special Publication*, **27**,127-38.

DASH, B. 1969. The structure of the Lewisian rocks between Strath Dionard and Rhiconich, Sutherland. *Scottish Journal of Geology*, **5**, 347-74.

DAVIES, F. B. 1976. Early Scourian structure in the Scourie-Laxford region and their bearing on the evolution of the Laxford front. *Journal of the Geological Society of London*, **132**, 543-54.

DEINES, P., LONGMUIR, D. & HARMON, R. S. 1974. Stable carbon isotope ratios and the existence of a gas phase in the evolution of a carbonate ground water. *Geochemica et Cosmochimica Acta*, **38**, 1147-64.

DUNNING, J. D., LEWIS, W. L. & DUNN, D. E. 1980. Chemomechanical weakening in the presence of surfactants. *Journal of Geophysical Research*, **85**, 5344-54.

ENGELDER, T. & SCHOLZ, C. H. 1981. Fluid flow along very smooth joints at effective pressures up to 200 megapascals. In: CARTER, N. L., FRIEDMAN, M., LOGAN, J. M. & STEARNS, D. W. (eds), *Mechanical Behaviour of Crustal Rocks. Geophysical monograph* **24**,147-52, American Geophysical Union.

ETHERIDGE, M. A., WALL, V. J. & VERNON, R. H. 1983. The role of fluid phase during regional metamorphism and deformation. *Journal of Metamorphic Geology*, **1**, 205-26.

EVANS, C. R. 1965. Geochronology of the Lewisian basement near Lochinver, Sutherland. *Nature*, **207**, 54-6.

EVANS, C. R. & TARNEY, J. 1964. Isotopic ages of Assynt dykes. *Nature*, **204**, 638-41.

EVANS, C.R. & LAMBERT, R. St. J. 1974. The Lewisian of Lochinver, Sutherland. The type area for the Invarian metamorphism. *Quarterly Journal of the Geological Society of London*, **130**, 125-50.

EVARTS, R. C. & SCHIFFMAN, P. 1983. Submarine hydrothermal metamorphism of the Del Puerto ophiolite, California. *American Journal of Science*, **283**, 289-340.

FAURE, G. 1977. *Principles of isotope geology*. Wiley.

FETTES, D. J. & MENDUM, J. R. 1981. The geology of the Outer Hebrides. *Institute of Geological Sciences Report.*

FEVES, M. & SIMMONS, G. 1976. Effects of stress on Westerly granite. *Bulletin of the Seismological Society of America*, **66**, 1755-65.

FEVES, M., SIMMONS, G. & SIEGFRIED, R. W. 1977. Microcracks in crustal igneous rocks: physical properties. *The Earths Crust, Geophysical Monograph* **20**, 95-177.

FINDLAY, D. 1970. Studies of fold tectonics in the Lewisian of the Durness region, Sutherland. *Unpublished Ph. D. Thesis*, University of Glasgow.

GANGI, A. F. 1978. Variation of whole and fractured porous rock permeability with confining pressure. *International Journal of RockMechanics, Mining Science and Geomechanical Abstracts*,**15**,249-57.

GILLEN, C. 1975. Structural and metamorphic history of The Lewisian gneiss around Loch Laxford, Sutherland, Scotland. *Krystalinikum*,**11**, 63-85.

GLASSLEY, W. 1974. A model for phase equilibria in the prehnite-pumpellyite facies. *Contributions to Mineralogy and Petrology*, **43**, 317-32.

GODFREY, J. D. 1962. The deuterium content of hydrous minerals from the East-Central Sierra Nevada and Yosemite National Park. *Geochemica et Cosmochimica Acta*, **26**, 1215-45

GRACIE, A. J. & STEWART, A. D. 1967. Torridonian sediments at Enard Bay, Ross-shire. *Scottish Journal of Geology*, **3**, 181-94.

GRAHAM, C. M., SHEPPARD, S. M. F. & HEATON T. H. E. 1980. Experimental hydrogen isotope studies 1. Systematics of hydrogen isotope fractionation in the systems epidote- H_2O, zoisite-H_2O and AlO(OH)-H_2O. *Geochemica et Cosmochimica Acta*,**44**, 353-64.

GRAHAM, C. M., & SHEPPARD, S. M. F. 1980. Experimental hydrogen isotope studies 2. Fractionations in the systems epidote-NaCl-H_2O, epidote-$CaCl_2$-H_2O and epidote-seawater, and the hydrogen isotope compositions of natural epidotes. *Earth and Planetary Sciences Letters,* **49**, 237-51.

GREEN, A. G., MILKERIT, B., MAYRAND, L., SPENCER, C., KURTZ, R. & CLOWES, R. M. 1987. Lithoprobe seismic reflection profiling across Vancouver Island: results from reprocessing. *Geophysical Journal of the Royal Astronomical Society*, **89**, 85-90.

HADLEY, K. 1976. Comparison of calculated and observed crack densities and seismic velocities in Westerly Granite. *Journal of Geophysical Research*, **81**, 3484-94.

HALL, J. 1986. The physical properties of layered rocks in deep continental crust. In: DAWSON, J. B., CARSWELL, H., HALL, J. & WEDEPOHL, H. (eds), *The nature of the lower continental crust. Geological Society Special Publication*, **24**, 51-62.

HALL, J. 1987. Physical properties of Lewisian rocks: implications for deep crustal structure. In: PARK, R. G. & TARNEY, J. (eds), *Evolution of the Lewisian and Comparable Precambrian High Grade Terrains. Geological Society Special Publication*, **27**, 185-92.

HALL, J. and ALI, M. 1985. Shear waves in a seismic survey of Lewisian basement: An extra control on lithological variation and porosity. *Journal of the Geological Society of London*, **142**, 677-688.

HALL, J. & SIMMONS, G. 1979. Seismic velocities of Lewisian metamorphic rocks at pressures to 8 kbar: relationship to crustal layering in North Britain. *Geophysical Journal of the Royal Astronomical Society*, **58**, 337-47.

HAY, S. J. , HALL, J., SIMMONS, G. & RUSSELL, M. J. 1988. Sealed cracks in the Lewisian: a record of 2 billion years of fluid circulation. *Journal of the Geological Society of London*, **145**, 819-30.

HAMILTON, P. J., EVENSEN, N. M., O'NIONS, R. K. & TARNEY, J. 1979. Sm-Nd systematics of Lewisian gneisses: Implications for the origin of granulites. *Nature*, **277**, 25-8.

HENYEY, T. E., OKAYA, D. A.,FROST, E. G. & McEVILLY, T. V. 1987. CALCRUST (1985) seismic reflection survey, Whipple mountains detachment terrain, California: An overview. *Geophysical Journal of the Royal Astronomical Society*, **89**, 111-8.

HOLSER, W. T. & KAPLAN, I. R. 1966. Isotope geochemistry of sedimentary sulphates. *Chemical Geology*, **1**, 93-135.

HUMPHRIES, F. J. & CLIFF, R. A. 1982. Sm-Nd dating and cooling history of Scourian granites, Sutherland. *Nature*, **295**, 515-7.

IWAI, K. 1976. Fundamental studies of fluid flow through a single fracture. *Ph. D. Thesis,* University of California, Berkeley.

JEHU, T. J. & CRAIG, R. M. 1923. Geology of the Outer Hebrides. Part I, The Barra Isles. *Transactions of the Royal Society of Edinburgh*, **53**, 419-41.

JEHU, T. J. & CRAIG, R. M. 1925. Geology of the Outer Hebrides. Part II, South Uist and Eriskay. *Transactions of the Royal Society of Edinburgh*, **53**, 615-41.

JEHU, T. J. & CRAIG, R. M. 1926. Geology of the Outer Hebrides. Part III, North Uist and Benbecula. *Transactions of the Royal Society of Edinburgh*, **54**, 467-89.

JEHU, T. J. & CRAIG, R. M. 1927. Geology of the Outer Hebrides. Part IV, South Harris. *Transactions of the Royal Society of Edinburgh*, **55**, 457-88.

JEHU, T. J. & CRAIG, R. M. 1934. Geology of the Outer Hebrides. Part V, North Harris and Lewis. *Transactions of the Royal Society of Edinburgh*, **57**, 839-74.

JENKIN, G. R. T. 1988. Stable isotope studies in the Caledonides of south-west Connemara, Ireland. *Unpublished Ph.D. Thesis*, Glasgow University.

JODICKE, B., UNTIEDT, J., OLGEMANN, W., SCHULTE, L. & WAGENITZ, V. 1983. Electrical conductivity structure of the crust and upper mantle beneath the Rhenish Massif. In: FUCHS, K. (ed), *Plateau Uplift*, 288-302, Springer-Verlag.

JOHNSON, M. R. W. 1983. Torridonian - Moine. In: CRAIG, G. Y. (ed), *Geology of Scotland, 2nd edition*, 49-75, Scottish Academic.

JOHNSON, M. R. W., KELLEY, S. P., OLIVER, G. J. H. & WINTER, D. A. 1985. Thermal effects and timing of thrusting in the Moine Thrust zone. *Journal of the Geological Society of London*, **142**, 836-74.

JOHNSON, B. & GANGI, A. F. 1980. Thermal cracking of non uniformly heated, thick-walled cylinders of Westerly Granite. *Proceedings of the 21st U.S. Symposium on Rock Mechanics,* 197-226, Rolla, Montanna.

JONES, A. G. 1987. MT and reflection: an essential combination. *Geophysical Journal of the Royal Astronomical Society*, **89**, 7-18.

JONES, E. M., RICE, C. M. & TWEEDIE, J. R. 1987. Lower Proterozoic stratiform sulphide deposits in the Loch Marie Group, Gairloch, northwest Scotland. *Transactions of the Institution of mining and Metallurgy, (Section B: Applied earth science)*, **96**, 128-40.

KHOURY, S. G. 1968. The structural geometery and geological history of the Lewisian rocks between Kylesku and Geisgeil, Sutherland, Scotland. *Krystalinikum*, **6**, 41-78.

KHOURY, S. G. 1969, Structural analysis of complex fold belts in the Lewisian North of Kylesku Sutherland, Scotland. *Scottish Journal of Geology*, **4**, 109-21.

KLEMPERER, S. 1987. A relation between continental heat flow and the seismic reflectivity of the Lower Crust. *Journal of Geophysics*, **61**, 1-11.

KLEMPERER, S. L., BROWN, L., OLIVER, J. E., AANDO, C. J., CZUCHRA, B. L. & KAUFMAN, S. 1985. Some results of COCORP seismic reflection profiling in the Grenville-age Adirondack Mountains, New York State, *Canadian Journal of Earth Sciences*, **22**, 141-53.

KRANZ, R. L. 1983. Microcracks in rocks: a review. *Tectonophysics*, **100**, 449-80.

LAMBERT, R. St. J. & HOLLAND, J. G. 1972. A geochronological investigation of the Lewisian from Loch Laxford to Durness, Sutherland, NW Scotland. *Quarterly Journal of the Geological Society of London*, **128**, 3-19.

LIOU, J. G. 1979. Zeolite facies metamorphism of basaltic rocks from the east Tiwan ophiolite. *American Mineralogist*, **64**, 1-14.

LIU, K. K. & EPSTEIN, S. 1984. The hydrogen isotope fractionation between Kaolinite and water. *Isotope Geoscience,* **2**, 335-50.

LOUIE, J. N. & CLAYTON, R. W. 1987. The nature of deep crustal structures in the Mojave Desert, California. *Geophysical Journal of the Royal Astronomical Society*, **89**, 125-32.

LYON, T. D. B. 1973. A geochronological investigation of the Lewisian rocks of North western Scotland. *Unpublished Ph. D. Thesis,* University of Strathclyde.

LYON, T. D. B. & BOWES, D. R. 1977. Rb-Sr, U-Pb and K-Ar isotope study of the Lewisian complex between Durness and Loch Laxford, Scotland. *Krystalinikum,* **13**, 53-72.

MAGARITZ, M. & TAYLOR, H. P. 1976. Oxygen, hydrogen and carbon isotope studies of the Franciscan Formation, Coast ranges, California. *Geochemica et Cosmochimica Acta,* **40**, 215-34.

MATSUHISA, Y., GOLDSMITH, J. R. & CLAYTON, R. N. 1979. Oxygen isotope fractionation in the system quartz-albite-anaathite-water. *Geochemica et Cosmochimica Acta*, **43**, 1131-40.

MATTHEWS, A., GOLDSMITH, J. R. & CLAYTON, R. N. 1983. Oxygen isotope fractionation between zoisite and water. *Geochemica et Cosmochimica Acta,* **47**, 645-54.

MATTHEWS, A., & SCHLIESTEDT, M. 1984. Evolution of the blueschist and greenschist facies rocks of Sifnos, Cyclades, Greece. *Contributions to Mineralogy and Petrology,* **88**, 150-63.

MATTHEWS, D. H. & CHEADLE, M. J. 1986 Deep reflections from the Caledonides and Voncides West of Britain and comparison with the Himalayas. In: BORAZANGI, M. & BROWN, L. *Reflection Seismology: A Global Perspective*. Geodynamics Series, **13**, 5-19 . American Geophysical Union.

McCREA, J. M. 1950. On the isotopic chemistry of carbonates and a paleotemperature scale. *Journal of Chemical Physics*, **18**, 849-57.

MEISSNER, R., SPRINGER, M., MURAWSKI, B., BARTELSEN, B., FLUH, E. R. & DURSCHNER, B. 1983. Combined seismic reflection - refraction investigations in the Rhenish Massif and their relation to recent tectonic movements. In: FUCHS, K. (ed), *Plateau Uplift*, 276-87. Springer-Verlag.

MILLS, H., HALLIDAY, A. N., ASHTON, J. H., ANDERSON, I. K. & RUSSELL, M. J. 1987. Origin of a giant orebody at Navan, Ireland. *Nature*, **327**, 223-5.

MONICARD, R. P. 1980. *Properties of reservoir rocks: core analysis*. Institut Francais du Petrole.

MOORBATH, S. 1969. Evidence of the age of deposition of the Torridonian sediments of northwest Scotland. *Scottish Journal of Geology*, **5**, 154-70.

MOORBATH, S. & PARK, R. G. 1972. The Lewisian chronology of the southern region of the Scottish mainland. *Scottish Journal of Geology*, **8**, 51-74.

MOORBATH, S., WELKE, H. & GALE, N.H. 1969. The significance of Lead isotope studies in ancient, high grade metamorphic basement complexes as exemplified by the Lewisian rocks of North West Scotland. *Earth and Planetary Science Letters*, **6**, 245-56.

MORROW, C. A., BO-CHONG, Z. & BYERLEE, J. D. 1986. Effective pressure law for permeability of westerly granite under cyclic loading. *Journal of Geophysical Research*,**91**, 3870-76.

NAKAJIMA, T., BANNO, S. & SUZUKI, T. 1977. Reactions leading to the disappearance of pumpellyite in Low-grade metamorphic rocks of the Sanbagawa metamorphic belt in Central Shikoki, Japan. *Journal of Petrology*, **18**, 263-84.

NICHOLSON, R. & POLLARD, D. D. 1985. Dilation and linkage of echelon cracks. *Journal of Structural Geology*, **7**, 583-90.

NUR, A. & SIMMONS, G. 1969. The effect of saturation on velocity in low porosity rocks. *Earth and Planetary Science Letters*, **7**, 183-93.

O'CONNELL, R. J. & BUDIANSKY, B. 1974. Seismic velocities in dry and saturated cracked solids. *Journal of Geophysical Research*, **79**, 5412-26.

O'HARA, M.J. 1961. Zoned ultrabasic and basic gneiss masses in the early Lewisian metamorphic complex at Scourie, Sutherland. *Journal of Petrology*, **2**, 248-76.

OHMOTO, H. 1986. Stable isotope geochemistry of ore deposits. In: VALLEY, J. W., TAYLOR, H. P. & O'NEIL, J. R.(eds), *Stable isotopes in high temperature geological processes. Mineralogy Society of America, Reviews in Mineralogy*,**16**, 491-560.

O'NEIL, J. R. 1986 a. Terminology and standards. In: VALLEY, J. W., TAYLOR, H. P. & O'NEIL, J. R.(eds), *Stable isotopes in high temperature geological processes. Mineralogy Society of America, Reviews in Mineralogy*,**16**, 561-70.

O'NEIL, J. R. 1986 b. Theoretical and experimental aspects of isotopic fractionation. In: VALLEY, J. W., TAYLOR, H. P. & O'NEIL, J. R.(eds), *Stable isotopes in high temperature geological processes. Mineralogy Society of America, Reviews in Mineralogy,*16, 1-40.

O'NEIL, J. R., CLAYTON, R. N. & MAYEDA, T. K. 1969. Oxygen isotope fractionation in divalent metal carbonates. *Journal of Chemical Physics,* **51**, 5547-58.

O'NEIL, J. R. & TAYLOR, H. P. 1967. The oxygen isotope and cation exchange chemistry of feldspars. *American mineralogist,* **52**, 1414-37.

O'NIONS, R. K., HAMILTON, P. J. & HOOKER, P. J. 1983. A Nd isotope investigation of sediments related to crustal development in the British Isles. *Earth and Planetary Science Letters*, **63**, 229-40.

PADOVANI, E., BATZLE, M. L. & SIMMONS, G. 1978. Characteristics of microcracks in samples from the drill hole Nordlingen 1973, in the Ries crater, Germany. *Proceedings of the 9th Lunar Science Conference.*

PADOVANI, E., SHIREY, S. B. & SIMMONS, G. 1982. Characteristics of microcracks in amphibolite and granulite facies grade rocks from southeastern Pennsylvania. *Journal of Geophysical Research*, **87**, 8605-30.

PALMER, T. J., McKERROW, W. S. & COWIE, J. W. 1980. Sedimentological evidence for a stratigraphical break in the Durness Group. *Nature*, **287**, 720-722.

PARK, R. G. 1966. The structural history of the Lewisian rocks of Gairloch, Wester Ross, Scotland. *Quarterly Journal of the Geological Society of London*, **120**, 397-434.

PARK, R. G. & CRESSWELL, D. 1972. Basic dykes in the Early Precambrian (Lewisian) of N. W. Scotland: their structural relations, conditions of emplacement and orogenic significance. *Proceedings of the 24th international Geological Congress*, **1**, 238-45.

PARK, R. G. & TARNEY, J. 1987. The Lewisian complex: a typical Precambrian high-grade terrain? In: PARK, R. G. & TARNEY, J. (eds), *Evolution of the Lewisian and Comparable Precambrian High Grade Terrains. Geological Society Special Publication*, **27**, 13-25.

PARK, S. & SIMMONS, G. 1982. Crack induced velocity anisotropy in the White Mountains, New Hampshire. *Journal of Geophysical Research*, **87**, 2972-84.

PEACH, B. N., HORNE, J., GUNN, W., CLOUGH, C. T., HINXMAN, L. W. & TEALL, J. J. 1907. The geological structure of the northwest Highlands of Scotland. *Memoirs of the Geological Survey, U. K.*

PIDGEON, R. T. & BOWES, D.R. 1972. Zircron U-Pb ages of granulites from the Central region of the Lewisian, northwestern Scotland. *Geological Magazine*, **109**, 247-58.

PINE, R. & BATCHELOR, A. 1984. Downward migration of shearing in jointed rock during hydraulic injections. *International Journal of Rock Mechanics, Mining Science and Geotechnical Abstracts*, **21**, 249-63.

PINET, B., MONTADERT,L., & the ECORS Scientific Party 1987. Deep seismic reflection and refraction profiling along the Aquitane shelf (Bay of Biscay). *Geophysical Journal of the Royal Astronomical Society*, **89**, 305-12.

PLYUSINA, L. P. & IVANOV, I. P. 1978. P-T limits and fluid balance of prehnite - pumpellyite facies of metamorphism from experimental data. *International Geological Reviews*, **20**, 741-801.

POTTER, R. W. 1977. Pressure corrections for fluid inclusion homogenization temperatures based on the volumeric properties of the system NaCl-H_2O. *United States Geological Survey Journal of Research*, **5**, 603-7.

RAMSAY, J. G. 1980. The crack seal mechanism of rock deformation. *Nature*, **284**, 135-9.

RAVEN, K. G. & GALE, J. E. 1985. Water flow in a natural rock fracture as a function of stress and sample size. *International Journal of RockMechanics, Mining Science and Geomechanical Abstracts*,**22**,251-61.

RICHTER, D. & SIMMONS, G. 1977. Microcracks in crustal igneous rocks: microscopy. In: HEACOCK, J. G. (ed.), *The Earths Crust: Its nature and physical properties.* Geophysical monograph **20**,149-80. American Geophysical Union.

ROEDDER, E. 1985. Fluid inclusions. *Mineralogical Society of America, Reviews in mineralogy,* **12**.

ROEDDER, E. & BODNAR, R. J. 1980. Geologic pressure determinations from fluid inclusion studies. *Annual Reviews of Earth and Planetary Sciences*, **8**, 263-301.

ROLLINSON, H. R. 1981. Garnet-pyroxene thermobarometery in the Scourie granulites, NW Scotland. *Lithos*, **14**, 225-38.

RONOV, A. B. & MIGDIJOV, A. A. 1971. Geochemical history of the crystalline basement and the sedimentary cover of the Russian and North American platforms. *Sedimentology,* **16**, 137-85.

RUSSELL, M. J. 1978. Downward - excavating hydrothermal cells and Irish-type ore deposits: importance of an underlying thick Caledonian prism. *Transactions of the Institution of Mining and Metallurgy*, (*Section B: Applied earth sciences*), **87**, 168-71.

RUSSELL, M. J. & ALLISON, I. 1985. Agalmatolite and maturity of sandstones of the Appin and Argyll groups and Eriboll sandstone. *Scottish Journal of Geology*, **21**, 113-22.

SAVAGE, D. & SILLS, J. D. 1980. High pressure metamorphism in the Scourian of Scotland: evidence from garnet granulites. *Contributions to Mineralogy and Petrology*, **74**, 153-63.

SCHIFFMAN, P. & LIOU, J. G. 1980. Synthesis and stability relations of Mg-Al pumpellyite, $Ca_4 Al_5 Mg Si_6 O_{21}(OH)_7$. *Journal of Petrology*, **21**, 441-74.

SCHIFFMAN, P. & LIOU, J. G. 1983. Synthesis of Fe-pumpellyite and its stability relations with epidote. *Journal of Metamorphic Geology*, **1**, 91-101.

SELLEY, R. C. 1969. Torridonian alluvium and quicksands. *Scottish Journal of Geology*, **5**, 328-46.

SHEPPARD, S. M. F. 1986. Characterization and isotopic variations in natural waters. In: VALLEY, J. W., TAYLOR, H. P. & O'NEIL, J. R.(eds), *Stable isotopes in high temperature geological processes. Mineralogy Society of America, Reviews in Mineralogy*,**16**, 165-84.

SHIREY, S. B., SIMMONS, G. & PADOVANI, E. M. 1980. Angular, orientated microtubes in metamorphic plagioclase. *Geology*, **8**, 240-4.

SIEGFRIED, R. W. & SIMMONS G. 1978. Characterization of orientated cracks with Differential Strain Analysis. *Journal of Geophysical Research*, **83**, 1269-78.

SIEGFRIED, R. W., SIMMONS, G., RICHTER, D. & HORZ, F. 1977. Microfractures produced by a laboratory scale hypervelocity impact into granite. *Proceedings of the 8th Lunar Science Conference*, 1249-70.

SIGVALDSON, G. E. 1963. Epidote and related minerals in two deep geothermal drill holes, Reykjavik and Hveragerdi, Iceland. *United States Geological Survey Professional Paper* **450-E**, E77-9.

SILLS, J. D. 1983. Mineralogical changes occurring during the retrogression of Archaean gneisses from the Lewisian complex of NW Scotland. *Lithos*, **16**, 113-24.

SILLS, J. D. & ROLLINSON, H. R. 1987. Metamorphic evolution of the mainland Lewisian complex. In: PARK, R. G. & TARNEY, J. (eds), *Evolution of the Lewisian and comparable Precambrian high grade terrains. Geological Society Special Publication*, **27**,81-92.

SIMMONS, G. 1964. Velocity of shear waves in rocks to 10 kb, part 1. *Journal of Geophysical Research*, **69**, 1123-30.

SIMMONS, G., BATZLE, M., COOPER, H., SIEGFRIED, R. & FEVES, M. 1978. Characterisation of microcracks. *Proceedings volume, Conference on Mechanisims of Deformation and Faulting.* (Lulea-Sweden), 151-157.

SIMMONS, G. & COOPER, H. W. 1978. Thermal cycling cracks in three igneous rocks. *International Journal Rock Mechanics, Mining Science and Geomechanical Abstracts*, **15**, 145-8.

SIMMONS, G. & RICHTER, D. 1976. Microcracks in rock. In: STRENS, R. G. J. (ed.), *The physics and Chemistry of Minerals and Rocks*, 105-37. Wiley.

SIMMONS, G., SIEGFRIED, R.W. & FEVES, M. 1974. Differential Strain Analysis: A new method for examining cracks in rocks *Journal Geophysical Research*, **79**, 4383-5

SMITHSON, S. B., JOHNSON, R. A., HURICH, C. A.,VALASEK, P. A., & BRANCH, C. 1987. Deep crustal structure and genesis from contrasting reflection patterns: an integrated approach. *Geophysical Journal of the Royal Astronomical Society*, **89**, 67-72.

SMYTHE, D. K., SOWERBUTTS, W. T. C., BACON, M. & MCQUILLIN, R. 1972. Deep sedimentary basin below northern Skye and the Little Minch. *Nature*, **236**, 87-9.

SPRUNT, E. & BRACE, W. F. 1974. Some permenent structural changes in rock due to pressure and temperature. *Proceedings of the 3rd Congress of the International Society of Rock Mechanics*, **II-A**, 524-9.

STEWART, A. D. 1969 Torridonian rocks of Scotland reviewed. In: KAY, M. (ed), *North Atlantic- geology and continental drift, American Association of Petroleum Geologists Memoir*, **12**, 595-608.

STEWART, A. D. 1982. Late Proterozoic rifting in NW Scotland: the genesis of the "Torridonian". *Journal of the Geology Society of London*, **139**, 413-20.

STEWART, A. D. 1988 a. The Stoer Group, Scotland. In: WINCHESTER, J. A. (ed), *Later Proterozoic stratigraphy of the northern Atlantic regions*, 97-103. Blackie.

STEWART, A. D. 1988 b. The Sleat and Torridon Groups. In: WINCHESTER, J. A. (ed), *Later Proterozoic stratigraphy of the northern Atlantic regions*, 104-12. Blackie.

SUTTON, J. & WATSON, J. V. 1951. The pre-Torridonian metamorphic history of the Loch Torridon and Scourie areas in the Northwest Highlands, and its bearing on the classification of the Lewisian. *Quarterly Journal of the Geological Society of London.* **106**, 241-308.

SUTTON, J. & WATSON, J. V. 1960. Sedimentary structures in the epidotic grits of Skye. *Geological Magazine*, **97**, 106-22.

SUTTON, J. & WATSON, J. V. 1962. Further observations on the margin of the Laxfordian complex of the Lewisian near Loch Laxford, Sutherland. *Transactions of the Royal Society of Edinburgh,* **45**, 90-106.

SUZUOKI, T. & EPSTEIN, S. 1976. Hydrogen isotope fractionation between OH- bearing minerals and water. *Geochemica et Cosmochimica Acta,* **40**, 1229-40.

SWETT, K. 1969. Interpretation of depositional and diagenetic history of Cambrian - Ordovician succession of northwest Scotland. In: KAY, M. (ed), *North Atlantic-geology and continental drift, American Association of Petroleum Geologists Memoir,***12**, 630-646.

TAKEUCHI, S. & SIMMONS, G. 1973. Elasticity of water-saturated rocks as a function of temperature and pressure. *Journal of Geophysical Research*, **78**, 3310-9.

TARNEY, J. 1973. The Scourie dyke suite and the nature of the Inverian event in Assynt. In: PARK, R. G. & TARNEY, J. (eds), *The Early Precambrian of Scotland and related rocks of Greenland*, 105-16. University of Keele.

TARNEY, J. & WEAVER, B. L. 1987. Mineralogy, petrology and geochemistry of the Scourie dykes: petrogenesis and crystallisation processes in dykes intruded at depth. In: PARK, R. G. & TARNEY, J. (eds), *Evolution of the Lewisian and comparable Precambrian high grade terrains. Geological Society Special Publication*, **27**, 217-33.

TAYLOR, B. E. & O'NEIL, J. R. 1977. Stable isotopes studies of metasomatic skarns and associated metamorphic and igneous rocks, Osgood Moutains, Nevada. *Contributions to Mineralogy and Petrology*, 63, 1-49.

UREY, H. C. 1947. The thermodynamic properties of isotopic substances. *Journal of the Chemical Society*,1947 ,562-81.

van BREEMEN, O., AFTALION, M. & PIDGEON, R. T. 1971. The age of the granitic injection complex of Harris, Outer Hebrides. *Scottish Journal of Geology*, **7**, 139-52.

VAUGHAN, P. J., MOORE, D. E., MORROW, E. A. & BYERLEE, J. D. 1986. Role of cracks in progressive permeability reduction during flow of heated aqueous fluids through granite. *Journal of Geophysical Research*, **91**, 7517-30.

VEIZER, J. 1976. $^{87}Sr/^{86}Sr$ evolution of seawater during geologic history and its significance as an index of erustal evolution. In: WINDLEY, B. F. (ed.) *The Early History of the Earth*, 569-78, Wiley-Interscience.

VEIZER, J., HOLSER, W. T. & WILGUS, C. K. 1980. Correlation of $^{13}C/^{12}C$ and $^{34}S/^{32}S$ secular variations. *Geochemica et Cosmochimica Acta*, **44**, 579-87.

WALSH, J. B. 1965. The effect of cracks on the compresibility of rock. *Jounal of Geophysical Research*, **70**, 381-389.

WALSH, J. B. 1981. Effect of pore pressure and confining pressure on fracture permeability. *International Journal of RockMechanics, Mining Science and Geomechanical Abstracts*,**18**,429-35.

WALSH, J. B. & BRACE, W. F. 1984. The effect of pressure on porosity and the transport properties of rock. *Journal of Geophysical Research*, **89**, 9425-32.

WALTON, E. N. K. 1983. Lower Palaeozoic - stratigraphy. In: Craig, G. Y. (ed), *Geology of Scotland, 2nd edition*, 105-110. Scottish Academic.

WANG, H. F. & SIMMONS, G. 1978. Microcracks in crystalline rock form 5.3 km depth in the Michigan Basin. *Journal of Geophysical Research*, **83**, 5849-56.

WATSON, E. B. & BREENAN, J. M. 1987. Fluids in the lithosphere, 1. Experimentally determined wetting characteristics of CO_2-H_20 fluids and their implications for fluid transport, host-rock physical properties, and fluid inclusion formation. *Earth and Planetary Science Letters*, **85**, 497-515.

WATSON, J. 1975. The Lewisian Complex. In: HARRIS, A. L., SHACKLETON, R. M., WATSON, J., DOWNIE, C., HARLAND, W. B. & MOORBATH, S., *Geological Society of London Special Report*, **6**, 15-29.

WATSON, J. 1983. Lewisian. In: Craig, G. Y. (ed), *Geology of Scotland, 2nd edition*, 23-47. Scottish Academic.

WHITE, J. C. & WHITE, S. H. 1981. On the structure of grain boundaries in tectonics. *Tectonophysics*, **78**, 613-28.

WILLIAMS, G. E. 1968. Torridonian weathering, and its bearing on Torridonian palaeoclimate and source. *Scottish Journal of Geology*, **4**, 164-84.

WILLIAMS, G. E. 1969. Petrography and origin of pebbles from Torridonian strata (Late Precambrian), northwest Scotland. In: KAY, M. (ed), *North Atlantic - geology and continental drift, American Association of Petroleum Geologists Memoir*, **12**, 609-29.

WITHERSPOON, P.A., WANG, J. S. Y., IWAI, K. & GALE, J. E. 1980. Validity of cubic law for fluid flow in a deformable rock fracture. *Water Resources Research*, **16**, 1016-24.

WOLFF, R. G. 1981. Porosity, permeability, distribution coefficients, and dispersivity. In: TOULOUKIAN, Y. S. & HO, C. Y. (eds), *Physical properties of rocks and minerals. McGraw-Hill/Cindas data series on material properties*, **II-2**, 45-82.

WRIGHT, A. E. 1985, Stratigraphy of the Lewisian complex. *Unpublished manuscript.*

YONG, C. & WANG, C-Y. 1980. Thermally induced acoustic emission in Westerly Granite. *Geophysical Research Letters*, **7**, 1089-92.

ZEN, E. 1974. Prehnite and pumpellyite bearing mineral assemblages, west side of the Appalachian metamorphic belt, Pennsylvania to Newfoundland. *Journal of Petrology*, **15**,197-242.

ZOBACK, M. D. & BYERLEE, J. D. 1975 a. The effect of microcrack dilatancy on the permeability of Westerly granite. *Journal of Geophysical Research,* **80**, 752-5.

ZOBACK, M. D. & BYERLEE, J. D. 1975 b. Permeability and effective stress. *American Association of Petroleum Geologists Bulletin,* **59**, 154-8.

APPENDIX 1

MICROSCOPY

A1.1 Preparation of the samples for microscopy

Samples were prepared as either, or both, standard thin sections, or thick polished sections. In the thin sections staining with eliseren red allowed the distinctions between K-feldspar and plagioclase to be seen.

The thick sections were prepared with rather more care following, as closely as possible, the method of Simmons & Richter (1976).

Firstly the thick slabs were cut using a Beuhler Isomet saw which, with its thin wafer blade, variable speed and light cutting weight, causes no new microcracks to be formed during cutting. The cutting speed was never greater than 100 rpm.

The slabs were then cold bonded onto probe slides using Epoxy resin and ground down to 90 -100 μm thick. Grinding down was achieved firstly by trimming to 2-3 mm thick with the Isomet saw and then grinding with a Logitech carborundum grinder. Again these steps were taken to ensure no new fracturing. The thick sections were then highly polished using Beuhler and Hypriez diamond pastes of 6μ, 1μ, and 0.25μ respectively. The polishing lap used 7" disks impregnated with the paste and no weight other than the holders weight was placed on the slides. Polishing times of 3-5 days, with 24-48 hours continuous polishing on each grade of paste proved to provide perfect smooth surfaces devoid of pluck marks.

Ultrasonic cleaning in 60-40% Petroleum Ether removed all paste and lubricant between grades and before coating. Carbon coating was used, and applied only in the thinest layer via evaporation. Thin layers allowed only the minimum absorption of electrons during scanning electron microscopy (S.E.M.) and also presented no interference with the energy dispersive X-ray spectroscopy (E.D.X.S) systems used.

A1.2 Microscopy

Both optical and S.E.M. analysis was used in the study, and optical microscopy requires no explanation. By using a scaled eyepiece and racking up and down, the true width of a fracture can be measured by the displacement of the fracture edge through the section. Optical microscopy was used in mineralogy, to measure the fracture sizes, and to study fracture - fracture relationships.

S.E.M. analysis proved to be a very powerful tool in defining the fracture sealing mineralogy and textural relationships of the sealing minerals, and in the estimation of

porosity due to both open and sealed fractures. Both secondary electron imaging (S.E.I.) and back scattered electron imaging (B.S.E.I) were used. S.E.I. was used for the open fractures as S.E.I. uses reflected electrons bounced off the sample surface and presents an image of the samples surface topography. B.S.E.I. was used on the sealed fractures as it offers a compositional image of the sample, and is almost immune to topographic effects. Back scattered electrons are electrons emitted from the sample when it is bombarded with the electron beam.

As electrons bombard the surface of the sample the electrons of the element, when hit, become excited and can make a jump from their usual, and present, electron shell to the next shell. On making this jump they become unstable and relax into their original shell. During this relaxation they must loose energy. They do this by emitting an electron which has an energy specific to that element.

The back scattered electrons are picked up by a back scattered detector inside the sample chamber. They are usually collected for 45-60 seconds with a spectrum of count against energy being recorded by the E.D.X.S. system. The spectrum produced after collection is specific to the elemental composition of the material being bombarded by the beam. The spectrum can then be normalized against a standard of known chemistry (quantitative analysis), or against the background energy (semiquantitative analysis), with a read out in wt% oxide provided for a set of previously specified elements.

A1.3 Scanning electron microscopes used and their operating conditions

The S.E.M.s used in this study were the ISI DS130 of Professor Gene Simmons at Massachusetts Institute of Technology (M.I.T), the Hitachi S570 housed in Biological Sciences at Memorial University of Newfoundland (M.U.N) and the Cambridge S600 housed in the Geology Department at Glasgow University.

The ISI and Hitachi were equipped with back scattered detectors and E.D.X.S. systems (Tracor Northern TN2000 and TN5000 respectively), with the Glasgow University machine having facilities only for S.E.I.. For these reasons sealed microcrack work was carried out at M.I.T. and M.U.N., and open microcrack work at Glasgow.

A1.3.1 S.E.M. operating conditions

High resolution operating conditions were required to provide a maximum image resolution and image contrast in the back scattered mode. Working distance was kept small, usually between 10-20 mm, with the voltage varied between 20 - 40 kv depending on the magnification required. At higher magnifications a higher voltage provided a clearer

image as more back scattered electrons are produced if the beam is stronger. Visual improvements in image can be obtained at slow scan speeds, but it then becomes impossible to see the whole image on the screen at once. Tilt angles of 5-10° (parallel to the detector) were supposed to provided the clearest image but no significant difference occurred when the sample was flat. Dynamic focus allowed the ISI and Hitachi microscopes to cope with tilted samples. The Cambridge 600 did not possess a dynamic focus facility, and to make mosaics of constant magnification the specimen was required to be flat.

In all cases, the whelnet capsule in the electron gun was in the high resolution position, close to the filament. The electron beam was aligned to produce maximum filament saturation. An unsaturated filament, unaligned gun, or a dirty capsule all drasticaly reduced the image clarity at low voltages. E.D.X.S. spectra were collected for 45 or 60 seconds at the maximum spot size and normalized semi-quantitatively.

A1.3.2 Photography

As the sample is contained in a chamber and cannot be seen during S.E.M. analysis, large (X20) blow-ups of the thin and thick sections at A2 size were used as crack-maps. On these, each S.E.M. picture was plotted, with each S.E.M. picture photocopied and stuck in the laboratory book with the E.D.X.S. analysis listed and marked on the photograph. This was the easiest way to work, and allowed rapid reanalysis of a sample, with the return to an analysis spot within 30 seconds once the slide is in the evacuated chamber and in focus. The sequential documentation also allowed speedy reanalysis of the micrographs at a later time.

Photography of the microcracks was done in three ways, spot photographs of important relationships or mineral textures, mosaics of micrographs to look at microcrack arrays and traverses across the sections to analyse microcrack porosity. Both the ISI and the Hitachi microscopes had built-in Polaroid cameras, and normal contrast Polaroid Type 52 and Type 60 film was used. The Cambridge machine used 35mm black & white film with a camera which took images from the S.E.M. screen.

A1.4 List of samples used in microscopy

A1.4.1 Thin and polished sections: basement sample sites

Actinolite = Ac, Apatite = Ap, biotite = Bi, calcite = Cc, clinozoisite = Cl, chlorite = Ch, clinopyroxene = Cpx, epidote = Ep, hornblende = Hb, K-feldspar = Kf, magnetite = Mt, muscovite = Mu, orthopyroxene = Opx, plagioclase = Pl, quartz = Q, sphene = Sp, tremolite = Tr, zircron = Zr.

SAMPLE	THIN	POLISHED	DESCRIPTION
K-1	√	√	Pyroxene granulite : Pl, Q, Cpx, Opx, Mt, (Bi, Cc, Hb).
KC-1	√	-	Core through quartz sealed crack.
M-1	√	-	Pyroxene granulite : Cpx, Opx, Pl, Hb, Q, (Mt, Ap).
M-2	√	√	Hornblende granulite : Hb, Pl, Q, Cl, (Mt, Sp, Ch, Cc, Ap).
M-3	√	-	Hornblende granulite : Hb, Pl, Q, Cl, Tr, Mt (Cc, Cpx, Opx).
M-3/2	-	√ √	Core through pumpellyite sealed crack.
M-4	√	√	Banded gneiss : Pl, Hb, Q, Cl, (Mt, Cc, Sp).
M-5	√	√	Banded gneiss : Pl, Hb, Q, Bi, (Mt, Sp, Cl, Mu,).
M-6	√	√	Banded gneiss : Pl, Hb, Q, Cl, (Bi, Mt, Cc).
M-7	√	-	Banded gneiss : Pl, Q, Hb, Bi, Cl, (Mt, Cc).
M-8	√	√ √	Banded gneiss : Hb, Q, Pl, Cl, Mt, Sp, (Bi, Cc).
M-14	-	√ √	Core through a pumpellyite sealed crack.
M-16/2	-	√ √ √	Core through a prehnite sealed crack.
M-18	√	√	Banded gneiss : Hb, Pl, Q, Bi, Mt, (Cc, Cl, Sp).
M-18/2		√ √	Core through a pumpellyite sealed crack.
M-C23	√	-	Core through quartz sealed crack.
M-C27	√	-	Core through pumpellyite sealed crack.
M-C32	√	√	Core through pumpellyite sealed crack.
M-C34	-	√	Core through prehnite sealed crack.
M-C39	√	√	Core through pumpellyite sealed crack.
M-C40	√	√	Core through pumpellyite sealed crack.
SD-1	√	√	Hornblende granulite : Pl, Hb, Q, Bi, (Mt, Ap).
SD-2/2	-	√ √	Hornblende granulite

SD-3	√	-	Hornblende granulite : Pl, Q, Bi, (Mt, Cl, Hb, Cc).
SD-4	√	√	Hornblende granulite : Pl, Q, Bi, Ch, Cl, (Mt, Cc, Hb).
SD-5	√ √	√	Granulite/dyke contact : Pl, Q, Bi, Hb, Cl, (Mt, Ch).
SD-6	√	√	Foliated dyke : Hb, Pl, Q, Mt, Cc, (Cl, Zr).
SD-7	√	√	Foliated dyke : Hb, Pl, Q, Cc, Mt, (Cl).
SD-8	√	√	Scourie dyke : Hb, Pl, Cpx, Q, Mt, (Cc, Kf, Ch).
SD-9	√	√	Scourie dyke : Pl, Hb, Cpx, Mt, Q, (Ep).
SD-10	√	√	Scourie dyke : Hb, Pl, Cpx, Mt, Q, (Cc, Ep).
SD-11	√	√	Scourie dyke : Pl, Hb, Cpx, Mt, Q.
SD-11/2	-	√	Core through prehnite sealed crack.
SD-25	-	√	Core through prehnite sealed crack.
DM-1	√	√	Foliated Scourie dyke : Hb, Pl, Q, Mt, Sp, Ep, (Bi, Ap, Mu).
DM-1/2	-	√ √ √	Core through prehnite sealed crack.
DM-2	√	√	Foliated Scourie dyke : Hb, Pl, Q, Mt, Bi, Cl, (Cc).
DM-3	√	√	Amphibolite schist : Hb, Pl, Q, Mt, Cl, Sp, (Ap).
DM-5	√	√	Hornblende/biotite schist : Q, Pl, Hb, Bi, Mt, (Ep, Ap, Cl).
DM-6	√	√	Hornblende granulite : Pl, Hb, Q, Cpx, Bi, (Mt, Cl, Sp, Cc).
DM-7	√	-	Banded gneiss : Pl, Q, Hb, Bi, Cl, (Mt, Ap).
DM-8	√	-	Banded gneiss : Pl, Q, Hb, Bi, Ep, (Mt, Ap, Cl).
DM-10	√	√	Hornblende granulite : Q, Pl, Hb, Bi, Ep, Mt, (Ap).
DM-12	√	√	Hornblende granulite : Pl, Q, Hb, Bi, (Cl, Mt).
SC-3	√	√	Mylonitic schist.
SC-5	√	√	Foliated dyke: Pl, Q, Hb, Bi, (Mt, Cl, Sp, Ap).
SC-7	√	-	Foliated dyke: Hb, Q, Pl, Mt, Bi, (Cl, Cc, Ap).
SC-9	√	√	Scourie dyke : Pl, Hb, Cpx, Mt, Q, Cl, Bi, (Cc).
SC-10	√	√	Hornblende granulite : Pl, Q, Bi, Cl, (Mt, Ap, Kf, Ch).
SC-11	√	-	Retrogressed granulite: Q, Pl, Bi, Hb, Mt, (Ap, Zr, Sp, Cl).
SC-12	-	√	Scourie dyke.
SC-14	√	-	Scourie dyke: Hb, Pl, Cpx, Mt, Cl, Bi, (Q).
LC-1	√	√	Hornblende granulite : Hb, Pl, Q, Bi, Mt, (Ap, Cl).
LC-2	-	√	Hornblende granulite.
LC-4	√	√	Hornblende granulite : Hb, Pl, Q, Bi, Mt, (Ap, Cl, Zr).
LC-5	√	-	Hornblende granulite : Pl, Hb, Q, Ac, (Mt, Bi, Cc).

LC-6	√	√	Hornblende granulite : Hb, Pl, Q, Bi, Mt, Cl (Ap, Cc).
LC-7	√	√	Amphibolite gneiss : Pl, Hb, Q, Ep, Mt, (Bi, Cc, Cl).
LC-8	√	-	Mylonitic schist.
LC-9	√	√	Amphibolite schist : Q, Pl, Hb, Ep, Mt, (Bi, Cc).
LC-18	√	-	Pumpellyite sealed crack.
LC-C5	-	√	Core through pumpellyite sealed crack.
LC-C10	√	√	Core through pumpellyite sealed crack.
LC-C13	√	√	Core through quartz sealed crack.
LC-C14	-	√ √	Core through banded gneiss.
LD-C2	√	√	Core through prehnite sealed crack.
LD-C4	-	√	Core through prehnite sealed crack.
LD-C5	√	-	Core through prehnite sealed crack.
LD-C10	-	√	Core through pumpellyite sealed crack.
LD-C11	√	-	Core through prehnite sealed crack.
LD-C14	√	-	Core through prehnite sealed crack.
LD-C15	√	√	Core through prehnite sealed crack.
G-1	√	√	Granite : Kf, Q, Pl, Bi, Mu, (Sp, Ap, Mt,).
G-2	√	-	Granite : Kf, Q, Pl, (Ap, Mt, Ep).
G-3	√	-	Contact-gneiss : Pl, Q, Kf, Bi, Ep, (Hb, Ap).
G-4	√	√	Feldspathic gneiss : Kf, Pl, Q, Hb, Ep, (Ap).
G-5	√	√	Feldspathic gneiss : Kf, Pl, Q, Hb, Ep, (Ap, Zr, Sp).
G-6	√	√	Gneiss : Pl, Hb, Q, Kf, Bi, Ep, Sp, (Ap).
G-7	√	-	Gneiss : Pl, Q, Hb, Bi, (Ep, Ap, Sp, Mt, Kf).
PE-1	√	√	Amphibolite gneiss : Pl, Hb, Bi, Cl, Q, (Ap, Sp, Mt).
PE-2	√	√	Amphibolite gneiss : Pl, Hb, Bi, Q, Cl, (Ap, Sp, Mt).
PE-3	√	√	Feldspathic gneiss : Pl, Hb, Q, Bi, (Ap, Sp, Cl, Mt).
PE-4	√	√	Quartzofeldspathic gneiss : Pl, Bi, Q, (Mt, Ep).
PE-5	√	-	Pegmatite : Pl, Q, Bi, Kf, (Cl).
PE-6	√	√	Pegmatite : Pl, Q, Kf, (Bi).
NR-C4	√	√	Core through K-feldspar+calcite sealed crack.
NR-C7	√	√	Core through K-feldspar + calcite sealed crack.

R-C4	√	√	Core through pumpellyite sealed crack.
R-C7	√	√	Core through pumpellyite sealed crack.
UB-C7	√	√	Core through chrisotile sealed crack.

A1.4.2 Thin and polished sections: unconformity sample sites

SAMPLE	THIN	POLISHED	DESCRIPTION
S-1	√	-	Weathered gneiss.
S-2	√	-	Fresh gneiss.
S-3	√	-	Basal Torridonian sandstone.
S-4	√	-	Weathered granite vein.
S-5	√	-	Torridonian sandstone.
D-1	√	-	Basal Torridonian conglomerate/grit.
D-2	√	-	Gneiss on unconformity surface.
STU-1	√	√	Core through Torridonian sand dyke.
STU-2	√	√	Core through K-feldspar + calcite sealed crack.
TUA-9	√	-	Core through pumpellyite sealed crack.
GB-1	√	-	Pumpellyite sealed crack in Torridonian Stoer group.
RC-4	√	-	Pumpellyite vein through gneiss.
RC-5	√	-	Section of a large pumpellyite vein.
RC-8	√	-	Pumpellyitized gneiss clast from Stoer conglomerate.
RC-13	√ √	-	Stoer Group conglomerate and matrix.
A-2	√	-	Agalmatolite gneiss.
A-4	√	-	Agalmatolite gneiss.

APPENDIX 2

A2.1Sealed crack sizes

All measurements in μm.

Grainboundary cracks

Length	Width
305	4.9
365	6.0
400	7.4
510	4.9
1025	4.9
860	4.9
410	3.7
235	7.5
245	4.8
140	1.9
245	2.5
495	5.0
380	1.1
220	2.5
200	3.7
200	2.5
225	2.5
490	2.5
370	2.4
270	2.4
330	2.4
260	2.5
500	3.7
570	2.4
240	2.5
605	2.5
450	1.2
200	2.4
410	1.2
315	4.9
405	2.4
375	2.5
660	1.2
460	0.8
545	2.4
380	1.6
450	2.4
275	6.2

Length	Width
62	9.9
535	1.2
1115	4.6
230	1.2
325	1.6
170	1.2
147	1.2
167	1.8
137	3.7
335	1.2
265	1.8
500	2.5
295	4.9
475	4.8
270	1.8
165	2.4
405	1.2
215	2.5
1035	2.4
415	2.5
225	4.1
530	4.9
425	8.6
280	4.9
190	1.2
435	3.7
335	2.5
485	4.9
225	4.9
190	3.7
290	2.5
165	2.4
280	1.2
255	7.4
305	2.4
235	2.5
225	3.7
285	3.7

Length	Width
200	5.0
250	5.0
140	3.7
95	1.2
145	2.4
150	2.4
185	1.1
200	2.5
425	7.4
175	0.7
235	1.6
90	1.2
265	4.3
155	4.9
250	2.3
160	2.4
200	2.3
180	0.6
145	1.6
215	2.4
405	2.4
165	0.9
475	1.2
300	5.8
235	7.5
275	3.7
85	1.2
325	0.7
260	2.5
180	1.8
500	4.9
185	1.2
200	2.4
165	2.5
135	2.5
225	1.2
250	1.2

Intragranular cracks

Length	Width	Length	Width	Length	Width
305	9.8	245	4.9	325	3.7
225	1.2	285	4.9	600	7.5
625	2.5	330	5.0	475	2.4
222	1.8	1085	17.5	235	2.5
97	1.2	1050	14.8	210	5.0
450	3.7	725	9.7	230	2.4
361	2.0	980	4.9	285	2.2
507	4.9	855	3.7	340	2.4
458	2.5	480	4.9	360	4.3
240	2.4	4425	15.0	440	4.9
570	6.2	900	2.4	115	2.4
475	4.9	385	1.2	205	3.7
350	2.5	480	2.4	167	2.5
665	2.4	865	2.5	187	2.4
400	2.5	452	12.3	385	2.5
1000	4.8	375	3.7	410	2.2
500	2.5	985	4.9	285	7.2
545	2.4	885	1.8	230	2.4
895	3.7	1475	5.0	385	2.5
1310	4.3	295	2.4	210	1.2
1025	3.7	1550	4.9	235	2.5
680	2.4	970	2.4	200	2.5
1545	3.7	250	2.5	425	2.5
250	2.4	145	2.5	400	5
305	2.4	1200	2.4	300	2.5
375	1.2	187	2.5	225	4.9
215	1.7	1050	3.7	625	1.2
430	5.0	325	2.5	475	0.8
225	2.4	640	1.9	182	2.4
300	5.0	1410	7.4	250	1.8
450	4.9	1300	7.4	110	2.4
770	4.9	500	7.4	205	0.5
250	2.5	375	2.4	285	2.4
200	1.2	185	2.4	255	0.6
125	1.2	555	2.5	470	1.2
200	1.2	395	1.2	160	0.4
355	2.5	290	2.4	405	0.4
117	2.5	595	2.4	500	1.2
155	2.4	355	4.9	260	3.1
475	2.4	580	2.4	600	5.0
300	5.4	250	2.4	175	1.2
145	12.4	400	2.4	425	1.2
142	9.8	315	2.4	530	2.5
480	8.7	650	2.4	260	3.7
490	1.2	120	2.4	610	1.2
600	8.7	500	2.4	175	10.0
265	2.4	235	2.4	345	2.5
255	6.2	300	7.5	470	1.2

Length	Width
165	1.2
210	1.2
160	2.5
155	1.8
240	2.0
200	3.7
475	3.7
230	1.2
225	1.6
285	6.2
230	2.5
340	5.0
240	1.2
223	4.4
442	2.5
357	4.9
140	5.0
345	3.7
250	1.2
605	12.1
380	3.7
280	4.9
175	7.4
215	2.4
313	3.7
325	2.4
685	2.4
330	6.2
515	4.9
720	2.5
475	2.4
620	6.1
660	8.6
430	1.6
310	3.7
320	2.5
225	2.4
300	2.4
500	3.7
560	2.4
325	1.8
825	3.7
235	2.5

Length	Width
138	1.2
125	1.2
205	1.2
195	1.2
415	5
283	0.8
455	1.1
295	2.4
255	2.4
400	1.8
305	1.2
260	2.4
465	1.2
265	1.1
170	5.0
475	2.5
265	2.4
180	1.2
315	1.2
185	1.2
150	2.5
250	2.3
135	2.3
235	2.4
260	1.2
390	2.5
355	2.4
415	1.2
410	3.7
395	1.2
425	0.8
290	1
435	2.5
510	1.2
525	2.4
180	1.2
157	1.2
270	2.4
185	1.2
145	0.8
245	3.5
175	0.8
225	0.6

Length	Width
255	1.2
335	2.4
315	2.4
285	3.7
505	2.4
220	1.2
245	0.6
190	1.8
480	1.2
325	6.2
417	1.2
333	3.6
833	2.5
380	1.2
867	2.5
733	3.1
467	2.4
250	1.8
917	6.2
410	4.9
533	4.3
483	2.4
600	3.7
1600	6.2
1067	6.2
600	3.7
180	1.8
125	2.5
140	1.2
265	4.9
425	4.9
250	4.6
140	2.4
127	1.8
265	5.0
132	2.4
140	2.5
250	2.4
290	1.6
380	1.2
230	2.5
195	2.5
320	3.7

Intergranular cracks

Length	Width
785	9.1
2250	14.
9666	200.0
13200	83.9
1385	32.9
9333	90.0
4033	36.9
11000	22.1
1545	19.5
912.5	19.7
13320	56.2
1510	24.9
890	10.9
1000	7.5
885	7.4
390	11.6
1790	19.9
1155	29.1
1205	17.3
1532	13.3
1505	16.3
2525	9.9
4583	12.4
5933	19.1
13167	74.4
3833	114.0
6167	125.0
7968	90.0
11833	22.5
7100	52.0
11833	17.4
8933	24.9
5100	9.9
3000	1.2
7667	40.2
7533	26.1
10067	19.9
16967	109.9
7700	17.5
4833	15.0
12833	36.9
5500	19.9
4667	12.4
3505	13.7
1215	17.3
385	2.4

Length	Width
1210	5.0
4725	7.4
1060	8.6
270	4.9
640	8.4
430	8.7
565	8.7
415	12.4
1250	7.4
120	5.0
6667	9.8
6267	15.0
5967	7.4
4800	19.9
4733	12.4
3055	9.9
5400	12.5
725	4.9
12833	87.5
7167	33.9
12367	66.5
5500	51.9
1633	12.3
12167	32.3
12333	24.9
13900	26.0
3633	41.2
645	4.9
1115	2.5
2033	61.6
24767	107.5
8067	55.7
15000	77.5
5633	49.8
17733	110.0
12733	87.2
4567	17.4
3533	7.5
13667	57.3
12233	57.3
1655	2.4
985	6.1
630	2.5
935	1.1
755	3.7
1585	6.2

Length	Width
675	7.4
530	6.6
1065	1.8
1000	2.5
4900	27.4
4433	24.2
1333	15.0
1900	7.4
2367	22.5
7433	66.5
2225	10.0
1833	9.9
900	3.7
7033	14.9
2033	19.7
4000	9.9
6733	12.5
10433	34.6
7700	22.4
5433	7.4
5167	12.5
3200	19.9
8067	80.0
2267	19.9
6000	22.4
3167	18.6
6867	39.2
18900	123.3
9733	29.9
3167	17.5
2200	17.4
4267	8.4
1167	5.0
6500	29.3
10067	15.0
1705	7.4
12967	34.8
16000	47.4
8167	29.5
8000	19.7
12667	34.8
12300	54.8
10733	14.9
8500	10.0
12733	7.4
9333	7.4

Length	Width
7400	21.2
1125	9.9
3600	13.7
3467	19.9
1267	12.4
1500	24.2
3067	22.4
4967	24.9
1933	13.7
3033	11.2
2733	6.2
3733	26.0
3300	30.0
2633	21.1
3200	32.0
3567	28.4
4000	56.1
3200	32.5
2867	13.7
1200	6.2
2633	6.1

Length	Width
1500	14.7
4333	24.8
7167	17.3
3433	8.7
9833	19.8
2900	31.5
11567	6.2
9833	16.2
470	2.5
1233	2.5
1067	5.0
1033	3.7
1050	39.8
2467	41.1
1033	25.0
3233	40.6
600	31.5
5567	32.3
1433	2.4
567	4.3
2000	12.0

Length	Width
1433	4.9
2033	8.7
1600	7.4
1600	1.2
1667	2.4
2500	12.5
1633	11.1
1667	2.5
4767	20.0
1333	4.9
310	3.3
867	3.7
900	3.6
767	2.3
1367	4.9
967	2.4
1833	11.9
775	3.7
12167	48.7

A2.2 Open crack sizes

All measurements in µm.

Grain boundary cracks

Width	Width
1.8	1
2.5	2
2.0	2.5
1.8	2
2.5	5
2.5	1.7
2	2
3	1.5
10	2
2	1
2	2
1.5	1
2.5	2
5.5	3.5
2.5	2
2	7.5
2	2
1	2
1	1.5
2	2
1.6	1.5

Intragranular cracks

Width	Width
0.9	3
1.5	3
2	3
2.5	1.7
1.7	2
0.9	3
1	1.5
2	1.2
1.7	1
1.5	1
2	2
7.5	1
2	1.5
1.5	1.3
2	1.7
1.7	2
2.2	1
2	2
1	2.5
2.5	2

APPENDIX 3

MAJOR ELEMENT CHEMISTRY OF COMMON CRACK SEALING MINERALS

A3.1 Prehnite (Normalized to 100%)

	LD-C15	LD-C15	M-C40	M-C40	LD-C14	LD-C14	LD-C11
SiO_2	42.73	40.39	37.17	37.15	39.22	39.74	40.93
TiO_2	0.09	0.24	0.24	0.21	0.09	0.03	0.06
Al_2O_3	21.83	21.22	17.28	17.5	18.42	20.19	19.70
FeO	1.6	2.16	10.41	8.91	6.86	5.24	6.68
MnO	0.0	0.16	0.03	0.27	0.19	0.12	0.11
MgO	0.48	0.46	0.82	0.52	0.72	0.38	0.56
CaO	32.11	33.62	32.56	33.59	32.69	32.82	30.59
Na_2O	0.57	0.79	0.93	0.79	0.83	0.66	0.59
K_2O	0.14	0.25	0.16	0.23	0.18	0.17	0.11
P_2O_5	0.46	0.7	0.4	0.48	0.54	0.61	0.65

	LD-C11	DM-1	DM-1	SD-25	SD-25	SD-25	SD-25
SiO_2	41.25	40.14	42.50	44.59	42.45	47. 48	56.83
TiO_2	0.2	0.11	0.26	0.0	0.09	0.0	0.0
Al_2O_3	18.9	21.25	21.18	22.53	21.76	22.69	4.73
FeO	7.75	3.92	2.86	1.72	4.72	0.87	0.17
MnO	0.03	0.13	0.1	0.03	0.0	0.0	0.0
MgO	0.66	0.31	0.51	0.44	0.75	0.6	0.6
CaO	29.56	33.08	31.17	29.13	28.51	26.73	35.39
Na_2O	0.66	0.44	0.62	0.69	0.82	0.89	0.91
K_2O	0.15	0.19	0.12	0.15	0.21	0.11	0.18
P_2O_5	0.84	0.44	0.69	0.74	0.7	0.64	0.99

	M-16	M-16	SD-11	SD-11	DM-1	DM-1	M-16
SiO_2	35.88	37.52	36.38	35.56	39.9	36.62	39.57
TiO_2	0.27	0.12	0.2	0.15	0.24	0.21	0.27
Al_2O_3	31.5	33.01	32.01	31.3	21.13	17.09	21.28
FeO	2.76	1.26	0.68	1.0	1.64	10.42	2.02
MnO	0.1	0.08	0.0	0.0	0.16	0.05	0.24
MgO	1.74	2.21	1.71	2.55	0.52	0.77	0.74
CaO	21.52	20.35	23.77	23.23	35.17	33.31	33.79
Na_2O	3.89	3.43	2.9	3.42	0.6	0.88	0.94
K_2O	0.23	0.17	0.19	0.19	0.23	0.21	0.3
P_2O_5	2.12	1.85	2.15	2.61	0.4	0.43	0.84

	M-16	M-18	M-18	DM-1	DM-1
SiO_2	39.97	35.27	36.32	35.08	16.85
TiO_2	0.24	0.21	0.2	0.15	0.04
Al_2O_3	21.18	31.05	31.95	30.88	31.73
FeO	1.55	1.27	0.89	2.41	0.45
MnO	0.08	0.1	0.13	0.05	0.08
MgO	0.47	2.40	1.94	2.47	1.19
CaO	34.99	23.04	23.73	22.93	23.58
Na_2O	0.75	3.97	3.09	3.58	3.46
K_2O	0.18	0.23	0.19	0.53	0.17
P_2O_5	0.59	2.48	1.55	1.92	2.5

A3.2 Pumpellyite (Normalized to 100%)

	M-C34	M-C34	M-C39	M-C39	M-C32	M-C32	LC-C10
SiO_2	32.95	33.05	32.07	32.45	35.86	34.66	31.64
TiO_2	0.3	0.2	0.2	0.2	0.38	0.18	0.42
Al_2O_3	22.03	19.94	21.06	21.57	22.56	22.5	20.02
FeO	14.44	15.8	16.7	15.43	7.82	8.64	17.42
MnO	0.24	0.12	0.33	0.39	0.53	0.57	0.42
MgO	0.92	2.22	0.91	2.14	2.42	2.30	0.73
CaO	27.59	26.75	26.87	25.65	29.02	29.92	27.45
Na_2O	0.97	1.15	1.29	1.28	0.82	0.65	1.07
K_2O	0.18	0.24	0.22	0.26	0.21	0.2	0.2
P_2O_5	0.36	0.54	0.36	0.63	0.37	0.38	0.62

	LC-C10	M-18	M-18	LC-4
SiO_2	30.99	33.8	33.28	37.85
TiO_2	0.39	0.14	0.16	0.22
Al_2O_3	18.91	21.47	21.06	16.48
FeO	19.34	12.04	12.59	12.03
MnO	0.28	0.08	0.17	0.05
MgO	0.67	1.65	1.78	0.47
CaO	27.67	29.66	29.68	30.28
Na_2O	0.91	0.77	0.65	0.6
K_2O	0.2	0.1	0.19	1.45
P_2O_5	0.65	0.3	0.45	0.57

A3.3 Stilpnomelane (Normalized to 100%)

	M-16	M-16	M-16	M-16	M-16	M-16	M-16
SiO_2	27.48	26.14	26.41	24.28	29.44	23.89	25.21
TiO_2	0.09	0.22	0.19	0.29	0.06	0.47	0.13
Al_2O_3	24.18	22.99	23.24	22.93	25.9	21.02	23.32
FeO	8.91	6.35	10.45	11.69	5.62	3.25	11.87
MnO	0.17	0.14	0.11	0.23	0.17	0.28	0.2
MgO	21.51	20.45	20.66	20.39	23.04	18.69	20.75
CaO	6.72	17.07	1.48	3.24	3.19	8.04	0.7
Na_2O	10.12	5.63	16.58	16.63	8.92	10.38	15.99
K_2O	0.81	1.02	0.28	0.53	3.64	13.44	0.08
P_2O_5	0.0	0.0	0.6	1.05	0.03	0.55	1.75

	M-16	SD-10	SD-10	SD-11	SD-11	SD-9	SD-9
SiO_2	25.76	25.34	25.9	25.62	26.93	24.99	25.92
TiO_2	0.86	0.26	0.11	0.07	0.15	0.11	0.04
Al_2O_3	22.67	22.31	22.8	22.56	23.7	21.98	22.82
FeO	11.53	10.82	11.76	14.97	7.7	14.86	12.28
MnO	0.2	0.16	0.13	0.13	0.2	0.16	0.1
MgO	20.16	19.84	20.28	20.06	21.08	19.55	20.29
CaO	0.38	0.7	0.39	0.36	0.93	0.46	1.25
Na_2O	16.2	14.92	15.92	16.05	16.92	15.69	16.29
K_2O	0.73	4.98	2.7	0.17	2.39	0.99	0.37
P_2O_5	1.7	0.66	0.0	0.0	0.0	1.2	0.66

A3.4 Actinolite (Normalized to 100%)

	DM-1	DM-1	DM-1	DM-1
SiO_2	39.67	40.37	36.07	28.97
TiO_2	0.13	0.09	0.44	0.04
Al_2O_3	1.8	2.17	10.53	12.97
FeO	38.09	36.85	9.35	9.74
MnO	1.97	1.79	0.36	0.51
MgO	3.68	3.72	27.31	22.26
CaO	12.35	12.77	8.90	16.38
Na_2O	1.7	1.65	5.45	7.36
K_2O	0.24	0.28	0.22	0.23
P_2O_5	0.19	0.31	1.37	1.27

A3.6 K-feldspar (Normalized to 100%)

	STU-2	STU-2	STU-2	STU-2	STU-2	STU-2
SiO_2	62.73	60.17	63.19	64.7	62.2	63.4
TiO_2	1.83	3.90	1.68	0.76	1.36	1.07
Al_2O_3	19.07	20.94	18.72	18.44	19.20	19.18
FeO	0.0	0.0	0.16	0.0	0.0	0.0
MnO	0.0	0.0	0.0	0.0	0.0	0.0
MgO	0.0	0.0	0.0	0.0	0.0	0.0
CaO	0.18	0.39	0.33	0.0	0.19	0.0
Na_2O	0.0	0.0	0.0	0.0	0.0	0.35
K_2O	16.18	14.59	15.63	16.01	16.05	16.0
P_2O_5	0.0	0.0	0.0	0.0	0.0	0.0

A3.6 Mol. % pistacite in prehnite

Sample	Mineral	Mol. % pistacite	Sample	Mineral	Mol. % pistacite
LD-C11	PREH.	0.338	LD-C11	PREH.	0.389
LD-C14	PREH.	0.366	LD-C14	PREH.	0.280
LD-C15	PREH.	0.094	LD-CI5	PREH.	0.126
SD-11	PREH.	0.023	SD-11	PREH.	0.033
SD-25	PREH.	0.096	SD-25	PREH.	0.229
SD-25	PREH.	0.050	SD-25	PREH.	0.176
M-16	PREH.	0.090	M-16	PREH	0.037
M-16	PREH.	0.094	M-16	PREH	0.114
M-18	PREH.	0.043	M-18	PREH.	0.030
M-C40	PREH.	0.533	M-C40	PREH.	0.484
DM-1	PREH.	0.210	DM-1	PREH.	0.162
DM-1	PREH	0.549	DM-1	PREH.	0.015
DM-1	PREH.	0.081			

A3.7 Mol. % pistacite pumpellyite

Sample	Mineral	Mol. % pistacite	Sample	Mineral	Mol. % pistacite
M-18	PUMP.	0.222	M-18	PUMP.	0.243
M-C32	PUMP.	0.176	M-C32	PUMP.	0.176
M-C34	PUMP.	0.243	M-C34	PUMP.	0.325
M-C39	PUMP.	0.294	M-C39	PUMP.	0.304
LC-C10	PUMP.	0.314	LC-C10	PUMP.	0.355
LC-4	PUMP.	0.219			

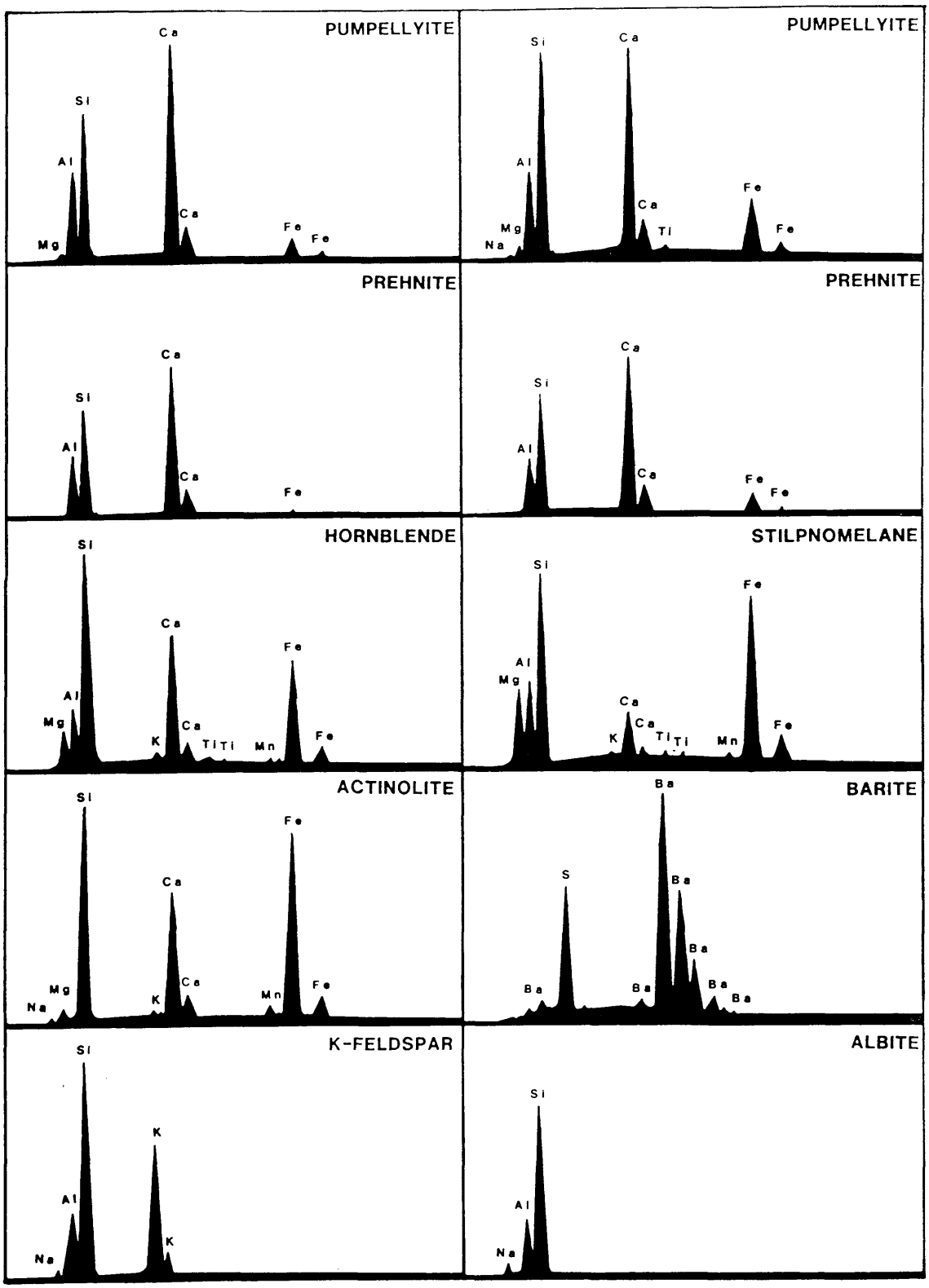

Figure A.1 E. D. X. S. spectra for some of the common minerals found in the Lewisian sealed cracks.

APPENDIX 4

STABLE ISOTOPE EXTRACTION

A4.1 Oxygen extraction from silicates

Extraction of oxygen was carried out by reaction with chlorine-trifluoride (ClF_3) following the method of Borthwick & Harmon (1982).

Powdered samples weighing in the region of 15 mg, were loaded into nickel reaction vessels. The vessels were loaded onto a vacuum extraction line and under vacuum, the samples were "pre-fluorinated", by allowing a short exposure to ClF_3, to remove any superficial mater from the sample and the vacuum line.

The samples were then evacuated and re-exposed to an excess of ClF_3 overnight at 650° C to release the silicate bound oxygen by oxidation. The mixture of reaction gases not condensed at -196 °C, was then passed over KBr powder to remove any fluorine. The bromine is substituted by fluorine forming KF and releasing Br gas which is frozen off. The free oxygen is then reacted with a heated Pt catalyst to produce CO_2. This CO_2 is then frozen down, using a liquid nitrogen trap, the yield measured, and then passed into a sample tube for analysis. Extraction was carried out on the FS-12 and FS-6 lines at SURRC

The oxygen isotope analysis was carried out on a VG Isogas SIRA 10 mass spectrometer. The 45/44 and 46/44 mass abundance ratios of the sample CO_2 were measured relative to a laboratory standard gas, precision is to ± 0.1 ‰.

Extraction and analysis was carried out with the technical assistance of Julie Gerc and Alison MacDonald.

A4.2 Hydrogen extraction from silicates

Hydrogen was liberated from the silicates in a similar method to that described by Godfrey (1962). 20-70 mg samples of powdered sample were loaded into degassed platinum crucibles housed in quartz reaction vessels. The loaded samples were then preheated overnight at 120° C,under vacuum, to drive off any free water within the sample.

The sample was then transferred to the extraction line where it was heated slowly to ~1400° C by Radyne induction coil. After heating and degasing, condensable gases (H_2O and CO_2) were frozen into a liquid nitrogen trap. The noncondensables (H_2, N_2 etc.) passing through the traps are pumped by a mercury Toepler pump into a manometer. The frozen CO_2 and H_2O mix is then is warmed to -78 °C using a CO_2/acetone slush bath, allowing CO_2 to sublimate. This is then volumetrically measured and pumped out, with the H_2O

remaining frozen. The H_2O is then evaporated and double passed over a uranium furnace (^{238}U) at 900 °C, forming uranium oxide and releasing free H_2 which is pumped by the mercury Toepler into the manometer where it is measured for yield calculation and transferred into a collection vessel.

The collected sample was analysed on a VG micromass 602 mass spectrometer with a modified mercury piston inlet system, allowing analysis of small samples of hydrogen. The sample was thoroughly mixed before the 3/2 ratio was measured relative to a standard gas, calibrated against SLAP (-428‰) and SMOW (0‰), precision is to ± 2 ‰.

A4.3 Carbon and Oxygen extraction from calcite

Carbon and oxygen were liberated from calcite following the method of McCrea (1950).

15 - 20 mg of powdered calcite was placed in a glass bucket, hung inside a glass reaction vessel. 5 ml of phosphoric acid was placed in the base if the reaction vessel, and the vessel was evacuated while heating the acid to drive off and dissolved gas. The evacuated vessel was then placed in a water bath at 25.18° C and left to equilibrate. The sample was then dropped into the acid and allowed to react. The vessel was replaced into the water bath, and the reaction allowed to proceed at 25° C for 3 hours. After reaction the H_2O and CO_2 were separated using an CO_2/acetone slush bath and a liquid nitrogen bath. CO_2 is then collected in a sample tube.

The oxygen and carbon isotope analysis was carried out on a VG Isogas SIRA 10 mass spectrometer. The 45/44 and 46/44 mass abundance ratios of the sample CO_2 were measured relative to a laboratory standard gas, precision is to ± 0.1 ‰.

A4.4 Extraction of Sulphur from barite

Sulphur was extracted from barite by a procedure similar to that of Coleman & Moore (1978). The only difference being that the reaction gases were passed through Cu gauze at the end of the main furnace, and then passed through a second furnace, filled with Cu. This ensured that all SO_3 was reduced to SO_2. The $\delta^{S3}4$ value was obtained using an ISOSPEC 64 mass spectrometer, with precision to ± 0.3 ‰. The single barite sample was kindly analysed by Adrian Boyce.

A4.5 Stable isotope values for Lewisian vein sealing minerals

SAMPLE	MINERAL	$\delta D_{(SMOW)}$	$\delta^{18}O_{(SMOW)}$	$\delta^{18}O_{(PDB)}$	$\delta^{13}C_{(PDB)}$	$\delta^{34}S_{(CDT)}$
DM-1	PREHNITE	-70.69	2.27			
	CALCITE		9.37	-20.84	-12.09	
GB-1	PUMPELLYITE	-66.52	7.25			
	CALCITE		11.42	-18.85	-1.13	
			11.72	-18.56	-1.19	
LC-C8	PUMPELLYITE	-37.18	4.57			
	CALCITE		9.66	-20.57	-6.75	
LC-C9	PUMPELLYITE	-41.21	4.62			
LC-C10	PUMPELLYITE	-42.62	5.33			
LC-C16	CALCITE		14.88	-15.50	-7.41	
LC-18	PUMPELLYITE	-41.82	15.77			
		-39.26				
LD-C2	PREHNITE	-80.27	5.54			
		-78.79				
	CALCITE		9.26	-20.95	-5.50	
LD-C5	PUMPELLYITE	-49.83	5.20			
LD-C6	PREHNITE	-75.42	2.97			
	CALCITE		13.39	-16.95	-5.81	
LD-C11	PREHNITE	-77.81	8.84			
	CALCITE		13.2	-17.13	-4.66	
LD-C14	PREHNITE	-80.41	4.96			
		-80.49				
	CALCITE		10.36	-19.89	-4.54	
			10.38	-19.87	-4.66	
LD-C15	CALCITE		12.70	-17.62	-4.68	
M-C34	PREHNITE	-68.79	7.49			
		-70.50				
M-C40	PUMPELLYITE	-62.52	6.35			
	BARITE					8.25
M-C45	CALCITE		15.97	-14.45	-5.48	
R-C1	PUMPELLYITE	-54.46	8.36			
RC-3	PUMPELLYITE	-47.85	8.26			
			6.52			
SD-C6	PREHNITE	-65.49	8.77			
	CALCITE		11.17	-19.10	-5.74	
STU-2	K-FELDSPAR		12.40			
	CALCITE		17.08	-13.7	-0.95	
STU-3	K-FELDSPAR		8.94			

APPENDIX 5

FLUID INCLUSION DATA

A5.1 Analysis of fluid inclusions

Homogenization and freezing temperatures of fluid inclusions were measured using a Linkam TH600 heating freezing stage, calibrated up to 300°C, but capable of measuring between -180 °C and 600 °C.

The stage consisted of a metal casing, in which a silver block was housed. An electrical resistance heater was embedded in the block, some 7 mm from the sample, to allow heating. Cooling was carried out by passing cooled nitrogen (passed through a liquid nitrogen bath) through a metal tubular ring around the silver block. The temperature was monitored by a platinum thermocouple, embedded in the silver block 3 mm from the sample, and linked to a digital display. Temperature of homogenization ($T_{(h)}$) and temperature of final melting ($T_{(m)}$) were measured, as well as noting the method of melting to ascertain the salinity of the fluid solution. In all cases the fluid was found to be of a mixed salt nature, containing NaCl, $CaCl_2$ and $MgCl_2$. Many inclusions were too small to allow easy measurement of $T_{(m)}$.

The stage was housed in the Department of Applied Geology at the University of Strathclyde, and used with the kind permission of Professor Mike Russell. Thin wafers for analysis were kindly prepared by the technicians at Strathclyde University.

A5.2 Values recorded for the sealed crack assemblages

SAMPLE	T(h)	Sal.	SAMPLE	T(h)	Sal.	SAMPLE	T(h)	Sal.
kspar-cal	295	-	preh-cal	233	13.549	pump-cal	180	-
	259	-		270	13.659		195	-
	210	-		208	11.833		170	-
	270	-		224	13.985		218	-
	232	-		204	18.004		173	-
	208	-		204	13.438		157	-
	312	-		281	-		159	-
	203	-		235	-		239	-
	303	-		251	-		225	-
	247	-		268	-		227	-
	252	-		245	-		205	-
	245	-		221	-		194	-
	278	-		210	7.010		191	-
	316	-		217	-		222	-
	308	-		225	-		215	-

SAMPLE	T(h)	Sal.	SAMPLE	T(h)	Sal.	SAMPLE	T(h)	Sal.
kspar-cal	313	-	preh-cal	197	-	pump-cal	239	-
	285	-		215	-		198	-
	304	-		182	-		197	-
	250	-		269	-		163	-
	313	-		235	-		157	-
	278	-		251	10.491		155	-
	286	-		232	6.724		195	-
	302	-		230	-		213	-
	312	-		246	-			
	356	-		247	-			
	275	-		240	-			
	308	-		256	-			
	274	-		246	-			
	291	-		252	12.764			
	290	-		253	-			
	271	-		187	-			
	308	-		192	-			
	261	-		211	3.534			
				240	-			
				231	-			
				216	-			
				236	-			
				238	-			
				240	-			
				248	-			
				195	-			
				256	-			

All temperatures are in ° C, and all salinities in "wt% NaCl equivalent".

APPENDIX 6

Rb-Sr ISOTOPE ANALYSIS

A6.1 Isotope dilution analysis

Isotope dilution analysis relies on the determination of the isotopic composition of an element in a mixture containing a known quantity of "spike' and an unknown quantity of "normal element in the sample.

The spikes are solutions of known isotopic composition, and are added to allow the calculation of the amount of normal element in the sample. The procedure was summarized by Faure (1977).

The isotope ratio R_{xy} for isotopes x and y in a mixture is given by the equation

$$R_{xy} = \frac{Abx_{(n)} N + Abx_{(s)} S}{Aby_{(n)} N + Aby_{(s)} S} ,$$

where Ab is abundance, N and S are the number of atoms of the normal element and spike, and (n) and (s) denote normal element and spike.

Measuring R_{xy} on a mass spectrometer, and knowing the composition of the spike, the only unknown is N. Solving for N gives

$$N = S\left[\frac{Abx_{(s)} - R_{xy} Aby_{(s)}}{R_{xy} Ab_{(n)} - Abx_{(n)}}\right] . \qquad \text{A 6.1}$$

Abundances can be converted to weights by dividing by Avagadro's number (A) and multiplying by atomic weights, $W_{(n)}$ and $A_{(s)}$. Since

$$N_{(W)} = N \times \frac{W_{(n)}}{A} \quad \text{and} \quad S_{(w)} = S \times \frac{W_{(s)}}{A}$$

then

$$N = N_{(w)} \times \frac{A}{W_{(n)}} \quad \text{and} \quad S = S_{(w)} \times \frac{A}{W_{(s)}}$$

where N and S are in terms of numbers of atoms. Substituting into equation A 6.1,

$$N_{(w)} = \frac{S_{(w)} \times W_{(n)}}{W_{(s)}} \times \left[\frac{Ax_{(s)} - R_{xy} Ay_{(s)}}{R_{xy} A_{(n)} - Ax_{(n)}} \right] ,$$

where $N_{(w)}$ and $S_{(w)}$ are weights of normal element and spike in the mixture.

A6.2 Rb-Sr analysis

The Rb-Sr technique is well known and widely used for age dating, with the Sr geochemistry often providing an indication as to the origin of the material. The isotopes of rubidium and strontium are summarized below:

Element	Isotope	Relative abundance
Rubidium	^{85}Rb	72.1654 %
	^{87}Rb	27.8346 %
Strontium	^{84}Sr	0.56 %
	^{86}Sr	9.87 %
	^{87}Sr	7.04 %
	^{88}Sr	82.53 %

All Sr isotopes are stable, as is ^{85}Rb, ^{87}Rb however is radioactive and decays to ^{87}Sr following the scheme

$$^{87}Rb \rightarrow {}^{87}Sr + \beta^- + \gamma + Q ,$$

where β^- is a beta particle, γ is an anti neutrino and Q the decay energy. The growth of ^{87}Sr from ^{87}Rb can be described by the equation

$$^{87}Sr_{(t)} = {}^{87}Sr_{(o)} + {}^{87}Rb\ (e^{\lambda t} - 1) ,$$

where $^{87}Sr_{(t)}$ is the present day value, $^{87}Sr_{(o)}$ the initial incorporated value, λ is the decay constant for ^{87}Rb (presently taken as $1.42 \times 10^{-11}\ Y^{-1}$), and t is the time since formation. Dividing by stable ^{86}Sr, which is constant throughout time, gives

$$\left(\frac{^{87}Sr}{^{86}Sr}\right)_{(t)} = \left(\frac{^{87}Sr}{^{86}Sr}\right)_{(o)} + \frac{^{87}Rb}{^{86}Sr}\left(e^{\lambda t} - 1\right) .$$

This equation is the basis for age determination by the Rb-Sr method.

A6.3 Rb-Sr sample analysis

Six samples of prehnite and pumpellyite were analysed for Rb and Sr at SURRC. The isotope dilution method was used to derive the concentrations of Rb and Sr in the sample.

After the spike was added, the sample was dissolved in hydrofluoric and nitric acids, in a teflon dissolution bomb. The separation of Rb and Sr was achieved by hydrochloric acid elution through cation exchange resin. After final separation and evaporation, both Rb and Sr were preserved as pure nitrate salt residues.

The samples were loaded onto filament beads for analysis. This entails diluting the residue sample with one drop of double distilled H_2O (for Rb) or PHO_5 (for Sr). A drop of the solution is then placed on a previously out gased filament and electrically evaporated. The Rb filament bead consisted of a triple tantalum filament, whereas the Sr bead was a single tantalum filament.

The analysis were carried out on a VG Isomass 54-E (for Sr) and a VG micromass 30-B (for Rb). For Sr, the mass spectrum was scanned according to the peak sequence, 86, 87, 88, 84, 90.5 and 85 (90.5 and 85 are background and Rb contamination peaks). Autoruns of between 40 and 120 measurements were carried out for each Sr sample.

Rb was scanned according to the peak sequence 85, 87 and 90.5. The MM30-B was not automated and manual runs of 6 - 12 measurements were made for each Rb sample.

The $^{87}Rb/^{86}Sr$ ratios are determined to a precision of $\pm$ 0.6%, and normalised to $^{86}Sr/^{88}SR$ ratio of 0.1194. Errors are reported as $\pm 2\sigma_n$.

A6.4 Rb/Sr values of Lewisian vein sealing minerals

SAMPLE	MINERAL	$Rb_{(n)}$ ppm	$Sr_{(n)}$ ppm
DM-1	PREHNITE	2.573626	31.75851
LD-C11	PREHNITE	0.6042648	39.92697
M-C34	PUMPELLYITE	0.5752382	1264.639
R-C1	PUMPELLYITE	0.1520515	7711.951
TUA-5	PUMPELLYITE	0.3754179	9095.448
LC-C10	PUMPELLYITE	12.07876	7585.607

SAMPLE	MINERAL	$^{87}Rb/^{86}Sr$	$2\sigma_n$	$^{87}Sr/^{86}Sr$	$2\sigma_n$
DM-1	PREH	0.2344455	----	0.7066850	7.3×10^{-5}
LD-C11	PREH	4.378091×10^{-2}	2.96×10^{-4}	0.7059140	4.7×10^{-5}
M-C34	PUMP	1.315476×10^{-3}	1.08×10^{-4}	0.7030475	4.0×10^{-5}
R-C1	PUMP	5.704207×10^{-5}	----	0.7069726	2.3×10^{-5}
TUA-5	PUMP	1.194046×10^{-4}	----	0.7060596	2.0×10^{-5}
LC-C10	PUMP	4.60812×10^{-3}	----	0.7069450	2.5×10^{-5}

APPENDIX 7

K-Ar ISOTOPIC ANALYSIS

A7.1 K-Ar analysis

The K-Ar age dating technique relies upon the decay of ^{40}K to ^{40}Ar. ^{40}K however, also decays to ^{40}Ca, and decay to ^{40}Ca is favored by 88.8% of ^{40}K atoms, whereas only 11.2% favour the decay to ^{40}Ar. The isotopes of potassium and argon are summarized below:

Element	Isotope	Relative abundance
Potassium	^{39}K	93.08 %
	^{40}K	0.0119 %
	^{41}K	6.91 %
Argon	^{36}Ar	0.337 %
	^{38}Ar	0.063 %
	^{40}Ar	99.60 %

The growth of radiogenic ^{40}Ar and ^{40}Ca in a K-bearing material, closed to K, Ar and Ca can be expressed by the equation

$$^{40}Ar + ^{40}Ca = ^{40}K \left(e^{\lambda t} - 1\right).$$

The two separate branches of ^{40}K decay have separate decay constants, and

$$\lambda = \lambda e + \lambda \beta .$$

Here λe refers to, $^{40}K \rightarrow ^{40}Ar$ and $\lambda \beta$ to, $^{40}K \rightarrow ^{40}Ca$ where,

$$\lambda e = 0.581 \times 10^{10}\ Y^{-1}, \text{ and}$$
$$\lambda \beta = 4.926 \times 10^{10}\ Y^{-1},$$

thus $$\lambda = 5.543 \times 10^{10}\ Y^{-1}.$$

The fraction of ^{40}K decaying to ^{40}Ar is given by $\left(\frac{\lambda e}{\lambda}\right)^{40}K$, and the growth of radiogenic ^{40}Ar in a K-bearing material can be written as

$$^{40}Ar = \left(\frac{\lambda e}{\lambda}\right) {}^{40}K \left(e^{\lambda t} - 1\right),$$

where $^{40}Ar = {}^{40}Ar_{(t)}$ as $^{40}Ar_{(o)} = 0$.

The $^{40}Ar/{}^{40}K$ ratio can be derived from the total Potassium content (K_T) and the total ^{40}Ar content by the equation

$$\frac{40_{Ar}}{40_{K}} = \frac{40_{Ar} \times 39.102 \times A}{\left(K_T \times 10^4\right) \times 0.000119 \times 39.9623\ A},$$

where 0.000119 is the abundance of ^{40}K, 39.9623 is the atomic weight of ^{40}Ar, 39.102 is the atomic weight of ^{40}K and A is Avagadro's number. The 10^4 factor is a scalar to convert from wt% to ppm.

A7.2 K-Ar sample analysis

One sample of K-feldspar was analysed for K and Ar at SURRC. Analysis and mass spectrometry were kindly carried out by Dr. R. M. Macintyre.

The potassium content was measured by flame photometry, and the argon content by isotope dilution.

A7.3 K/Ar isotopic values of Lewisian vein K-feldspar

SAMPLE	MINERAL	K_T	$^{40}Ar/^{38}Ar$	$^{36}Ar/^{38}Ar$	^{40}Ar (mol/g)	^{40}K (mol/g)
NR-C4	K-feld	8.76	9.1311926	1.57376×10^{-3}	5.76639128	2.61501768

APPENDIX 8

PERMEABILITY AND POROSITY VALUES OF LEWISIAN ROCKS

A8.1 Porosity core test data for the Lewisian cores.

	POROSITY %				
CORE	RUN 1	RUN 2	RUN 3	RUN 4	AVERAGE
JH330	0.6577	0.5108	2.0378	---	1.069
JH332	0.8841	0.2080	0.2674	---	0.4532
JH360Y	1.0650	0.8200	0.4367	1.2886	0.9026
JH360Z	1.6117	0.8595	0.6124	0.8703	0.7516
JH368Y	0.0223	0.3345	0.7581	0.8139	0.4822
JH368Z	0.6513	0.7599	0.4885	0.4342	0.5835
JH371Y	0.5254	0.4728	0.6304	1.0402	0.6672
JH371Z	1.1745	0.4378	0.5339	0.6726	0.7047
JH373X	0.7522	0.6233	0.8704	0.9994	0.8113
JH373Z	0.6612	0.6364	0.6119	0.8933	0.7007
JH374Z	1.2671	0.9187	0.6441	0.6969	0.8817
JH375X	1.1684	0.9958	0.6373	1.1949	0.9991
JH375Y	1.2114	1.0240	1.0615	0.8617	1.0397
JH375Z1	1.6113	1.1842	0.5630	0.4853	0.9610
JH375Z2	1.0940	0.8332	0.6144	0.7406	0.8116
JH375Z3	1.2017	1.7214	1.6564	1.4940	1.5184
JH375Z4	1.1389	0.4393	0.7484	0.6020	0.7322
JH389X1	0.4986	0.2168	0.2927	0.5420	0.3875
JH389X2	0.5266	0.2430	0.5347	0.4780	0.4456
JH389Y	0.6430	0.3751	0.4394	0.5680	0.5034
JH389Z	0.5925	0.6356	0.3232	0.5494	0.5252
JH391XY	0.8780	1.0913	1.5679	1.1540	1.1728
JH391XY	0.3973	0.1673	0.1673	0.3659	0.2745
JH391Z	0.2125	0.4037	0.5418	0.3293	0.3734
JH397XY	2.0041	0.8017	1.1357	1.3806	1.3319
JH397Z	1.3881	1.1389	1.0855	1.3703	1.2464
JH401X	0.7097	0.7886	1.0139	1.0252	0.8843
JH401Y	0.7842	0.7524	0.6146	0.7418	0.7248
JH401Z	1.0772	0.4524	0.8186	0.8510	0.8177
JH402Z	1.0520	0.6838	0.9468	0.8205	0.8758

A8.2 Permeability core test data for the Lewisian core samples

Permeability core tests were made by M. A. Omran, as part of this study, and made available by Jeremy Hall.

Pc = Confining pressure (bars), **ΔP** = pressure head (bars), K_{N_2} = gas permeability K_{H_2O} = water permeability. Permeabilities and errors are given in darcys.

A8.2.1 Samples run at constant confining pressure, variable pressure head

CORE	P_c	ΔP	K_{N_2}	+ ERROR	- ERROR	K_{H_2O}	+ ERROR	- ERROR
FB3-2	1.0	1.0	0.2452e-3	0.2026e-4	0.1931e-4	0.4266e-5	0.3525e-6	0.3360e-6
FB3-2	1.0	2.0	0.2050e-3	0.1185e-4	0.1134e-4	0.3567e-5	0.2061e-6	0.1974e-6
FB3-2	1.0	3.0	0.1903e-3	0.1229e-4	0.1165e-4	0.3312e-5	0.2138e-6	0.2027e-6
FB3-2	1.0	4.0	0.1825e-3	0.1335e-4	0.1249e-4	0.3175e-5	0.2324e-6	0.2174e-6
FB3-2	1.0	5.0	0.1596e-3	0.1278e-4	0.1183e-4	0.2777e-5	0.2224e-6	0.2058e-6
FB3-2	1.0	2.0	0.1587e-3	0.4173e-5	0.4095e-5	0.2761e-5	0.7261e-7	0.7126e-7
FB3-2	1.0	3.0	0.1488e-3	0.3988e-5	0.3912e-5	0.2589e-5	0.6940e-7	0.6807e-7
FB3-2	1.0	4.0	0.1502e-3	0.4086e-5	0.4005e-5	0.2614e-5	0.7109e-7	0.6969e-7
FB3-2	1.0	5.0	0.1318e-3	0.3674e-5	0.3598e-5	0.2294e-5	0.6392e-7	0.6260e-7
FB5-3	1.0	2.0	0.4929e-3	0.2367e-4	0.2325e-4	0.8576e-5	0.4119e-6	0.4045e-6
FB5-3	1.0	3.0	0.4609e-3	0.2252e-4	0.2209e-4	0.8019e-5	0.3919e-6	0.3843e-6
FB5-3	1.0	4.0	0.3952e-3	0.1979e-4	0.1937e-4	0.6877e-5	0.3444e-6	0.3371e-6
FB5-3	1.0	5.0	0.3621e-3	0.1866e-4	0.1822e-4	0.6301e-5	0.3247e-6	0.3171e-6
FB5-3	1.0	2.0	0.4100e-3	0.1968e-4	0.1933e-4	0.7133e-5	0.3424e-6	0.3363e-6
FB5-3	1.0	3.0	0.3530e-3	0.1731e-4	0.1697e-4	0.6143e-5	0.3012e-6	0.2953e-6
FB5-3	1.0	4.0	0.3382e-3	0.1706e-4	0.1669e-4	0.5885e-5	0.2968e-6	0.2903e-6
FB5-3	1.0	5.0	0.3217e-3	0.1667e-4	0.1627e-4	0.5598e-5	0.2900e-6	0.2830e-6
FB8-3	1.0	0.5	0.1284e-1	0.9671e-3	0.8879e-3	0.2234e-3	0.1683e-4	0.1545e-4
FB8-3	1.0	1.0	0.1104e-1	0.9992e-3	0.8924e-3	0.1922e-3	0.1739e-4	0.1553e-4
FB8-3	1.0	1.5	0.9307e-2	0.9904e-3	0.8611e-3	0.1619e-3	0.1723e-4	0.1498e-4
FB8-3	1.0	2.0	0.7553e-2	0.5884e-3	0.5339e-3	0.1314e-3	0.1024e-4	0.9290e-5
FB8-3	1.0	2.5	0.8144e-2	0.8405e-3	0.7318e-3	0.1417e-3	0.1462e-4	0.1273e-4
FB8-3	1.0	3.0	0.7889e-2	0.6698e-3	0.5999e-3	0.1373e-3	0.1165e-4	0.1044e-4
FB19-3	1.0	1.0	0.4408e-4	0.5996e-5	0.5765e-5	0.7670e-6	0.1043e-6	0.1003e-6
FB19-3	1.0	2.0	0.4878e-4	0.4319e-5	0.4152e-5	0.8487e-6	0.7514e-7	0.7224e-7
FB19-3	1.0	3.0	0.4223e-4	0.3398e-5	0.3261e-5	0.7348e-6	0.5913e-7	0.5674e-7
FB19-3	1.0	4.0	0.3475e-4	0.2065e-5	0.1992e-5	0.6047e-6	0.3593e-7	0.3466e-7
FB19-3	1.0	5.0	0.3087e-4	0.1829e-5	0.1761e-5	0.5372e-6	0.3182e-7	0.3065e-7
FB19-3	1.0	2.0	0.4880e-4	0.1077e-5	0.1065e-5	0.8490e-6	0.1874e-7	0.1854e-7
FB19-3	1.0	3.0	0.4874e-4	0.1095e-5	0.1082e-5	0.8480e-6	0.1905e-7	0.1883e-7
FB19-3	1.0	4.0	0.3278e-4	0.7299e-6	0.7218e-6	0.5704e-6	0.1270e-7	0.1256e-7
FB19-3	1.0	5.0	0.2853e-4	0.6431e-6	0.6357e-6	0.4964e-6	0.1119e-7	0.1106e-7

CORE	P_c	ΔP	K_{N_2}	+ ERROR	- ERROR	K_{H_2O}	+ ERROR	- ERROR
FH1-1	1.0	2.0	0.2382e-5	0.3869e-6	0.3565e-6	0.4145e-7	0.6731e-8	0.6204e-8
FH1-1	1.0	3.0	0.2431e-5	0.3621e-6	0.3345e-6	0.4231e-7	0.6301e-8	0.5821e-8
FH1-1	1.0	5.0	0.1925e-5	0.2091e-6	0.1955e-6	0.3350e-7	0.3639e-8	0.3402e-8
JH330	1.0	2.0	0.2329e-3	0.2071e-4	0.1936e-4	0.4053e-5	0.3603e-6	0.3368e-6
JH330	1.0	3.0	0.2118e-3	0.1927e-4	0.1797e-4	0.3686e-5	0.3352e-6	0.3127e-6
JH330	1.0	4.0	0.1846e-3	0.1798e-4	0.1665e-4	0.3213e-5	0.3128e-6	0.2897e-6
JH330	1.0	5.0	0.1726e-3	0.1647e-4	0.1528e-4	0.3003e-5	0.2866e-6	0.2658e-6
JH330	1.5	0.6	0.2918e-3	0.3392e-4	0.3111e-4	0.5077e-5	0.5901e-6	0.5413e-6
JH330	1.5	1.0	0.3023e-3	0.4123e-4	0.3734e-4	0.5261e-5	0.7173e-6	0.6496e-6
JH330	1.5	1.5	0.2483e-3	0.3466e-4	0.3127e-4	0.4320e-5	0.6032e-6	0.5441e-6
JH330	1.5	2.0	0.2589e-3	0.3162e-4	0.2876e-4	0.4504e-5	0.5502e-6	0.5004e-6
JH330	1.5	2.5	0.2244e-3	0.3360e-4	0.2995e-4	0.3905e-5	0.5847e-6	0.5211e-6
JH330	1.5	3.0	0.2238e-3	0.2584e-4	0.2357e-4	0.3893e-5	0.4496e-6	0.4100e-6
JH330	1.0	2.0	0.2758e-3	0.2184e-4	0.2063e-4	0.4799e-5	0.3800e-6	0.3589e-6
JH330	1.0	3.0	0.2417e-3	0.1929e-4	0.1820e-4	0.4205e-5	0.3357e-6	0.3168e-6
JH330	1.0	4.0	0.2158e-3	0.1731e-4	0.1633e-4	0.3755e-5	0.3012e-6	0.2841e-6
JH330	1.0	5.0	0.1884e-3	0.1525e-4	0.1437e-4	0.3278e-5	0.2653e-6	0.2500e-6
JH330A	1.0	1.0	0.1902e-2	0.1885e-3	0.1785e-3	0.3309e-4	0.3279e-5	0.3106e-5
JH330A	1.0	2.0	0.1659e-2	0.1769e-3	0.1655e-3	0.2887e-4	0.3079e-5	0.2879e-5
JH330A	1.0	3.0	0.1425e-2	0.1350e-3	0.1283e-3	0.2480e-4	0.2349e-5	0.2232e-5
JH330B	1.0	1.0	0.3262e-3	0.2719e-4	0.2581e-4	0.5676e-5	0.4732e-6	0.4491e-6
JH330B	1.0	2.0	0.2775e-3	0.2425e-4	0.2289e-4	0.4829e-5	0.4219e-6	0.3983e-6
JH330B	1.0	3.0	0.2432e-3	0.1748e-4	0.1661e-4	0.4232e-5	0.3042e-6	0.2891e-6
JH330B	1.0	2.0	0.2907e-3	0.1333e-4	0.1297e-4	0.5058e-5	0.2319e-6	0.2256e-6
JH330B	1.0	3.0	0.2491e-3	0.1163e-4	0.1130e-4	0.4334e-5	0.2024e-6	0.1967e-6
JH330B	1.0	4.0	0.2425e-3	0.1138e-4	0.1106e-4	0.4220e-5	0.1981e-6	0.1924e-6
JH330B	1.0	5.0	0.2351e-3	0.1106e-4	0.1074e-4	0.4091e-5	0.1924e-6	0.1868e-6
JH330C	1.0	1.0	0.7653e-4	0.6838e-5	0.6489e-5	0.1332e-5	0.1190e-6	0.1129e-6
JH330C	1.0	2.0	0.5490e-4	0.5593e-5	0.5271e-5	0.9552e-6	0.9731e-7	0.9171e-7
JH330C	1.0	3.0	0.4561e-4	0.3671e-5	0.3495e-5	0.7935e-6	0.6387e-7	0.6081e-7
JH330D	1.0	2.0	0.4053e-3	0.6962e-5	0.6853e-5	0.7053e-5	0.1211e-6	0.1192e-6
JH330D	1.0	3.0	0.3561e-3	0.6111e-5	0.6014e-5	0.6197e-5	0.1063e-6	0.1046e-6
JH330D	1.0	4.0	0.3222e-3	0.5731e-5	0.5636e-5	0.5606e-5	0.9972e-7	0.9806e-7
JH330D	1.0	5.0	0.3014e-3	0.5699e-5	0.5596e-5	0.5244e-5	0.9916e-7	0.9738e-7

CORE	P_c	ΔP	K_{N_2}	+ ERROR	- ERROR	K_{H_2O}	+ ERROR	- ERROR
JH331	1.0	2.0	0.1203e-2	0.4692e-4	0.4534e-4	0.2093e-4	0.8164e-6	0.7889e-6
JH331	1.0	3.0	0.1184e-2	0.4862e-4	0.4685e-4	0.2060e-4	0.8460e-6	0.8152e-6
JH331	1.0	4.0	0.1052e-2	0.4511e-4	0.4337e-4	0.1831e-4	0.7849e-6	0.7546e-6
JH331	1.0	5.0	0.1127e-2	0.5260e-4	0.5030e-4	0.1961e-4	0.9153e-6	0.8752e-6
JH331	1.0	2.0	0.1527e-2	0.6081e-4	0.5870e-4	0.2656e-4	0.1058e-5	0.1021e-5
JH331	1.0	3.0	0.1486e-2	0.6260e-4	0.6024e-4	0.2585e-4	0.1089e-5	0.1048e-5
JH331	1.0	4.0	0.1507e-2	0.7064e-4	0.6754e-4	0.2622e-4	0.1229e-5	0.1175e-5
JH331	1.0	5.0	0.1529e-2	0.8077e-4	0.7655e-4	0.2660e-4	0.1405e-5	0.1332e-5
JH331A	1.0	1.0	0.4421e-4	0.3354e-5	0.3198e-5	0.7693e-6	0.5836e-7	0.5565e-7
JH331A	1.0	2.0	0.3655e-4	0.5561e-5	0.5137e-5	0.6359e-6	0.9676e-7	0.8939e-7
JH331A	1.0	3.0	0.3300e-4	0.3505e-5	0.3282e-5	0.5742e-6	0.6099e-7	0.5711e-7
JH331A	1.0	5.0	0.2907e-4	0.2172e-5	0.2072e-5	0.5058e-6	0.3780e-7	0.3606e-7
JH332	1.0	2.0	0.5131e-3	0.1283e-4	0.1245e-4	0.8927e-5	0.2233e-6	0.2167e-6
JH332	1.0	3.0	0.3858e-3	0.9753e-5	0.9462e-5	0.6713e-5	0.1697e-6	0.1646e-6
JH332	1.0	4.0	0.2985e-3	0.7743e-5	0.7508e-5	0.5195e-5	0.1347e-6	0.1306e-6
JH332	1.0	5.0	0.2690e-3	0.7065e-5	0.6849e-5	0.4680e-5	0.1229e-6	0.1192e-6
JH332D	1.0	2.0	0.2214e-3	0.4874e-5	0.4759e-5	0.3853e-5	0.8480e-7	0.8280e-7
JH332D	1.0	3.0	0.8830e-4	0.2009e-5	0.1961e-5	0.1536e-5	0.3496e-7	0.3412e-7
JH332D	1.0	4.0	0.7332e-4	0.1615e-5	0.1577e-5	0.1276e-5	0.2811e-7	0.2745e-7
JH332D	1.0	5.0	0.7245e-4	0.1579e-5	0.1542e-5	0.1261e-5	0.2748e-7	0.2683e-7
JH333	1.0	1.0	0.2387e-2	0.1999e-3	0.1852e-3	0.4154e-4	0.3479e-5	0.3222e-5
JH333	1.0	1.5	0.1999e-2	0.1838e-3	0.1683e-3	0.3478e-4	0.3197e-5	0.2929e-5
JH333	1.0	2.0	0.1722e-2	0.1278e-3	0.1192e-3	0.2997e-4	0.2224e-5	0.2073e-5
JH333	1.0	2.0	0.6755e-3	0.5368e-4	0.4999e-4	0.1175e-4	0.9341e-6	0.8699e-6
JH333	1.0	3.0	0.1168e-2	0.9199e-4	0.8526e-4	0.2033e-4	0.1601e-5	0.1484e-5
JH333D	1.0	2.0	0.5775e-3	0.2400e-4	0.2317e-4	0.1005e-4	0.4176e-6	0.4031e-6
JH333D	1.0	3.0	0.5095e-3	0.2165e-4	0.2088e-4	0.8865e-5	0.3768e-6	0.3633e-6
JH333D	1.0	4.0	0.4243e-3	0.1842e-4	0.1774e-4	0.7383e-5	0.3205e-6	0.3087e-6
JH333D	1.0	5.0	0.4167e-3	0.1854e-4	0.1783e-4	0.7250e-5	0.3226e-6	0.3103e-6
JH334	1.0	0.5	0.1135e-3	0.4404e-4	0.4082e-4	0.1975e-5	0.7663e-6	0.7103e-6
JH334	1.0	1.0	0.9052e-4	0.7950e-5	0.7529e-5	0.1575e-5	0.1383e-6	0.1310e-6
JH334	1.0	2.0	0.9196e-4	0.1835e-4	0.1686e-4	0.1600e-5	0.3193e-6	0.2933e-6
JH334	1.0	2.0	0.8062e-4	0.7312e-5	0.6899e-5	0.1403e-5	0.1272e-6	0.1200e-6
JH334	1.0	3.0	0.1444e-3	0.9827e-5	0.9299e-5	0.2513e-5	0.1710e-6	0.1618e-6
JH334	1.0	4.0	0.2039e-3	0.2538e-4	0.2284e-4	0.3547e-5	0.4417e-6	0.3974e-6
JH334	1.0	4.0	0.2093e-3	0.1022e-4	0.9786e-5	0.3641e-5	0.1779e-6	0.1703e-6

A8.2.2 Samples run at variable confining pressure, constant pressure head

CORE	P_c	ΔP	K_{N_2}	+ ERROR	- ERROR	K_{H_2O}	+ ERROR	- ERROR
JH331B	20.0	5.0	0.3810e-5	0.4714e-6	0.4378e-6	0.6630e-7	0.8202e-8	0.7617e-8
JH331B	40.0	5.0	0.3286e-5	0.4772e-6	0.4405e-6	0.5718e-7	0.8303e-8	0.7665e-8
JH331B	80.0	5.0	0.2585e-5	0.2891e-6	0.2697e-6	0.4498e-7	0.5031e-8	0.4694e-8
JH331B	120.0	5.0	0.1883e-5	0.1366e-6	0.1304e-6	0.3277e-7	0.2377e-8	0.2269e-8
JH331B	20.0	5.0	0.2602e-5	0.4786e-6	0.4387e-6	0.4527e-7	0.8328e-8	0.7633e-8
JH331B	40.0	5.0	0.1085e-5	0.1441e-6	0.1336e-6	0.1888e-7	0.2508e-8	0.2325e-8
JH331B	80.0	5.0	0.6967e-6	0.2633e-6	0.2382e-6	0.1212e-7	0.4581e-8	0.4145e-8
JH360Y	50.0	5.0	0.1260e-4	0.4126e-6	0.4050e-6	0.2192e-6	0.7180e-8	0.7047e-8
JH360Y	100.0	5.0	0.1068e-4	0.3920e-6	0.3846e-6	0.1858e-6	0.6820e-8	0.6692e-8
JH360Y	150.0	5.0	0.9859e-5	0.4396e-6	0.4311e-6	0.1715e-6	0.7649e-8	0.7501e-8
JH360Y	200.0	5.0	0.7558e-5	0.4146e-6	0.4063e-6	0.1315e-6	0.7213e-8	0.7070e-8
JH360Y	300.0	5.0	0.2582e-5	0.2649e-6	0.2595e-6	0.4493e-7	0.4609e-8	0.4516e-8
JH360Y	400.0	5.0	0.4225e-5	0.2825e-6	0.2769e-6	0.7352e-7	0.4915e-8	0.4818e-8
JH360Y	500.0	5.0	0.3286e-5	0.2724e-6	0.2670e-6	0.5718e-7	0.4740e-8	0.4645e-8
JH360Y	400.0	5.0	0.3651e-5	0.2232e-6	0.2188e-6	0.6353e-7	0.3884e-8	0.3808e-8
JH360Y	300.0	5.0	0.4332e-5	0.1965e-6	0.1928e-6	0.7537e-7	0.3420e-8	0.3355e-8
JH360Y	200.0	5.0	0.4507e-5	0.1418e-6	0.1393e-6	0.7842e-7	0.2467e-8	0.2423e-8
JH360Y	100.0	5.0	0.2131e-4	0.2755e-6	0.2716e-6	0.3707e-6	0.4794e-8	0.4725e-8
JH360Z	100.0	5.0	0.1675e-2	0.3327e-4	0.3250e-4	0.2914e-4	0.5790e-6	0.5655e-6
JH360Z	150.0	5.0	0.1017e-2	0.1543e-4	0.1517e-4	0.1770e-4	0.2684e-6	0.2640e-6
JH360Z	200.0	5.0	0.6634e-3	0.9448e-5	0.9304e-5	0.1154e-4	0.1644e-6	0.1619e-6
JH360Z	300.0	5.0	0.2832e-3	0.3608e-5	0.3560e-5	0.4927e-5	0.6277e-7	0.6195e-7
JH360Z	400.0	5.0	0.1727e-3	0.2650e-5	0.2612e-5	0.3006e-5	0.4612e-7	0.4544e-7
JH360Z	500.0	5.0	0.1031e-3	0.2021e-5	0.1989e-5	0.1795e-5	0.3517e-7	0.3460e-7
JH360Z	400.0	5.0	0.1080e-3	0.2212e-5	0.2175e-5	0.1879e-5	0.3849e-7	0.3785e-7
JH360Z	300.0	5.0	0.1170e-3	0.2313e-5	0.2274e-5	0.2037e-5	0.4024e-7	0.3958e-7
JH360Z	200.0	5.0	0.1362e-3	0.2524e-5	0.2484e-5	0.2370e-5	0.4392e-7	0.4321e-7
JH360Z	100.0	5.0	0.4624e-3	0.6412e-5	0.6319e-5	0.8046e-5	0.1116e-6	0.1100e-6
JH368Y	50.0	5.0	0.7848e-6	0.9643e-7	0.9449e-7	0.1366e-7	0.1678e-8	0.1644e-8
JH368Y	100.0	5.0	0.7848e-6	0.1406e-6	0.1377e-6	0.1366e-7	0.2446e-8	0.2396e-8
JH368Y	200.0	5.0	0.6802e-6	0.6002e-7	0.5883e-7	0.1183e-7	0.1044e-8	0.1024e-8
JH368Y	300.0	5.0	0.4628e-6	0.2517e-7	0.2469e-7	0.8053e-8	0.4379e-9	0.4295e-9
JH368Y	400.0	5.0	0.3488e-6	0.9182e-7	0.8993e-7	0.6069e-8	0.1598e-8	0.1565e-8
JH368Y	500.0	5.0	0.3488e-6	0.9182e-7	0.8993e-7	0.6069e-8	0.1598e-8	0.1565e-8

CORE	P_c	ΔP	K_{N_2}	+ ERROR	- ERROR	K_{H_2O}	+ ERROR	- ERROR
JH368Z	50.0	5.0	0.1237e-3	0.1687e-5	0.1662e-5	0.2152e-5	0.2935e-7	0.2891e-7
JH368Z	100.0	5.0	0.1012e-3	0.1374e-5	0.1354e-5	0.1762e-5	0.2391e-7	0.2355e-7
JH368Z	150.0	5.0	0.8364e-4	0.1137e-5	0.1120e-5	0.1455e-5	0.1978e-7	0.1948e-7
JH368Z	200.0	5.0	0.6996e-4	0.9878e-6	0.9729e-6	0.1217e-5	0.1719e-7	0.1693e-7
JH368Z	300.0	5.0	0.4955e-4	0.7658e-6	0.7538e-6	0.8623e-6	0.1332e-7	0.1312e-7
JH368Z	400.0	5.0	0.3498e-4	0.6072e-6	0.5974e-6	0.6087e-6	0.1057e-7	0.1039e-7
JH368Z	500.0	5.0	0.3000e-4	0.4994e-6	0.4915e-6	0.5219e-6	0.8690e-8	0.8551e-8
JH368Z	400.0	5.0	0.2893e-4	0.5414e-6	0.5324e-6	0.5033e-6	0.9420e-8	0.9263e-8
JH368Z	300.0	5.0	0.3319e-4	0.5877e-6	0.5781e-6	0.5774e-6	0.1023e-7	0.1006e-7
JH368Z	200.0	5.0	0.3673e-4	0.5529e-6	0.5444e-6	0.6391e-6	0.9621e-8	0.9473e-8
JH368Z	100.0	5.0	0.4574e-4	0.7243e-6	0.7129e-6	0.7959e-6	0.1260e-7	0.1240e-7
JH371Y	50.0	5.0	0.7536e-4	0.1177e-5	0.1161e-5	0.1311e-5	0.2048e-7	0.2020e-7
JH371Y	100.0	5.0	0.6470e-4	0.9459e-6	0.9335e-6	0.1126e-5	0.1646e-7	0.1624e-7
JH371Y	150.0	5.0	0.4934e-4	0.8654e-6	0.8526e-6	0.8585e-6	0.1506e-7	0.1483e-7
JH371Y	200.0	5.0	0.4301e-4	0.6901e-6	0.6805e-6	0.7484e-6	0.1201e-7	0.1184e-7
JH371Y	300.0	5.0	0.2819e-4	0.5153e-6	0.5076e-6	0.4906e-6	0.8967e-8	0.8832e-8
JH371Y	400.0	5.0	0.4829e-5	0.7244e-7	0.7149e-7	0.8402e-7	0.1261e-8	0.1244e-8
JH371Y	500.0	5.0	0.1392e-4	0.3470e-6	0.3410e-6	0.2421e-6	0.6037e-8	0.5933e-8
JH371Y	400.0	5.0	0.1500e-4	0.3598e-6	0.3536e-6	0.2610e-6	0.6260e-8	0.6153e-8
JH371Y	300.0	5.0	0.1825e-4	0.3981e-6	0.3916e-6	0.3176e-6	0.6927e-8	0.6814e-8
JH371Y	200.0	5.0	0.2223e-4	0.4450e-6	0.4380e-6	0.3868e-6	0.7743e-8	0.7621e-8
JH371Y	100.0	5.0	0.3485e-4	0.6499e-6	0.6400e-6	0.6065e-6	0.1131e-7	0.1114e-7
JH371Z	50.0	5.0	0.2563e-4	0.3565e-6	0.3531e-6	0.4460e-6	0.6203e-8	0.6144e-8
JH371Z	100.0	5.0	0.2136e-4	0.3312e-6	0.3280e-6	0.3716e-6	0.5763e-8	0.5707e-8
JH371Z	150.0	5.0	0.2034e-4	0.3252e-6	0.3220e-6	0.3539e-6	0.5658e-8	0.5603e-8
JH371Z	200.0	5.0	0.1627e-4	0.2434e-6	0.2411e-6	0.2832e-6	0.4235e-8	0.4194e-8
JH371Z	300.0	5.0	0.1279e-4	0.1294e-6	0.1283e-6	0.2225e-6	0.2251e-8	0.2232e-8
JH371Z	400.0	5.0	0.8509e-5	0.6862e-7	0.6810e-7	0.1481e-6	0.1194e-8	0.1185e-8
JH371Z	500.0	5.0	0.7284e-5	0.6647e-7	0.6594e-7	0.1267e-6	0.1157e-8	0.1147e-8
JH373X	50.0	5.0	0.3342e-4	0.5346e-6	0.5271e-6	0.5814e-6	0.9302e-8	0.9172e-8
JH373X	100.0	5.0	0.2694e-4	0.4898e-6	0.4825e-6	0.4687e-6	0.8523e-8	0.8396e-8
JH373X	150.0	5.0	0.2171e-4	0.4342e-6	0.4275e-6	0.3778e-6	0.7555e-8	0.7439e-8
JH373X	200.0	5.0	0.1474e-4	0.2065e-6	0.2038e-6	0.2565e-6	0.3593e-8	0.3546e-8
JH373X	300.0	5.0	0.1117e-4	0.1372e-6	0.1356e-6	0.1943e-6	0.2388e-8	0.2360e-8
JH373X	400.0	5.0	0.7827e-5	0.1901e-6	0.1870e-6	0.1362e-6	0.3308e-8	0.3254e-8
JH375X	500.0	5.0	0.8149e-5	0.1934e-6	0.1903e-6	0.1418e-6	0.3366e-8	0.3312e-8

CORE	P_c	ΔP	K_{N_2}	+ ERROR	- ERROR	K_{H_2O}	+ ERROR	- ERROR
JH373Y	50.0	5.0	0.7614e-5	0.2470e-6	0.2443e-6	0.1325e-6	0.4297e-8	0.4251e-8
JH373Y	100.0	5.0	0.7328e-5	0.2745e-6	0.2715e-6	0.1275e-6	0.4776e-8	0.4724e-8
JH373Y	150.0	5.0	0.4608e-5	0.2290e-6	0.2265e-6	0.8018e-7	0.3985e-8	0.3941e-8
JH373Y	200.0	5.0	0.5209e-5	0.2326e-6	0.2300e-6	0.9064e-7	0.4048e-8	0.4003e-8
JH373Y	300.0	5.0	0.2671e-5	0.1049e-6	0.1038e-6	0.4648e-7	0.1825e-8	0.1805e-8
JH373Y	400.0	5.0	0.1959e-5	0.1008e-6	0.9970e-7	0.3409e-7	0.1754e-8	0.1735e-8
JH373Y	500.0	5.0	0.1580e-5	0.3220e-7	0.3188e-7	0.2749e-7	0.5602e-9	0.5548e-9
JH373Z	50.0	5.0	0.1425e-4	0.2635e-6	0.2608e-6	0.2479e-6	0.4584e-8	0.4538e-8
JH373Z	100.0	5.0	0.1175e-4	0.2487e-6	0.2462e-6	0.2045e-6	0.4328e-8	0.4283e-8
JH373Z	150.0	5.0	0.1042e-4	0.2637e-6	0.2609e-6	0.1813e-6	0.4588e-8	0.4540e-8
JH373Z	200.0	5.0	0.7671e-5	0.8153e-7	0.8084e-7	0.1335e-6	0.1419e-8	0.1407e-8
JH373Z	300.0	5.0	0.6155e-5	0.5590e-7	0.5545e-7	0.1071e-6	0.9726e-9	0.9648e-9
JH373Z	400.0	5.0	0.4660e-5	0.5598e-7	0.5549e-7	0.8109e-7	0.9740e-9	0.9655e-9
JH373Z	500.0	5.0	0.3925e-5	0.4388e-7	0.4350e-7	0.6830e-7	0.7634e-9	0.7569e-9
JH374Z	50.0	5.0	0.5939e-4	0.8666e-6	0.8550e-6	0.1033e-5	0.1508e-7	0.1488e-7
JH374Z	100.0	5.0	0.4793e-4	0.7450e-6	0.7346e-6	0.8340e-6	0.1296e-7	0.1278e-7
JH374Z	150.0	5.0	0.4209e-4	0.6830e-6	0.6733e-6	0.7323e-6	0.1188e-7	0.1172e-7
JH374Z	200.0	5.0	0.3671e-4	0.6259e-6	0.6168e-6	0.6387e-6	0.1089e-7	0.1073e-7
JH374Z	300.0	5.0	0.3016e-4	0.5564e-6	0.5481e-6	0.5248e-6	0.9682e-8	0.9536e-8
JH374Z	400.0	5.0	0.2268e-4	0.4770e-6	0.4695e-6	0.3946e-6	0.8300e-8	0.8169e-8
JH374Z	500.0	5.0	0.2081e-4	0.4572e-6	0.4499e-6	0.3621e-6	0.7954e-8	0.7828e-8
JH374Z	400.0	5.0	0.2128e-4	0.5032e-6	0.4950e-6	0.3702e-6	0.8756e-8	0.8613e-8
JH374Z	300.0	5.0	0.2619e-4	0.5557e-6	0.5469e-6	0.4557e-6	0.9670e-8	0.9517e-8
JH374Z	200.0	5.0	0.2619e-4	0.5557e-6	0.5469e-6	0.4557e-6	0.9670e-8	0.9517e-8
JH374Z	100.0	5.0	0.3328e-4	0.6316e-6	0.6220e-6	0.5791e-6	0.1099e-7	0.1082e-7
JH375X	50.0	5.0	0.1893e-4	0.4158e-6	0.4082e-6	0.3293e-6	0.7236e-8	0.7103e-8
JH375X	100.0	5.0	0.1373e-4	0.3532e-6	0.3465e-6	0.2389e-6	0.6146e-8	0.6029e-8
JH375X	150.0	5.0	0.1175e-4	0.2536e-6	0.2490e-6	0.2044e-6	0.4413e-8	0.4333e-8
JH375X	200.0	5.0	0.9801e-5	0.2359e-6	0.2315e-6	0.1705e-6	0.4104e-8	0.4028e-8
JH375X	250.0	5.0	0.8682e-5	0.1358e-6	0.1336e-6	0.1511e-6	0.2363e-8	0.2325e-8
JH375X	300.0	5.0	0.6170e-5	0.8991e-7	0.8852e-7	0.1074e-6	0.1564e-8	0.1540e-8
JH375X	400.0	5.0	0.4778e-5	0.1028e-6	0.1009e-6	0.8314e-7	0.1788e-8	0.1756e-8
JH375X	500.0	5.0	0.3817e-5	0.5579e-7	0.5493e-7	0.6641e-7	0.9707e-9	0.9558e-9

CORE	P_c	ΔP	K_{N_2}	+ ERROR	- ERROR	K_{H_2O}	+ ERROR	- ERROR
JH375Y	50.0	5.0	0.1350e-4	0.2802e-6	0.2751e-6	0.2349e-6	0.4875e-8	0.4787e-8
JH375Y	100.0	5.0	0.8232e-5	0.2249e-6	0.2204e-6	0.1432e-6	0.3913e-8	0.3835e-8
JH375Y	50.0	5.0	0.6905e-5	0.1943e-6	0.1904e-6	0.1202e-6	0.3381e-8	0.3313e-8
JH375Y	100.0	5.0	0.5462e-5	0.1755e-6	0.1719e-6	0.9504e-7	0.3054e-8	0.2991e-8
JH375Y	150.0	5.0	0.4754e-5	0.1795e-6	0.1756e-6	0.8272e-7	0.3123e-8	0.3056e-8
JH375Y	200.0	5.0	0.3027e-5	0.8846e-7	0.8668e-7	0.5267e-7	0.1539e-8	0.1508e-8
JH375Y	300.0	5.0	0.2033e-5	0.4604e-7	0.4519e-7	0.3537e-7	0.8012e-9	0.7862e-9
JH375Y	400.0	5.0	0.1546e-5	0.9833e-7	0.9607e-7	0.2690e-7	0.1711e-8	0.1672e-8
JH375Y	500.0	5.0	0.1044e-5	0.7219e-7	0.7052e-7	0.1816e-7	0.1256e-8	0.1227e-8
JH375Z2	20.0	5.0	0.7389e-5	0.2654e-6	0.2623e-6	0.1286e-6	0.4618e-8	0.4565e-8
JH375Z2	50.0	5.0	0.6607e-5	0.2494e-6	0.2465e-6	0.1150e-6	0.4339e-8	0.4290e-8
JH375Z2	100.0	5.0	0.6194e-5	0.2468e-6	0.2439e-6	0.1078e-6	0.4294e-8	0.4245e-8
JH375Z2	150.0	5.0	0.5162e-5	0.2403e-6	0.2375e-6	0.8981e-7	0.4181e-8	0.4132e-8
JH375Z2	200.0	5.0	0.4317e-5	0.2159e-6	0.2134e-6	0.7512e-7	0.3757e-8	0.3713e-8
JH375Z2	300.0	5.0	0.3716e-5	0.1615e-6	0.1596e-6	0.6466e-7	0.2810e-8	0.2778e-8
JH375Z2	400.0	5.0	0.2851e-5	0.1164e-6	0.1151e-6	0.4961e-7	0.2025e-8	0.2002e-8
JH375Z3	20.0	5.0	0.9095e-5	0.2748e-6	0.2697e-6	0.1582e-6	0.4782e-8	0.4693e-8
JH375Z3	50.0	5.0	0.4961e-5	0.1734e-6	0.1700e-6	0.8632e-7	0.3017e-8	0.2958e-8
JH375Z3	100.0	5.0	0.2140e-5	0.1309e-6	0.1278e-6	0.3723e-7	0.2279e-8	0.2224e-8
JH375Z3	150.0	5.0	0.1167e-5	0.1163e-6	0.1133e-6	0.2031e-7	0.2024e-8	0.1971e-8
JH375Z3	200.0	5.0	0.4458e-6	0.5180e-7	0.5045e-7	0.7757e-8	0.9013e-9	0.8778e-9
JH375Z3	300.0	5.0	0.2675e-6	0.2761e-6	0.2675e-6	0.4654e-8	0.4804e-8	0.4654e-8
JH375Z4	50.0	5.0	0.6808e-5	0.2241e-6	0.2194e-6	0.1185e-6	0.3900e-8	0.3818e-8
JH375Z4	100.0	5.0	0.5473e-5	0.2067e-6	0.2022e-6	0.9523e-7	0.3597e-8	0.3519e-8
JH375Z4	150.0	5.0	0.4806e-5	0.1980e-6	0.1936e-6	0.8362e-7	0.3445e-8	0.3369e-8
JH375Z4	200.0	5.0	0.3337e-5	0.1788e-6	0.1747e-6	0.5807e-7	0.3111e-8	0.3040e-8
JH375Z4	300.0	5.0	0.3204e-5	0.1133e-6	0.1109e-6	0.5575e-7	0.1972e-8	0.1930e-8
JH375Z4	400.0	5.0	0.2225e-5	0.7349e-7	0.7197e-7	0.3871e-7	0.1279e-8	0.1252e-8
JH375Z4	500.0	5.0	0.2100e-5	0.4468e-7	0.4387e-7	0.3654e-7	0.7774e-9	0.7633e-9
JH389X	50.0	5.0	0.1093e-4	0.4163e-6	0.4077e-6	0.1903e-6	0.7244e-8	0.7093e-8
JH389X	100.0	5.0	0.7734e-5	0.3736e-6	0.3654e-6	0.1346e-6	0.6500e-8	0.6358e-8
JH389X	150.0	5.0	0.6401e-5	0.3558e-6	0.3478e-6	0.1114e-6	0.6190e-8	0.6051e-8
JH389X	200.0	5.0	0.4800e-5	0.2954e-6	0.2887e-6	0.8353e-7	0.5140e-8	0.5023e-8
JH389X	300.0	5.0	0.3086e-5	0.9775e-7	0.9587e-7	0.5370e-7	0.1701e-8	0.1668e-8
JH389X	400.0	5.0	0.2155e-5	0.4928e-7	0.4845e-7	0.3750e-7	0.8575e-9	0.8431e-9
JH389X	500.0	5.0	0.1524e-5	0.1744e-6	0.1702e-6	0.2652e-7	0.3034e-8	0.2961e-8
JH389X	400.0	5.0	0.2311e-5	0.2106e-6	0.2056e-6	0.4022e-7	0.3664e-8	0.3577e-8
JH389X	300.0	5.0	0.1600e-5	0.2916e-6	0.2843e-6	0.2784e-7	0.5074e-8	0.4947e-8
JH389X	200.0	5.0	0.2774e-5	0.2529e-6	0.2469e-6	0.4826e-7	0.4401e-8	0.4296e-8
JH389X	100.0	5.0	0.4000e-5	0.3237e-6	0.3160e-6	0.6961e-7	0.5632e-8	0.5499e-8

CORE	P_c	ΔP	K_{N_2}	+ ERROR	- ERROR	K_{H_2O}	+ ERROR	- ERROR
JH389Y	50.0	5.0	0.1653e-4	0.3623e-6	0.3575e-6	0.2877e-6	0.6304e-8	0.6221e-8
JH389Y	100.0	5.0	0.8966e-5	0.2740e-6	0.2702e-6	0.1560e-6	0.4768e-8	0.4702e-8
JH389Y	150.0	5.0	0.7172e-5	0.2742e-6	0.2703e-6	0.1248e-6	0.4770e-8	0.4703e-8
JH389Y	200.0	5.0	0.4890e-5	0.2428e-6	0.2393e-6	0.8509e-7	0.4224e-8	0.4164e-8
JH389Y	300.0	5.0	0.3985e-5	0.2128e-6	0.2098e-6	0.6933e-7	0.3703e-8	0.3651e-8
JH389Y	400.0	5.0	0.2415e-5	0.7861e-7	0.7755e-7	0.4202e-7	0.1368e-8	0.1349e-8
JH389Y	500.0	5.0	0.1956e-5	0.3614e-7	0.3570e-7	0.3404e-7	0.6289e-9	0.6211e-9
JH389Y	400.0	5.0	0.2173e-5	0.1532e-6	0.1510e-6	0.3782e-7	0.2666e-8	0.2628e-8
JH389Y	300.0	5.0	0.3260e-5	0.2073e-6	0.2043e-6	0.5673e-7	0.3607e-8	0.3556e-8
JH389Y	200.0	5.0	0.3260e-5	0.2073e-6	0.2043e-6	0.5673e-7	0.3607e-8	0.3556e-8
JH389Y	100.0	5.0	0.7245e-5	0.2377e-6	0.2344e-6	0.1261e-6	0.4135e-8	0.4078e-8
JH389Z	50.0	5.0	0.1161e-4	0.2769e-6	0.2724e-6	0.2020e-6	0.4819e-8	0.4741e-8
JH389Z	100.0	5.0	0.6150e-5	0.1997e-6	0.1963e-6	0.1070e-6	0.3476e-8	0.3415e-8
JH389Z	150.0	5.0	0.1364e-4	0.2785e-6	0.2742e-6	0.2373e-6	0.4845e-8	0.4770e-8
JH389Z	200.0	5.0	0.1290e-4	0.1972e-6	0.1946e-6	0.2244e-6	0.3432e-8	0.3385e-8
JH389Z	300.0	5.0	0.8422e-5	0.1091e-6	0.1077e-6	0.1465e-6	0.1898e-8	0.1875e-8
JH389Z	400.0	5.0	0.8288e-5	0.2222e-6	0.2185e-6	0.1442e-6	0.3867e-8	0.3802e-8
JH389Z	500.0	5.0	0.7754e-5	0.2166e-6	0.2130e-6	0.1349e-6	0.3769e-8	0.3706e-8
JH389Z	400.0	5.0	0.7486e-5	0.1864e-6	0.1833e-6	0.1303e-6	0.3243e-8	0.3190e-8
JH389Z	300.0	5.0	0.8140e-5	0.1443e-6	0.1422e-6	0.1416e-6	0.2512e-8	0.2475e-8
JH389Z	200.0	5.0	0.8794e-5	0.2123e-6	0.2088e-6	0.1530e-6	0.3693e-8	0.3633e-8
JH389Z	100.0	5.0	0.1315e-4	0.2456e-6	0.2420e-6	0.2289e-6	0.4274e-8	0.4210e-8
JH391XY	50.0	5.0	0.9605e-6	0.1459e-6	0.1436e-6	0.1671e-7	0.2538e-8	0.2499e-8
JH391XY	100.0	5.0	0.9605e-6	0.1459e-6	0.1436e-6	0.1671e-7	0.2538e-8	0.2499e-8
JH391XY	150.0	5.0	0.9605e-6	0.1459e-6	0.1436e-6	0.1671e-7	0.2538e-8	0.2499e-8
JH391XY	200.0	5.0	0.7057e-6	0.8449e-7	0.8323e-7	0.1228e-7	0.1470e-8	0.1448e-8
JH391XY	300.0	5.0	0.5489e-6	0.1149e-6	0.1132e-6	0.9551e-8	0.2000e-8	0.1969e-8
JH391XY	400.0	5.0	0.2744e-6	0.2724e-7	0.2684e-7	0.4775e-8	0.4739e-9	0.4670e-9
JH391XY	500.0	5.0	0.2744e-6	0.1405e-6	0.1383e-6	0.4775e-8	0.2444e-8	0.2406e-8
JH391XY	400.0	5.0	0.1830e-6	0.1859e-6	0.1830e-6	0.3184e-8	0.3234e-8	0.3184e-8
JH391XY	300.0	5.0	0.1830e-6	0.1859e-6	0.1830e-6	0.3184e-8	0.3234e-8	0.3184e-8
JH391XY	200.0	5.0	0.2744e-6	0.1405e-6	0.1383e-6	0.4775e-8	0.2444e-8	0.2406e-8
JH391XY	100.0	5.0	0.5004e-6	0.2008e-7	0.1980e-7	0.8708e-8	0.3494e-9	0.3445e-9

CORE	P_c	ΔP	K_{N_2}	+ ERROR	- ERROR	K_{H_2O}	+ ERROR	- ERROR
JH391Z	50.0	5.0	0.5442e-6	0.1414e-6	0.1393e-6	0.9469e-8	0.2461e-8	0.2423e-8
JH391Z	100.0	5.0	0.3628e-6	0.9425e-7	0.9281e-7	0.6313e-8	0.1640e-8	0.1615e-8
JH391Z	150.0	5.0	0.3061e-6	0.1949e-7	0.1920e-7	0.5327e-8	0.3391e-9	0.3342e-9
JH391Z	200.0	5.0	0.2721e-6	0.1393e-6	0.1371e-6	0.4735e-8	0.2424e-8	0.2386e-8
JH391Z	300.0	5.0	0.1814e-6	0.9283e-7	0.9141e-7	0.3156e-8	0.1615e-8	0.1590e-8
JH391Z	400.0	5.0	0.1814e-6	0.9283e-7	0.9141e-7	0.3156e-8	0.1615e-8	0.1590e-8
JH391Z	500.0	5.0	0.6803e-7	0.1766e-7	0.1739e-7	0.1184e-8	0.3073e-9	0.3027e-9
JH391Z	400.0	5.0	0.1088e-6	0.1106e-6	0.1088e-6	0.1894e-8	0.1924e-8	0.1894e-8
JH391Z	300.0	5.0	0.1361e-6	0.1382e-6	0.1361e-6	0.2367e-8	0.2405e-8	0.2367e-8
JH391Z	200.0	5.0	0.2721e-6	0.1393e-6	0.1371e-6	0.4735e-8	0.2424e-8	0.2386e-8
JH391Z	100.0	5.0	0.1361e-6	0.1382e-6	0.1361e-6	0.2367e-8	0.2405e-8	0.2367e-8
JH401X	50.0	5.0	0.2738e-3	0.3461e-5	0.3422e-5	0.4764e-5	0.6023e-7	0.5955e-7
JH401X	100.0	5.0	0.2010e-3	0.2801e-5	0.2768e-5	0.3497e-5	0.4874e-7	0.4816e-7
JH401X	150.0	5.0	0.1738e-3	0.2555e-5	0.2524e-5	0.3024e-5	0.4446e-7	0.4391e-7
JH401X	200.0	5.0	0.1301e-3	0.2159e-5	0.2131e-5	0.2264e-5	0.3757e-7	0.3708e-7
JH401X	300.0	5.0	0.9028e-4	0.1798e-5	0.1773e-5	0.1571e-5	0.3129e-7	0.3086e-7
JH401X	400.0	5.0	0.6796e-4	0.1596e-5	0.1573e-5	0.1182e-5	0.2776e-7	0.2737e-7
JH401X	500.0	5.0	0.4951e-4	0.1428e-5	0.1407e-5	0.8615e-6	0.2486e-7	0.2448e-7
JH401X	400.0	5.0	0.5436e-4	0.1351e-5	0.1331e-5	0.9459e-6	0.2350e-7	0.2317e-7
JH401X	300.0	5.0	0.6386e-4	0.1435e-5	0.1415e-5	0.1111e-5	0.2496e-7	0.2461e-7
JH401X	200.0	5.0	0.7335e-4	0.1518e-5	0.1498e-5	0.1276e-5	0.2642e-7	0.2606e-7
JH401X	100.0	5.0	0.1407e-3	0.2113e-5	0.2087e-5	0.2447e-5	0.3676e-7	0.3632e-7
JH401Y	50.0	5.0	0.1006e-2	0.1521e-4	0.1497e-4	0.1751e-4	0.2647e-6	0.2604e-6
JH401Y	100.0	5.0	0.6917e-3	0.7975e-5	0.7884e-5	0.1204e-4	0.1388e-6	0.1372e-6
JH401Y	150.0	5.0	0.5459e-3	0.6856e-5	0.6773e-5	0.9499e-5	0.1193e-6	0.1178e-6
JH401Y	200.0	5.0	0.4031e-3	0.5036e-5	0.4977e-5	0.7014e-5	0.8762e-7	0.8660e-7
JH401Y	300.0	5.0	0.2597e-3	0.3157e-5	0.3123e-5	0.4519e-5	0.5494e-7	0.5434e-7
JH401Y	400.0	5.0	0.2198e-3	0.3200e-5	0.3160e-5	0.3825e-5	0.5569e-7	0.5499e-7
JH401Y	500.0	5.0	0.1466e-3	0.2339e-5	0.2310e-5	0.2551e-5	0.4070e-7	0.4019e-7
JH401Y	400.0	5.0	0.1509e-3	0.2573e-5	0.2539e-5	0.2626e-5	0.4477e-7	0.4417e-7
JH401Y	300.0	5.0	0.1557e-3	0.2616e-5	0.2582e-5	0.2708e-5	0.4552e-7	0.4492e-7
JH401Y	200.0	5.0	0.1234e-3	0.2572e-5	0.2535e-5	0.2147e-5	0.4476e-7	0.4410e-7

CORE	P_c	ΔP	K_{N_2}	+ ERROR	- ERROR	K_{H_2O}	+ ERROR	- ERROR
JH401Z	50.0	5.0	0.7307e-4	0.3396e-5	0.3344e-5	0.1271e-5	0.5909e-7	0.5818e-7
JH401Z	100.0	5.0	0.9018e-4	0.4225e-5	0.4158e-5	0.1569e-5	0.7352e-7	0.7235e-7
JH401Z	150.0	5.0	0.5765e-4	0.2865e-5	0.2808e-5	0.1003e-5	0.4985e-7	0.4886e-7
JH401Z	200.0	5.0	0.5046e-4	0.2488e-5	0.2440e-5	0.8779e-6	0.4328e-7	0.4245e-7
JH401Z	300.0	5.0	0.4321e-4	0.2171e-5	0.2126e-5	0.7519e-6	0.3777e-7	0.3699e-7
JH401Z	400.0	5.0	0.3773e-4	0.1715e-5	0.1691e-5	0.6565e-6	0.2984e-7	0.2943e-7
JH401Z	500.0	5.0	0.4875e-4	0.2273e-5	0.2237e-5	0.8482e-6	0.3954e-7	0.3893e-7
JH401Z	400.0	5.0	0.3113e-4	0.1642e-5	0.1604e-5	0.5417e-6	0.2857e-7	0.2790e-7
JH401Z	300.0	5.0	0.2335e-4	0.1302e-5	0.1267e-5	0.4063e-6	0.2265e-7	0.2204e-7
JH401Z	200.0	5.0	0.4482e-4	0.2241e-5	0.2196e-5	0.7799e-6	0.3899e-7	0.3821e-7
JH401Z	100.0	5.0	0.4536e-4	0.2264e-5	0.2219e-5	0.7892e-6	0.3940e-7	0.3861e-7
JH402Y	50.0	5.0	0.2842e-3	0.6004e-5	0.5940e-5	0.4946e-5	0.1045e-6	0.1034e-6
JH402Y	100.0	5.0	0.2181e-3	0.4734e-5	0.4681e-5	0.3794e-5	0.8238e-7	0.8145e-7
JH402Y	150.0	5.0	0.1749e-3	0.3720e-5	0.3680e-5	0.3044e-5	0.6472e-7	0.6403e-7
JH402Y	200.0	5.0	0.1569e-3	0.3269e-5	0.3236e-5	0.2730e-5	0.5688e-7	0.5630e-7
JH402Y	300.0	5.0	0.6889e-4	0.1558e-5	0.1539e-5	0.1199e-5	0.2711e-7	0.2679e-7
JH402Y	400.0	5.0	0.4692e-4	0.1149e-5	0.1133e-5	0.8164e-6	0.2000e-7	0.1972e-7
JH402Y	500.0	5.0	0.3352e-4	0.9592e-6	0.9426e-6	0.5833e-6	0.1669e-7	0.1640e-7
JH402Y	400.0	5.0	0.3797e-4	0.9829e-6	0.9680e-6	0.6607e-6	0.1710e-7	0.1684e-7
JH402Y	300.0	5.0	0.6346e-4	0.1457e-5	0.1439e-5	0.1104e-5	0.2536e-7	0.2504e-7
JH402Y	200.0	5.0	0.1302e-3	0.2769e-5	0.2740e-5	0.2265e-5	0.4818e-7	0.4767e-7
JH402Y	100.0	5.0	0.1936e-3	0.4266e-5	0.4217e-5	0.3370e-5	0.7423e-7	0.7337e-7

A8.3 Permeability and porosity samples: cores and polished sections

Samples followed by A, B, C, or D are multiple cores from the same sample. Samples followed by X, Y, or Z denote cores parallel to the X, Y or Z tectonic fabric direction. All samples are unblasted unless stated.

SAMPLE	CORE	POLISHED	DESCRIPTION
JH-330	√	√ √	Laxfordian granite: Loch Laxford.
JH-330A	√	-	As JH-330.
JH-330B	√	-	As JH-330.
JH-330C	√	-	As JH-330.
JH-330D	√	-	As JH-330.
JH-331	√	√ √	Laxfordian amphibolite: Laxford Front.
JH-331A	√	-	As JH-331.
JH-331C	√	-	As JH-331.
JH-332	√	√ √	Scourie dyke amphibolite: Scourie (sample site SD).
JH-332A	√	-	As JH-332.
JH-332D	√	-	As JH-332.
JH-333A	√	√ √	Foliated Scourie dyke amphibolite: As with JH-332.
JH-333C	√	-	As with JH-333A.
JH-333D	√	-	As with JH-333A.
JH-334A	√	√ √	Badcallian mafic granulite.
JH-340	-	√ √	Chelmsford granite: H. E. Fletcher quarry.
JH-360Y	√	-	Kylesku granulite: Loch a Mhinidh (sample site DM).
JH-360Z	√	-	As with JH-360Y.
JH-368Y	√	-	Amphibolite gneiss: Laxford Bridge
JH-368Z	√	-	As with JH-368Y.
JH-371Y	√	-	Biotite amphibolite gneiss: Laxford Bridge.
JH-371Z	√	-	As with JH-371Y.
JH-373X	√	-	Amphibolite gneiss: Car park, Rispond.
JH-373Z	√	-	As with JH-373X.
JH-374Z	√	-	Quartzo-feldspathic gneiss: Car park, Rispond.
JH-375X	√	-	Laxfordian gneiss: Car park, Rispond.
JH-375Y	√	-	As with JH-375X.

JH-375Z	√	√	√	√ - As with JH-375X.
JH-389X	√	√	-	Quartzo-feldspathic amphiboe gneiss: Skerricha.
JH-389Y	√		-	As with JH-389X.
JH-389Z	√		-	As with JH-389X.
JH-391XY	√	√	-	Kylesku Group granulite: Loch Duartbeg (Blasted).
JH-391Z	√		-	As with JH-391XY.
JH-397XY	√		-	Basic intrusion: Achiltibuie (Lowest part).
JH-397Z	√		-	As with JH-397XY.
JH-401X	√		-	Amphibolite gneiss: Durness.
JH-401Y	√		-	As with JH-401X.
JH-401Z	√		-	As with JH-401X.
JH-402Z	√		-	Quartz biotite gneiss: Durness.
FB3-2	√		-	Quartz, feldspar, hornblende gneiss: Rispond.
FB5-3	√		-	Quartz, feldspar, hornblende gneiss: Rispond.
FB8-3	√		-	Amphibolite: Gualin.
FB19-3	√		-	Laxfordian granite: Loch Laxford.
FH1-1	√		-	Scourie dyke amphibolite.

APPENDIX 9

POROSITY AND CRACK DENSITY

Calculated porosity and linear crack density as measured from S.E.M. pictures

A9.1 Open crack thin sections

JH-330B

Photo	Orthogonal Porosity %	Parallel Porosity %	Orthogonal Cracks / mm	Parallel Cracks /mm
# 1	0.24	0.34	1.64	3.36
# 2	0.15	0.13	2.06	1.12
# 3	0.35	0.31	3.70	2.24
# 4	0.28	0.45	0.41	3.92
# 5	0.42	0.22	1.23	2.24
# 6	1.02	0.79	1.65	2.25
# 7	0.	0.	0.	0.
# 8	0.03	0.	0.41	0.
# 9	0.	0.19	0.	2.26
#10	0.	0.	0.	0.
#11	0.12	0.27	0.82	1.68
#12	0.02	0.08	0.41	0.56
#13	0.10	0.	0.41	0.
#14	0.39	0.23	1.65	1.13
#15	0.32	0.23	2.06	1.68
#16	0.44	0.35	2.47	2.82
#18	0.40	0.14	0.41	0.56
#19	0.40	0.30	2.47	2.26
#20	0.15	0.71	2.06	3.37
#21	0.06	0.08	0.41	0.56
#22	0.52	0.13	4.12	1.12
#23	0.36	0.60	2.06	2.81
#24	0.43	0.22	1.10	2.25
#25	0.44	0.34	2.88	2.83
#26	0.69	0.28	4.94	2.26
#27	0.24	0.37	1.24	1.12
#28	0.66	0.39	3.71	2.25
#29	0.55	0.47	3.70	3.39
#30	0.	0.	0.	0.
#31	0.10	0.74	0.82	5.05
#32	0.52	0.56	2.88	3.37
#33	0.46	0.39	3.30	1.70
Total orthogonal porosity		0.31%	orthogonal cracks/mm	1.72
Total parallel porosity		0.29%	parallel cracks/mm	1.88
Total average porosity		**0.30%**	average cracks/mm	1.80

JH-333

Photo	Orthogonal Porosity %	Parallel Porosity %	Orthogonal Cracks / mm	Parallel Cracks /mm
#34	0.24	0.13	0.63	0.43
#35	0.06	0.02	0.31	0.46
#36	0.31	0.29	1.25	2.62
#37	0.26	0.30	1.57	1.74
#38	0.89	0.28	0.94	1.29
#39	0.20	0.02	0.94	0.88
#40	0.25	0.	1.25	0.
#41	0.08	0.26	0.31	1.73
#42	0.10	0.28	0.63	2.16
#43	0.07	0.14	0.31	0.44
#44	0.	0.	0.	0.
#45	0.27	0.17	1.88	1.28
#46	0.28	0.35	0.94	3.00
#47	0.45	1.29	1.57	4.34
#48	0.53	0.09	2.19	0.43
#49	0.55	0.35	1.88	1.29
#50	0.	0.	0.	0.
#51	0.23	0.	0.94	0.
#52	0.23	0.24	1.25	1.30

Total orthogonal porosity	0.26%	orthogonal cracks/mm	0.99
Total parallel porosity	0.22%	parallel cracks/mm	1.23
Total average porosity	0.24%	average cracks/mm	1.11

JH-340B

Photo	Orthogonal Porosity %	Parallel Porosity %	Orthogonal Cracks / mm	Parallel Cracks /mm
#55	0.57	0.18	3.10	1.43
#57	0.56	0.39	3.8	2.36
#58	0.69	0.21	4.48	1.42
#59	0.74	0.47	4.83	4.26
#60	0.49	0.42	2.76	2.83
#62	0.26	0.28	1.72	2.35
#65	3.36	1.58	2.07	3.31
#66	0.97	0.79	3.79	0.94
#67	0.44	0.23	2.77	1.41
#68	0.51	0.32	1.38	1.89
#70	0.69	0.44	4.83	1.42
#71	0.07	0.17	0.69	0.47
#72	0.36	0.18	2.67	1.42
#74	0.37	0.11	2.77	0.48
#75	0.80	0.24	5.18	1.88
#76	0.54	0.65	2.42	2.86
#77	2.09	1.20	10.00	5.70
#78	0.23	0.2	2.07	1.42
#79	0.27	0.23	1.73	1.88
#80	0.34	1.00	3.11	6.61
#81	0.77	0.41	4.48	1.90
#82	0.45	0.66	3.11	3.33
#83	2.30	0.80	5.17	6.62
#84	0.73	0.74	5.87	4.77
#85	1.20	0.70	6.90	6.17
#86	0.38	0.33	3.45	1.44
#87	0.30	0.62	1.38	4.25

Total orthogonal porosity	0.76%	orthogonal cracks/mm	3.58
Total parallel porosity	0.50%	parallel cracks/mm	2.77
Total average porosity	0.63%	average cracks/mm	3.18

JH-332

Photo	Orthogonal Porosity %	Parallel Porosity %	Orthogonal Cracks / mm	Parallel Cracks /mm
#101	0.53	0.70	3.11	5.27
#102	0.86	0.56	3.88	5.28
#103	0.58	0.34	4.66	3.17
#104	0.33	0.03	1.55	1.06
#105	0.44	0.12	3.11	1.07
#106	0.23	0.12	3.11	2.12
#107	0.04	0.30	0.78	2.13
#108	0.08	0.39	0.78	3.20
#109	0.35	0.16	3.11	3.21
#110	0.58	0.71	1.55	5.27
#111	0.30	0.31	2.33	3.17
#112	0.33	0.64	3.11	5.33
#113	0.04	0.08	0.78	1.08
#114	0.	0.15	0.	2.12
#115	0.20	0.26	2.33	2.13
#117	0.33	0.42	3.89	4.25

Total orthogonal porosity	0.33%	orthogonal cracks/mm	2.38
Total parallel porosity	0.33%	parallel cracks/mm	3.12
Total average porosity	0.33%	average cracks/mm	2.75

JH-334

Photo	Orthogonal Porosity %	Parallel Porosity %	Orthogonal Cracks / mm	Parallel Cracks /mm
#139	0.88	0.31	1.31	0.99
#140	0.63	0.82	1.61	1.98
#141	1.55	1.43	2.92	2.19
#142	2.51	0.92	1.46	1.99
#143	1.76	2.01	1.90	2.18
#144	4.62	3.87	2.34	2.38
#145	0.27	0.38	1.17	1.19
#146	0.	0.	0.	0.
#147	0.	0.	0.	0.
#148	0.	0.	0.	0.
#149	0.	0.	0.	0.
#150	0.	0.	0.	0.
#151	0.	0.	0.	0.

Total orthogonal porosity	0.94%	orthogonal cracks/mm	0.98
Total parallel porosity	0.75%	parallel cracks/mm	0.99
Total average porosity	0.85%	average cracks/mm	0.99

A9.2 Sealed crack thin sections

SD-25

Photo	Orthogonal Porosity %	Parallel Porosity %	Orthogonal Cracks / mm	Parallel Cracks /mm
#11	0.34	0.26	4.32	3.70
#12	1.59	2.49	10.96	9.44
#13	1.63	1.75	7.41	8.24
#14	15.63	11.42	4.62	3.71
#15	30.28	33.33	11.34	11.08
#16	2.08	3.49	7.49	11.50
#17	3.93	5.38	17.49	14.85
#18	5.90	6.22	7.02	9.46
#20	3.43	2.95	4.26	1.65
#21	2.58	5.05	2.12	2.89

SD-25 continued

#22	12.80	21.34	3.51	2.46
#23	10.64	5.10	3.53	3.71
#24	42.14	46.00	1.77	1.24
#25	1.13	1.00	2.12	1.24
#26	11.48	8.50	3.17	0.82
#27	8.60	9.00	2.47	3.71
#28	1.63	0.55	3.18	6.60
#29	1.92	3.00	2.47	3.71
#30	1.66	2.40	0.70	1.65
#31	0.25	0.30	2.02	2.06
#32	1.88	2.10	3.52	2.06
#33	0.77	0.65	3.18	2.06
#34	0.73	0.50	3.52	3.30
#35	0.17	1.05	1.05	1.65
#36	0.47	0.25	1.40	0.82
#37	0.64	0.75	3.17	3.30
#38	0.98	1.30	3.16	2.88
#39	1.22	2.84	2.83	2.46
#40	2.14	2.30	4.23	2.89
#41	0.81	0.50	2.82	2.05
#42	10.27	16.15	8.57	6.60
#43	1.38	0.50	3.19	3.71
#44	0.62	1.05	3.18	5.35
#45	0.13	0.40	0.71	2.89
#46	0.15	0.25	1.78	0.82
#47	0.	0.	0.	0.
#47	0.19	0.25	1.77	2.88
#48	0.22	0.20	2.49	1.65
#50	0.45	0.37	4.62	4.53
#51	0.15	0.14	1.79	1.65
#52	0.26	0.17	2.49	1.65
#54	0.26	0.15	1.80	1.24
#55	0.22	0.23	2.15	2.06
#56	0.35	0.22	2.18	0.82
#57	0.36	0.40	0.86	1.24

Total orthogonal porosity	4.10%	orthogonal cracks/mm	3.74
Total parallel porosity	4.49%	parallel cracks/mm	3.65
Total average porosity	4.30%	average cracks/mm	3.70

LC-4

Photo	Orthogonal Porosity %	Parallel Porosity %	Orthogonal Cracks / mm	Parallel Cracks /mm
#58	0.52	0.57	2.51	4.95
#59	0.35	0.20	2.51	2.06
#60	0.48	0.35	1.81	2.48
#61	0.74	0.55	3.58	2.48
#62	0.36	0.25	2.49	2.87
#63	0.15	0.45	1.43	3.69
#64	9.88	6.57	3.56	2.46
#65	0.56	0.35	3.59	3.69
#66	0.27	0.25	2.15	3.28
#67	0.89	0.65	5.00	4.51
#68	0.56	0.47	3.58	2.05
#69	0.35	0.51	1.78	4.10
#70	0.26	0.24	1.78	1.64
#71	0.10	0.48	1.07	2.47
#72	0.61	0.57	3.23	0.82

LC-4 continued

#73	1.06	1.49	3.58	8.61
#74	0.43	0.30	1.43	1.23
#75	1.34	1.90	1.79	3.25
#76	0.22	0.12	1.08	0.82
#77	0.65	0.57	1.78	3.70
#78	41.44	42.97	2.86	2.88
#79	4.50	3.39	2.50	2.06
#80	0.	0.	0.	0.
#81	0.63	3.06	4.33	1.65
#82	0.74	0.52	4.30	2.87
#83	0.57	1.57	2.51	5.74
#84	0.91	1.30	2.50	2.47
#85	0.74	0.34	2.86	2.05
#86	0.17	0.50	1.08	2.88
#87	0.71	0.48	3.56	3.28
#88	0.66	0.41	3.59	3.70
#89	0.22	0.86	1.79	2.05
#90	0.61	0.58	2.88	3.29
#91	0.57	0.53	2.89	2.88
#92	0.56	0.35	1.79	0.82

Total orthogonal porosity	2.08%	orthogonal cracks/mm	2.55
Total parallel porosity	2.11%	parallel cracks/mm	2.85
Total average porosity	2.09%	average cracks/mm	2.70

DM-1

Photo	Orthogonal Porosity %	Parallel Porosity %	Orthogonal Cracks / mm	Parallel Cracks /mm
#93	1.15	1.87	6.78	9.85
#94	0.99	1.08	4.29	4.11
#95	0.16	0.34	1.07	2.46
#96	4.40	4.92	7.16	4.52
#97	0.54	0.29	3.92	2.46
#98	2.35	6.05	6.78	4.93
#99	58.64	53.35	3.20	3.29
#100	29.33	30.57	12.91	7.40
#101	88.00	91.30	1.78	2.06
#102	0.09	1.99	1.07	0.41
#103	1.42	1.39	6.82	4.94
#104	0.55	0.34	2.87	2.88
#105	0.73	0.59	6.76	4.11
#106	0.91	1.64	3.57	3.28
#107	0.10	0.20	0.71	1.65
#108	0.30	0.47	1.79	3.30
#109	0.17	0.13	1.78	1.23
#110	0.41	0.26	2.86	2.46
#111	1.00	0.22	4.28	2.87
#112	0.35	0.27	3.24	2.46
#113	29.15	31.56	4.28	2.05
#115	93.14	99.45	2.52	2.05
#116	15.92	18.71	4.67	2.86
#117	0.46	0.96	3.92	4.50
#118	0.41	0.32	2.16	2.88
#119	1.10	0.10	2.53	0.82
#120	0.23	0.45	2.13	2.46
#121	0.47	0.15	2.13	0.82
#122	0.18	0.28	1.44	0.82
#123	50.27	51.51	2.50	1.64
#124	0.74	0.16	2.51	1.64

DM-1 continued

#125	8.97	0.94	43.39	2.45
#126	2.12	3.68	3.93	5.75
#127	1.61	2.43	3.22	5.34
#128	0.10	0.30	1.07	2.87
#129	0.17	0.03	0.72	0.41
#130	0.14	0.22	1.19	1.64
Total orthogonal porosity		10.72%	orthogonal cracks/mm	4.54
Total parallel porosity		11.04%	parallel cracks/mm	3.02
Total average porosity		10.88%	average cracks/mm	3.78

SC-10

Photo	Orthogonal Porosity %	Parallel Porosity %	Orthogonal Cracks / mm	Parallel Cracks /mm
#131	0.27	0.60	0.53	0.77
#132	0.76	0.40	1.19	0.58
#133	0.43	1.03	0.68	0.98
#134	1.25	2.48	1.01	1.37
#135	0.30	0.75	0.67	0.98
#136	0.13	0.20	0.17	0.39
#137	0.49	0.13	0.84	0.19
#138	0.13	0.	0.17	0.
#139	0.	0.	0.	0.
#140	0.38	0.10	0.84	0.19
#141	0.10	0.25	0.34	0.59
#142	0.78	0.95	1.69	1.95
#143	1.13	0.52	2.19	0.98
#144	0.17	0.17	0.39	0.39
Total orthogonal porosity		0.45%	orthogonal cracks/mm	0.76
Total parallel porosity		0.54%	parallel cracks/mm	0.67
Total average porosity		0.50%	average cracks/mm	0.72

G-5

Photo	Orthogonal Porosity %	Parallel Porosity %	Orthogonal Cracks / mm	Parallel Cracks /mm
#145	0.	0.	0.	0.
#146	0.18	0.20	1.09	0.83
#147	0.	0.	0.	0.
#148	0.69	0.	0.71	0.
#149	0.	0.10	0.	0.41
#150	0.	0.	0.	0.
#151	1.56	1.05	1.43	0.41
#152	0.	0.	0.	0.
#153	0.10	0.10	0.71	0.41
#154	0.06	0.05	0.36	0.41
#155	0.09	0.	0.71	0.
#156	0.59	1.36	2.85	3.32
#157	0.28	0.27	2.14	1.66
#158	0.39	0.55	2.50	3.73
#159	0.13	0.17	1.43	0.83
#160	0.43	0.62	3.22	4.14
#161	0.86	1.20	3.94	5.15
#162	3.32	3.24	5.71	4.55
#165	0.	0.	0.	0.
#164	0.	0.	0.	0.
#163	0.43	0.20	2.13	0.83
#166	0.	0.	0.	0.
#167	0.	0.	0.	0.

G-5 continued

#168	0.	0.	0.	0.
Total orthogonal porosity	0.36%	orthogonal cracks/mm	1.16	
Total parallel porosity	0.36%	parallel cracks/mm	1.07	
Total average porosity	0.36%	average cracks/mm	1.11	

M-16

Photo	Orthogonal Porosity %	Parallel Porosity %	Orthogonal Cracks / mm	Parallel Cracks /mm
#170	3.50	4.10	22.21	26.12
#171	2.47	1.90	16.70	12.92
#172	0.53	0.40	2.85	1.66
#173	1.48	1.76	13.21	15.32
#174	3.45	2.76	17.92	17.80
#175	2.54	2.74	18.65	20.27
#176	3.18	2.22	12.78	14.08
#178	3.15	2.99	17.12	18.23
#179	58.35	43.68	15.08	15.74
#180	9.44	13.77	16.96	14.07
#181	1.65	2.08	13.55	14.10
#182	2.58	1.96	11.99	14.50
#183	1.69	2.02	13.31	14.03
#184	1.99	1.48	10.37	10.77
#185	1.06	0.75	7.17	6.23
#187	0.89	0.82	5.70	4.97
#188	0.70	0.85	4.99	4.57
#189	1.37	2.33	9.64	8.71
#190	1.69	1.22	9.65	9.94
#191	1.63	1.71	14.70	12.01
#192	1.51	1.39	9.25	9.94
#193	2.08	1.58	16.05	12.44
#194	1.43	1.24	11.06	10.36
#195	3.47	2.28	14.95	15.76
#196	2.22	2.02	11.77	10.78
#197	2.15	3.00	15.03	13.65
#198	1.46	1.88	9.31	10.36
#199	1.83	1.70	13.29	13.27
#200	0.95	1.49	10.31	6.67
#201	1.05	0.79	8.25	6.62
#202	0.60	0.41	5.05	4.97
#203	2.07	1.91	12.89	10.35
#204	1.34	1.38	11.12	9.11
#205	1.80	1.27	11.99	10.77
Total orthogonal porosity	3.74%	orthogonal cracks/mm	12.20	
Total parallel porosity	3.35%	parallel cracks/mm	11.80	
Total average porosity	3.55%	average cracks/mm	12.00	

SD-11

Photo	Orthogonal Porosity %	Parallel Porosity %	Orthogonal Cracks / mm	Parallel Cracks /mm
#206	0.	0.02	0.	0.20
#207	4.72	6.27	0.67	1.36
#208	7.03	7.79	2.34	2.73
#209	0.	0.	0.	0.
#210	0.15	0.19	0.84	1.36
#211	0.38	0.	1.17	0.
#212	0.13	0.02	0.83	0.19
#213	0.15	0.03	0.67	0.39

SD-11 continued

#214	0.76	0.75	1.35	0.97
#215	0.04	0.03	0.17	0.39
#216	0.22	0.15	1.18	0.78
#217	0.17	0.17	0.85	0.58
#218	0.43	0.23	1.52	1.17
#219	0.24	0.23	1.01	1.36
#220	0.06	0.17	0.17	0.59
#221	16.43	20.07	1.18	0.58
#222	0.64	0.25	2.35	0.78
#223	1.26	0.69	2.00	1.17
#224	17.56	14.20	1.34	0.58
#225	1.07	0.59	3.19	1.57
#226	1.38	0.48	3.02	0.58

Total orthogonal porosity	2.51%	orthogonal cracks/mm	1.23
Total parallel porosity	2.49%	parallel cracks/mm	0.83
Total average porosity	2.50%	average cracks/mm	1.03

G-1

Photo	Orthogonal Porosity %	Parallel Porosity %	Orthogonal Cracks / mm	Parallel Cracks /mm
#227	0.	0.	0.	0.
#228	0.	0.	0.	0.
#229	0.09	0.17	0.24	0.55
#230	0.95	0.51	3.33	1.11
#231	0.67	0.57	2.14	1.66
#232	0.47	0.66	1.67	2.21
#233	0.10	0.07	0.48	0.55
#234	0.	0.	0.	0.
#235	0.	0.	0.	0.
#236	0.	0.	0.	0.
#238	0.	0.	0.	0.
#239	0.	0.	0.	0.
#240	0.	0.	0.	0.
#241	0.	0.	0.	0.
#242	0.39	0.20	0.48	0.28
#243	0.	0.	0.	0.
#244	0.	0.	0.	0.
#245	0.	0.	0.	0.
#246	0.	0.	0.	0.
#247	0.	0.	0.	0.
#248	0.	0.	0.	0.
#249	0.	0.	0.	0.

Total orthogonal porosity	0.12%	orthogonal cracks/mm	0.38
Total parallel porosity	0.10%	parallel cracks/mm	0.29
Total average porosity	0.11%	average cracks/mm	0.33

LC-6

Photo	Orthogonal Porosity %	Parallel Porosity %	Orthogonal Cracks / mm	Parallel Cracks /mm
#250	0.06	0.75	0.71	1.66
#251	0.20	1.03	0.72	1.24
#252	0.12	0.26	0.72	0.83
#253	0.	0.	0.	0.
#254	0.29	0.	1.07	0.
#255	0.37	0.20	1.43	0.41
#256	0.23	0.45	1.42	2.07
#257	0.44	0.50	2.15	0.83
#258	0.	0.	0.	0.

LC-6 continued

#259	0.04	0.	0.36	0.
#260	0.09	0.09	1.07	0.83
#261	0.	0.	0.	0.
#262	0.60	0.	2.51	0.
#263	0.35	1.10	2.14	1.24
#264	0.26	0.	1.79	0.
#265	0.79	0.56	2.51	0.83
#266	0.61	0.46	2.15	0.83
#267	0.41	0.20	1.43	0.41
#269	15.37	20.00	2.49	0.41
#270	0.93	0.80	2.51	0.41
#271	0.83	1.01	3.21	0.41
#272	0.	0.03	0.	0.41
#273	0.13	0.	0.72	0.
#274	0.28	0.	1.07	0.
#275	0.30	0.30	1.79	0.41
#276	0.06	0.06	0.36	0.41
#277	0.29	0.	2.14	0.
#278	2.03	4.24	5.34	4.55
#279	0.57	0.80	2.53	0.41
#280	0.57	0.48	2.87	0.83
#281	0.23	0.25	1.08	1.24
#282	0.19	0.03	1.43	0.41

Total orthogonal porosity	0.83%	orthogonal cracks/mm	1.55
Total parallel porosity	1.05%	parallel cracks/mm	0.66
Total average porosity	0.94%	average cracks/mm	1.11

M - 5

Photo	Orthogonal Porosity %	Parallel Porosity %	Orthogonal Cracks / mm	Parallel Cracks /mm
#283	0.20	0.17	2.49	2.89
#284	0.73	0.11	1.77	2.07
#285	2.06	1.96	2.83	2.48
#286	0.89	1.16	3.54	2.47
#287	1.94	2.21	3.89	6.06
#288	0.	0.	0.	0.
#289	0.	0.	0.	0.
#290	0.80	0.48	3.54	2.47
#291	0.35	0.28	1.77	0.41
#292	0.76	0.67	2.12	1.23
#293	1.24	1.29	1.77	2.06
#294	4.41	4.01	4.60	4.95
#295	1.83	1.92	2.14	1.65
#296	13.68	7.15	6.38	4.54
#297	4.78	6.46	3.88	3.30
#298	2.14	1.12	3.54	3.30
#299	2.18	0.32	2.12	0.83
#300	0.47	0.18	1.12	0.41
#301	0.	0.	0.	0.
#302	1.08	0.52	2.12	0.82
#303	0.	0.	0.	0.
#304	0.52	0.37	1.78	1.24
#305	0.	0.	0.	0.
#306	2.03	1.50	2.12	2.06
#307	0.52	0.50	1.79	0.82
#308	0.66	0.12	1.41	0.82
#309	0.	0.	0.	0.

M-5 continued

#310	1.00	1.14	2.48	1.23
#311	2.67	2.43	5.35	4.53
#312	0.90	2.16	2.13	1.64
#313	35.06	33.53	1.76	1.65
#314	0.76	0.31	2.46	3.29
#315	2.07	0.76	3.54	3.28
#316	2.12	21.30	4.59	4.93
#317	5.03	8.13	5.64	8.22
#318	3.19	5.34	7.10	11.93

Total orthogonal porosity	2.67%	orthogonal cracks/mm	2.55
Total parallel porosity	2.99%	parallel cracks/mm	2.43
Total average porosity	2.83%	average cracks/mm	2.49

APPENDIX 10

COMPUTER PROGRAMMES

A10.1 PORE: the calculation of porosity and density of core samples

```
      program pore
c
c POROSITY/DENSITY CALCULATION
c
c BY STEPHEN HAY..... March 1988
c
c This program will calculate the bulk and void volume, density and porosity
c of a rock core using the caliper and saturation technique. Input is from a
c file in matrix form. Containing in order; sample number (up to 7 characters);
c vacuum dry weight (grams); saturated weight (grams); core length (cm);
c and core diameter (cm).
c Input is in free format, output of density is in kg/m3, porosity is in %.
c It is assumed water used in measurements is at 4 °C.
c
c Reference:- Brown, E. T. 1981. ROCK CHARACTERIZATION TESTING & MONITORING
c                    ISRM Suggested Methods, 81-89, Pergamon Press.
c
c Declare programme variables
c
        dimension  A(11,300),  B(11,300)
        character file 1 *9
        character file 2 *9
        character *7  NAME(300)
c
        write(6,*) '"POROSITY / DENSITY CALCULATION"'
        write(6,*) ' BY STEPHEN HAY      1988 '
c
c Assign local file names
c
        write(6,*) 'ENTER NAME OF INPUT FILE'
        read(5,*)  file  1
        write(6,*) 'ENTER NAME OF OUTPUT FILE TO BE CREATED'
        read(5,*)  file  2
c
c Assign input/output files to program channels
c
        open(2,file=file  1)
        open(3,file=file  2)
c
c Write titles to the output file and the screen
c
        write(3,10) 'CORE',' Ms ',' Msat ',' BVol ',' VVol',
        *' DENSITY',' POROSITY'
        write(3,*)  ' '
        write(6,10) 'CORE',' Ms ',' Msat ',' BVol ',' VVol',
        *' DENSITY',' POROSITY'
        write(6,*)  ' '
c
c Calculate density and porosity
c
        do  100,  j=1,100
        read   (2,*,end=200)   NAME(j),(A(i,j),i=1,4)
```

```
c
c Assign labels to matrix columns
c
      DRYWT = A(1,j)
      SATWT = A(2,j)
      CL = A(3,j)
      CD = A(4,j)
c
c Calculations
c
      BV = ((3.1415927 * (CD**2)) / 4) * CL
      VV = SATWT - DRYWT
      DRYDENS = (DRYWT / BV) * 1000
      APOROS = (VV / BV) * 100
c
c Write to output matrix
c
      B(1,j) = DRYWT
      B(2,j) = SATWT
      B(3,j) = BV
      B(4,j) = VV
      B(5,j) = DRYDENS
      B(6,j) = APOROS
      write(3,20)  NAME(j),  (B(i,j),  i=1,6)
      write(6,20)  NAME(j),  (B(i,j),  i=1,6)
100   continue
200   continue
c
      write(6,*) 'FOR LIST OF VALUES PRINT OUTPUT FILE',file 2
c
c Format statements
c
10    format  (a7,4a9,2a10)
20    format  (a7,4f9.2,f10.2,f10.4)
      stop
      end
```

A10.2 PERM: the calculation of core permeability

```
      program perm
c
c PERMEABILITY CALCULATION
c
c BY STEPHEN HAY..... January 1988
c
c This program will calculate the water and N2 permeability from a data
c file in matrix form. Containing in order; sample number (up to 7 characters);
c confining pressure (bars); gas pressure(bars); volume of gas (cm); error on
c the volume (cm); time for the volume of gas to pass (sec.);
c error in the time parameter (sec); core length (cm);
c error on the core length (cm); core surface area (cm); error on the core
c surface area (cm). Input is free format, output in darcys.
c The programme assumes that there is no error in the pressure parameters.
c
c Reference:- Monicard, R. P. 1980 Properties of reservoir rocks: Core
c                    analysis. Inststut Francais du Petrole.
c
c Declare programme variables
c
        dimension  A(11,300),  B(11,300)
        character file 1 *9
        character file 2 *9
        character *7  NAME(300)
c
        write(6,*) '"PERMEABILITY CALCULATION"'
        write(6,*) ' BY STEPHEN HAY    1988 '
c
c Assign local file names
c
        write(6,*) 'ENTER NAME OF INPUT FILE'
        read(5,*)  file  1
        write(6,*) 'ENTER NAME OF OUTPUT FILE TO BE CREATED'
        read(5,*)  file  2
c
c Assign input/output files to program channels
c
        open(2,file=file  1)
        open(3,file=file  2)
c
c Write titles to output file and screen
c
        write(3,10) 'CORE','CONF','N2P','N2 PERM','+ ERROR','- ERROR',
        *'H20 PERM','+ ERROR','- ERROR'
        write(3,*)  ' '
        write(6,10) 'CORE','CONF','N2P','N2 PERM','+ ERROR','- ERROR',
        *'H20 PERM','+ ERROR','- ERROR'
        write(6,*)  ' '
c
c Calculate permeability values and errors
c
        do  100,  j=1,100
        read   (2,*,end=200)   NAME(j),(A(i,j),i=1,10)
c
c Assign lables to matrix columns
c
        CONFP = A(1,j)
```

```
      GASPRE = A(2,j)
      DV = A(3,j)
      EV = A(4,j)
      DT = A(5,j)
      ET = A(6,j)
      CL = A(7,j)
      CLE = A(8,j)
      CSA = A(9,j)
      CSAE = A(10,j)
c
c Calculations
c
      Vave = DV / DT
      Vmax = (DV + EV) / (DT - ET)
      Vmin = (DV - EV) / (DT + ET)
      RATIO = CL / CSA
      Rmax = (CL + CLE) / (CSA - CSAE)
      Rmin = (CL - CLE) / (CSA + CSAE)
      DIF = 2.0 / (((GASPRE + 1.0) ** 2.0) - 1.0)
      GASP = Vave * RATIO * DIF
      GASPERH = (Vmax * Rmax * DIF) - GASP
      GASPERL = GASP - (Vmin * Rmin * Dif)
      WATP = GASP * 0.0174
      WATPERH = GASPERH * 0.0174
      WATPERL = GASPERL * 0.0174
c
c Write to output matrix and screen
c
      B(1,j) = CONFP
      B(2,j) = GASPRE
      B(3,j) = GASP
      B(4,j) = GASPERH
      B(5,j) = GASPERL
      B(6,j) = WATP
      B(7,j) = WATPERH
      B(8,j) = WATPERL
      write(3,20) NAME(j), (B(i,j), i=1,8)
      write(6,20) NAME(j), (B(i,j), i=1,8)
100   continue
200   continue
c
      write(6,*) 'FOR LIST OF VALUES PRINT OUTPUT FILE', file 2
c
c Format statements
c
10    format (a6,a7,a5,a9,5a10)
20    format (a7,f6.1,f5.1,6E10.4Ee)
      stop
      end
```

A10.3 FPORE: the calculation of fracture porosity from S.E.M. photographs.

```
      program fpore
c
c Calculation of fracture-porosity
c
c BY STEPHEN HAY.....May 1988
c
c Program will calculate the fracture porosity from SEM
c photos. It is set up to read in 2 sets of 5 lines of data, taken at 90°
c to each other, measured from SEM photos. Data input is free format as
c length of fractures, total length of picture and # of cracks
c counted in the picture.
c
c Declare program variables
      character file 1 *9
      character file 2 *9
      character *10 name
      dimension A(3,1000), B(2,1000)
      real mu, length, opicpore, ototpore, ppicpore, ptotpore
      real opicdens, ototdens, ppicdens, ptotdens
c
c Assign local file names
c
      write(6,*)'CALCULATION OF SEM FRACTURE POROSITY'
      write(6,*)'BY STEPHEN HAY     1988'
      write(6,*)'  '
      write(6,*) 'ENTER NAME OF INPUT FILE'
      read(5,*)  file1
      write(6,*) 'ENTER NAME OF OUTPUT FILE'
      read(5,*)  file2
      write(6,*) 'ENTER THE Mu SCALE BAR LENGTH IN Mu'
      read(5,*)  scale
      write(6,*) 'ENTER THE MEASURED LENGTH OF THE SCALE BAR IN Cm'
      read(5,*)  length
c
c Assign input/output channels for files
c
      open(2,file=file1)
      open(3,file=file2)
c
c Calculate palaeoporosity
c
      avepore = 0.0
      avedens = 0.0
      ptotpore = 0.0
      ototpore = 0.0
      ptotdens = 0.0
      ototdens = 0.0
      m=0
      mu = scale / length
      read(2,*)  name
      write(3,*)  name
100   do 900, j=1+m,1+m
      read(2,*,end=300)  numb
900   continue
      do 200, j=1,10
      read(2,*)   (A(i,j),i=1,3)
```

```
      if(A(1,j).eq.0.0)then
      B(1,j) = 0.0
      else
      B(1,j) = (A(1,j) / A(2,j)) * 100
      endif
      if(A(3,j).eq.0.0)then
      B(2,j) = 0.0
      else
      B(2,j) = ((A(3,j) / A(2,j)) * 1000) / mu
      endif
200   continue
      opicpore = (B(1,1)+B(1,2)+B(1,3)+B(1,4)+B(1,5)) * 0.2
      ppicpore = (B(1,6)+B(1,7)+B(1,8)+B(1,9)+B(1,10)) * 0.2
      opicdens = (B(2,1)+B(2,2)+B(2,3)+B(2,4)+B(2,5)) * 0.2
      ppicdens = (B(2,6)+B(2,7)+B(2,8)+B(2,9)+B(2,10)) * 0.2
      write(3,10) numb, opicpore, ppicpore, opicdens, ppicdens
      avepore = avepore + ((opicpore + ppicpore) * 0.5)
      avedens = avedens + ((opicdens + ppicdens) * 0.5)
      ototpore = ototpore + opicpore
      ptotpore = ptotpore + ppicpore
      ototdens = ototdens + opicdens
      ptotdens = ptotdens + ppicdens
      n = (m * 0.10) + 1
      m = m + 10
      goto 100
300   continue
      avepore = avepore / n
      avedens = avedens / n
      ototpore = ototpore / n
      ptotpore = ptotpore / n
      ototdens = ototdens / n
      ptotdens = ptotdens / n
      write(3,20) ototpore, ototdens
      write(3,30) ptotpore, ptotdens
      write(3,40) avepore, avedens
      write(6,*) 'FOR LIST OF CALCULATED VALUES PRINT FILE', file2
c
c Format statements
c
10    format ('#',i5,2x,'opor%',f7.2,2x,'ppor%',f7.2,2x,'odens',f7.2,
     *2x,'pdens',f7.2)
20    format ('Total orthogonal porosity',f7.2,'%',2x,'Total orthogonal',
     *' cracks/mm',f7.2)
30    format ('Total parallel porosity',f7.2,'%',2x,'Total parallel',
     *' cracks/mm',f7.2)
40    format ('Total average porosity',f7.2,'%',2x,'Total average',
     *' cracks/mm',f7.2)
      stop
      end
```

A10.4 MODEL: the calculation of fracture permeability from S.E.M photographs

```
      program model
c
c PERMEABILITY MODELLING PROGRAMME
c BY STEPHEN HAY .....August 1988
c This program applies the cubic law for fracture permeability
c to fractures measured from SEM photographs, or any fracture
c array of known dimensions. The equations used are derived
c from Witherspoon et al.(1980), and
c relates to Darcy's law for permeability to straight flow.
c
c PRINCIPAL VARIABLES USED IN THIS PROGRAM
c
c                              DIMENSIONS
c
c D = core diameter                                   (L)
c L = core length                                     (L)
c A = core surface area                               (L2)
c iwidth = intergranular crack width                  (L)
c bwidth = background crack width                     (L)
c idens = intergranular crack density                 - - -
c bdens = background crack density                    - - -
c Ro = fluid density (water)                          (M/L3)
c Mu = dynamic viscosity (water)                      (M/LT)
c G = acceleration due to gravity                     (L/T2)
c iE = intergranular asperitie height                 (L)
c bE = background asperitie height                    (L)
c Z = derived crack length                            (L)
c P = differential pressure head                      (bars)
c nc = no. of background cracks/core length           - - -
c R = square root function of crack length            (L)
c Tor = flow path tortuosity                          (L)
c AW = crack width-length function                    - - -
c F = frictional component due to asperities          - - -
c Cs = permeability function                          - - -
c Qrat = rate of fluid flow                           (L3/T)
c Qb = background flow rate                           (L3/T)
c Ki = intergranular flow rate                        (L3/T)
c Ki = intergranular crack permeability               (L2)
c Kis = total intergranular permeability              (L2)
c Kb = background crack permeability                  (L2)
c Kbs = total background permeability                 (L2)
c Ks =total system permeability                       (L2)
c
c All measurements are recalculated to darcys, with the units
c used for the dimensions being; centimeters (L), seconds (T),
c grams (M)and viscosity measured in centipoise.
c Differential pressure head is in bars.
c The permeability is calculated for water at 20 °C as the fluid,
c with the final permeability being calculated in darcys.
c
c Declare program variables
c
      real  Ki(9),Kb(9),Kis(9),Kbs(9),Ks(9)
```

```
      real  Qi(9),Qb(9)
      character  file1  *9
      character *7 NAME
      real  D,L,AW,Ro,Mu,G,iE,bE,F,Cs,Tor,Z,nc,Qrat,R
      real  bdens,bwidth,idens,iwidth,bnumb,inumb,P,A
c
c.....
c program constants
c
      G = 981.183
      Ro = 0.99821
      Mu   = 1.0019
c
      write(6,*) 'PERMEABILITY MODELLING PROGRAM.'
      write(6,*) 'BY STEPHEN HAY      1988.'
c
      write(6,*) 'ENTER THE NAME OF THE SAMPLE'
      read(5,*)  NAME
      write(6,*) 'ENTER THE NAME OF THE OUTPUT FILE TO BE CREATED'
      read(5,*)   file1
c
c Assign input/output files to program channels
c
      open(3,file  =  file1)
c.....
c Select core size
c
      write(6,*)'WAS THE SAMPLE RUN AS A JACKETED CORE?',
      *'ENTER 1 FOR YES, 2 FOR NO.'
      read(5,*)  core
      if(core.eq.1)then
      D = 4.4
      else
      D = 5.45
      endif
      write(6,*) 'ENTER THE CORE LENGTH (cm)'
      read(5,*)  L
      A  =  3.1415927  *  ((D**2)/  4)
c
c Read in the density and widths of the cracks for sample
c
      write(6,*) 'WERE THERE INTERGRANULAR CRACKS IN THIS SAMPLE?',
      *'ENTER 1 FOR YES, OR 2 FOR NO.'
      read(5,*)  cracktype
      if(cracktype.eq.1)then
      goto 100
      else
      goto 200
      endif
100   continue
      write(6,*) 'ENTER THE INTERGRANULAR CRACK DENSITY (cracks/mm)'
      read(5,*)  idens
      idens = idens * 10
      write(6,*) 'ENTER THE AVERAGED WIDTH OF THESE CRACKS (um)'
      read(5,*)  iwidth
      iwidth = iwidth / 10000
200   continue
      write(6,*) 'ENTER THE BACKGROUND CRACK DENSITY (cracks/mm)'
      read(5,*)  bdens
      bdens = bdens * 10
```

```
        write(6,*) 'ENTER THE AVERAGED WIDTH OF THESE CRACKS (um)'
        read(5,*)  bwidth
        bwidth = bwidth / 10000
c
c Enter any asperite values
c
        write(6,*)'DO YOU WANT TO INCLUDE ASPERITIES?',
        *'ENTER 1 FOR YES, 2 FOR NO.'
        read(5,*)  asper
        if(asper.eq.1)then
        if(cracktype.eq.1)then
        write(6,*)'PLEASE ENTER INTERGRANULAR ASPERITIE HEIGHT (um)'
        read(5,*)  iE
        iE = iE / 10000
        write(6,*)'PLEASE ENTER BACKGROUND ASPERITIE HEIGHT (um)'
        read(5,*)  bE
        bE = bE / 10000
        goto 300
        else
        write(6,*)'PLEASE ENTER BACKGROUND ASPERITIE HEIGHT (um)'
        read(5,*)  bE
        bE = bE / 10000
        goto 400
        endif
        else
        iE = 0.0
        bE = 0.0
        if(cracktype.eq.1)then
        goto 300
        else
        goto 400
        endif
        endif
c.....
c Calculation of the intergranular system
c
300     continue
c
c Calculate the number of cracks of this size there would be in a core
c
        inumb = idens * D
c
c Derive the permeability of the intergranular crack system
c
        F  =  1+(6.0  *((iE/iwidth)**1.5))
        AW  =  (log(iwidth)+1.3)/0.7
        Z = exp(AW)
        Cs  =  (Ro*G)/(12*Mu)
        write(6,*) 'INTERGRANULAR PERMEABILITY - STRAIGHT FLOW'
        Qrat  =  (Cs/F)*(iwidth**3)
c
c Calculation of flow rate at variable pressure gradient
c
        write(6,*) '     Q    ', '     Kf    ', '     Ks    '
        do500,  i=1,5
        P = i
        Qi(i) = Qrat *i
        Ki(i)  =  (Mu*Qi(i))*(L/A)*(2/(((1  +  P)**2)-1))
c
```

```
c Calculate the permeability of this system
c
      Kis(i) = Ki(i) * inumb
      write(6,*) Qi(i), Ki(i), Kis(i)
500   continue
c
c Calculation of the background system
c
400   continue
c
c Calculate the number of cracks of this size there would be in a core
c
      bnumb = A*(2*(bdens*bdens-1)
c
c Calculation of permeability
c
      F = 1+(6.0 *((bE/bwidth)**1.5))
      AW = (log(bwidth)+1.3)/0.7
      Z = exp(AW)
      nc = L / Z
      R = sqrt((Z**2)+(Z**2))
      Tor = R * nc
      Cs = (Ro*G)/(12*Mu)
      write(6,*) 'BACKGROUND PERMEABILITY - STRAIGHT FLOW'
      Qrat = (Cs/F)*(bwidth**3)
c
c Calculation of flow rate at variable pressure gradient
c
      write(6,*) '    Q    ', '    Kf    ', '    Ks    '
      do600, i=1,5
      P = i
      Qb(i) = Qrat *i
      Kb(i) = (Mu*Qb(i))*(Tor/A)*(2/(((1 + P)**2)-1))
c
c Calculate the permeability of this system
c
      Kbs(i) = Kb(i) * bnumb
      write(6,*) Qb(i), Kb(i), Kbs(i)
600   continue
c
c Calculate the total permeability
c
      write(6,*) 'TOTAL PERMEABILITY FOR THE SYSTEM MODELED'
      if(cracktype.eq.1)then
      do700, i=1,5
      Ks(i) = (Kbs(i) + Kis(i))
      write(6,*) 'Ks(total) = ', Ks(i)
700   continue
      else
      do800, i=1,5
      Ks(i) = Kbs(i)
      write(6,*) Ks(i)
800   continue
      endif
c.....
c Remodel options
c
      write(6,*)'DO YOU WANT TO REMODEL THE PERMEABILITY?',
     *'ENTER 1 FOR YES, 2 FOR NO.'
```

```
      read(5,*)  remodel
      if(remodel.eq.1)then
      goto 1000
      else
      goto 1300
      endif
c
c Remodel asperities
c
1000  write(6,*)'DO YOU WANT TO CHANGE ASPERITIE VALUES?',
     *'ENTER 1 FOR YES, 2 FOR NO.'
      read(5,*)  asper
      if(asper.eq.1)then
      if(cracktype.eq.1)then
      write(6,*)'PLEASE ENTER INTERGRANULAR ASPERITIE HEIGHT (um)'
      read(5,*)  iE
      iE = iE / 10000
      write(6,*)'PLEASE ENTER BACKGROUND ASPERITIE HEIGHT (um)'
      read(5,*)  bE
      bE = bE / 10000
      else
      write(6,*)'PLEASE ENTER BACKGROUND ASPERITIE HEIGHT (um)'
      read(5,*)  bE
      bE = bE / 10000
      endif
      else
      goto 1100
      endif
c
c Remodel widths
c
1100  write(6,*)'DO YOU WANT TO CHANGE THE WIDTHS?',
     *'ENTER 1 FOR YES, 2 FOR NO.'
      read(5,*)  width
      if(width.eq.1)then
      if(cracktype.eq.1)then
      write(6,*)'PLEASE ENTER NEW INTERGRANULAR WIDTHS (um)'
      read(5,*)  iwidth
      iwidth = iwidth / 10000
      write(6,*)'PLEASE ENTER NEW BACKGROUND WIDTHS (um)'
      read(5,*)  bwidth
      bwidth = bwidth / 10000
      else
      write(6,*)'PLEASE ENTER NEW BACKGROUND WIDTHS (um)'
      read(5,*)  bwidth
      bwidth = bwidth / 10000
      endif
      else
      goto 1200
      endif
c
c Remodel crack density
c
1200  write(6,*)'DO YOU WANT TO CHANGE THE CRACK DENSITIES?',
     *'ENTER 1 FOR YES, 2 FOR NO.'
      read(5,*)  density
      if(density.eq.1)then
      if(cracktype.eq.1)then
      write(6,*)'PLEASE ENTER NEW INTERGRANULAR DENSITY (cracks/mm)'
      read(5,*)  idens
```

```
      idens = idens * 10
      write(6,*)'PLEASE ENTER NEW BACKGROUND DENSITY (cracks/mm)'
      read(5,*)  bdens
      bdens = bdens * 10
      goto 300
      else
      write(6,*)'PLEASE ENTER NEW BACKGROUND DENSITY (cracks/mm)'
      read(5,*)  bdens
      bdens = bdens * 10
      goto 400
      endif
      else
      if(cracktype.eq.1)then
      goto 300
      else
      goto 400
      endif
      endif
1300  continue
c
c output of results
c
      iE = iE * 10000
      bE = bE * 10000
      iwidth = iwidth * 10000
      bwidth = bwidth * 10000
      idens = idens / 10
      bdens = bdens / 10
c
      write(6,20)  NAME
c
      if(cracktype.eq.1)then
      write(6,*) 'STRAIGHT FLOW'
      write(6,30)  iwidth,  idens
      write(6,40)  bwidth,  bdens
      write(6,50)  iE,  bE
      else
      write(6,*) 'STRAIGHT FLOW'
      write(6,40)  bwidth,  bdens
      write(6,60)  bE
      endif
      do1400,  i=1,5
      P = i
      write(3,*)  P,  Ks(i)
      write(6,70)  P,  Ks(i)
1400  continue
c
c format statements
c
10    format(a9)
20    format('SAMPLE',a9,5x,'PERMEABILITY FINAL MODEL')
30    format('inter  width=',x,f6.1,'um',5x,'inter  density=',x,f8.5)
40    format('bckgrnd  width=',x,f6.1,'um',5x,'bckgrnd  density=',x,f8.5)
50    format('inter asp ht.=',x,f5.2,'um',5x,'Bckgrnd asp ht.=',
      *x,f5.2)
60    format('Background asperite height =',x,f5.2)
70    format('press.=',f5.1,'bar','/','perm.=',E11.6Ee)
      stop
      end
```

A10.5 RBSR: the calculation of Rb-Sr initial ratio and model age

```
      program rbsr
c
c Rb/Sr MODELLING PROGRAMME
c BY STEPHEN HAY.....June 1988
c
c  This program will model the Rb/Sr age of minerals
c or the initial ratios for systems of a model age.
c  input is by a free format file containing:-
c 1. sample name.  2. 87Rb/86Sr present ratio. and
c 3. 87Sr/86Sr present ratio.
c Min. and Max. model ages or model initial ratios are
c input on prompt.
c
c Program variables
      real intrat
      dimension  A(3,50)
      character  file1 *9
      character  file2 *9
      character  name(20) *9
c
c Name and open output file
c
      write(6,*)'Rb/Sr MODELLING PROGRAMME'
      write(6,*)'BY STEPHEN HAY     1988'
      write(6,*)' ENTER THE NAME OF THE INPUT FILE.'
      read(5,*)  file1
      open(2,file=file1)
      write(6,*)' ENTER THE NAME OF THE OUTPUT FILE.'
      read(5,*)  file2
      open(3,file=file2)
c
c Choose model
c
100   write(6,*)'DO YOU WANT TO MODEL AGE OR INITIAL RATIO?'
      write(6,*)'TYPE 1 FOR AGE, 2 FOR INITIAL RATIO OR 3 TO EXIT'
      read(5,*)  choice
      if(choice.eq.1)then
      write(6,*)'Rb/Sr AGE MODELLING.'
      write(6,*)'ENTER MIN. 87Sr/86Sr INITIAL RATIO'
      read(5,*)  X
      write(6,*)'ENTER MAX. 87Sr/86Sr INITIAL RATIO'
      read(5,*)  Y
      do 200 j=1,10
      read(2,*,end=600)  name(j),  (A(i,j),  i=1,2)
      if(j.gt.1)then
      write(6,*)'DO TOU WANT TO KEEP THE SAME Sr(i) RANGE?'
      write(6,*)'1= YES    2= NO'
      read(5,*)  cho
      endif
      if(cho.eq.2)then
      write(6,*)'ENTER MIN. 87Sr/86Sr INITIAL RATIO'
      read(5,*)  X
      write(6,*)'ENTER MAX. 87Sr/86Sr INITIAL RATIO'
      read(5,*)  Y
      endif
      rbratiof  =  A(1,j)
```

```
      srratiof = A(2,j)
      write(3,10) name(j), rbratiof, srratiof
      write(6,10) name(j), rbratiof, srratiof
c
c Calculation of Rb/Sr age
c
      do 300 srratioi=X, Y, 0.0001
      age = ((2.303/1.42e-11) * (LOG10 (((A(2,j) - srratioi)
      * /A(1,j)) + 1.0))) / 10.0e5
      write(3,20) srratioi, age
      write(6,20) srratioi, age
300   continue
200   continue
600   goto 100
      elseif(choice.eq.2)then
      write(6,*)'Rb/Sr INITIAL RATIO MODELLING.'
      write(6,*)'ENTER MIN. PRESUMED AGE OF BLOCKING (Ma)'
      read(5,*) X
      write(6,*)'ENTER MAX. PRESUMED AGE OF BLOCKING (Ma)'
      read(5,*) Y
      do 400 j=1,10
      read(2,*,end=700) name(j), (A(i,j), i=1,2)
      if(j.gt.1)then
      write(6,*)'DO YOU WANT TO KEEP THE SAME AGE RANGE?'
      write(6,*)'1= YES   2= NO'
      read(5,*) cho
      endif
      if(cho.eq.2)then
      write(6,*)'ENTER MIN. PRESUMED AGE OF BLOCKING (Ma)'
      read(5,*) X
      write(6,*)'ENTER MAX. PRESUMED AGE OF BLOCKING (Ma)'
      read(5,*) Y
      endif
      rbratiof = A(1,j)
      srratiof = A(2,j)
      write(3,10) name(j), rbratiof, srratiof
      write(6,10) name(j), rbratiof, srratiof
c
c Calculation of initial ratio
      do 500 agep=X, Y, 5.0
      grad = (EXP(1.42e-11*(agep*1000000.0)))-1.0
      delsr = (grad * rbratiof)
      intrat = srratiof - delsr
      write(3,30) agep, intrat
      write(6,30) agep, intrat
500   continue
400   continue
700   goto 100
      elseif(choice.eq.3)then
      goto 800
      endif
800   continue
c
c Format statements
10    format('Sample',x,a7,3x,'87Rb/86Sr(t)=',x,f10.7,3x,'87Sr/86Sr(t)=',
      * x,f10.7)
20    format('modeled  87Sr/86Sr(i)=',x,f10.7,3x,'Age',x,f10.3,x,'Ma.')
30    format('modeled  age',x,f10.3,x,'Ma.',3x,'87Sr/86Sr(i)=',x,f10.7)
      stop
      end
```

A10.6 PREH: calculation of the ionic formula of prehnite

```
      program preh
c
c CALCULATION OF PREHNITE IONIC FORMULA
c BY STEPHEN HAY.....May 1988
c
c This programme will take an oxide wt% formula for prehnite
c (Si,Ti,Al,Fe,Mn,Mg,Ca,Na,K in that order) with Fe as Fe2O3.
c It will then calculate the ionic formula for prehnite, providing
c W, X, Y and Z site norm ratios. Analysis is based on 24 oxygens
c and assumes a formula of W4 X2 Y2 Z6 O10 OH2. With a pumpellyite
c formula of Ca2 Al (AlSi3 O10)(OH)2 -> Ca2 Fe (AlSi3 O10)(OH)2
c Where W = Ca,Na,K. X = Al,Mg,Mn. Y = Al,Fe3+,Ti. Z = Si.
c
c Declare program variables
c
      dimension A(15,300), B(15,300), C(15,300), D(15,300)
      dimension E(15,300), fwt(9), aox(9), rat(9)
      character file1 *9
      character file2 *9
      character *15 name(100)
      data fwt/60.085,79.899,101.961,159.692,70.937,40.304,56.079,
      *61.979,92.195/
      data aox/2.0,2.0,3.0,3.0,1.0,1.0,1.0,1.0,1.0/
      data rat/2.0,2.0,1.5,1.5,1.0,1.0,1.0,0.5,0.5/
c
      write(6,*) 'CALCULATION OF PREHNITE IONIC FORMULA'
      write(6,*) 'BY STEPHEN HAY    1988'
c
c Assign local file names
c
      write(6,*) 'ENTER NAME OF INPUT FILE'
      read(5,*) file1
      write(6,*) 'ENTER NAME OF OUTPUT FILE'
      read(5,*) file2
c
c Assign input/output files to program channels
c
      open(2,file=file1)
      open(3,file=file2)
c
c Read input file
c
      do 100, j=1,100
      read(2,*,end=150) name(j), (A(i,j),i=1,9)
c
c Calculate molecular proportions of oxides
c
      do 200, i=1,9
      B(i,j) = A(i,j)/fwt(i)
200   continue
c
c Calculate the atom proportion of oxygen for each mol.
c
      subtot = 0
      do 300, i=1,9
      C(i,j) = B(i,j) * aox(i)
```

```
      subtot = subtot + C(i,j)
300   continue
c
c Calculate the No of anions on the basis of 24 oxygens
c
      tot = 24/subtot
      do 400, i=1,9
      D(i,j) = C(i,j) * tot
400   continue
c
c Calculate the No of ions in the formula
c
      do 500, i=1,9
      E(i,j) =  D(i,j)/rat(i)
500   continue
c
c Normalization of the Z site.
c
      if(E(1,j).gt.6.0)then
      E(1,j) = 6.0
      alz = 0.0
      else
      E(1,j) =   E(1,j)
      alz = 6.0 - E(1,j)
      E(3,j) = E(3,j) - alz
      endif
c
c Calculate and normalize the W site
c
      wtot = E(7,j) + E(8,j) + E(9,j)
      if(wtot.eq.4.0)then
      wtot = wtot
      else
      do 600 i=7,9
      E(i,j) =(4.0/wtot) * E(i,j)
600   continue
      endif
c
c Calculate the Fe-Al ratio of the Y site
c
      alt = E(3,j)
      E(3,j) = alt * 0.5
      ytot = E(2,j) + E(3,j) + E(4,j)
      if(ytot.eq.2.0)then
      ytot = 2.0
      else
      do 700 i=2,4
      E(i,j) = (2.0/ytot) * E(i,j)
700   continue
      aly = E(3,j)
      endif
c
c Normalize the X site
c
      fex = 0
      E(3,j) = alt * 0.5
      xtot =  E(5,j) + E(6,j) + E(3,j)
      if(xtot.eq.2.0)then
      xtot = 2.0
      else
```

```
      do 800 i=2,4
      E(i,j) = (2.0/xtot) * E(i,j)
800   continue
      alx = E(3,j)
      endif
c
c Calculate the Y site Fe3+ - Al3+ ratio
c
      fepist = E(4,j) / (aly + E(4,j))
      feclin = aly / (aly + E(4,j))
c
      E(3,j) = alx + aly
c
c Write the results to the screen and file
c
      write(3,*) ' '
      write(6,*) ' '
      write(3,10)  name(j)
      write(6,10)  name(j)
      write(3,*) 'Number of ions in formula, 24 (O).'
      write(6,*) 'Number of ions in formula, 24 (O).'
      write(3,20)  'Si','Ti','Al','Fe3+','Mn2+',
      *'Mg','Ca','Na','K'
      write(6,20)  'Si','Ti','Al','Fe3+','Mn2+',
      *'Mg','Ca','Na','K'
      write(3,30)  (E(i,j),  i=1,9)
      write(6,30)  (E(i,j),  i=1,9)
      write(3,40)  E(1,j),alz
      write(6,40)  E(1,j),alz
      write(3,50)  E(4,j),aly
      write(6,50)  E(4,j),aly
      write(3,60)  fex,alx
      write(6,60)  fex,alx
      write(3,70)  fepist
      write(6,70)  fepist
      write(3,80)  feclin
      write(6,80)  feclin
100   continue
150   continue
      write(6,*) 'FOR LIST OF CORRECTED NORMS PRINT FILE', file2
c
c Format statements
c
10    format  (a15)
20    format  (3x,9a7)
30    format  (3x,9f7.3)
40    format ('Si in Z site =',f6.3,5x,'Al in Z site =',f6.3,)
50    format ('Fe3+ in Y site =',f6.3,3x,'Al in Y site =',f6.3,)
60    format ('Fe3+ in X site =',f6.3,3x,'Al in X site =',f6.3,)
70    format ('mol% Fe3+ in Y=',f6.3,2x,'(mol% pistacite)')
80    format ('mol% Al3+ in Y=',f6.3,2x,'(mol% clinozoisite)')
      stop
      end
```

A10.7 PUMP: calculation of the ionic formula of pumpellyite

```
      program pump
c
c CALCULATION OF PUMPELLYITE IONIC FORMULA
c BY STEPHEN HAY.....May 1988
c
c This programme will take an oxide wt% formula for pumpellyite
c (Si,Ti,Al,Fe,Mn,Mg,Ca,Na,K in that order) with Fe as FeO.
c it will then calculate the ionic formula for pumpellyite, providing
c W, X, Y and Z site norm ratios. Analysis is based on 14 oxygens
c and assumes a formula of W4 X2 Y4 Z6 O21 OH7. With a pumpellyite
c formula of Ca4 (Mg,Fe2+) (Al,Fe3+)5 Si6O21 (OH)7. With an X
c configuration of (Mg,Fe2+,Mn)2-x (Fe3+,Al)x ,(With x=1). Z = Si,Al.
c Y = Fe3+,Al,Ti and W = Ca,NA,K.
c
c Pumpellyite structure taken from:
c Nakajima et al. 1977. Journal of Petrology, 18, 263-84; and
c Coombs et. al. 1976. Journal of Petrology, 17, 440-71.
c
c Declare program variables
c
      dimension A(15,300), B(15,300), C(15,300), D(15,300)
      dimension E(15,300), F(15,300), fwt(9), aox(9), rat(9)
      character file1 *9
      character file2 *9
      character *15 name(100)
      data fwt/60.085,79.899,101.961,71.846,70.937,40.304,56.079,
      *61.979,92.195/
      data aox/2.0,2.0,3.0,1.0,1.0,1.0,1.0,1.0,1.0/
      data rat/2.0,2.0,1.5,1.0,1.0,1.0,1.0,0.5,0.5/
c
      write(6,*) 'CALCULATION OF PUMPELLYITE IONIC FORMULA'
      write(6,*) 'BY STEPHEN HAY    1988'
c
c Assign local file names
c
      write(6,*) 'ENTER NAME OF INPUT FILE'
      read(5,*)  file1
      write(6,*) 'ENTER NAME OF OUTPUT FILE'
      read(5,*)  file2
c
c Assign input/output files to program channels
c
      open(2,file=file1)
      open(3,file=file2)
c
c Read input file
c
      do 100, j=1,100
      read(2,*,end=150)  name(j),  (A(i,j),i=1,9)
c
c Calculate molecular proportions of oxides
c
      do 200, i=1,9
      B(i,j) =    A(i,j)/fwt(i)
200   continue
c
```

```
c Calculate the atom proportion of oxygen for each mol.
c
        subtot = 0
        do 300, i=1,9
        C(i,j) = B(i,j) * aox(i)
        subtot = subtot + C(i,j)
300     continue
c
c Calculate the No of anions on the basis of 14 oxygens
c
        tot = 14/subtot
        do 400, i=1,9
        D(i,j) = C(i,j) * tot
400     continue
c
c Calculate the No of ions in the formula
c
        do 500, i=1,9
        E(i,j) = D(i,j)/rat(i)
500     continue
c
c Calculate the Fe2+ and Fe3+ values from Fe*
c
        Fe2 = 0.5 - (E(6,j) + E(5,j))
        Fe3 = E(4,j) - Fe2
c
        F(1,j) = E(1,j)
        F(2,j) = E(2,j)
        F(3,j) = E(3,j)
        F(4,j) = Fe3
        F(5,j) = Fe2
        F(6,j) = E(5,j)
        F(7,j) = E(6,j)
        F(8,j) = E(7,j)
        F(9,j) = E(8,j)
        F(10,j) = E(9,j)
c
c Calculate and normalize the Z site
c
        if(F(1,j).gt.3.0)then
        F(1,j) = 3.0
        alz = 0.0
        else
        F(1,j) = F(1,j)
        alz = 3.0 - sil
        F(3,j) = F(3,j) - alz
        endif
c
c Calculate and normalize the W site
c
        wtot = F(8,j) + F(9,j) + F(10,j)
        if(wtot.eq.2.0)then
        wtot = wtot
        else
        do 600 i=8,10
        F(i,j) =(2.0/wtot) * F(i,j)
600     continue
        endif
c
```

```
c Calculate the Fe Al ratios of the X and Y sites
c
      feal = F(4,j) / (F(3,j) + F(4,j))
      xfe3 = 0.5 * feal
      xal3 = 0.5 - xfe3
      yfe3 = F(4,j) - xfe3
      yal3 = F(3,j) - xal3
c
c Normalize the X site
c
      xtot = xfe3 + xal3 + F(5,j) + F(6,j) + F(7,j)
      if(xtot.eq.1.0)then
      xtot = 1.0
      else
      F(5,j) = (0.5/xtot) * F(5,j)
      F(6,j) = (0.5/xtot) * F(6,j)
      F(7,j) = (0.5/xtot) * F(7,j)
      endif
c
c Normalize the Y site
c
      ytot = yfe3 + yal3 + F(2,j)
      if(ytot.eq.2.0)then
      ytot = 2.0
      else
      yfe3 = (2.0/ytot) * yfe3
      yal3 = (2.0/ytot) * yal3
      F(2,j) = (2.0/ytot) * F(2,j)
      endif
      F(3,j) = xal3 + yal3
      F(4,j) = xfe3 + yfe3

c
c Calculate the Y site Fe3+ - Al3+ ratio
c
      fepist = yfe3/(yfe3 + yal3)
      feclin = yal3/(yfe3 + yal3)
c
c Write the results to the screen and file
c
      write(3,*) ' '
      write(6,*) ' '
      write(3,10) name(j)
      write(6,10) name(j)
      write(3,*) 'Number of ions in formula, 14 (O).'
      write(6,*) 'Number of ions in formula, 14 (O).'
      write(3,20) 'Si','Ti','Al','Fe3+','Fe2+','Mn2+',
     *'Mg','Ca','Na','K'
      write(6,20) 'Si','Ti','Al','Fe3+','Fe2+','Mn2+',
     *'Mg','Ca','Na','K'
      write(3,30) (F(i,j), i=1,10)
      write(6,30) (F(i,j), i=1,10)
      write(3,40) F(1,j),alz
      write(6,40) F(1,j),alz
      write(3,50) yfe3,yal3
      write(6,50) yfe3,yal3
      write(3,60) xfe3,xal3
      write(6,60) xfe3,xal3
      write(3,70) fepist
```

```
      write(6,70)  fepist
      write(3,80)  feclin
      write(6,80)  feclin
100   continue
150   continue
      write(6,*) 'FOR LIST OF CORRECTED NORMS PRINT FILE',file2
c
c Format statements
c
10    format  (a15)
20    format  (3x,10a7)
30    format  (3x,10f7.3)
40    format ('Si in Z site =',f6.3,5x,'Al in Z site =',f6.3,)
50    format ('Fe3+ in Y site =',f6.3,3x,'Al in Y site =',f6.3,)
60    format ('Fe3+ in X site =',f6.3,3x,'Al in X site =',f6.3,)
70    format ('mol% Fe3+ in Y=',f6.3,2x,'(mol% pistacite)')
80    format ('mol% Al3+ in Y=',f6.3,2x,'(mol% clinozoisite)')
      stop
      end
```